Slip Partitioning, Crustal Tectonics and Deformation of the Queen Charlotte Margin and Northern Vancouver Island

by

Sabine Hippchen
Diplom, Eberhard Karls Universität Tübingen, 2005

A Dissertation Submitted in Partial Fulfillment
of the Requirements for the Degree of

DOCTOR OF PHILOSOPHY

in the School of Earth and Ocean Sciences

Supervisory Committee

Slip Partitioning, Crustal Tectonics and Deformation of the Queen Charlotte Margin and Northern Vancouver Island

by

Sabine Hippchen
Diplom, Eberhard Karls Universität Tübingen, 2005

Supervisory Committee

Dr. Stephane Mazzotti (School of Earth and Ocean Sciences)
Co-Supervisor

Dr. George D. Spence (School of Earth and Ocean Sciences)
Co-Supervisor

Dr. Roy D. Hyndman (School of Earth and Ocean Sciences)
Departmental Member

Dr. Eileen Van der Flier-Keller (School of Earth and Ocean Sciences)
Outside Member

Abstract

Supervisory Committee
Co-Supervisor
Dr. Stephane Mazzotti (School of Earth and Ocean Sciences)
Co-Supervisor
Dr. George D. Spence (School of Earth and Ocean Sciences)
Departmental Member
Dr. Roy D. Hyndman (School of Earth and Ocean Sciences)
Outside Member
Dr. Eileen Van der Flier-Keller (School of Earth and Ocean Sciences)

Part I of this thesis investigates current deformation in western British Columbia from northern Vancouver Island in the south to Haida Gwaii in the north. The area is characterized by transition from the Cascadia subduction zone to the Queen Charlotte transform fault. The tectonic setting involves interactions between the Pacific, North America, Juan de Fuca, and Explorer plates, and the Winona block, involving a number of plate boundaries: the mainly strike-slip Queen Charlotte, Revere-Dellwood-Wilson and Nootka faults, the Explorer ridge, and the Cascadia subduction zone. Using GPS campaign data from 1993 to 2008 I derive a new crustal velocity field for Northern Vancouver Island and the adjacent mainland, and integrate it with previous velocity fields developed for Haida Gwaii, southern Vancouver Island and the adjacent mainland. The northern limit of the subduction zone is confirmed to be at Brooks Peninsula, where the direction of the crustal motion changes abruptly from ENE to NNE. I use viscoelastic models to explore what percentage of the observed deformation is transient, related to the earthquake cycle, and how much is permanent ongoing deformation, distributed off the continental margin. Previous authors have developed two competing end-member models that can each explain how the Pacific/North America plate convergence is accommodated

off Haida Gwaii. These models assume either internal crustal shortening or underthrusting of the Pacific plate. These new GPS data allow me to conclude that underthrusting does occur, and that a small component (<15%) of the observed data reflects long-term deformation. South of Haida Gwaii the distinction between transient and long-term deformation is not as clear; however, I conclude that transient deformation alone cannot fully explain the observed velocities, and so long-term deformation likely must also occur.

Part II of the thesis investigates the updip and downdip limits of the seismogenic zone of the Sumatra megathrust fault. Temperature and downdip changes in formation composition are controls proposed for these limits. To examine the thermal control I developed 2-D finite element models of the Sumatra subduction zone with smoothly varying subduction dip, variable thermal properties of the rock units, frictional heating along the rupture plane, and an appropriate thermal state for the incoming plate. The common updip thermal limit for seismic behaviour of 100-150°C occurs close to or at the trench in agreement with the rupture limit of the 2004 earthquake. Off central Sumatra the common downdip thermal limit range of 350-450°C occurs at 30-60 km depth. The 350°C isotherm location is in agreement with the earthquake limits but 450°C is deeper. North of Sumatra, 350°C occurs ~14 km deeper than the earthquake rupture limit. The proposed composition control for the downdip limit, the intersection of the subduction thrust with the forearc mantle, is at a depth of ~30 km, 140-200 km from the trench, in good agreement with the earthquake limits. These results support the conclusion that the Sumatra updip seismogenic limit is thermally controlled, but the downdip limit is governed by the intersection of the downgoing plate with the forearc Moho.

Table of Contents

List of Tables

List of Figures

Acknowledgements

I would like to thank my supervisors, Dr. Stephane Mazzotti and Dr. George Spence, as well as Dr. Roy Hyndman, for their support and guidance during my research. I also want to thank my committee members, Dr. Eileen Van der Flier – Keller and Dr. Elisabeth Hearn for their time and valuable suggestions.

I would like to thank Dr. John He at the Pacific Geoscience Centre (PGC) for developing the finite element computer code, and for patiently answering all my questions regarding numerical modeling.

Thanks to the researchers and staff at PGC, particularly to Bruce Johnson and Steve Taylor for their IT support. Thanks to Dr. Ikuko Wada and Dr. Natalie Balfour for answering my many questions about GMT. I would also like to thank my field assistant Dr. Lucinda Leonard, as well as Mike Schmidt, Lisa Nykolaishen and Dr. Stephane Mazzotti who completed the fieldwork in 2007. Thanks to Dr. Ralph Currie for helping quickly and without bureaucracy when it was needed.

Many thanks to the staff at the SEOS office, particularly Allison Rose, for her help in getting everything organized.

My thanks to all my friends and fellow grad students for their support and good times.

Mein besonderer Dank geht an meine Familie, fuer ihre Unterstuetzung und Ermutigung.

Preamble

This study consists of two parts:

In Part 1, I present a study of the current tectonics and dynamics of the transition regime between Northern Cascadia Subduction Zone and southern Queen Charlotte margin, using geodetic data and viscoelastic modeling.

In Part II, I investigate the updip and downdip limits of the megathrust seismogenic zone in Sumatra, using structural and thermal models.

Part I
Chapter 1
Introduction

1.1 Motivation and Objectives

The area of western British Columbia from Northern Vancouver Island to Haida Gwaii (formerly Queen Charlotte Islands) is a tectonically complex region, where the challenge of deciphering current crustal deformation is complicated by a lack of data due to the remoteness of the west coast. While other major tectonic systems along the margin off the west coast of North America have been intensively studied (e.g., San Andreas fault, Cascadia subduction zone) based on an abundance of geodetic, structural and other data, the challenge here is to conduct surveys in relatively inaccessible regions and then interpret the collected data in terms of a complex transition tectonic system. This can be quite difficult due to large gaps in the data coverage (geographically as well as in time).

In this thesis, several different steps are in involved in the investigation of current crustal deformation in the context of slip partitioning (transient or permanent deformation, margin-parallel and margin-normal deformation):

(1) Collection of Global Positioning System (GPS) data and update of the velocity field for the west coast of British Columbia

(2) Decomposition of the observed horizontal velocity data into margin-parallel and margin-normal components

(3) Development of a strike-slip model to interpret the margin-parallel velocity component

(4) Development of a convergence model to interpret the margin-normal component

The viscoelastic models are used to investigate whether all observed margin-parallel and margin-normal deformation is transient and therefore related to the earthquake cycle, and if not, how much of it is permanent deformation.

During the modeling part of the study, several questions were addressed.

- What parameterizations do the models require to provide the best-fit possible, and are the parameters providing the best fit reasonable for this particular tectonic and geological setting?
- Can both model types noted above provide a best-fit model while using the same parameterization?
- Do viscoelastic models provide a better fit to the observed velocities than the previously used elastic models?

1.2 Previous work

Over the last two decades, the use of geodetic data, especially Global Positioning System (GPS) data, have become important in the study of current crustal deformation. In order to use geodetic data to investigate the dynamics of faults and the associated earthquake hazard, it is important to understand how the Earth's rheology controls the deformation process related to earthquake cycles. Mazzotti et al. [2003a, b] have analyzed GPS data in the study area previously and used elastic models to interpret the data in the context of transient and permanent deformation. One goal of this thesis is to compare the results of the viscoelastic models to those of the elastic models in order to determine whether the inclusion of a viscoelastic component in the model significantly improves the fit to the GPS data and modifies the results derived from elastic models, or whether elastic models can sufficiently explain the observed data. An important

limitation in this region is the sparse availability of data, which can introduce large uncertainties in model parameter values. For the more complex viscoelastic model, limited data can become more of a difficulty than for the simpler, elastic models. However, when trying to study earthquake cycle related deformation, viscoelastic models are the better approach because they are more realistic than the elastic models. Purely elastic models assume that the deformation of the crust responds instantaneously to the fault motion, and any time-dependence of the deformation is attributed to time-dependent fault slip. However, the mantle as well as the lower crust show an approximately Maxwell viscoelastic behaviour, where imposed stress (e.g., an earthquake) relaxes with time (e.g., Turcotte and Schubert, 2002).

Hence I use 2.5-dimensional viscoelastic dislocation models to investigate the margin-parallel and the margin-normal components of the observed geodetic data.

Chapter 2
Tectonic Setting and Development of the Queen Charlotte Margin and the Northern Cascadia Subduction Zone

2.1 Introduction

Deformation defined by GPS data in the study area along the margin of south-western British Columbia is controlled by the forces of plate interactions across the margin. Three different tectonic systems are identified in this region: (1) Transpressive, dextral strike-slip along the Queen Charlotte fault and the margin west of Haida Gwaii (formerly Queen Charlotte Islands); (2) a transition area between the southern end of the Queen Charlotte fault and the northern end of the Cascadia subduction zone; and (3) the northern Cascadia subduction zone. The principal part of this thesis studies the consequences on the continent of these offshore plate interactions. In this chapter, I review these plate interactions, discuss plate properties including heat flow and crustal thickness, and review previous studies of deformation using GPS methods.

The main plates are the Pacific and the North American plates in contact along the Queen Charlotte margin, as well as the intervening oceanic Juan de Fuca plate system to the south. This series of small plates includes the Juan de Fuca plate off southern Vancouver Island, the Explorer plate off central Vancouver Island north of Nootka Island, and the Winona block north of Brooks Peninsula (e.g., Davis and Riddihough, 1982; Riddihough, 1984; Spindler et al., 1997) (Figure 1).

The Juan de Fuca plate is subducting beneath the North American plate along the Cascadia subduction zone. The Juan de Fuca and Explorer plates are connected across the Nootka fault zone, a left-lateral transform fault (Hyndman et al., 1979). The intersection of this fault with the margin is a triple junction, where the Juan de Fuca, the Explorer and

the North American plates intersect. At the triple junction, the Juan de Fuca plate subducts nearly orthogonally to the margin at about 40 mm/yr, while the Explorer plate to the north subducts at a slower rate of about 20 mm/yr (Davis and Riddihough, 1982; Wilson, 1993; Spindler et al., 1997; Braunmiller and Nabelek, 2002, Mazzotti et al., 2003a).

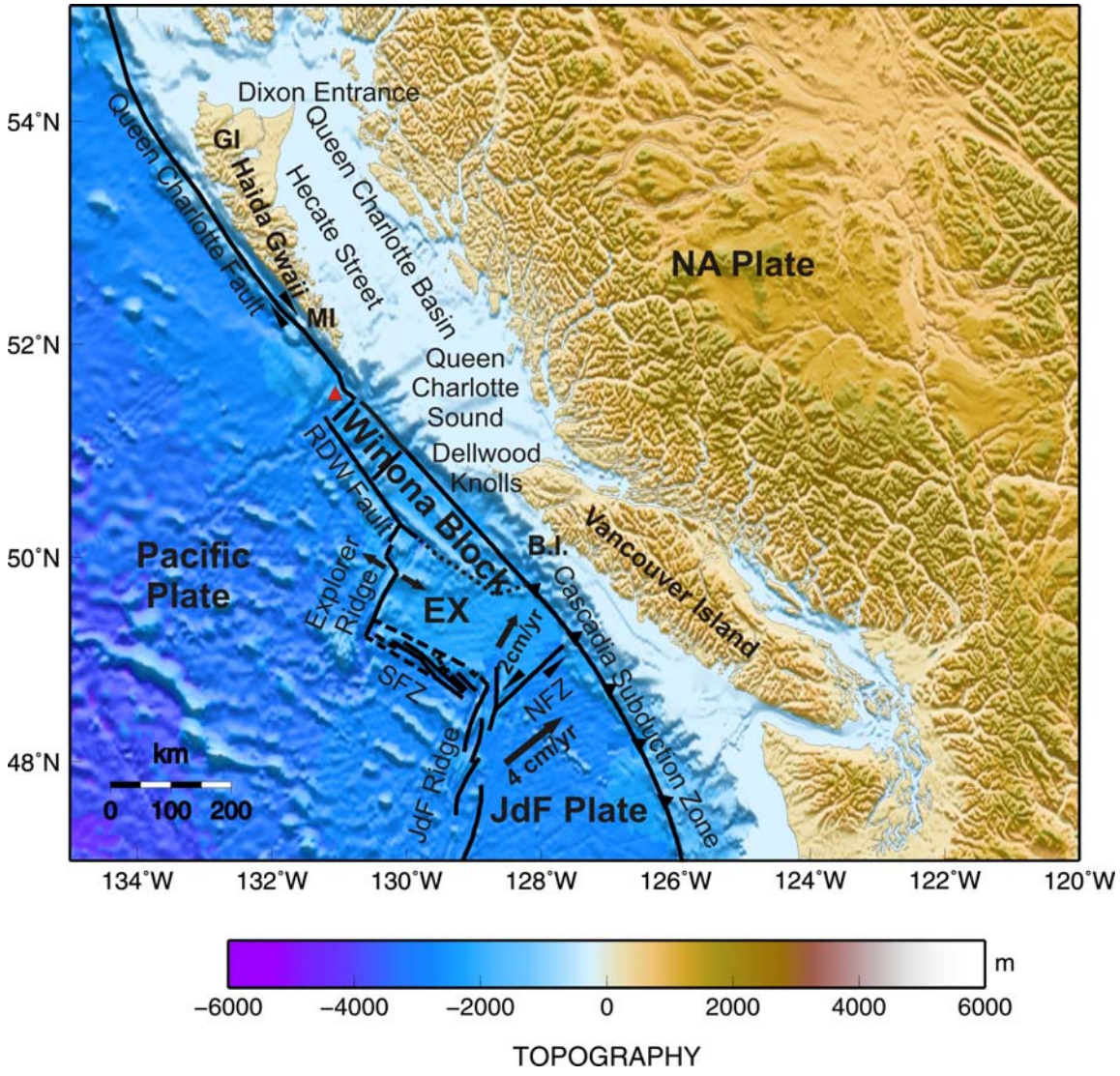

Figure 1 : Tectonic overview of the study area. JDF: Juan de Fuca. NFZ: Nootka Fault Zone. RDW: Revere-Dellwood-Wilson. SFZ: Sovanco Fracture Zone. Ex: Explorer Plate. MI: Moresby Island. GI: Graham Island. B.I.: Brooks Peninsula. Red triangle: Tuzo Wilson seamounts.

2.2 Geological Background

Southern British Columbia can be subdivided into five roughly margin-parallel belts. From west to east, those belts are the Insular Belt, Coast Belt, Intermontane Belt, Omineca Crystalline Belt, and the Foreland Belt (e.g., Monger et al., 1972) (Figure 2).

The *Insular Belt* consists of volcanic and sedimentary rock, as well as intrusions of granitic rock. Deposition of sediments is still ongoing in continental shelf basins. The bedrock of the *Coast Belt* is mainly (80%) granitic rock that includes plutons and batholiths. Those intrusions form the Coast Plutonic Complex. Other rocks in the Coast Belt include metamorphosed, folded and faulted volcanic and sedimentary rock, which are similar to the rocks found in the Insular Belt to the west, and in the Intermontane Belt in the east. The *Intermontane Belt* underlies much of south central British Columbia. It consists of volcanic and sedimentary rocks and granitic intrusions. The *Omineca Belt* contains metamorphic as well as some granitic rock and contains the boundary between new continental crust and rocks eroded from the old continent. The *Foreland Belt* contains sedimentary rocks with a minimum thickness of about 15 km (descriptions of all belts from http://gsc.nrcan.gc.ca/cordgeo/index_e.php and references therein).

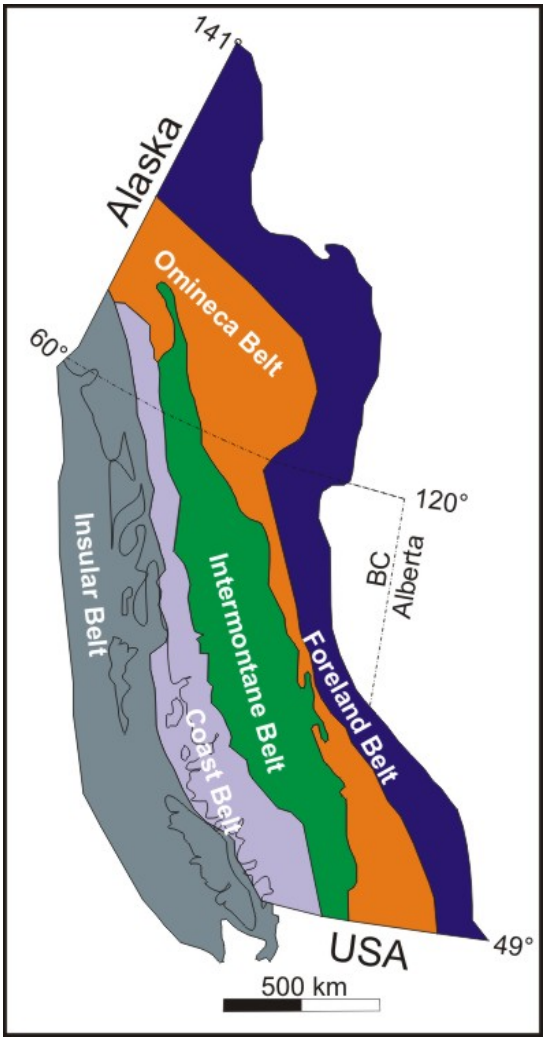

Figure 2: Map of Canadian Cordillera, showing Insular, Coast, Intermontane, Omineca, and Foreland Belt (after Wheeler and McFeely, 1991).

The Canadian Cordillera was formed by the accretion of several microplates and terranes that have been substantially deformed and translated north-westward over the past ~300 Ma (Coney et al. 1980; Monger et al. 1982; Mahoney et al. 1999; Enkin et al., 2008; and others).

With the accretion of terranes since the late Palaeozoic era, the North American continental margin has shifted about 800 km to the west. During this time, the margin has been characterized by tectonics associated with subduction or transform faults (e.g.,

Frisch and Meschede, 2005). The oceanic Pacific plate subducted mostly obliquely beneath the continental North American plate, which led to terranes moving towards the continent and attaching to it (Figure 3), along with northerly translation. The main terranes in our study area are the Stikinia Terrane, Alexander Terrane, and Wrangellia Terrane (Figure 3) (see also Johnston, 2008).

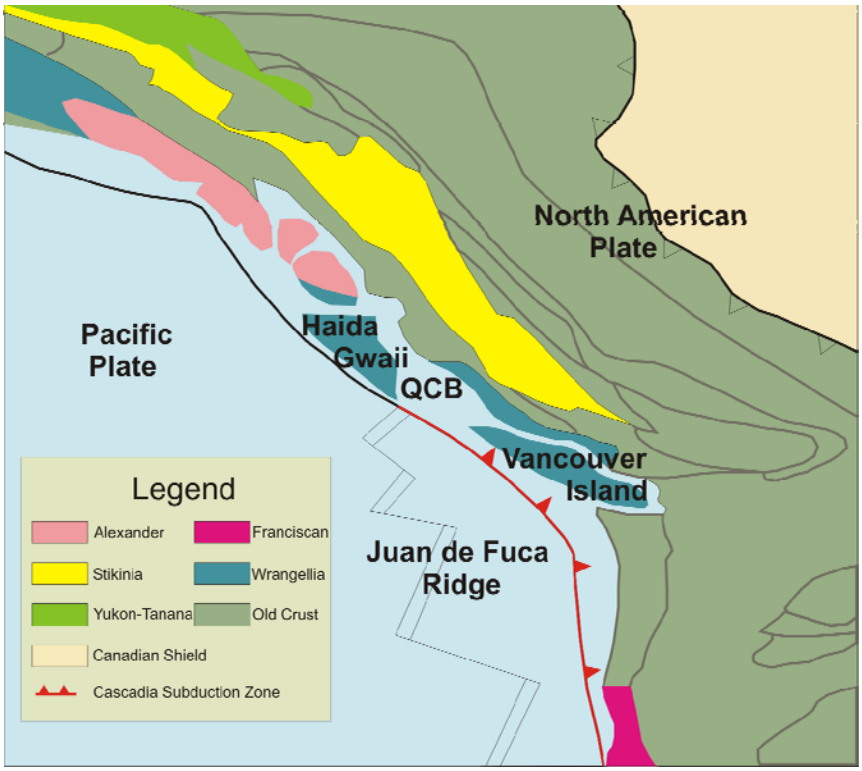

Figure 3: Simplified map of terranes and microplates on the Pacific margin of Canada (after Frisch and Meschede, 2005). QCB: Queen Charlotte Basin. QCF: Queen Charlotte Fault.

The *Yukon – Tanana Terrane* is a continental crustal sliver that collided with North America at least several 100 km south of its current position (e.g., Frisch and Meschede, 2005). It moved northwards along steep dipping fault zones, and is situated in its present position since the Early Tertiary.

The *Alexander* Terrane underlies much of SE Alaska, the Saint Elias Mountains, Yukon Territory and BC, as well as parts of the central west coast of British Columbia. It

consists of upper-Proterozoic – Cambrian through Middle Jurassic rocks, and accredit to North America in the Late Cretaceous or early Tertiary (Gehrels and Saleeby, 1987).

The *Stikinia Terrane* is an accumulation of several small terranes that accreted to North America during the Upper Jurassic, which led to deformation and the formation of tectonic layers due to thrusting. After the accretion the terrane moved northwards along the continental margin, with some motion as late as mid-Tertiary.

The *Wrangellia Terrane* amalgamated with the Peninsular Terrane (a former southern island arc) and the Alexander Terrane in the Middle Jurassic. Deformations with folding and thrusting dating from the Cretaceous indicate that this was probably the time of the collision with North America (e.g.; Frisch and Meschede, 2005). As a result of that collision parts of the terrane were dispersed. The last substantial deformation in this part of the Cordillera was a mid-Tertiary strike-slip motion (e.g., Gabrielse and Yorath, 1991). However, mid to late Tertiary extension occurred in the Queen Charlotte Basin (e.g., Irving et al, 1992).

2.3 Main tectonic features in the study area

2.3.1 Queen Charlotte Fault

The Queen Charlotte fault produced the largest recorded earthquake in Canada, with a magnitude of M=8.1, in 1949. The locking / seismogenic depth of the Queen Charlotte fault is given at depths ranging from 9 km in the North (Schell and Ruff, 1989) to 20 km, where the maximum depth is constrained by micro-earthquake locations off Haida Gwaii (Hyndman and Ellis, 1981). It is a primarily dextral transform fault that separates the oceanic Pacific plate from the continental North American plate. North of Haida Gwaii, the fault motion is purely strike-slip, and the fault runs parallel to the relative motion direction between the two plates (DeMets et al., 1990). At the latitude of Haida Gwaii,

the Pacific plate moves at about 50 – 60 mm/yr northwards, with a component of convergence of about 15 – 20 mm/yr (Engebretson et al., 1985; DeMets et al., 1987; 1990; Hyndman and Hamilton, 1993) corresponding to a ~ 20° difference between the fault trend and the relative plate motion direction (Figure 1). Several theories have been postulated that explain how the convergence component of the relative motion is accommodated, the two most widely discussed ones being (1) slip partitioning into strike-slip motion parallel to the margin and convergent underthrusting motion normal to the margin (Hyndman et al., 1982; Scheidhauer, 1997; Prims et al., 1997; Bustin et al., 2007); or (2) slip partitioning into strike-slip and compressional crustal shortening deformation within either the continent or the adjacent oceanic plate (e.g., Rohr et al., 2000).

2.3.2 Queen Charlotte Basin

Further east, Tertiary sediments and volcanics beneath Dixon Entrance, Hecate Strait, and Queen Charlotte Sound constitute the Queen Charlotte Basin, an approximately 500 km long and 100 km wide basin (Lowe and Dehler, 1995) (Figure 1). The basin was formed mainly by extension in the mid-Tertiary (e.g., Hyndman and Hamilton, 1993). It contains mid-Tertiary lavas, plutons and dykes (the Masset Igneous Complex), as well as marine and non-marine sedimentary rocks dating from the Eocene to Present (e.g., Rohr and Dietrich, 1992; Irving et al., 2000).

Indicators of basin extension are grabens and half-grabens, bound by faults, as identified on reflection seismic data (Rohr and Dietrich, 1992). Further evidence for extension includes the distribution of extensional type volcanism and associated dyke swarms (Hyndman and Hamilton, 1993; Irving et al., 1992), as well as higher heat flow

in the basin compared to the surrounding areas (Lewis et al., 1991; cf. below). The amount of extension estimated for the entire Queen Charlotte region is ~ 20%, based on thermal models, and up ~ 150% in the main basin (Hyndman and Hamilton, 1993).

Various models have been proposed to explain the tectonic evolution of the Queen Charlotte Basin, the most widely accepted one by Irving et al. [1990, 2000]. Mainly based on the studies of Rohr and Dietrich [1992] and Hyndman and Hamilton [1993], Irving et al. [2000] identify three phases of evolution. *Phase 1* is identified as a transtensional phase, in which the formation of the basin was initiated due to a change in the direction of plate motion from strong convergence to transtension in the Eocene (Engebretson et al., 1985; Stock and Molnar, 1988). This transtensional system remained in place for ~ 25 Ma, and most of the Masset Igneous Complex and sediments were deposited during that time. The general sense of extension is east-west, with most of the extensional faults in Hecate Strait and Queen Charlotte Sound oriented in a north-south direction (Rohr and Dietrich, 1992; Rohr and Currie, 1997). During *Phase 2* in the Middle and/or Late Miocene, the plate margin became purely transform, and the east-west extension as well as the igneous activity slowed and eventually stopped. Subsidence of the basin and accordingly deposition of sediments began. The still ongoing *Phase 3* begins in the latest Miocene or earliest Pliocene, when plate motion becomes highly oblique convergent (Engebretson et al., 1985; Stock and Molnar, 1988). This change in plate motion direction leads to uplift and erosion of Haida Gwaii (Yorath and Hyndman, 1983), during which time the subsidence of the basin and deposition of sediments, that started in phase 2, is still ongoing.

Rohr and Dietrich [1995] present a tectonic model explaining the evolution of the Queen Charlotte Basin based on Tertiary plate interactions involving distributed right-lateral shear along the margin. The three different areas of the basin (Dixon Entrance, Hecate Strait, Queen Charlotte Sound) are characterized by different structural trends, due to different responses to the change from transtension in the Miocene to transpression in the Pliocene. Transtension in the Miocene formed half-grabens and grabens, with the faults exhibiting northwest striking right-lateral strike-slip (parallel to the principal displacement direction) as well as dip-slip components of movement (Figure 4 A and C). The faulting ended between the middle and late Miocene (Rohr and Dietrich, 1995). During transpression particularly in the Late Pliocene, large inversion structures and uplifts were formed in Hecate Strait (Figure 4 B), whereas Queen Charlotte Sound does not show any inverted structures (Figure 4 D). One explanation for the different susceptibility of the crust to the transpressive deformation in the Hecate Strait and the Queen Charlotte Basin is variation in crustal thickness (Rohr and Dietrich, 1995).

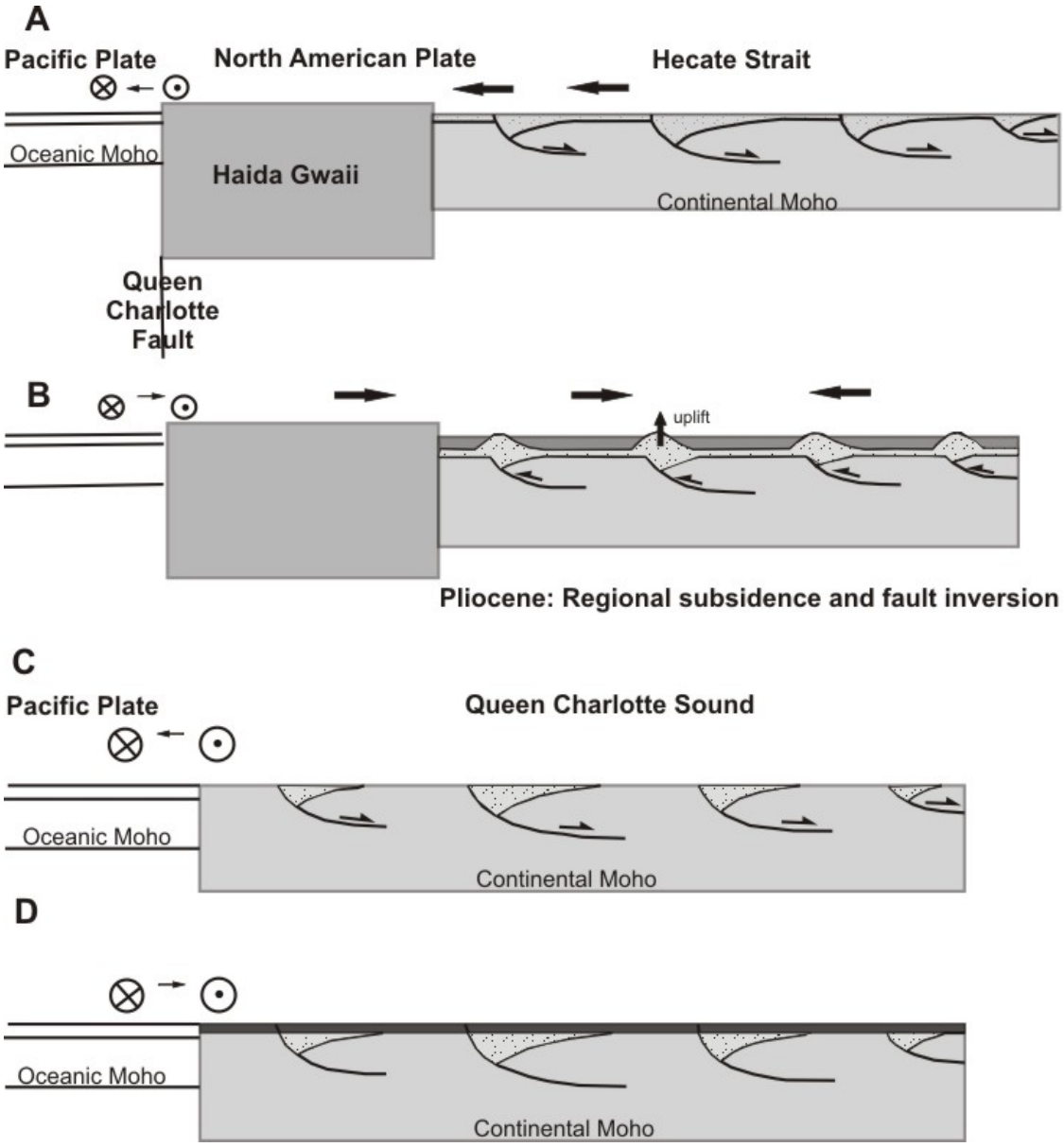

Figure 4: Cross sections showing Hecate Strait (A & B) and Queen Charlotte Sound (C & D). Miocene transtension results in a network of sedimentary subbasins in Hecate Strait and Queen Charlotte Sound (A and C). Pliocene transpression leads to inversion of those basins only in Hecate Strait (B and D) (after Rohr and Dietrich, 1995).

2.3.3 Coast Mountains and Coast Shear Zone

To the east, the Queen Charlotte Basin is bounded by the mainland coast of British Columbia, which includes the Coast Mountains and the Coast Shear Zone (Figure 5).

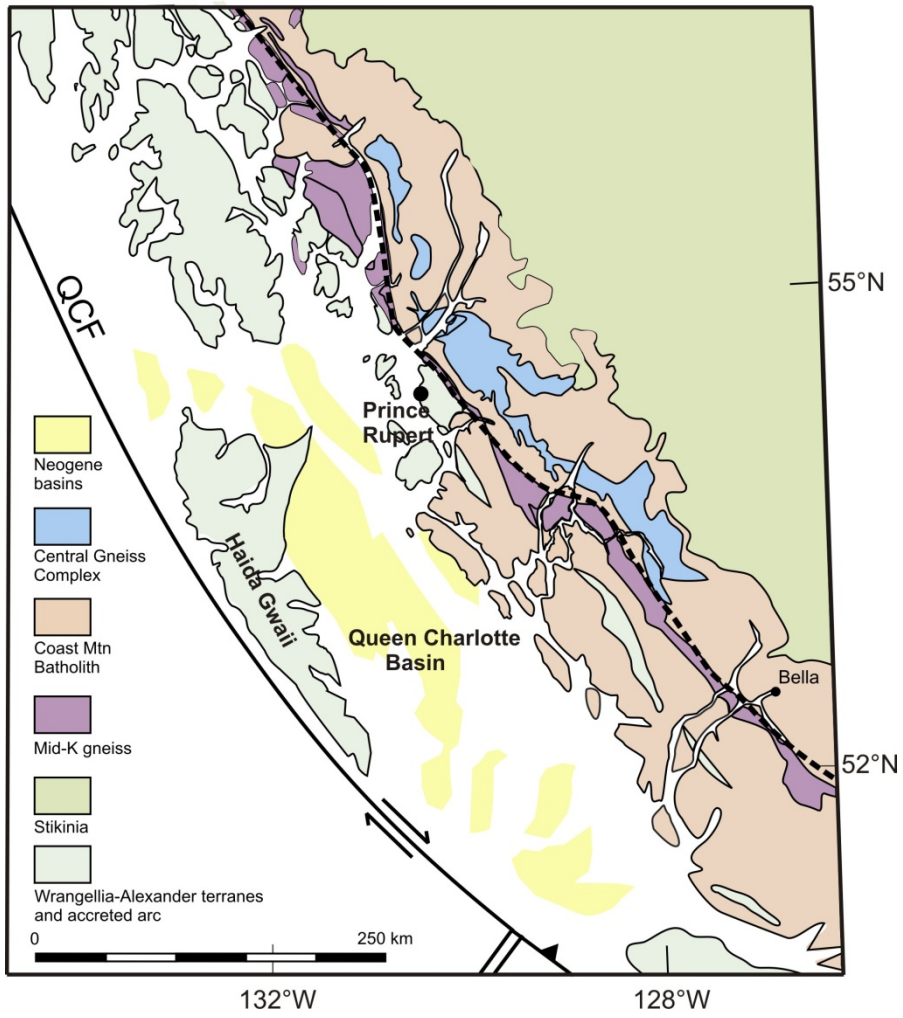

Figure 5: Simplified map of Coast Mountain region. QFC: Queen Charlotte Fault. Black dashed line: Coast Shear Zone (after Rusmore et al., 2010).

The Coast Shear Zone defines the western boundary of the Coast Mountain Plutonic Complex, and is a near vertical, ~ 1200 km long fault zone. It runs parallel to the margin and is characterized by synkinematic plutons and mylonite zones. Although commonly represented by a single line in maps, it is known as a feature with a finite width. The Coast Shear Zone is considered a magmatic front between the Coast Mountain Belt and

the Insular Belt (Figure 2), as well as a thermal age contrast, with the plutons in the Coast Mountain Belt being between 85 and 50 Ma old, and the ones in the Insular Belt older than 80 Ma (Hollister and Andronicos, 2006). It also represents a profound break in the metamorphic grade between the Central Gneiss Complex in the Coast Mountain Belt, which represents a moderate to high metamorphic grade (750°C, ~ 5kBar, ~ 55 Ma), and the Insular Belt, where the metamorphic grade is lower and increases towards the Coast Shear Zone to about 600°C at 8kBar, and where peak metamorphosis took place 90 Ma. The pressure and temperature conditions within the Central Gneiss Complex represent a high thermal gradient and heat flow, which is characteristic of a backarc, whereas the rocks in the Insular Belt represent a significantly lower thermal gradient (Hollister and Andronicos, 2006), possibly a forearc.

Conclusive statements about the sense of shear are very difficult due to a lack of kinematic indicators (Hollister and Andronicos, 2006), and the shear sense determined from non-coaxial structures is variable across the shear zone; however, there is some evidence indicating dextral strike-slip translation in the western part. The southern part is believed to have become active mainly between 55 and 66 Ma ago (Davidson et al., 2003), whereas the northern part was beginning to be active about 50 Ma ago (Rusmore et al., 2010). Neither region shows any evidence of deformation younger than 30 Ma, which is the age of pseudotachylyte veins and indications of brittle deformation in the area of Prince Rupert (Davidson et al., 2003). Hence, although the Coast Shear Zone is a prominent, mainly strike-slip fault zone, there is no geological evidence for significant recent motion. However, such motion cannot be excluded due to a lack of data as a result of the inaccessibility of the area, and the Coast Shear Zone is an important tectonic

feature that has to be considered when interpreting possible current crustal deformation based on geodetic data.

2.3.4 Triple junction and Explorer region

The region west of the margin between 47°N and 52°N is characterized by the interaction between the Juan de Fuca, Explorer, Pacific, and North American plates and the Winona Block. The main tectonic feature is the triple junction, currently located near the Dellwood Knolls and the Tuzo Wilson seamounts, marking the intersection of the spreading ridge system between the Juan de Fuca and the Pacific plates, the Cascadia subduction zone between the North American and the Juan de Fuca plates, and the transpressive Queen Charlotte fault between the Pacific and the North American plates. Several studies (e.g., Carbotte et al., 1989; Riddihough and Hyndman, 1989; Hyndman and Hamilton, 1993) postulate that the triple junction moved to its current position when spreading initiated at the Dellwood spreading centre about 1 Ma. Before that, the triple junction was situated off Brooks Peninsula on Vancouver Island. Another theory is based on the lack of compressive structures in the Queen Charlotte Sound compared to Hecate Strait, which, according to Rohr et al. [2000], indicates that transpression only occurred to the north of the Tuzo Wilson Seamounts. This means that the triple junction has been in its current position for about 5 Ma (Rohr et al., 2000). It is also possible that the move of the triple junction to its current position happened in the context of the formation of the Winona Basin (Davis and Riddihough, 1982).

The tectonic history of the Explorer plate is tightly interwoven with the triple junction. The Explorer plate is bounded to the southeast by the left-lateral Nootka fault, which separates the Explorer plate from the Juan de Fuca plate. The Sovanco Fracture Zone and

the Explorer Ridge define the boundary between the Explorer Plate and the Pacific plate to the southwest and northwest, respectively (Figure 1). Two different tectonic models have been proposed for the region encompassing the triple junction and the Explorer plate:

[1] One model assumes an independent Explorer plate (Riddihough, 1977; 1984). The Farallon plate has been decreasing in size since the Tertiary due to multiple break-up stages (e.g., Engebretson et al., 1985). The first major break-up stage occurred 55-50 Ma ago, when the Farallon – Pacific spreading centre moved towards the Farallon – North America subduction zone, which lead to the formation of the San Andreas and the Queen Charlotte transform faults (Stock and Molnar, 1988; Atwater, 1989). One of the pieces of the former Farallon plate, the Juan de Fuca plate, continued to decrease in size due to migrations of the triple junctions and to further plate break-ups. One particularly noteworthy break-up occurred over the last few million years, when the Gorda deformation zone and the Explorer plate in the south and the north, respectively, moved separately from the remaining Juan de Fuca plate (e.g.; Riddihough, 1980; Barr and Chase, 1974; Botros and Johnson, 1988 and references therein). This breaking apart resulted in different orientations of the Explorer ridge and Juan de Fuca ridge for at least the last 4 Ma, which requires an independent Explorer plate since that time (Riddighough, 1984; Botros and Johnson, 1988). Also postulated is an independent Winona block, based on the shift of the northern end of the Juan de Fuca ridge system from offshore Brooks Peninsula to the area of the Dellwood Knolls and the Tuzo Wilson seamounts 1 – 2 Ma ago (Riddihough et al., 1980). This leads to a Revere-Dellwood-Wilson transform fault more northerly oriented than the Explorer ridge's spreading

direction; subsequently, it leads to an independent Winona microplate which shows a small margin-normal component (Davis and Riddihough, 1982). In conclusion, an independent Explorer plate also suggests an independent Winona block, a theory supported by a deformed accretionary sedimentary wedge (including Pleistocene sediments) along the Explorer as well as the Winona margin, which can be considered evidence for recent convergence and underthrusting (e.g.; Davis and Hyndman, 1989).

[2] Other authors (e.g., Barr and Chase, 1974; Rohr and Furlong, 1995; Rohr and Tyron, 2010) postulate that a new Pacific – North American plate boundary was formed by a northerly transform fault zone cutting through the Explorer region. Independent motion of the Explorer plate as well the Winona block relative to North America would have stopped before the plates were entirely subducted. This model is similar to so-called plate-captures documented for microplates offshore California and Baja California (Lonsdale, 1991). This would leave the remains of the Explorer plate attached to the Pacific and North American plate on either side and result in little to no convergence along the margin north of Nootka fault.

The plate-capture model appears to be inconsistent with GPS data on northern Vancouver Island and the adjacent mainland (Henton et al., 2000; Mazzotti et al., 2003a; also new data presented in this thesis for northernmost Vancouver Island). It is also inconsistent with the presence of the Winona block accretionary sedimentary prism, which can not be explained with this model. It is however possible that microplate capture started only recently, as indicated by the slow convergence, and complete plate capture may happen in the geological near future.

Another important tectonic feature in the area is the Revere-Dellwood-Wilson fault (Figure 1), a seismically very active (Figure 12) right-lateral transform fault which separates the Pacific plate from the Explorer region (Figure 1). It is more north-westerly oriented than the southern part of the Queen Charlotte fault, and hence it is not possible that the Revere-Dellwood-Wilson fault fully accommodates the northerly oriented Pacific – North American motion (Braunmiller and Nabelek, 2002). Either that motion is accommodated by slip-partitioning, where the fault acts as an offset extension of the Queen Charlotte fault, therefore forming the Pacific – North American boundary, with the margin-normal component accommodated within the North American plate. Or the Revere-Dellwood-Wilson fault forms the Pacific –Explorer (Winona) transform boundary, which means that the Pacific and North American plate are separated by the Explorer plate and the Winona block. In that case, convergence is accommodated between the North American and Explorer (Winona) plates (Braunmiller and Nabelek, 2002).

2.4 Crustal structure

Data from several seismic refraction surveys conducted during the 70s and 80s as well as receiver function data were used in numerous studies to interpret the crustal structure of the Hecate Strait, Queen Charlotte Sound and the Queen Charlotte fault region (e.g., Horn et al., 1984; Dehler and Clowes, 1988; Spence and Long, 1995 and references therein; Cassidy et al., 1998; Bustin, 2006).

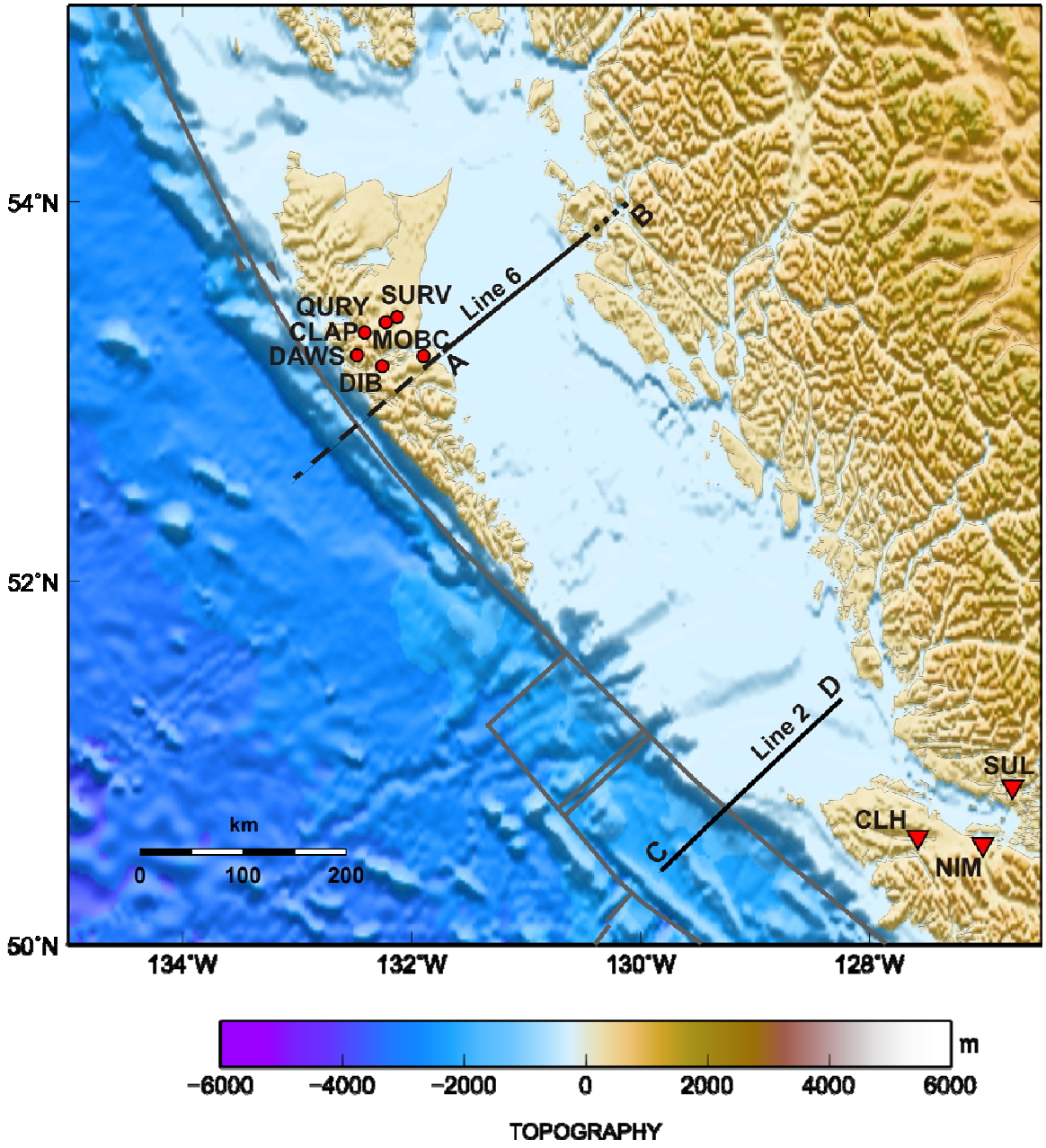

Figure 6: Map of the Queen Charlotte Basin, showing seismic lines 2 (Yuan et al., 1992) and 6 (Spence and Asudeh, 1993). Dashed line: Haida Gwaii refraction experiment (Dehler and Clowes, 1988; Mackie et al., 1989). Inverted red triangles:location of portable three-component broadband seismograph stations installed in 1992 (Cassidy et al., 1998). Red circles: stations used for teleseimic receiver function analysis by Bustin [2006].

2.4.1 Crustal structure of Haida Gwaii and Hecate Strait

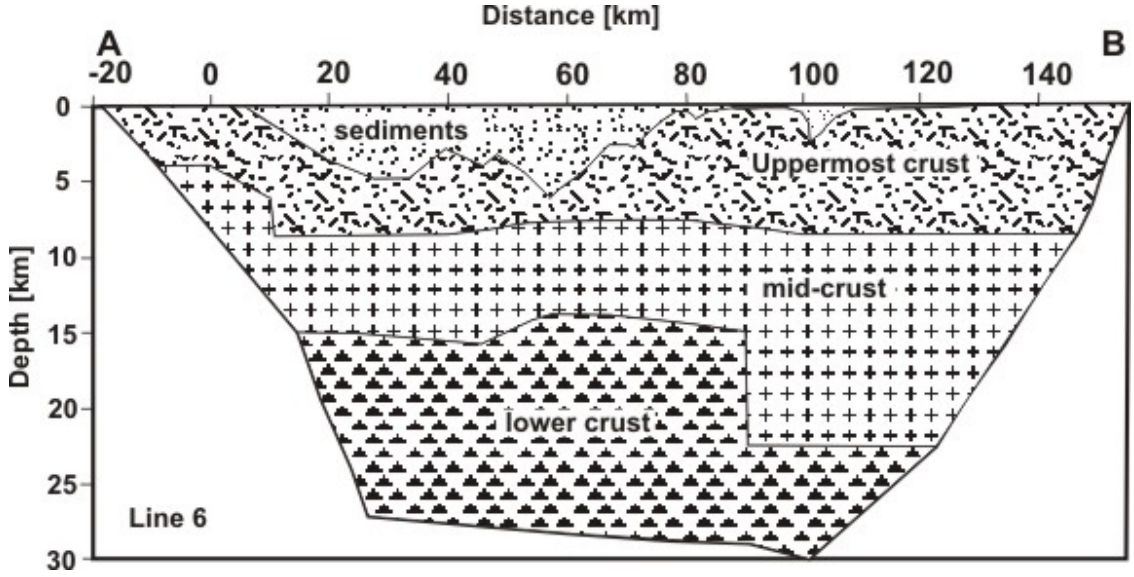

Figure 7: Simplified crustal model of line 6 across Hecate Strait (see Figure 6) after Spence and Asudeh [1993].

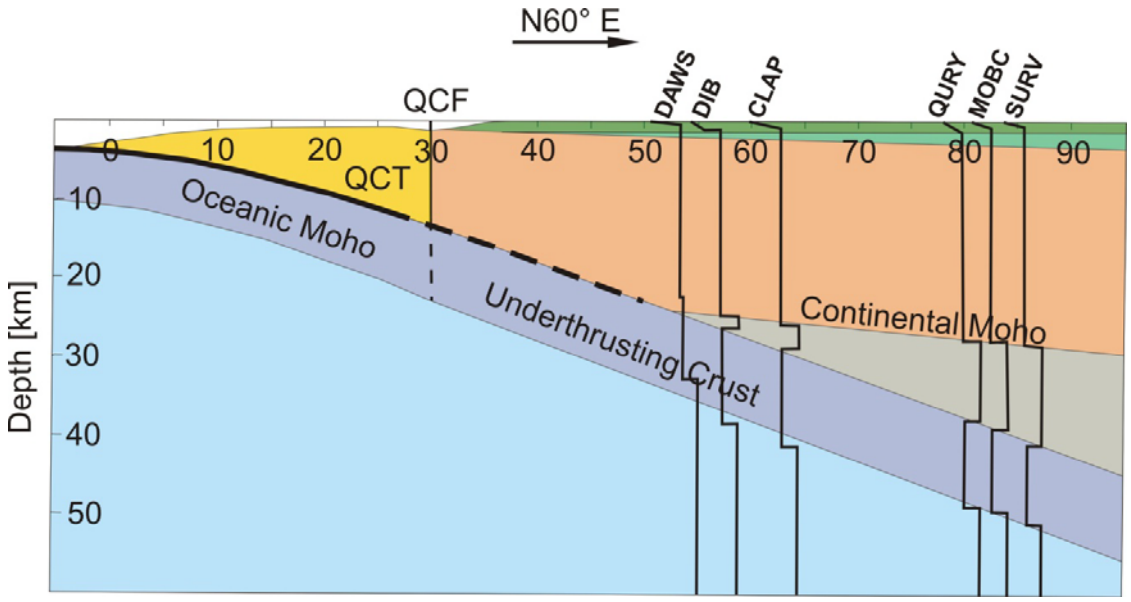

Figure 8: Model of crustal structure underneath southern Graham Island (dashed part of line 6 on Figure 6) based on teleseismic receiver function analysis with data from stations DAWS, DIB, CLAP, QURY, MOBC and SURV. Black lines underneath stations are velocity profiles (Bustin 2006). QCF: Queen Charlotte Fault. QCT: Queen Charlotte Terrace. After Bustin [2006]. Solid black line: locked zone. Dashed black line: Transition Zone (after Smith 1999).

The Moho depth varies between 18 km and 29 km in the Queen Charlotte area, with the deepest Moho detected just east of the islands in the western Hecate Strait (Hole et al., 1993). Dehler and Clowes [1988] and Mackie et al. [1989] concluded that in the ocean basin west of northern Moresby Island the Moho dips eastward at an angle of 2 – 5°. Beneath the 30 km wide and 2 km deep terrace just west of Haida Gwaii, the Moho dips at, ~ 19° to reach a depth of 20 km underneath the Queen Charlotte fault. Across Hecate Strait, the Moho dips gently eastward at depths of 26 – 28 km depth (Figure 7) (Spence and Asudeh, 1993). In Queen Charlotte Sound, the crust thins to about 18 km (Figure 9) (Yuan et al., 1992; Lowe and Dehler, 1995).

Bustin [2006] modelled the structure of the continental crust and the underthrusting Pacific crust, based on receiver functions for a profile across southern Graham and northern Moresby Island, (Figure 8). The teleseismic receiver function analysis confirms the results of the study by Spence and Asudeh [1993], with depths for the continental Moho of 28 km underneath eastern Haida Gwaii and about 25 km underneath the western Haida Gwaii (Figure 8).

Bustin (2006) concludes that the thin continental crust cannot support a tectonic model for internal deformation, since significant crustal thickening would have occurred in that case (Bustin, 2006). A east-northeastward dip of ~ 10° is proposed, which leads to a ~ 5 km deepening of the continental crust towards the east. The shallower crust beneath western Hecate Strait, relative to eastern Hecate Strait, is possibly a result of the upward flexure of the North American plate due to underthrusting (Bustin, 2006; Hyndman and Hamilton, 1993; Prims et al., 1997).

2.4.2 Crustal structure of Queen Charlotte Sound

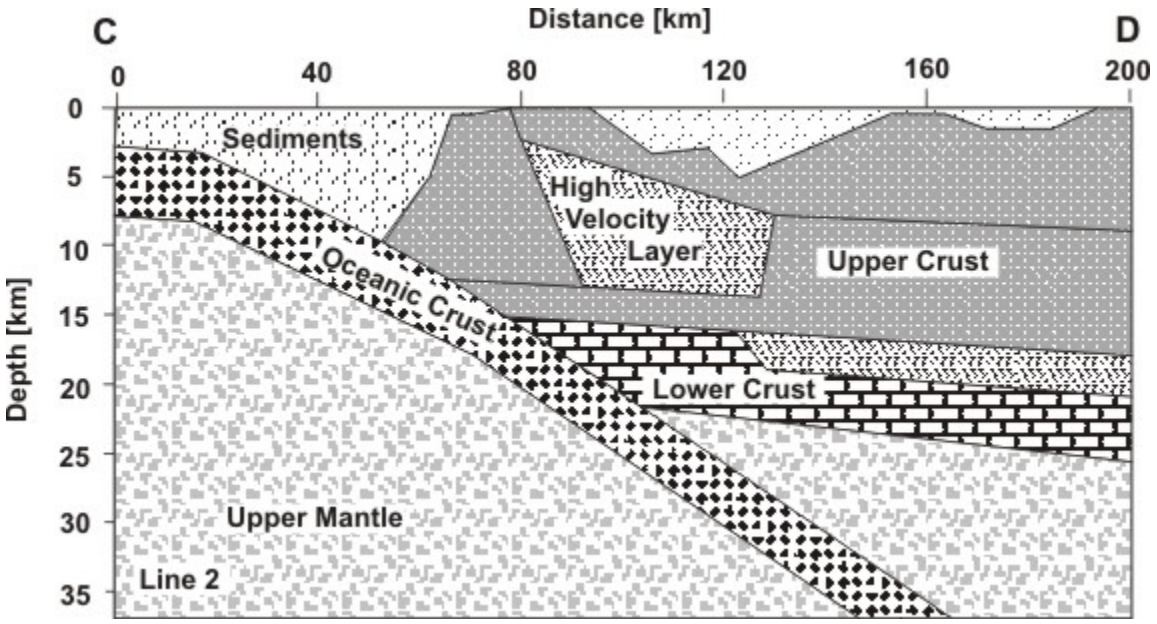

Figure 9: Simplified crustal model for line 2 across southern Queen Charlotte Sound (see Figure 6) after Yuan et al. [1992].

Within Queen Charlotte Sound, the Moho becomes shallower westwards towards the transform fault (Figure 9). Near the Queen Charlotte Fault, subducting oceanic crust is at a depth of less than 10 km. Yuan et al. [1992] also model the Moho to shallow southward, from a depth of 27 km off the coast of southern Moresby Island to 23 km off northern Vancouver Island, which could suggest crustal thinning due to extension. Rohr and Tyron [2010] use a variety of data (e.g., seismic reflection data, gravity data, micoseismicity) to study a region including the Queen Charlotte Sound. Their study postulates a crustal thickness of ~ 20 km just northeast of the northernmost tip of Vancouver Island, which agrees with the study of Yuan et al. [1992].

2.4.3 Crustal structure of Northern Vancouver Island

Beneath North Vancouver Island north of Brooks Peninsula (Figure 6), Cassidy et al. [1998] found a well-defined Moho depth of 37-38 km, based on receiver function

analysis of three broadband seismograph stations (Figure 6). South of Brooks Peninsula, the S-wave velocity structure becomes more complicated, with pronounced low-velocity zones dipping to the NE, which are interpreted as the subducting oceanic crust. They conclude that the northern edge of the subducting oceanic plate occurs just south of Brooks Peninsula, a result that is in good agreement with the profound changes seen in topography, heat flow, gravimetry and geochemistry, and it also agrees with a receiver function study by Audet et al. [2008].

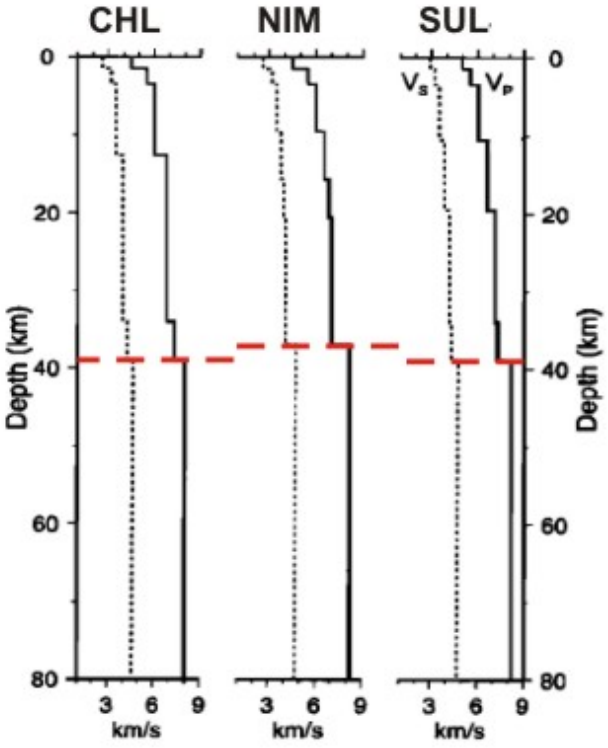

Figure 10: Teleseismic receiver function analysis, showing a velocity discontinuity at 37 - 39 km (marked by red dashed line), interpreted as the continental Moho (after Cassidy et al, 1998).

2.5 Heat flow and thermal structure

Heat flow and the resulting thermal gradients are of interest when investigating crustal deformation using viscoelastic models, since viscosity is highly dependent on the thermal structure of the material. Numerous studies have been conducted measuring heat flow in

the Queen Charlotte Basin, on Haida Gwaii, Vancouver Island and adjacent areas (e.g., Davis and Riddihough, 1982; Yorath and Hyndman, 1983; Lewis et al., 1985; Lewis et al., 1991; Lewis et al., 1997) (Figure 11). Heat flow values in the ocean basin west of Haida Gwaii are irregular reaching >200mW/m^2, which is expected for young oceanic crust (~ 7 Ma) (Hyndman et al., 1982). Eastward the values decrease to between 68 and 80 mW/m^2 just off the west coast of Haida Gwaii across the 2 km deep terrace (Figure 11, Inset A). The main thermal contrast is on the seaward edge of the terrace, which suggests oblique underthrusting of ocean floor underneath the terrace (Hyndman et al., 1982). On Haida Gwaii heat flow ranges from 47 – 70 mW/m^2, with the lowest values on the west coast of Moresby Island close to the average value measured for the Coast Insular Belt. In the Queen Charlotte Basin heat flow values between 57 – 90 mW/m^2 can be found, with the lowest values located just south of Haida Gwaii. Those values are much higher than the average for the Insular Belt on Vancouver Island south of the Brooks Peninsula and the nearby mainland. The high values in the Queen Charlotte Basin could be due to nearby oceanic rifting and/or sediment erosion (Hyndman et al., 1982).

Just off the north-western tip of Vancouver Island in the Winona Basin, values range from 23 to 147 mW/m^2. The lowest values are found closest to the coast (Figure 11, Inset B). It is suggested that the high values are due to a young ocean crustal age (<10 Ma), and that differences in the observed values are due to underthrusting and variations in sediment cover (Davis and Riddihough, 1982). On Vancouver Island, values north of Brooks Peninsula are

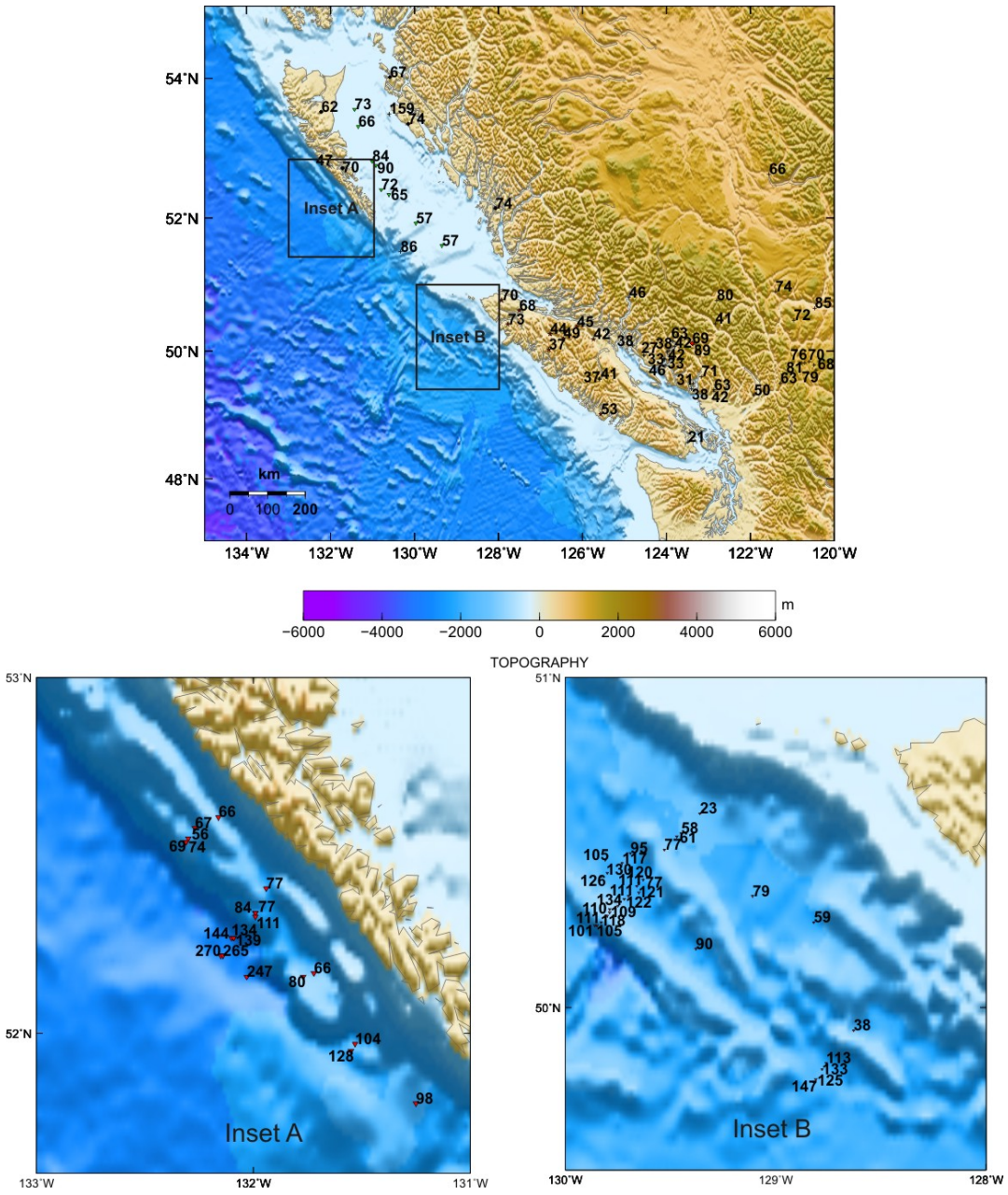

Figure 11: Heat flow values from different studies: red stars - Lewis et al., 1997; black dots - Lewis et al., 1991, from wells; green triangles - Lewis et al., 1997, from boreholes. Inset A shows data from Hyndman et al., 1982. Inset B shows data from Davis and Riddihough, 1982.

between 68 – 73 mW/m^2, whereas values further south are lower, between 21 and 53 mW/m^2. It is proposed that this change from higher to lower heat flow marks the northern edge of the subducting Juan de Fuca plate. To the south, the lower values can be explained by the cooling effect of the subducting plate, whereas the higher values to the

north are caused by heating associated with crustal extension (Lewis et al., 1997). The thermal regime on Vancouver Island north of Brooks Peninsula is very similar to the one in the southern Queen Charlotte Basin, with average heat flow values of ~ 67 +/- 4 mW/m^2 and 69 +/- 5mW/m^2, respectively.

2.6 Seismicity and GPS data

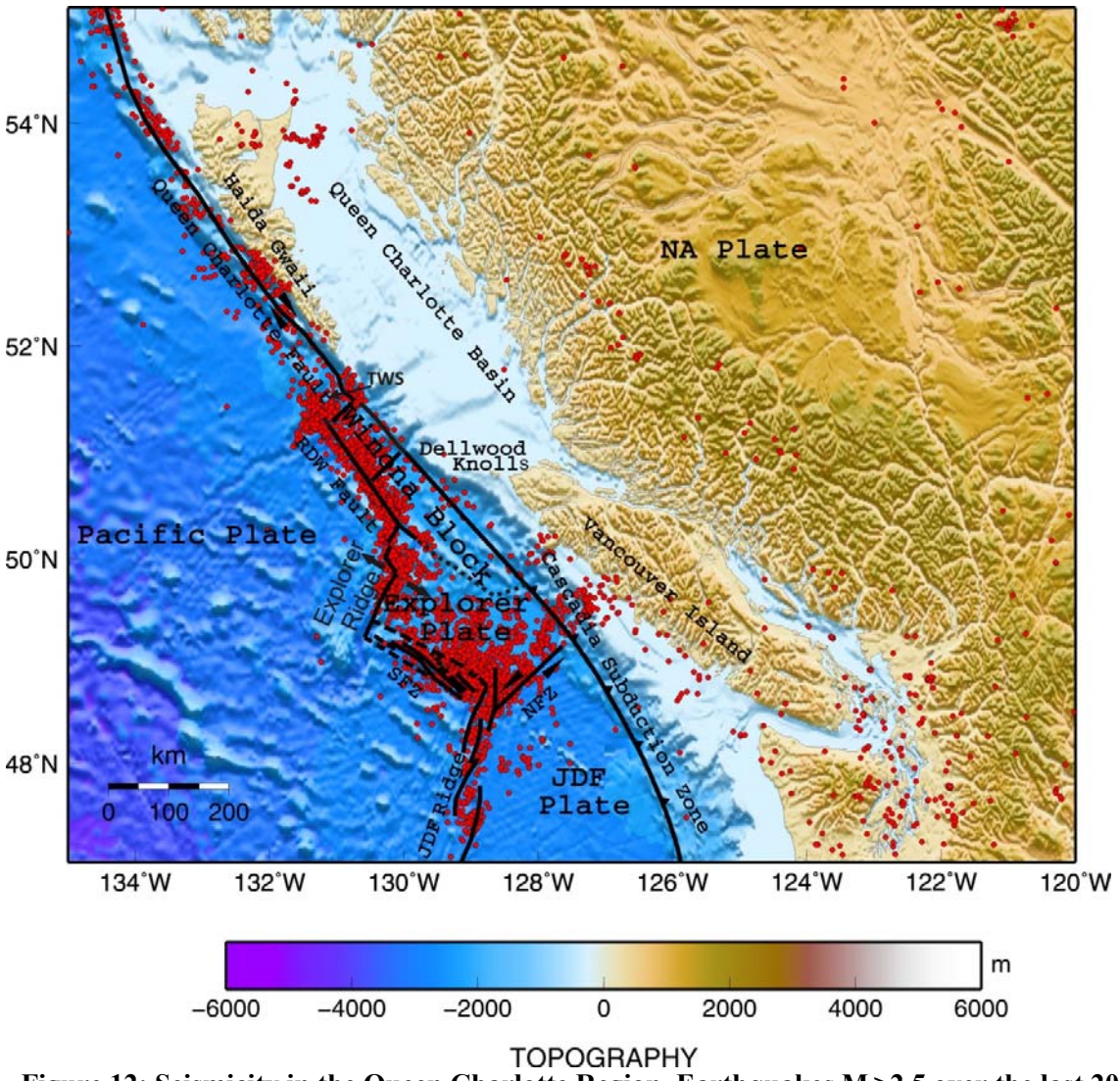

Figure 12: Seismicity in the Queen Charlotte Region. Earthquakes M_l>2.5 over the last 20 years are shown (from Earthquakes Canada). Seismicity is concentrated along plate boundaries, barely any seismicity along the coast and in the interior (RDW: Revere-Dellwood fault. TWS: Tuzo Wilson seamounts)

Seismicity is mainly concentrated along the faults offshore, with most of the events recorded along the Queen Charlotte fault, Explorer Ridge, Sovanco Fracture Zone, Nootka fault zone, and Juan de Fuca Ridge (Figure 12) (see also Rohr and Tryon, 2010). Offshore OBS recording showed most events located close to the physiographic expressions of the fault and spreading centres (Hyndman and Rogers, 1981). Very little seismicity (M_l>2.5) has been recorded east of the margin during the last 20 years. Especially on the mainland, close to the coast, a distinct low level of seismicity can be noted (Figure 12). A discrepancy between the seismicity and the observed GPS velocities is apparent (Mazzotti et al., 2003a,b), since the GPS velocities clearly indicate movement in on northern Vancouver Island and the mainland where little seismicity is recorded (Figure 13).

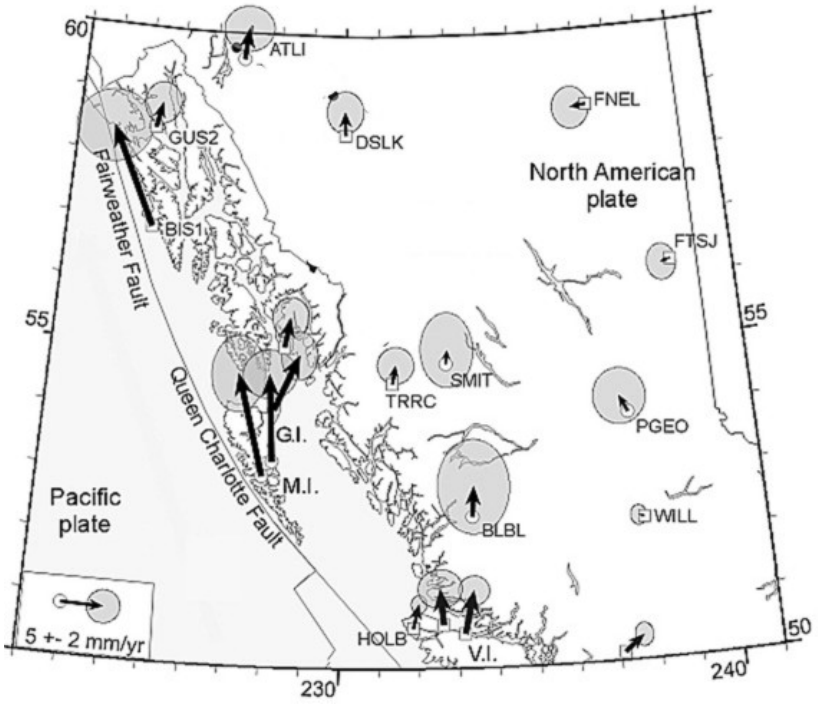

Figure 13: GPS velocity vectors relative to stable North America (after Mazzotti et al., 2003b).

Across the northern Queen Charlotte margin, most of the Pacific/North American transpressive motion is accommodated along the currently locked Queen Charlotte and Fairweather faults. Dextral shear also plays an important role in a ~ 200 km wide region across the margin, where 6 – 7 mm/yr of the relative plate motion are accommodated (Mazzotti et al., 2003a). On the northern tip of Vancouver Island, transient and/or permanent deformation is detected which is related to the Explorer plate (margin-normal deformation) and possibly the Queen Charlotte fault (margin-parallel component of observed deformation). Further south, across Northern Vancouver Island, GPS data provide evidence for an independent Explorer plate underthrusting underneath the North American plate at least as far north as Brooks Peninsula (Mazzotti et al., 2003a).

Near the Queen Charlotte Fault north of ~ 53°N, moment tensor solutions show strike-slip fault mechanisms, with a small thrust component, consistent with the strike of the Queen Charlotte fault (Ristau et al., 2007). The moment tensor solutions for the offshore Queen Charlotte fault region south of 53°N are mainly thrust mechanisms on high-angle faults, indicating a significant amount of convergence between the Pacific and North American plates; some have a small strike-slip component (Ristau et al., 2007) (Figure 14). The lack of low-angle thrust faulting may indicate deformation within the North American plate, and does not suggest underthrusting of the Pacific plate (Ristau et al., 2007). However, subduction thrust faults are often aseismic between events.

Stress analysis shows that for the northern part for the Queen Charlotte fault (north of 53°N) the stress tensor has a σ_1 of 18°, which results in an angle of 43° with the northern Queen Charlotte fault. This is in agreement with the common maximum shear stress of 45° on a fault. For the southern segment of the Queen Charlotte fault the azimuth of

σ_1=36°, resulting in an angle with the Queen Charlotte fault of 76°. Since the mechanisms are mostly thrust events with small strike-slip components, the expected P axis orientation should be close to, but not quite 90° (Ristau et al., 2007).

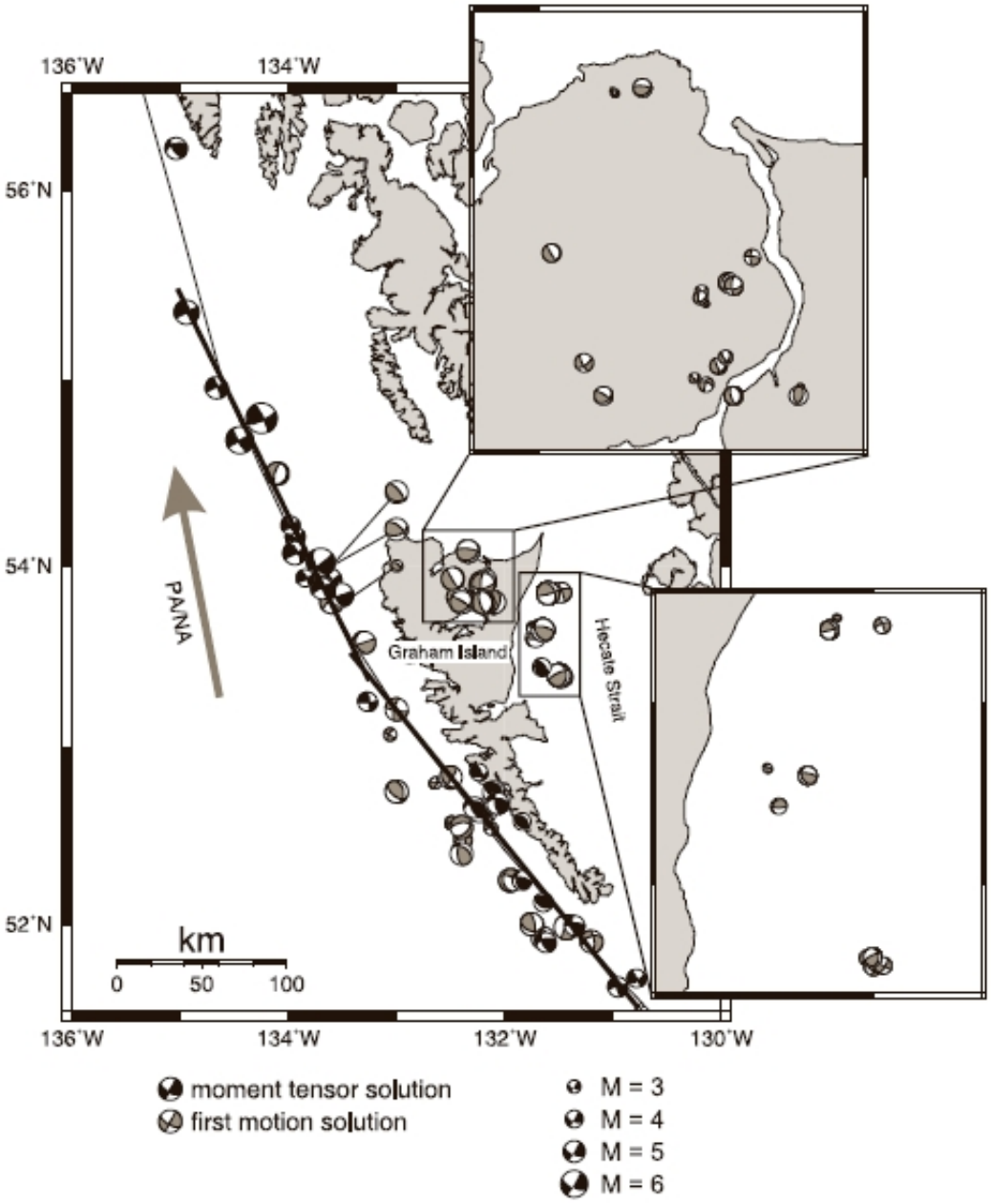

Figure 14: Moment tensor and first-motion solution for Haida Gwaii (Ristau et al., 2007).

Chapter 3
Current Deformation of Northern Vancouver Island, Haida Gwaii, and the Adjacent Mainland Inferred from Global Positioning System Measurements

New Global Positioning System (GPS) measurements collected on northern Vancouver Island and the adjacent mainland are analyzed in this thesis study to constrain the current deformation (direction and rate of movement of sites) in that region with respect to the stable North American plate. In conjunction with geological and seismicity data, as well as the results of viscoelastic modeling, these GPS solutions provide constraints on the current tectonics of the area (see Chapter 0).

3.1 Introduction to Global Positioning System

Hoffman-Wellenhof et al. [2001] offer a detailed and comprehensive description of the NAVSTAR (NAVigation Satellite Timing And Ranging) Global Positioning System (GPS). It is currently the primary and most used global satellite-based navigation system and is funded and controlled by the United States Department of Defence. Several other more limited systems are operating (e.g., GLONASS) or in development (e.g., Galileo). With standard code-based GPS, positions can be determined with a precision better than 10 metres. Using high-precision GPS, where the site position is determined using the signal phase, the precision is within millimetres. Precision is greatly improved with the use of precise satellite orbits and clocks generated by the IGS (International GNSS Service (GNSS: Global Navigation Satellite System)).

As of February 2011, the GPS constellation consists of 32 satellites that circle the earth in six orbital planes approximately every 12 hours. This constellation ensures that there are at least six satellites above the horizon at any point on the earth at any time. The satellites send out microwave signals, which can be received via special antennas.

Standard (low-precision) GPS receiver estimates the range to the satellites using the estimated satellite positions included in the signals the satellites send out. With four satellites the receiver is able to calculate its own position (longitude, latitude, elevation).

3.1.1 Satellite Signal

Each GPS satellite sends out a signal that contains several components, which are all derived from the fundamental frequency of the satellite oscillator f_0 (Table 1). The two carrier frequencies f_1 and f_2 are modulated with codes and navigation messages to transmit information (e.g., readings of the satellite clocks, orbital parameters) (Dach et al., 2007).

Table 1: Components of the satellite signal (modified from Dach et al., 2007).

Component	**Frequency [MHz]**	**Wavelength**
Fundamental Frequency	$f_o = 10.23$	
Carrier L1	$f_1 = 154\ f_0 = 1575.42$	$\Lambda_1 = 19.0$ cm
Carrier L2	$f_2 = 120\ f_0 = 1227.60$	$\Lambda_2 = 24.4$ cm
P-code P(t)	$f_0 = 10.23$	
C/A-code C(t)	$f_0/10 = 1.023$	
Navigation Message D(t)	$f_0/204600 = 50 \times 10^{-6}$	

Carriers L1 and L2 are modulated by the Precise Code (P); L1 is also modulated by the Coarse Acquisition (C/A) code and the Navigation Message, which includes information about the satellite orbit, its clock, and its "health" status. Both the P-code (limited to military use) and the C/A-code consist of pseudo-random noise (PRN) sequences (Dach et al., 2007).

The receiver has an internal clock which is synchronized with those of the satellites, and it contains the code information necessary to co-generate the code structure. The cross-correlation of the received signal with its internal code allows for the determination of a time delay (signal transit time). Multiplying the transit time by the speed of light results in the distance (range) from the satellite to the receiver. There are multiple sources of error (satellite position, satellite and receiver clock timing biases, effects of path delays); therefore the range estimate is called pseudo-range (Dach et al., 2007).

The precision generally achieved with basic processing is not high enough for geodetic purposes. To achieve the necessary precision to be able to measure tectonic motion of only several millimetres per year, the L1 and L2 carrier phase information is used. The receiver starts to track a satellite and measures the fractional part of the arriving signal phase. Then it tracks the phase continuously. The shorter wavelength makes the fractional phase length measurement much more precise (~1 mm accuracy) than a simple code measurement. The number of wavelengths between the source and the receiver is initially unknown and must be determined by a process of ambiguity resolution.

The receiver needs at least three satellites to perform a trilateration to determine its position, and a fourth one to enable the receiver to calculate its clock offset relative to the satellites and so correct for clock errors.

Differential GPS improves the accuracy even further. A receiver at a nearby fixed site of assumed accurate position is used to calculate satellite errors by estimating the difference between the measured and the known range between itself and each satellite. The necessary corrections are then either transmitted to survey receivers (real-time differential GPS) or are applied to the survey data after the data collection (post-

processing differential GPS). Post-processing differential GPS allows corrections for error sources that are common to both the reference receiver as well as to the measurement station. In this study I use differential GPS, where the positions of sites are calculated relative to a reference station. That way, there is less need for correction because common errors are automatically subtracted.

3.1.2 Potential sources of error

- Orbital Position Errors (Lachapelle, 1990; Loomis et al., 1989): These are errors due to an uncertainty in the satellite position estimates. The precise orbits required for millimetre-precision positioning are generated by the IGS using 106 globally distributed sites with accurately known positions constrained by GPS, VLBI (Very Long Baseline Interferometry) and/or SLR (Satellite Laser Ranging) measurements (Beutler et al., 1995; http://igscb.jpl.nasa.gov/). The GPS satellite orbits are now known with ~ 3 cm precision and ~ 5 cm accuracy.
- Clock Errors (Wells et al., 1986): The internal receiver clock is not perfectly synchronized with those of the satellites. The clock errors can be reduced if a single receiver tracks at least four satellites, or if two satellites are tracked by two receivers (double differencing).
- Multipath Errors (e.g., Lachapelle et al., 1989): If radio signals from the satellites do not reach the antenna directly, but are reflected by nearby objects or even the ground before reaching the antenna, the distance between the satellite and the antenna is overestimated. One way to reduce multipath errors is by using a choke-ring antenna that rejects most near- or sub-horizontal waves (e.g., Tranquilla et al., 1994).

- Atmospheric Errors (e.g., Wells et al., 1986): Atmospheric variations, in particular the moisture content, can significantly affect the propagation velocity of the satellite signals. Signal delays arise from the ionosphere and troposphere. The ionosphere is frequency dispersive, and the use of a dual-frequency receiver allows a large reduction in most of the ionospheric errors. Most of the non-dispersive atmospheric delay is associated with the troposphere and contains both dry (90%) and wet (10%) components. The dry delay arises from atmospheric molecules in hydrostatic equilibrium and is typically about 2.3 m path length at zenith near sea level. The zenith wet delay is about an order of magnitude smaller, and both delays are larger at other elevation angles towards horizontal for which the paths are longer. Tropospheric refraction modeling can decrease non-dispersive atmospheric errors.
- Site-Specific Noise: Errors can arise from a number of sources at the observation site, such as monument instability, inclement weather (snow on the antenna), wildlife/human disturbances, or user error. Since those errors can not always be avoided, it is important to have accurate and detailed field notes, so that sources of site-specific noise can be identified.

3.1.3 Relative Antenna Phase Centres versus Absolute Antenna Phase Centres

As discussed previously, in order to use GPS to observe crustal deformation, a high precision is needed. To be able to achieve such high precision, it is necessary to know the exact position of the phase centre of the transmitting as well as of the receiving GPS antenna (Schmid et al., 2003). Up until spring 2011, absolute phase centre offsets and variations were available for IGS products released after December 2006; for previous

products, only relative phase centre offsets and variations could be used, estimated from data collected on a short well-known baseline.

By using relative phase centre corrections, several disadvantages are introduced (Schmid et al., 2003):

(1) The relative phase centre corrections are based upon the arbitrary assumption that the phase centre variations (PCVs) of the reference antenna AOAD/M_T are zero.

(2) It is not possible to correctly take into account the phase centre positions when processing long intercontinental baselines, or when the receiver antenna is tilted.

(3) It neither permits a homogeneous distribution of observations with regard to the antenna hemisphere nor the estimation of PCVs below an elevation angle below 10°.

(4) Relative receiver antenna PCVs contain site-dependent multipath effects.

(5) The systematic PCVs of the different satellite blocks cannot be taken into account using relative receiver phase centre corrections only.

The use of absolute phase centre corrections eliminates all these disadvantages. The absolute robot calibration can provide better results than relative field calibration because it is almost free of multipath, offers a homogenous distribution of observations and permits the estimation of PCVs also for low elevations (Schmid et al., 2003).

3.2 Campaign GPS survey

3.2.1 Fieldwork

Two GPS campaigns were carried out in 2007 and 2008 as part of this thesis study. To ensure consistent satellite coverage as well as to minimize errors due to diurnal and other short-term variations, the occupation of each site was at least 48 hours. For the 2007 and

2008 campaigns, the antenna models used were ASH701945C_M, and the receiver models were Ashtech Z-Xtremes. Usually the same units (each unit consisting of a mast/tripod, antenna and receiver) are used for repeat occupations of sites, but due to equipment upgrades since the last two surveys in 1993 and 1999, that was not an option for the 2007 and 2008 surveys. All sites except for ROBI are mast set-ups with cables to bedrock anchors. There is not enough bedrock to drill anchors for the mast set-up at ROBI; therefore a tripod had to be used (Figure 15A).

Figure 15: A) Tripod set-up at ROBI. (B) Mast set-up at FHAR. (C) Marker at KASH.

The guyed mast set-ups are preferred since they are more stable. However, enough bedrock is needed to drill three steel anchors into it at some distance from the marker. The anchors are connected to the mast by steel cables, which stabilize the mast (Figure 15; Figure 16). If not enough bedrock is available, then a tripod setup is used (Figure 15, Figure 16). For both mast and tripod set-ups, the antenna has to be stabilized and levelled over the centre point of the marker.

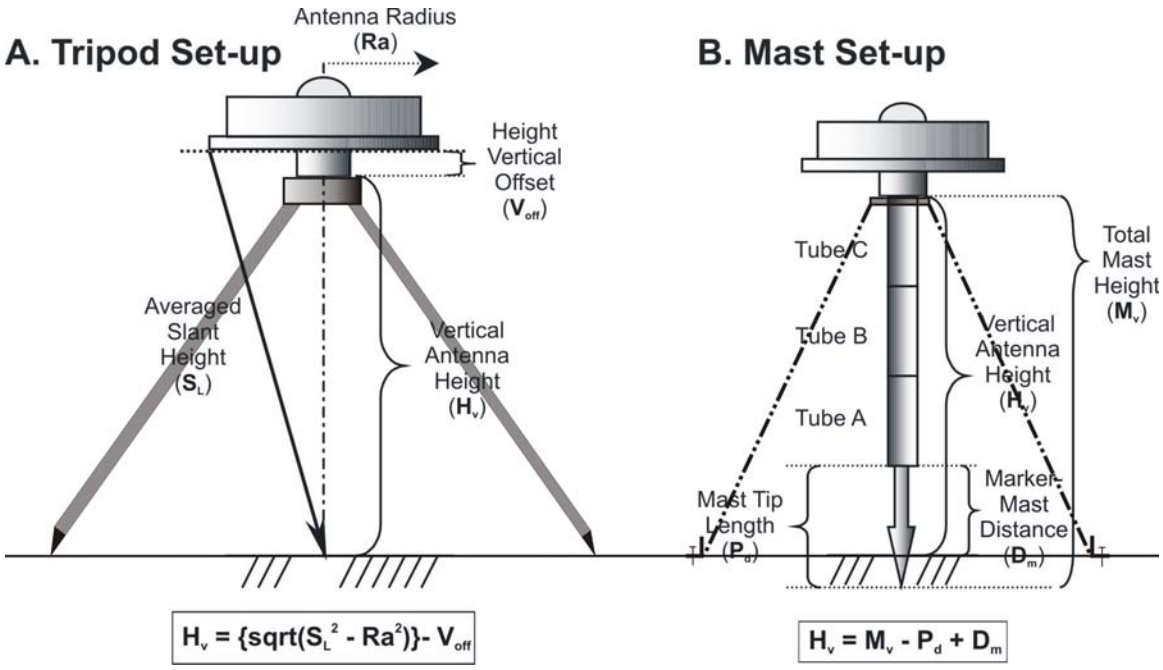

Figure 16: Schematic sketch of (A) a tripod set-up, and (B), a mast set-up. (A) Calculation of the antenna height using a geodetic tripod. (B) Calculation of the antenna height using a TECH 2000 GPS mast set-up (after Leonard, 2006).

3.2.2 Previous campaigns (1993 and 1999)

The first GPS data set stems from a survey in summer 1993, conducted by the Geodetic Survey Division (GSD). During that survey, data was collected at sites ALIC, BULL, CALV, COXI, HARD, JENS, KING, KLUC, KOPR, MOOR, ROBI, SCAR, SEYM, SHUS, and STPA (Table 2). In 1999, a second survey was conducted, and all the aforementioned sites were revisited, with the exception of MOOR (Table 2), where the

marker could not be found. This survey was part of a bigger campaign, conducted by the GSD, which included 40 stations in two networks on Vancouver Island: the Tofino-Port Alberni-Sechelt network and the Queen Charlotte Sound network (for more details see Henton, 2000). That project was part of a joint program between the Pacific Geoscience Centre (PGC) and GSD to monitor crustal movement in seismically active areas in SW British Columbia (see Mazzotti et al., 2003 for a summary). Both surveys used mostly helicopters and boats to gain access to the sites.

3.2.3 2007 and 2008 campaigns North Vancouver Island

During the 2007 survey, five sites were occupied, four of them on the mainland, using helicopter access (KING, CALV, SEYM, ROBI), and one on Vancouver Island (ALIC) (Figure 17). The proposed sites BULL and KOPR could not be occupied. BULL was overgrown and no place for the helicopter to land nearby could be found; KOPR was not occupied due to involvement in an automobile accident on the way there.

Figure 17: GPS sites for 2007 North Vancouver Island Campaign. Grey shaded sites were not occupied (BULL, KOPR).

In 2008, it was planned to occupy the two sites in the Kyuquot Inlet (FHAR and KASH) and 2 sites just west of the Inlet (LOOK and MCQI) (Figure 18). We learned on arriving in Zeballos that MCQI can only be reached by helicopter (which was suspected). Access to LOOK was attempted by water taxi and canoe, but the site could not be reached due to dangerously choppy seas. Since two days with perfect conditions would be needed to occupy this site safely by boat, LOOK should be considered a helicopter site in the future.

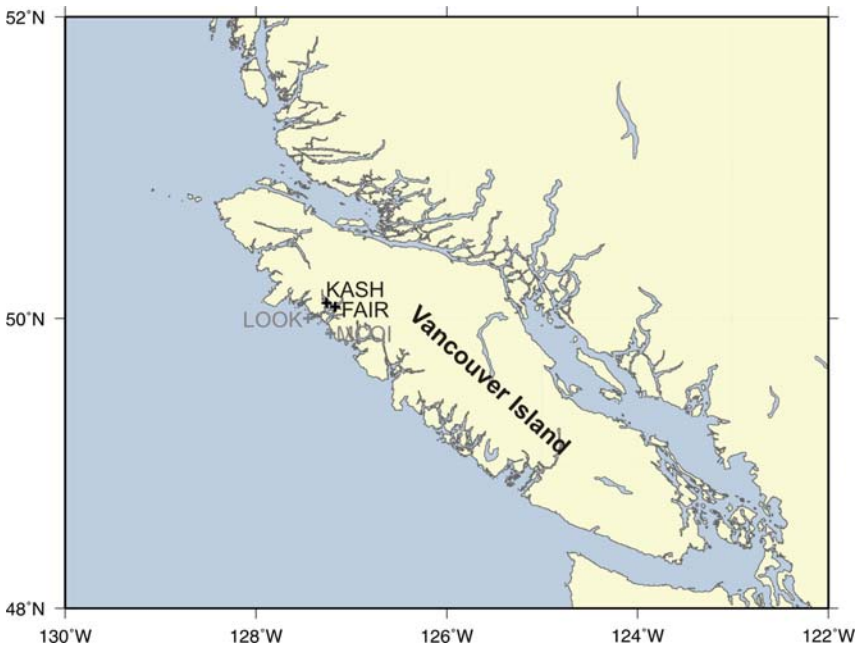

Figure 18: GPS sites for the 2008 Kyuquot Survey. Grey shaded sites were not occupied (LOOK, MCQI).

Figure 19 and Table 2 show all sites occupied during one or several of the GPS campaigns in 1993, 1999, 2007 and 2008.

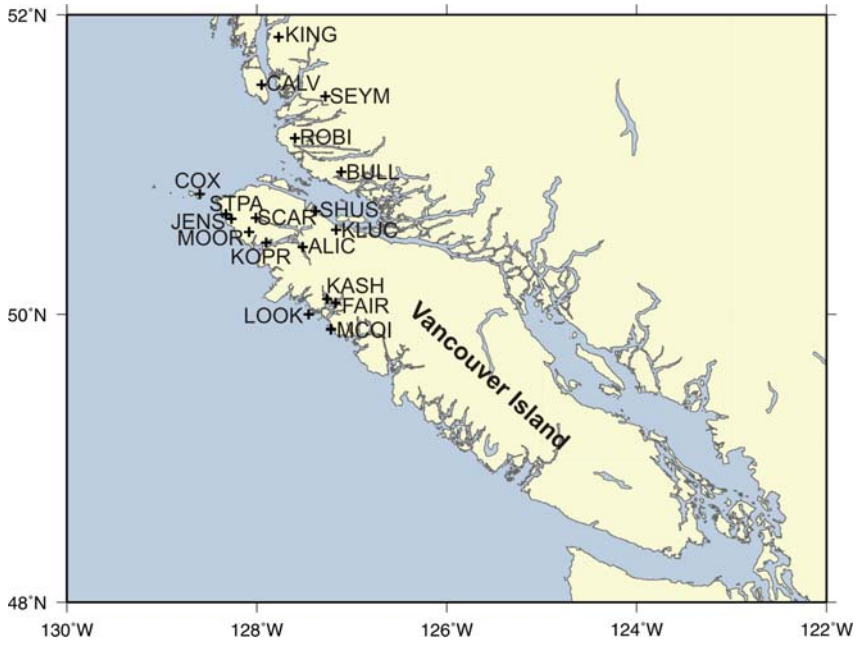

Figure 19: Campaign sites surveyed during 1993, 1999, 2007, 2008 campaigns.

Table 2: X in yellow cell indicates station employed that year.

	Station	1993	1999	2007	2008
Port Alice	ALIC	X	X	X	
Bullock	BULL	X	X		
Calvert Island	CALV	X	X	X	
Cox	COXI	X	X		
Fair Harbour	FHAR		X		X
Port Hardy	HARD	X	X		
Jensen	JENS	X	X		
Kash	KASH		X		X
King	KING	X	X	X	
Klucksiwi 2	KLUC	X	X		
Koprino	KOPR	X	X		
Look Island	LOOK		X		
McQuarry Island	MCQI		X		
Moore	MOOR	X			
Robinson	ROBI	X	X	X	
Scarlet	SCAR	X	X		
Seymour	SEYM	X	X	X	
Shushartie	SHUS	X	X		
St. Patrick	STPA	X	X		

3.3 Campaign GPS data processing

The campaign GPS data were processed using Bernese Version 5.0 (Dachs et al., 2007). Before the actual processing, the raw files were converted to RINEX (Receiver Independent Exchange; Gurtner et al., 1989) format using the program teqc. The headers of the RINEX files give information on the site, equipment used, and the antenna height. The input files contain the site names and numbers, receiver/antenna pairs used, ocean tidal loading at each site, antenna heights, and the processing strategy (e.g., which sites will be processed for which days, the reference for the site motions, troposphere model parameters, ambiguity resolution strategy, etc.).

The data were processed relative to one reference site, the position of which was fixed and kept identical throughout the time series. This approach could potentially cause

network distortion; however, since the footprint of the stations with new data is less than ~ 500 km, it is assumed that it does not have any significant effects (Mazzotti et al., 2005). The approach using a fixed reference site was chosen in order to be able to incorporate new data with the previous data which could not be re-processed. It would have been preferable to use a number of reference sites, encircling the study area, however, only one reference site (DRAO, Penticton, BC) could be used that provided data during all surveys (1993, 1999, 2007, 2008).

Processing of the GPS campaign data provides daily positions for each site in the International Terrestrial Reference Frame 2000 ((ITRF2000), Altamimi et al., 2002). The site velocities are transformed to a stable North American reference frame using the North America/ITRF2000 rotation vector from Altamimi et al. (2002).

The daily positions are computed using an ionospheric-free, double difference phase-solution. Precise satellite orbits and Earth rotation parameters from IGS are used and held fixed, and data are sampled at 30 s. Ocean tide loading corrections are made using the program OLMPP (http://www.oso.chalmers.se/%7Eloading/index.html, M.S. Bos and H.-G. Scherneck), incorporating the FES2004 global ocean tide model. The "quasi-ionosphere-free" strategy is used; and tropospheric delay corrections are applied using Dry Niell mapping function (Niell, 1996) with 24 zenith delay estimates and four gradient parameters estimates per 24-hour session. A priori coordinates of the stations are defined as their ITRF00 epoch 1997.0 value.

The long-term velocity at each site is estimated by assuming a constant rate between the surveys. There were no large earthquakes in the area during the period of the surveys; hence no abrupt offsets are expected. The site velocity is taken as the weighted best fit

linear rate between the daily positions of the occupations. See also Mazzotti et al. [2003 a, b] for description of the processing.

3.3.1 Analysis of uncertainties and errors for campaign GPS data

There are several sites with only two occupations; hence they do not provide a reliable estimate of the weighted root mean square (WRMS) of daily scatter of individual time series. In order to calculate the minimum uncertainties on the data, I use a continuous site (HOLB), and analyzed the time series as a campaign site by constraining a time-period of about four weeks around the time of the campaign surveys. I then randomly choose two consecutive days within those four weeks and calculated the velocities and their uncertainties (Table 3). These calculated standard deviations are very low and probably do not give a direct measure of the "real" uncertainty on the campaign rates; however, those values serve as a minimum. Based on that, the minimum uncertainty on the horizontal velocities is $\sigma_{min} = 0.13$ mm/yr.

Table 3: Mean and standard deviations for HOLB

Station	North		East		Up	
	Mean [mm/yr]	σ_N [mm/yr]	Mean [mm/yr]	σ_E [mm/yr]	Mean [mm/yr]	σ_U [mm/yr]
HOLB	1.25	0.13	-0.49	0.12	-3.00	0.53

Mazzotti et al. [2003a] calculated an error budget of ~ 1.2 mm/yr for the campaign data used in their study. This value was based on three potential error sources. Following this approach, I calculate a maximum error budget of ~ 0.74 mm/yr for the horizontal velocities, based on the following three potential errors for the campaign data in this study: (1) a possible position bias due to pre-1996 slow slip events, which are not well constrained in extent and amplitude (Dragert et al., 2002). This translates to a possible error of up to ~ 0.6 mm/yr in the estimated velocity over a nine - year time-series. (2) A

change of antenna type, dome, or skirt at the reference station can affect the position of the other stations by several millimetres in the horizontal component. The possible error in the estimated horizontal velocities can be up to ~ 0.3 mm/yr. (3) An uncertainty of ~ 0.3 mm/yr has to be considered for the horizontal velocities over a nine-year time-series due to the error introduced by set up variations during the repeated set up of the GPS antenna over a marker, as well as tripod deformation during the surveys.

With this estimate of potential error, the uncertainties on the velocities are estimated by directly scaling the formal standard errors with empirical constants (Table 4), so that the horizontal uncertainty averages the estimated error of ~ 0.74 mm/yr. Since the continuous sites are processed like campaign data, I calculate and apply a scaling factor to those sites as well.

Table 4: Uncertainty Scaling Factor

	WCDA*	QCS*	QCI*
North	5.3	2.0	1.3
East	6.58	0.94	0.18

*: WCDA: Western Canada Deformation Array (permanent). QCS: Queen Charlotte Strait. QCI Queen Charlotte Islands network.

3.3.2 Different approaches to processing

I test different approaches to process the new campaign data in order to deal with two different issues:

(1) The first problem is the previously discussed change from relative to absolute PCVs in December 2006. The 1993 data had been processed using relative PCVs. The 2007 and 2008 data could only be processed using absolute PCVs.

Only data from 1999 could be processed using either absolute or relative PCVs. In order to analyze the effect this change could have on the time-series I processed the data once using relative PCVs for 1999, and then using absolute PCVs for 1999.The University of LaRochelle (ULR) provided orbits based on absolute PCVs for data collected post-1994, the orbits using relative PCVs are provided by the IGS. The resulting time-series only show minor effects due to the change (within 0.2 mm/yr for horizontal velocities, up to 1 mm/yr for vertical velocities) (see Appendix A for all time series, Figure 20 A and B for an example). It can be concluded that geographically small surveys with long timelines are largely unaffected by the change from relative to absolute PCVs. I chose to use the absolute PCVs provided by IGS for data collected after GPS week 1400 (November 2006), and the relative PCVs, also provided by IGS, for data collected before that time.

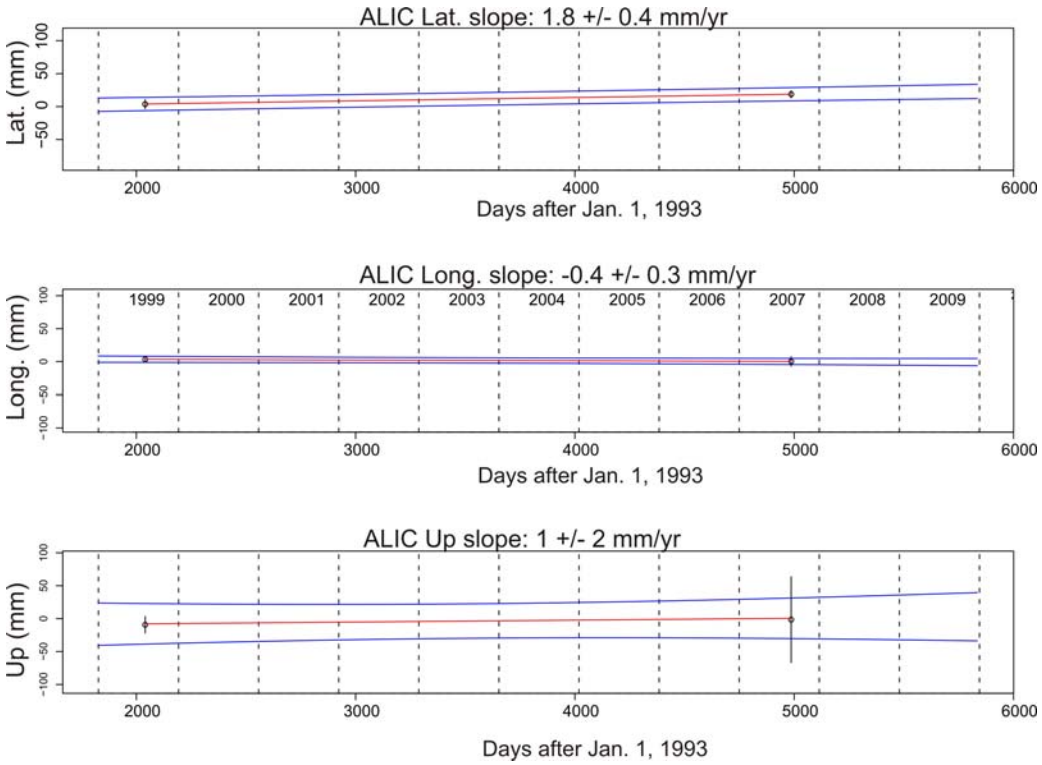

Figure 20 A: Time-series and estimated uncertainties for ALIC, using relative PCVs for 1999 and absolute PCVs for 2007 data. RMS scatter not calculated.

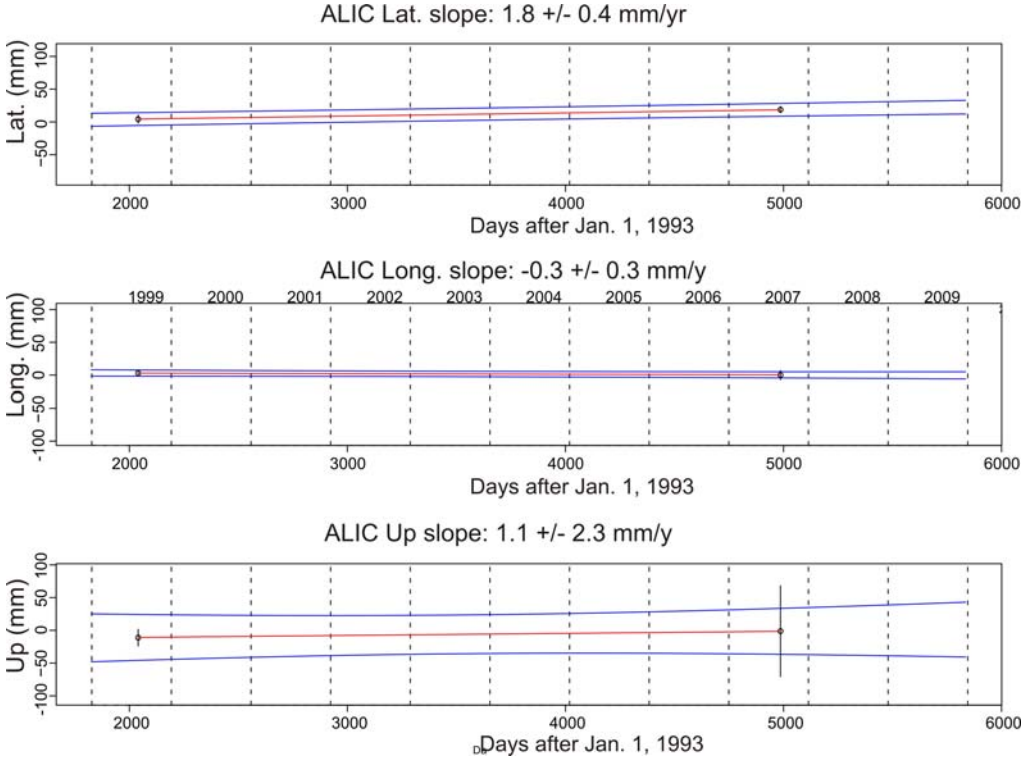

Figure 20 B: Time series and estimated uncertainties for ALIC, using absolute PCVs for 1999 and for 2007 data. RMS scatter not calculated.

(2) The data from 1993 could not be re-processed using BERNESE 5.0 (it was previously processed using BERNESE 4.2). Major problems included the file format of the RINEX data which was not in compact RINEX ver.1.0-2.0, and the inability of the program to produce the zero-difference code and phase observation files (.PZH and .CZH files) for each station.

I calculated the velocity vectors using all the data including 1993 data and using only the data from 1999 - 2008 (Figure 21). In general, the two results agree on the general direction of movement. For ALIC (Figure 22), velocity magnitudes also agree, but for other sites (e.g., SEYM) the calculated velocities in the latitude (Vn) and longitude (Ve) directions differ by up to 2 mm/yr, more than that in the vertical (Vu) direction (Appendix A). Since the data collected in 1993 are the result of surveys that only lasted for a couple of hours, instead of the now common 48 or more hours per survey, as well as major improvements in the accuracy of GPS data since 1993, I exclude the 1993 data from further processing and interpretation.

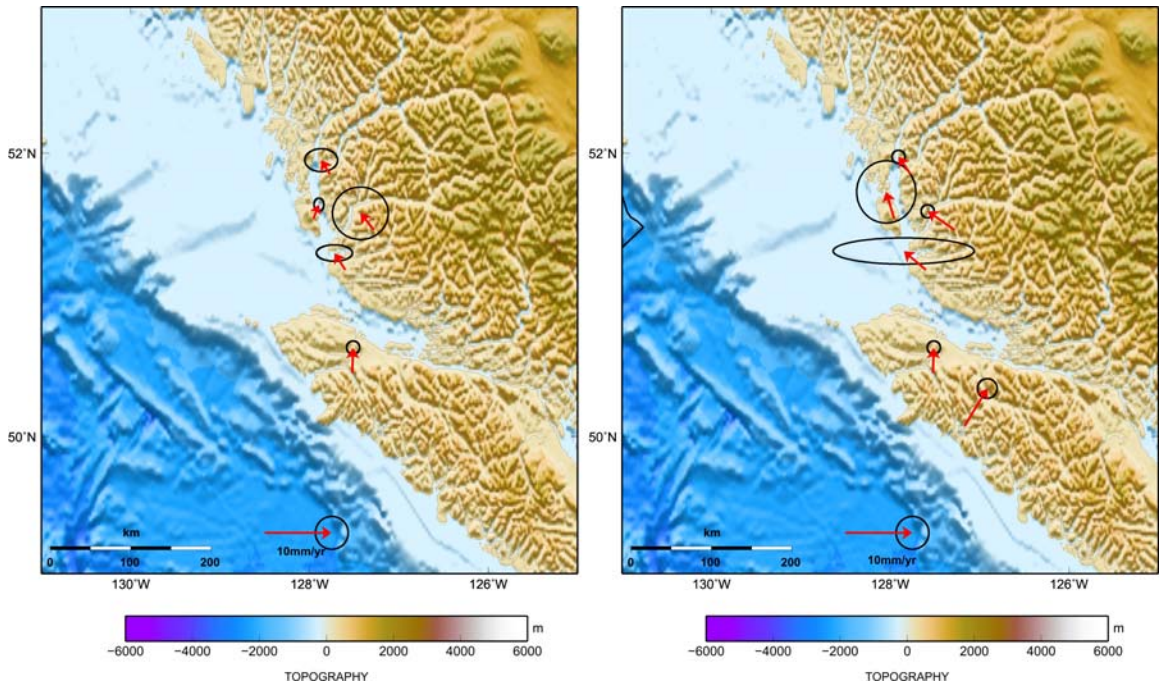

Figure 21: Velocity vectors of campaign data including the 1993 data (1993-2008; left) and excluding it (1999-2008; right).

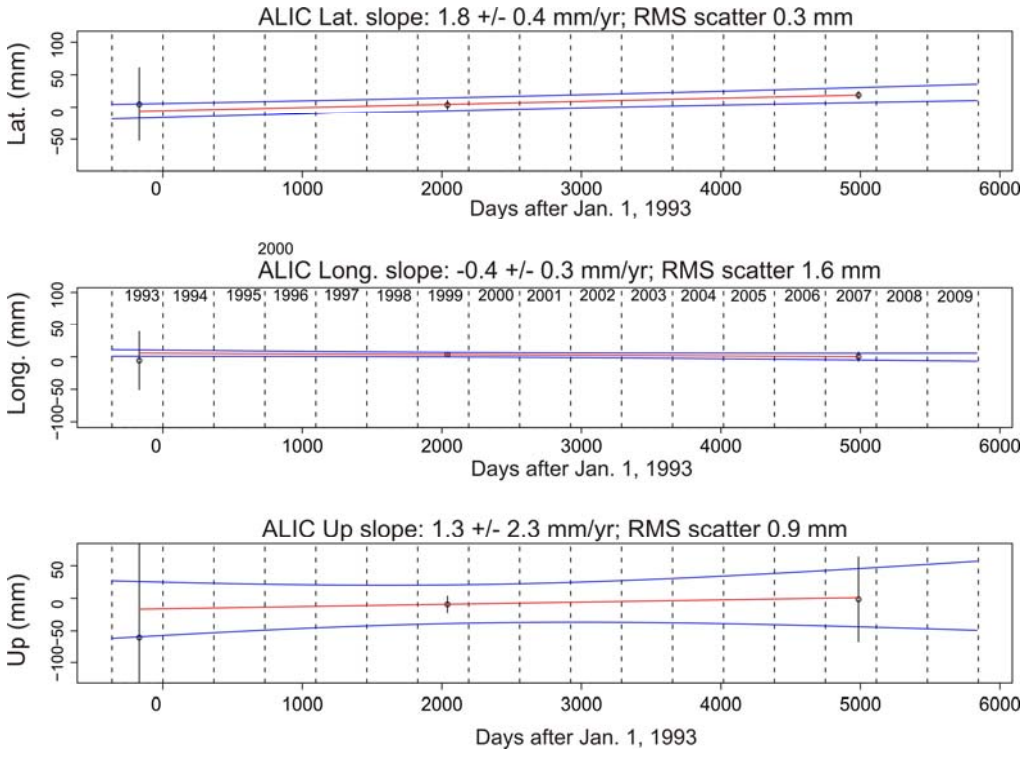

Figure 22 A: Horizontal and vertical velocities for ALIC, including data for three campaigns (1993, 1999, 2007).

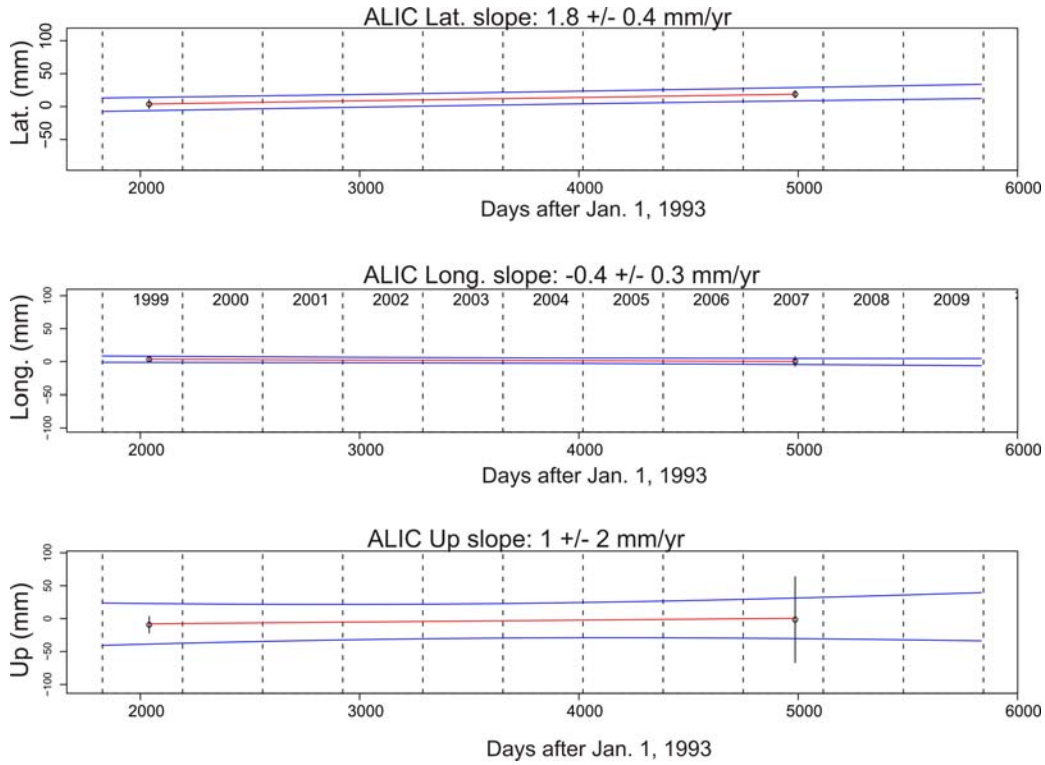

Figure 22 B: Horizontal and vertical velocities for ALIC, including data for two campaigns (1999, 2007). RMS scatter not calculated.

3.4 Campaign GPS results

In order to be able to analyze the new GPS data in the context of current crustal deformation along the margin off the west coast of British Columbia, I include continuous and campaign GPS data from previous surveys on Haida Gwaii and southern Vancouver Island, as well as the adjacent mainland (Mazzotti et al., 2003a, b; 2008). The new GPs data was integrated to the existing velocity field by using the same reference frame (ITRF2000, transformed to a stable North America reference frame using the North America/ITRF2000 rotation vector from Altamimi et al. [2002]). Table 5 and Figure 23 provide an overview of all stations used for the interpretation.

Table 5: GPS site velocities for all sites used for further interpretation

Station	Latitude °N	Longitude °E	Vn [mm/yr]	Ve [mm/yr]	Vu [mm/yr]	σn [mm/yr]	σe [mm/yr]	σu [mm/yr]	Network
ALBH	48.39	236.51	3.1	4.7	-3.1	0.2	0.1	0.7	WCDA
ALIC*	50.46	232.48	1.8	-0.4	1	0.4	0.3	2	QCS
CALV*	51.54	232.05	2.1	-1.8	-3.4	1.9	1.8	6.5	QCS
CHWK	49.16	237.99	0.6	1.4	-3.5	0.2	0.2	0.9	WCDA
FHAR*	50.08	232.83	3.7	3	0.4	0.6	0.6	2.2	QCS
KING*	51.85	232.23	0.7	-2.5	-1.1	0.3	0.3	1.8	QCS
NANO	49.29	235.91	3.4	3.8	-2	0.2	0.2	0.6	WCDA
PGC5	48.65	236.55	3.1	4.3	0.3	0.1	0.1	0.7	WCDA
ROBI*	51.19	232.40	0.9	-3.9	-1.6	0.8	4.3	1.6	QCS
SEYM*	51.46	232.72	1	-4.6	0.2	0.4	0.4	1.2	QCS
WSLR	50.13	237.08	0.6	1.6	-1.5	0.2	0.2	1	WCDA
HOLB	50.64	231.87	5.1	0.1	-0.3	0.6	0.6	2	WCDA
WILL	52.24	237.83	1.8	0.3	1	0.6	0.5	1.8	WCDA
BCPR	54.28	229.57	4.9	-0.5	-2.7	1.2	1	3.4	WCDA
BCSS	53.25	228.19	10.3	-0.3	1	1.4	1.4	3.9	WCDA
BCDI	52.16	231.89	4.6	-1.9	2.8	1.3	1.3	4	WCDA
BCDL	58.43	229.97	1.7	1.1	-1.7	0.7	0.9	2.1	WCDA
BELL	52.39	233.41	3	-0.8	5	0.6	0.3	1.5	WCDA
BARI	52.58	228.25	18.6	-2.9	3.1	0.7	2.8	4.6	QCI
LANG	54.26	226.94	14.6	-1.4	-0.4	1.3	12.8	5.1	QCI
MORE	53.02	227.91	12	-2.9	1.5	1.2	1.4	1.6	QCI
STJA	51.94	228.99	14.3	-5.8	-2.2	0.9	16	7.1	QCI
YAKA	54.07	228.16	8.8	2.7	2.3	2	1.4	1.4	QCI
CHWK	49.157	237.992	2.6	1.9	1.7	0.6	0.1	0.8	WCDA
ELIZ	49.873	232.877	6.2	5.4	1	0.6	0.3	1	WCDA
HOLB	50.64	231.865	2.8	-0.4	2.3	0.6	0.2	0.9	WCDA
NANO	49.295	235.914	4.8	4.6	1.8	0.6	0.2	0.7	WCDA
NTKA	49.592	233.383	6.8	7.5	2.7	0.7	0.3	0.9	WCDA
PGC5	48.649	236.549	4.6	4.7	0.1	0.6	0.2	0.8	WCDA
PTHY	50.686	232.625	3.7	-0.3	3.6	0.6	0.3	1.1	WCDA
UCLU	48.926	234.458	7.9	9.3	2.5	0.6	0.2	0.8	WCDA
WILL	52.237	237.832	0.4	-0.6	2.1	0.6	0.1	0.8	WCDA
BCOV	50.544	233.157	3.8	0.9	2.8	0.6	0.3	0.9	WCDA
TRRC	54.51	231.37	2.6	0.2	1.6	0.7	0.6	1.7	WCDA
SMIT	54.82	232.81	1.6	-0.1	2.1	0.1	0.3	0.9	WCDA

*: sites surveyed in 2007/2008; all other sites from Mazzotti et al., [2003a,b, 2008]
QCI: Queen Charlotte Island campaign. QCS: Queen Charlotte Strait campaign. WCDA: Western Canada Deformation Array, permanent.

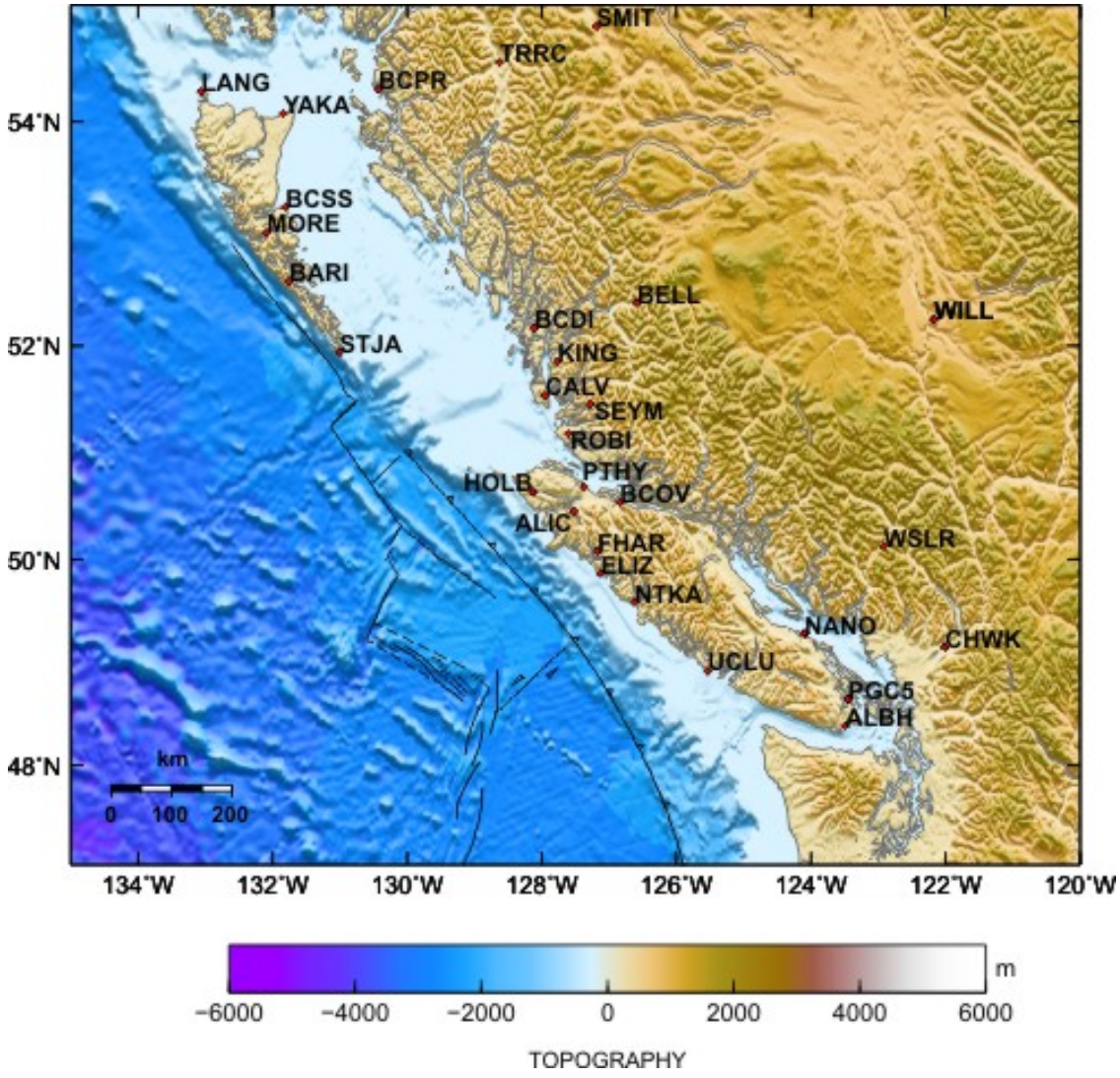

Figure 23: Locations and names of all stations that provided data for this study.

Stations not included in this table were excluded from this study because they only had two occupations (in 1993 and 1999) and hence large uncertainties, or there were issues with the raw data that could not be resolved. All time-series can be found in Appendix A.

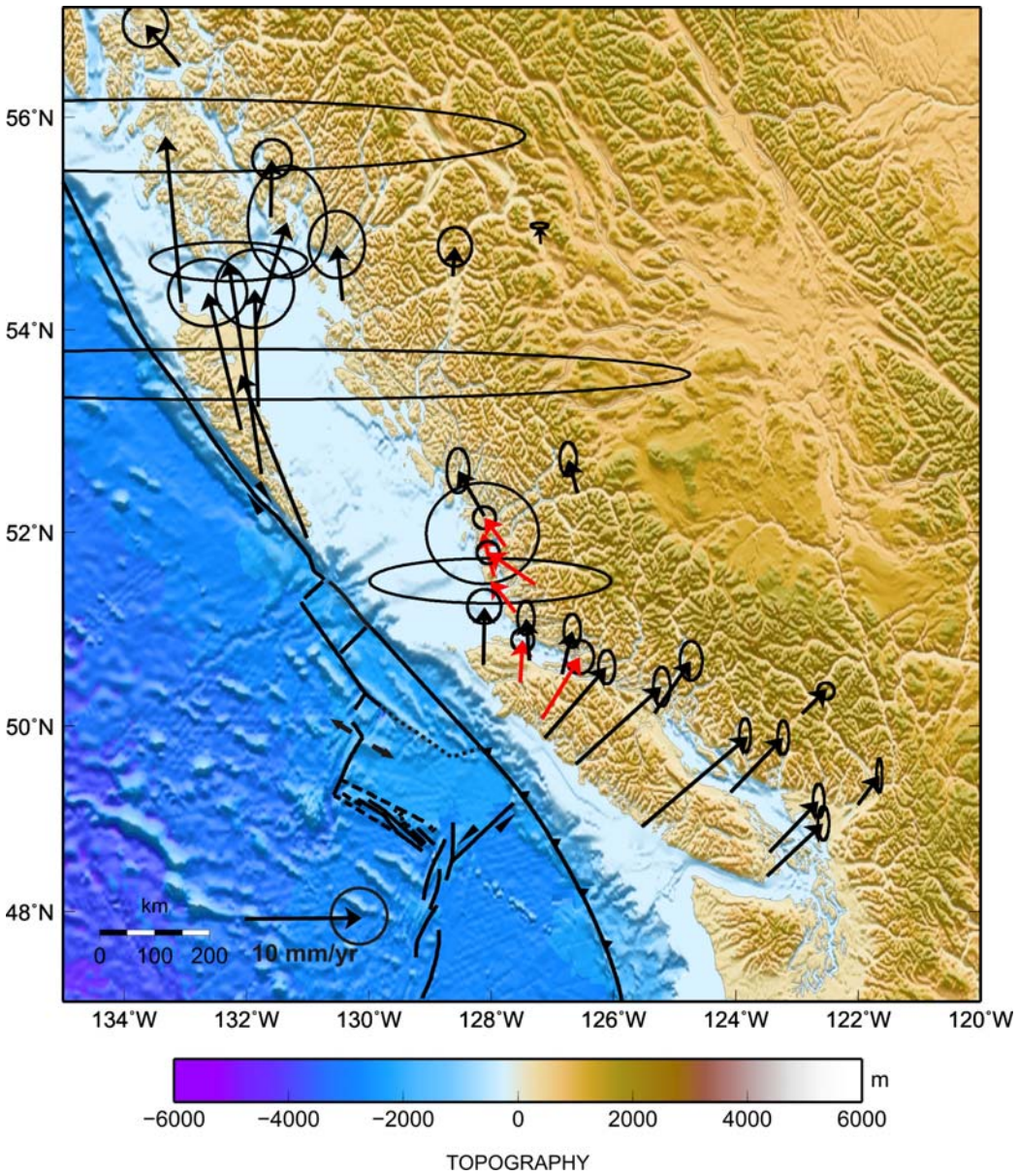

Figure 24: Horizontal velocity vectors for campaign sites with new data (red arrows) integrated into velocity field of previous surveys (black arrows) relative to stable North America.

Based on the updated velocity field, the margin can be divided into three different areas:

(1) Northern Cascadia subduction zone, south of until Brooks Peninsula

(2) Transition area between Brooks Peninsula and southern tip of Haida Gwaii

(3) Queen Charlotte fault in the north.

The velocity field in the Cascadia subduction zone indicates a north-eastward motion approximately parallel to the plate convergence direction. Velocities shift to a north-northwest, roughly margin-parallel motion between the Cascadia subduction zone and the Queen Charlotte fault. North of the southern tip of Haida Gwaii, the vectors rotate to an almost fully northward direction (Figure 24), ~ 20° from the margin orientation. These general directions of movement have already been established by Mazzotti et al. [2003 a,b]. The new data clarify the direction and velocity of crustal deformation in the area between Brooks Peninsula and southern Haida Gwaii.

The Brooks Peninsula area is particularly interesting, with stations FHAR and ALIC just to the south and the north, respectively, of the estimated northern limit of the Cascadia subduction zone. These two new velocity vectors indicate that the Brooks Peninsula is indeed the northern limit of the orthogonally converging Cascadia subduction zone (Figure 24). FHAR moves to the northeast, at an azimuth of about N32°E, and at a horizontal velocity of 4.8 mm/yr. It is clearly influenced by elastic interseismic strain accumulated on the locked subduction fault. The station ALIC moves in a northern direction, at a much smaller horizontal velocity of 1.8 mm/yr.

The stations south of Brooks Peninsula are all influenced by the subduction zone and move in a similar direction of ~ N32°E, at velocities of up to 12 mm/yr (e.g., UCLU, west coast of Vancouver Island, Figure 24), with decreasing velocities landward. Stations between Brooks Peninsula and the southern tip of Haida Gwaii show velocities of up to 5 mm/yr, at azimuth N0°W on Vancouver Island and at azimuths between N40°W and N45°W further north. In this thesis I investigate what these velocities represent, especially to distinguish between earthquake cycle related deformation and permanent

deformation. An interesting aspect of this area of GPS determined deformation is that most of the seismicity is concentrated along the plate boundaries and faults offshore, whereas there is a lack of seismicity along the mainland coast (Figure 25).

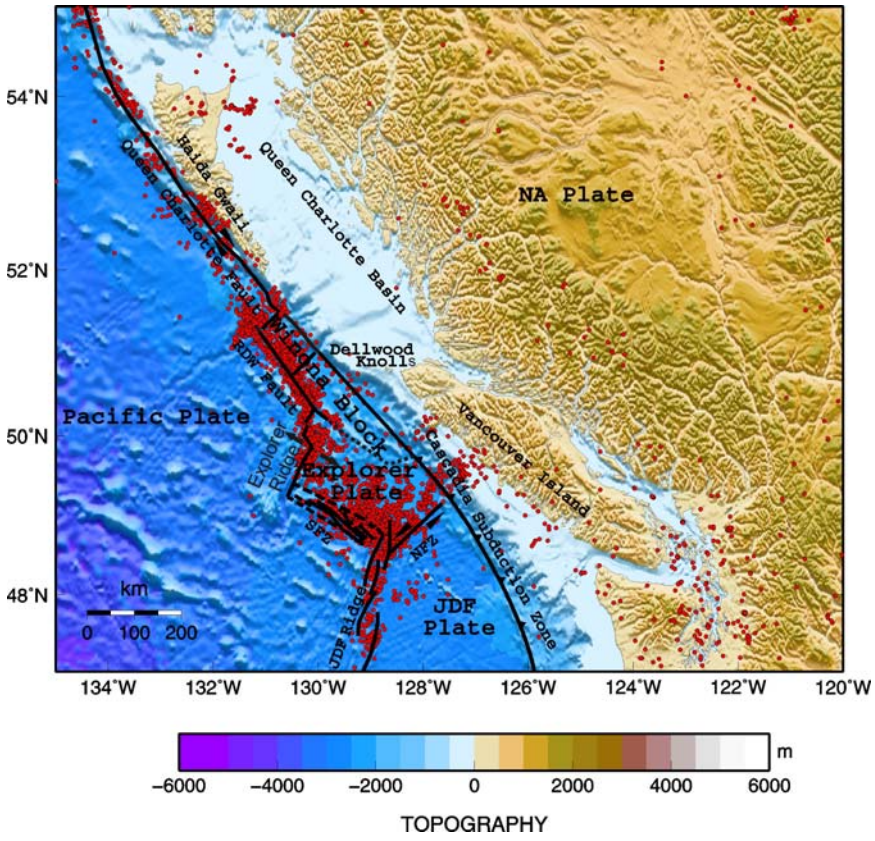

Figure 25: Seismicity in the study area. Red dots are earthquakes between 1998 and 2008 with Mw>2 (Earthquakes from Geol. Survey of Can. Database).

The stations on Haida Gwaii and the adjacent mainland move at high velocities of up to 18.8 mm/yr (decreasing landward), in directions between N0°W and N25°W, with the exception of YAKA (Figure 24), which moves north-westward (with significant uncertainty).

Chapter 4
Numerical models of earthquake cycle related deformation

4.1 Introduction

The GPS data discussed in Chapter 3 show a clearly decreasing inland strain rate for the Haida Gwaii region. Previously, this strain rate was interpreted as simple elastic strain loading associated with the near-vertical locked zone on the Queen Charlotte fault, and possibly northern end of Cascadia subduction zone; however, purely elastic interseismic loading under-predicts the observed velocities (Mazzotti et al., 2003b) (Figure 26).

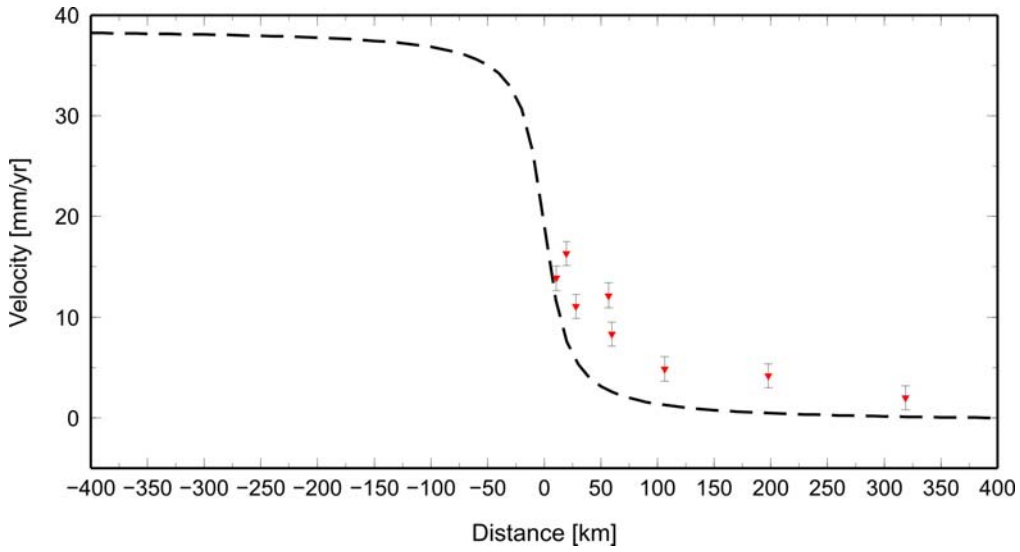

Figure 26: Simple elastic dislocation model (dashed black line), calculated after Savage and Burford [1973]. A slip rate of 39 mm/yr, locking depth of fault 15 km, a uniform elastic halfspace and an infinite fault are assumed. Observed horizontal margin-parallel velocities on the Queen Charlotte margin (red triangles). The elastic model underpredicts the observed velocities by about 2 – 10 mm/yr. To fit the data the locking depth of the fault would have to extend deeper than 20 km, which is not supported by any data (Chapter 2).

Therefore I postulate two different options to explain the observed velocities:

(1) Long-term deformation, or

(2) Viscoelastic, rather than pure elastic, deformation, related to the earthquake cycle.

In this chapter, I focus on the viscoelastic modeling of deformation associated with the earthquake cycle.

Deformation associated with the earthquake cycle

Geodetic observations associated with the 1906 San Francisco earthquake on the northern San Andreas fault led to the recognition of elastic rebound and the earthquake cycle (Reid, 1910). It has subsequently been recognized that the earthquake cycle is not entirely elastic.

Deformation is viewed as postseismic and interseismic deformation. Postseismic response describes the deformation following a seismic event. An earthquake introduces a sudden increase of differential stress in the surrounding region and induces viscous flow in the upper mantle. This flow causes a transfer of stress back to the upper crust, inducing geodetically observable postseismic surface deformation (e.g., Nur and Mavko, 1974; Savage and Prescott, 1978; Freed et al., 2010). Interseismic deformation refers to the relatively steady motion that occurs after the postseismic transient has decayed (e.g., Hetland and Hager, 2006).

Post- and interseismic deformation can be defined in terms of what is observed, i.e. a large, fast relaxation signal that decreases quickly in the first few years to decades after an earthquake (postseismic signal), and a close to steady signal that is mostly independent of time in the decades long before and after an earthquake (interseismic signal). Another approach, commonly used to simplify numerical models, is to define the postseismic and interseismic signal independently as due to mantle relaxation after an earthquake and as due to fault locking, respectively. In this study, the latter definition is used, making it possible to plot and interpret post- and interseismic deformation independently, which is particularly helpful for areas where the date of the last earthquake is not known (e.g., Northern Vancouver Island) (Y. Hu, S. Mazzotti, pers. Comm.).

In order to explain the GPS velocities in the context of earthquake cycle - related deformation, finite element models (FEM) of postseismic and interseismic deformation for a strike-slip fault and a thrust fault were developed in collaboration with Dr. Jiangheng He at the Pacific Geoscience Centre, Geological Survey of Canada.

4.2 Parameters constraining the numerical models

Two different types of models are used to account for the observed horizontal deformation across the margin. It is assumed that the two components are independent. [1] A *strike-slip model* portrays the margin-parallel component of the observed GPS velocities, and [2] a *subduction zone model* is used to portray the observed margin-normal component. The parameters used in both numerical models are elastic thickness, locking depth of fault, and uniform Newtonian viscosity, as well as dip angle and down-dip length of subducting slab for model 2.

4.2.1 Calculating effective viscosity

For a first-order estimate of viscosity, I calculate the effective viscosity based on heat flow and resulting geotherms, strain rate, and laboratory crustal and upper mantle rheologies (code by S. Mazzotti, detailed description of the calculations of differential stress profiles can be found in Hyndman et al. [2009, Appendix B]). The program calculates the differential stress for a stratified medium and a given set of parameters. The effective viscosity ($\eta = \sigma/2\dot{\varepsilon}$) associated with a power-law rheology is given by

$$\eta = \sigma^{(1-n)}\, e^{(Q/RT)} / A,$$

where $\dot{\varepsilon}$ is the strain rate (s^{-1}), A is a material constant [$MPa^{-n}s^{-1}$], σ is the differential stress [MPa], n is the power law exponent, Q is the activation energy [kJ mol^{-1}], R is the universal gas constant [J $mol^{-1}K^{-1}$], and T is temperature [K]. The thickness of the

continental crust varies along the margin, from about 18 km in the Queen Charlotte Sound to ~ 39 km underneath Northern Vancouver Island (Chapter 2). The average heat flow in the Queen Charlotte margin area is calculated to be ~ 90 mW/m^2, and 87 mW/m^2 in the transition area (Chapter 2). Strain rate έ is calculated using GPS velocities presented in Chapter 3. In the Haida Gwaii area, velocities decrease from 15.4 mm/yr to 1.6 mm/yr over a distance of ~ 400 km resulting in a strain rate of $\acute{\varepsilon} \approx 10^{-15}\ s^{-1}$. For the transition area, observed horizontal velocities decrease from 5.1 mm/yr to 3.1 mm/yr over a distance of ~200 km, which leads to a strain rate of about $3 \times 10^{-16}\ s^{-1}$. To accommodate the different values for strain rate, heat flow and crustal thickness across the margin, a suite of models has been calculated (Table 6) (Appendix B). Several different rheologies (Table 7) can be used for the crust and the mantle. The Queen Charlotte margin used to be part of an active subduction zone; hence a wet rheology is assumed. There is not enough knowledge to determine with certainty whether granite or quartz-diorite are the main components of the crust, nor can I determine whether the mantle is mainly composed of dunite or olivine. I tested different rheologies (Table 7), which are not shown here, and concluded that changes in the composition have a minor (less than ten) effect on the resulting effective viscosity. Other parameters used are shown in Table 8.

Table 6: Parameters constraining three sets of models based on two different continental thicknesses.

	Set I		**Set II**		**Set III**	
upper crust [km]	0 - 9		0 - 9		0 - 9	
middle crust [km]	9 -20		9 - 20		9 – 20	
lower crust [km]			20 - 30		20 – 40	
upper mantle	20 - 400		30 - 400		40 - 400	
av. heat flow [mW/m^2]	80 - 100		80 – 100		80 -100	
strain rate [s^{-1}]	10^{-15}	3.2×10^{-16}	10^{-15}	3.2×10^{-16}	10^{-15}	3.2×10^{-16}

Table 7: Rheological parameter for the upper mantle used in the power law model

Mineral/Rock	Wet/Dry	A[$Pa^{-n}s^{-1}$]	n	Q[J/mol]	Reference
Granite (GRW)	Wet	$7.94x10^{-16}$	1.9	$137x10^{3}$	Hansen and Carter, 1982
Quartz-Diorite (QDW)	Wet	$1.26x10^{-16}$	2.4	$212x10^{3}$	Carter and Tsenn, 1987
Felsic granulite (FGW)	Wet	$2.01x10^{-21}$	3.1	$243x10^{3}$	Wilks and Carter, 1990
Mafic granulite (MGW)	Wet	$8.83x10^{-22}$	4.2	$445x10^{3}$	Wilks and Carter, 1990
Diabase (DIW)	Wet	$7.94x10^{-25}$	3.4	$260x10^{3}$	Shelton and Tullis, 1981
Dunite (DUW)	Wet	$4.89x10^{-15}$	3.5	$535x10^{3}$	Hirth and Kohlstedt, 1996
Olivine (OLW)	Wet	$6.51x10^{-16}$	3.0	$430x10^{3}$	Karato and Wu, 1993

Table 8: Parameters used in all models to calculate effective viscosity. (* see Table 7 for explanation)

	Upper crust	Mid crust	Lower crust	Upper mantle
Pore fluid pressure	0.4	0.4	0.4	0.4
Rheology *	GRW	QDW	DIW	DUW
Av. Density [kg/m^3]	2700	2800	3000	3300
Heat generation [W/m^3]	$3.0*10^{-6}$	$0.8*10^{-6}$	$0.2*10^{-6}$	$0.02*10^{-6}$
Heat conductivity [W/(m*K]	3.0	3.0	2.5	3.5
Surface temp. [°C]	0	--------	--------	--------
Heat flow [W/m^2]	80 - 100	--------	--------	--------
Av. Strain rate [1/s]	10^{-15}; $3.2*10^{-16}$	10^{-15}; $3.2*10^{-16}$	10^{-15}; $3.2*10^{-16}$	10^{-15}; $3.2*10^{-16}$

Based on the parameters discussed above, I calculate a suite of different effective viscosities with varying continental crustal thickness, strain rates, and geotherms (Figures for all models showing differential stress, effective viscosity and geotherm in Appendix B). These results provide a first order estimate of plausible effective viscosity values for the viscoelastic part of the FEM models used to calculate post- and interseismic velocity profiles.

The continental crust of the model is effectively elastic on the time scale of the earthquake cycle of 300 years, with an effective viscosity of more than 10^{22} Pa s in each case. The effective viscosity in the lithospheric mantle is also quite high (> 10^{21} Pa s); hence the only part of the modeled Earth that has a viscous behaviour is the non-lithospheric mantle, which has an effective viscosity ranging from 3.2 x 10^{19} Pa s to 3.2x10^{20} Pa s for all calculated models (Appendix B). Those values agree with effective viscosities calculated in other studies for similar tectonic environments (e.g., James et al., 2009 for NW British Columbia). In the finite element models an effective viscosity calculated for the deeper non-lithospheric mantle is used as an approximation for the Newtonian viscosity of the viscoelastic layer, since the focus of this study is a time more than 50 years after an earthquake. Power-law is characterized by very fast initial deformation and much slower later deformation (Wang, 2007). The contribution of a stress perturbation (e.g., earthquake) can be neglected if it is much smaller than the background stress associated with mantle convection (Melosh, 1980). When the contribution of stress perturbation is neglected, then the effective viscosity depends only on the background stress, thus can be regarded as a Newtonian viscosity (Wang, 2007). 20 years after an earthquake, time does not play as important a role anymore for the

postseismic deformation; hence the stress perturbation for 20 years and more after an earthquake is "sufficiently small to justify the use of a Newtonian viscosity" (Wang, 2007).

4.3 Viscoelastic strike-slip model to calculate postseismic and interseismic margin-parallel deformation

4.3.1 Introduction

The viscoelastic model used in this study consists of a uniform elastic layer and a uniform viscoelastic layer. Unlike previously used elastic dislocation models, it takes into account the deeper viscous part of the mantle. A material is considered viscoelastic when it behaves elastically on short timescales (1 to 10^4 seconds), and viscously on long timescales (10^{11} to 10^{17} seconds) (e.g., Turcotte and Schubert, 2002). The Maxwell model of a viscoelastic material consists of a material in which the rate of strain, $\dot{\varepsilon}$ is the superposition of a linear elastic strain rate, $\dot{\varepsilon}_e$ produced by the rate of change of stress σ', and a linear viscous strain rate, $\dot{\varepsilon}_f$ produced by the stress σ. The fundamental rheological law relating strain rate, stress, and the rate of change of stress for a Maxwell viscoelastic material is:

$$\frac{d\varepsilon}{dt} = \frac{1}{2\mu}\sigma + \frac{1}{E}\frac{d\sigma}{dt};$$

where ε is the total strain, the sum of the elastic and the fluid strains, E is Young's modulus, μ is the viscosity, and σ is the stress. This equation governs the mantle rheology of a viscoelastic model (e.g., Turcotte and Schubert, 2002).

4.3.2 Model description

I use the finite-element code 3dev. This code was developed by Dr. Jiangheng He at the Pacific Geoscience Centre, Geological Survey of Canada, and is described in detail

by Hu et al. [2004]. In order to study first-order postseismic and interseismic deformation, the model is simplified and focuses on the essential aspects of the fundamental physical processes involved (Hu et al., 2004).

To model post- and interseismic deformation in the study area, I use a simple 2.5-dimensional model, which is described in greater detail by Hu et al., [2004]. The model consists of three main features (Figure 27):

(1) The elastic layer, with a thickness based on the crustal thickness in the study area. As detailed in Chapter 2, the continental crustal thickness in the Queen Charlotte margin is roughly between 20 and 30 km, and hence I start with a model that has an elastic layer thickness of 20 km. Other values are tested since that value varies significantly across the margin.

(2) The underlying viscoelastic layer to the bottom of the mesh at 400 km depth (the middle of the mantle transition zone), with a prescribed Newtonian viscosity (several viscosities are tested). Changes in depth have very little effect on the horizontal velocities on the surface (E. Hearn, pers. Comm.).

(3) The fault with a prescribed fault slip, which is described as a uniform slip of 11.75 m in dextral direction during an earthquake. The effects of transient after-slip and any possible pre-slip in the coseismic step are included by adding a 10 km deep zone of transition downwards from the rupture zone (Hu et al., 2004). The fault is assumed to be locked along its entire length; hence the locked and interseismic transition zones are extended to the northern and southern mesh boundaries. The locking of the fault is described using Savage's [1983] method of back-slip. If the strike-slip process is

considered purely seismic, it will take 300 years to build up enough slip deficit for the next 11.7 m rupture event with a back-slip rate of ~ 39 mm/yr.

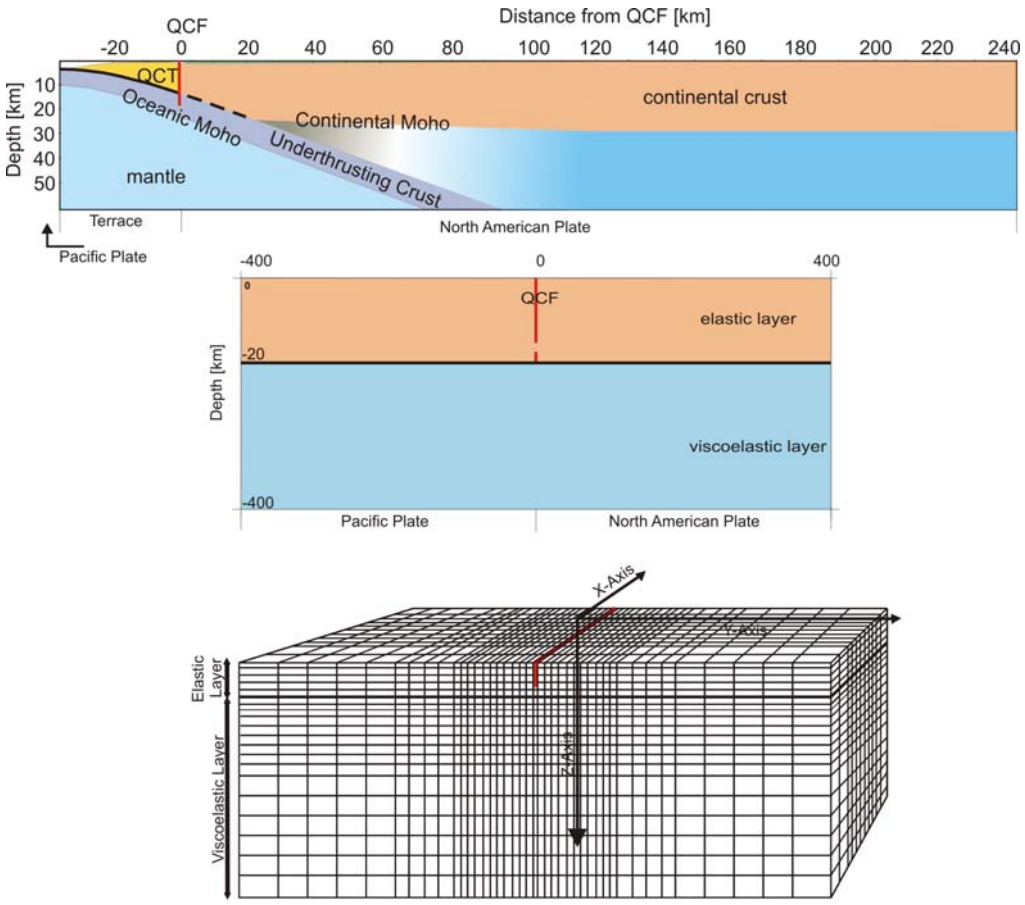

Figure 27: Top: Simplified cross-section for the Queen Charlotte Fault strike-slip model based on Line 6 (Chapter 2). Solid black line: locked portion of fault. Dashed black line: transition zone. Middle: simple 1-D model based on the cross-section, with the elastic layer and the viscoelastic layer corresponding to the continental crust and the upper mantle, respectively. Solid red line: locked zone. Dashed red line: transition zone, extending downward from fully locked to full slip. Bottom: Mesh of the finite element model for the strike-slip system.

The model consists of 13,520 isoparametric trilinear hexahedral elements, with a fine grid around the fault and a coarse grid near the model boundaries, and a mesh extending 400 km east and west of the fault and a length of 800 km along-strike (Figure 27, bottom). Displacement perpendicular to each model boundary is fixed at zero (except for the free upper surface), and displacements parallel to the boundary are not constrained.

Following Wang et al. [2001], the Young's modulus of the elastic plates and mantle are assumed to be 120 GPa and 160 GPa, respectively, and the Poisson's ratio and rock density are assumed to be 0.25 and 3.3 g/cm^3, respectively, for the entire system. The gravitational acceleration is assumed to be 10 m/s^2.

4.3.3 Effect of time passed since earthquake on modeled deformation

60 years have passed since the last major earthquake on the Queen Charlotte fault, a M_w 8.1 event in 1949 (epicentre: latitude 53.62°N, longitude 133.27°W). The fault ruptured about 500 km in total, from the southern west coast of Moresby Island to southeast Alaska (Bostwick, 1984). The focal mechanism for the 1949 earthquake indicates virtually pure strike-slip movement with a northwest striking nodal plane corresponding to the strike of the fault (Rogers, 1986).

Hence, the timeframe for the modeling is well constrained. However, investigating the effect of time on post- and interseismic deformation helps to benchmark the model. It also clarifies which deformation process is important at any given time since the earthquake. I use a starting model with an elastic layer of 20 km, a seismogenic fault depth of 15 km (Chapter 2), and a viscosity of the viscoelastic layer of 10^{19} Pa s, as discussed earlier.

Postseismic Deformation

As described earlier in Chapter 4.1, postseismic deformation is transient and decays over time. The decay is most rapid during the first two decades after a seismic event, then slows in the decades after (Figure 28). Postseismic deformation is mainly concentrated within 150 km of the fault; however, there are still velocities up to ~ 5 mm/yr detectable farther away in the ~50 years after the earthquake.

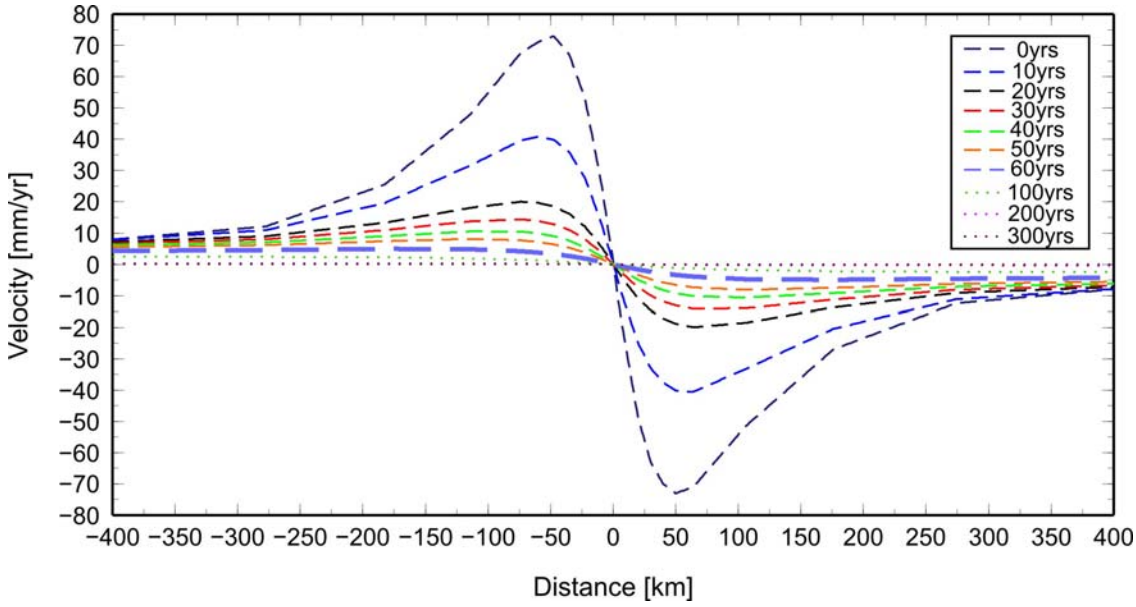

Figure 28: Change of postseismic response over time. Thick dashed blue line: 60 years after event. The profiles of fault-parallel velocities are plotted relative to the location of the fault.

Interseismic Deformation

The velocity profile has the highest gradient right at the time of the rupture (0 years) right at the fault, and then becomes slightly lower, with measurable velocities farther away from the fault (Figure 29). However, time does not have a significant influence on the interseismic deformation. It emphasizes the fact that, while postseismic deformation is predominant during the first two decades after an earthquake and then declines quickly, interseismic deformation remains close to steady over time.

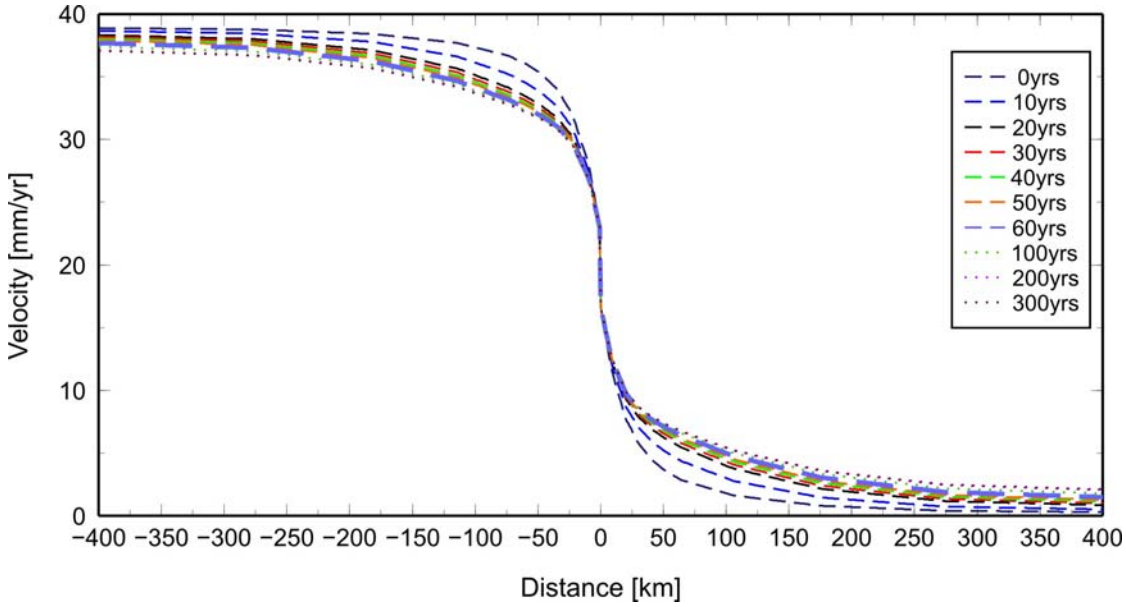

Figure 29: Change of interseismic response over time. Thick dashed blue line: 60 years since event. The velocity profiles are plotted relative to the eastern far-field of the model.

Combined Deformation

The combined response is a linear combination of the interseismic and postseismic response to an earthquake, and the combined velocities can be compared to the ones measured with GPS (Chapter 5). Postseismic deformation is the dominant deformation mechanism until about 20 years after the earthquake, when the influence of the postseismic deformation becomes less, whereas the interseismic deformation remains steady (Figure 30). The effect of time on interseismic deformation is negligible, thus the change in combined response is only affected by the decline of the postseismic response over time. 60 years after a seismic event (e.g., Mw 8.1 in 1949), interseismic deformation is the main contributing factor to the combined deformation.

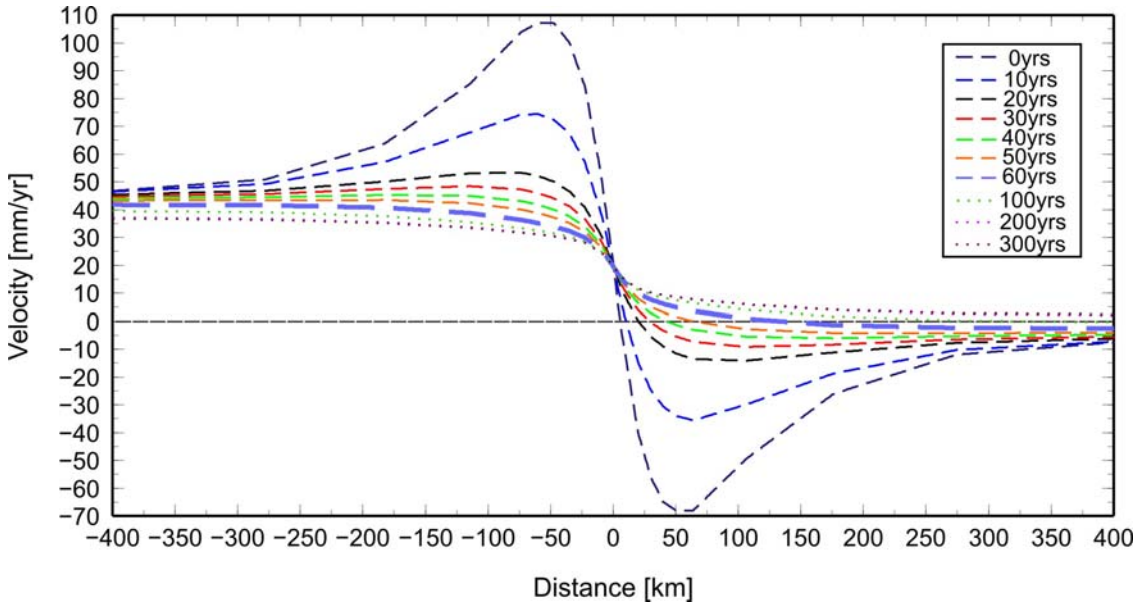

Figure 30: Change of combined response over time. Thick blue dashed line: 60 years after event.

4.3.4 Effect of changes in viscosity

For the following models, I only look at velocity profiles 60 years after the event. Postseismic deformation does not have a significant effect on the combined deformation 60 years after the event (see 4.3.3), so in the following figures, post- and interseismic deformation are not independently plotted.

I look at a starting geometry model and vary viscosity: The elastic layer thickness is 20 km, the fault depth is 15 km, and the viscosity varies between 10^{18} and 10^{23} Pa s.

The velocity profiles for low viscosities ($<10^{18}$ Pa s) and high viscosities ($\geq 10^{22}$, Pa s) are within ~3% (~1 mm/yr) of the *interseismic* velocity profiles (not plotted), since the postseismic deformation with these parameters is negligible. For a viscosity of 10^{19} Pa s, the influence of *postseismic* deformation on combined velocities is only significant at distances farther than 100 km away from the fault. For viscosities of 10^{20} Pa s and 10^{21} Pa s, *postseismic* deformation has a minor (less than 3 mm/yr) effect on the combined

response for a distance greater than 100 km away from the fault. The lower the viscosity, the lower is the velocity gradient of the *combined* velocity profile, with measurable velocities (> 1 mm/yr) up to 400 km away from the fault. The higher the viscosity, the higher the velocity gradient, with velocity distribution concentrated close to the fault. Results using viscosities higher than 10^{21} Pa s are similar to elastic deformation models. Results for viscosities of 10^{18} to 10^{20} Pa s are the ones that depart the most from the elastic model (Figure 31).

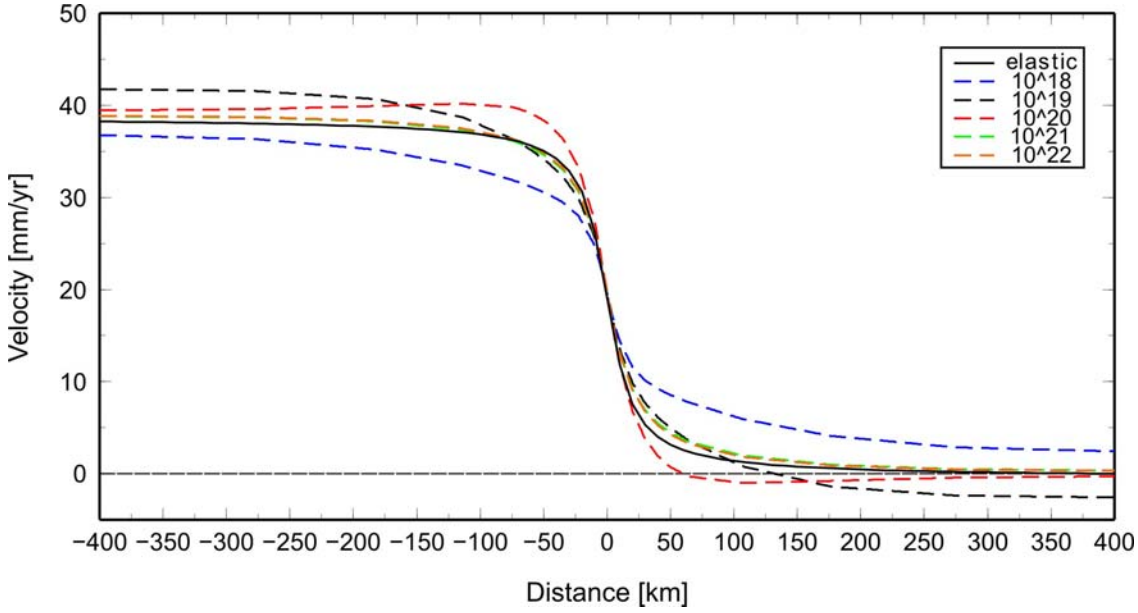

Figure 31: Influence of changes in viscosities of the combined respsonse. 60 years after event. Small negative values are due to ongoing mantle relaxation (postseismic deformation).

4.3.5 Effect of changes in thickness of elastic layer

As stated in Chapter 4.2, the crustal thickness, which is described by the elastic layer in the viscoelastic models, varies along the margin. Since the elastic layer has the same thickness across the margin within each model, I investigate the effect of changing that thickness on the velocity profiles. I keep the fault depth constant at 15 km, and change the elastic layer thickness from 20 to 30 to 50 km.

Combined Deformation

Changing the thickness of the elastic layer while keeping the fault depth constant at 15 km has some effect on the velocity profile (Figure 32). After 60 years, the *postseismic* deformation for a viscosity of 10^{18} Pa s is negligible, and it is less than ~ 5 mm/yr for a viscosity of 10^{19} Pa s, which is still small compared to the interseismic deformation. The changes of the *interseismic* velocity profiles are within less than ~5 mm/yr for viscosities of 10^{18} and 10^{19} Pa s (Figure 32).

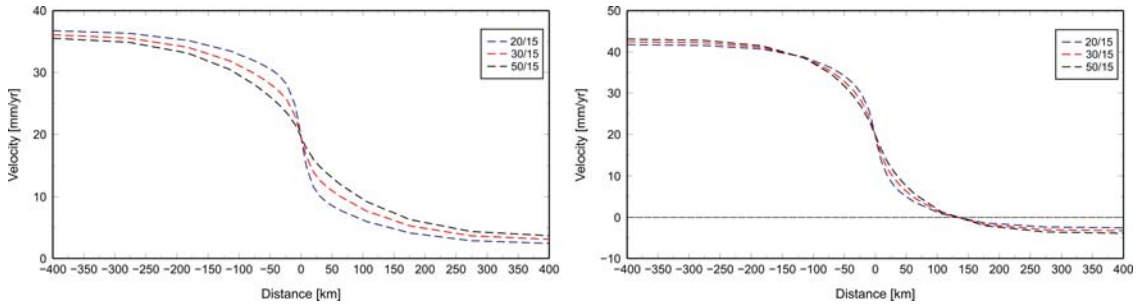

Figure 32: Effect of changes in thickness of elastic layer on combined response, 60 yrs after event. First number in the legend indicates thickness of elastic layer, second number maximum depth of the fault. Left: viscosity 10^{18} Pa s. Right: viscosity 10^{19} Pa s. Note difference in vertical scale.

4.3.6 Effect in changes of fault seismogenic / locking depth

As seen in 4.3.5, the depth of the fault in relation to the thickness of the elastic layer can be an important control on the resulting velocity profiles.

Combined Deformation

Figure 33 illustrates the effects of changes in fault seismogenic / locking depth in relation to the thickness of the elastic layer. Changes in the maximum fault depth have no significant effect on the velocity profile if the elastic layer is 50 km thick, i.e., neither the *postseismic* nor the *interseismic* velocity profiles show a difference of more than ~ 2 mm/yr with different fault depths. In contrast, when a thinner elastic layer (30 km) is

used, varying the fault depth results in changes in the velocity profile for the *combined* response of up to 7 mm/yr. The effect on *postseismic* deformation is more significant at distances farther than 50 km away from the fault, but it still small (maximum 2 mm/yr) compared to the *interseismic* deformation.

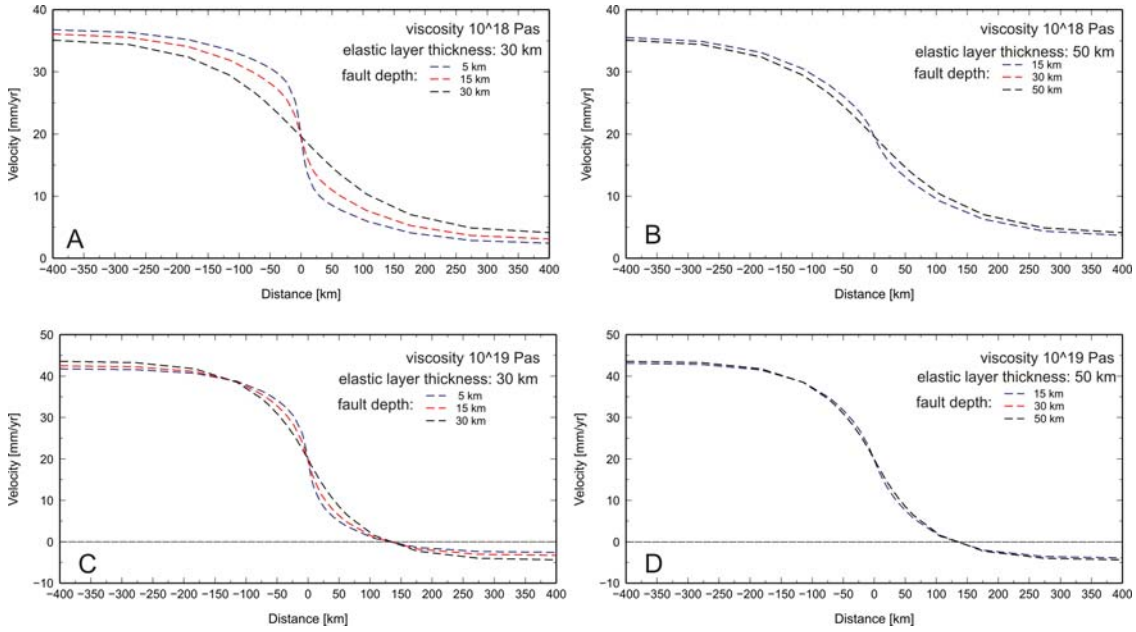

Figure 33: Effect of changes to fault depth and effect of fault depth in relation to thickness of elastic layer on combined velocity profiles. Model A and B (top row) have viscosity of 10^{18} Pa s, models C and D (bottom row) of 10^{19} Pa s.

The combined response is affected as follows:

(1) A thin elastic layer (< 30 km) in conjunction with a shallow fault (< 10 km) results in a curve with a steep gradient, with the velocity profile decreasing quickly close to the fault (within the nearest ~50 km).

(2) A thin elastic layer (< 30 km) in conjunction with a deep fault (>15 km) results in a curve with a gentler slope, with velocities up to 5 mm/yr more than 200 km away from the fault.

(3) The fault depth has no significant impact (< 3 mm/yr) on the velocity profile when combined with a thick elastic layer (50 km).

4.4 Preferred Model

On the basis of geological and seismic data described in the previous chapters, the elastic layer thickness can be averaged as 30 km, and the fault depth is given at 15 km. Based on the strain rate and the geotherms, the effective viscosity for power law flow is constrained to be 10^{19} Pa s or more. Therefore, I discuss the velocity profiles with viscosities of 10^{19} and 10^{20} Pa s. The last earthquake at the Queen Charlotte Fault was the 8.1 Mw in 1949, and based on that I examine the postseismic and interseismic deformation 60 years after an event. Assuming a 300 year earthquake cycle and a slip rate of 39 mm/yr, the preferred model based on the parameter constraints results in a combined response that is reflected in a curve with a high velocity gradient, with most of the deformation concentrated close to the fault. With a viscosity of 10^{20} Pa s, the response is very close to a purely elastic model. Postseismic deformation is still measurable, but interseismic deformation is the dominant deformation process (Figure 34). All models with reasonable parameters show a more rapid reduction in velocities with landward distance from strike-slip fault than the observed values.

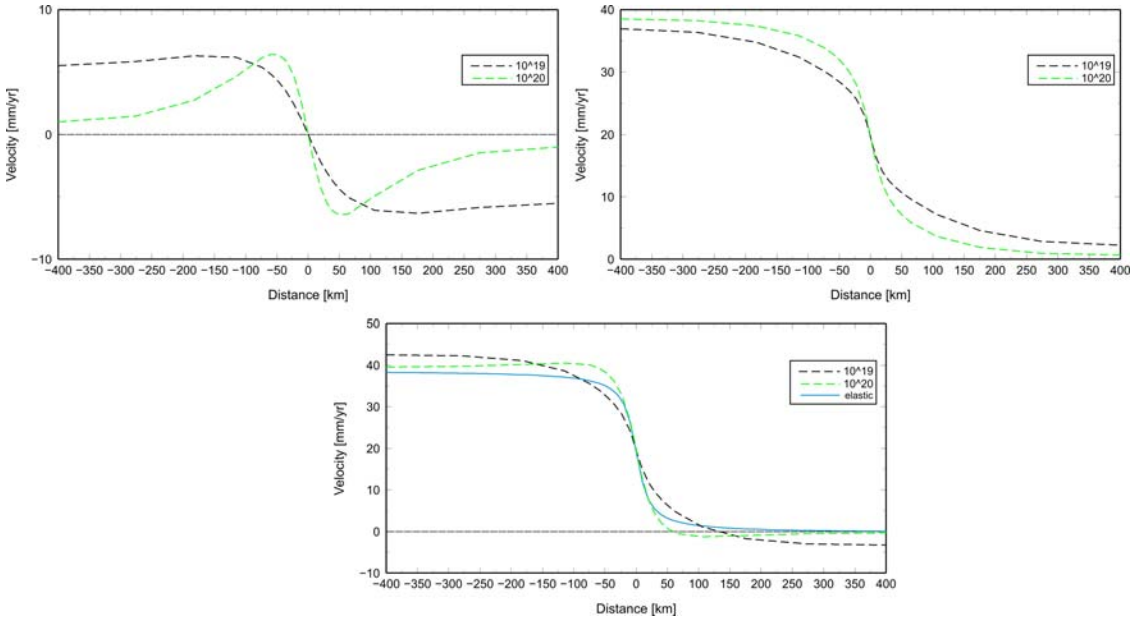

Figure 34: Preferred model, postseismic (top left), interseismic (top right) and combined (bottom) velocity profiles. Thickness of elastic layer: 30 km, fault depth 15 km, viscosity: 10^19 and 10^20 Pa s. Combined velocity profiles compared to elastic profile (blue solid line). Note different vertical scales.

4.5 Viscoelastic subduction zone model to calculate postseismic and interseismic margin-normal deformation

4.5.1 Model description

The code used was developed by John He at the Pacific Geoscience Centre. It is a simple 2.5-D model developed to study post- and interseismic crustal deformation. The model and parameters are similar to the viscoelastic strike-slip model (Section 4.3). Only parameters specific to this model are described below:

(1) an elastic layer representing the oceanic crust with a thickness of 5 km. The actual thickness of the oceanic crust and downgoing slab is not significant in this modelling exercise, since its effect on the velocities modeled on the continental side of the fault is negligible compared to the effect of the thickness and viscosity of the continental crust (J. He, pers. Communication). To simplify the

terminology, I refer to the 5 km layer as the oceanic elastic layer or downgoing slab in the following (Figure 35).

(2) An elastic layer representing the continental crust with a specified crustal thickness of 39 km (Figure 35). Sediments above the subducting oceanic crust are considered to have similar properties as continental crust.

(3) A viscoelastic layer representing the oceanic upper mantle with a specified viscosity, and a viscoelastic layer representing the continental upper mantle with a specified viscosity (Figure 35). I only tested models where the viscosity for oceanic and continental upper mantle was identical.

(4) A thrust fault with prescribed fault slip as well as locked and transition zones. The fault is assumed to be locked along its entire length, and the locking of the fault is described using Savage's [1983] method of backslip (see 4.3.2).

The mesh of the model extends 800 km to the east and to the west of the fault and 800 km along strike.

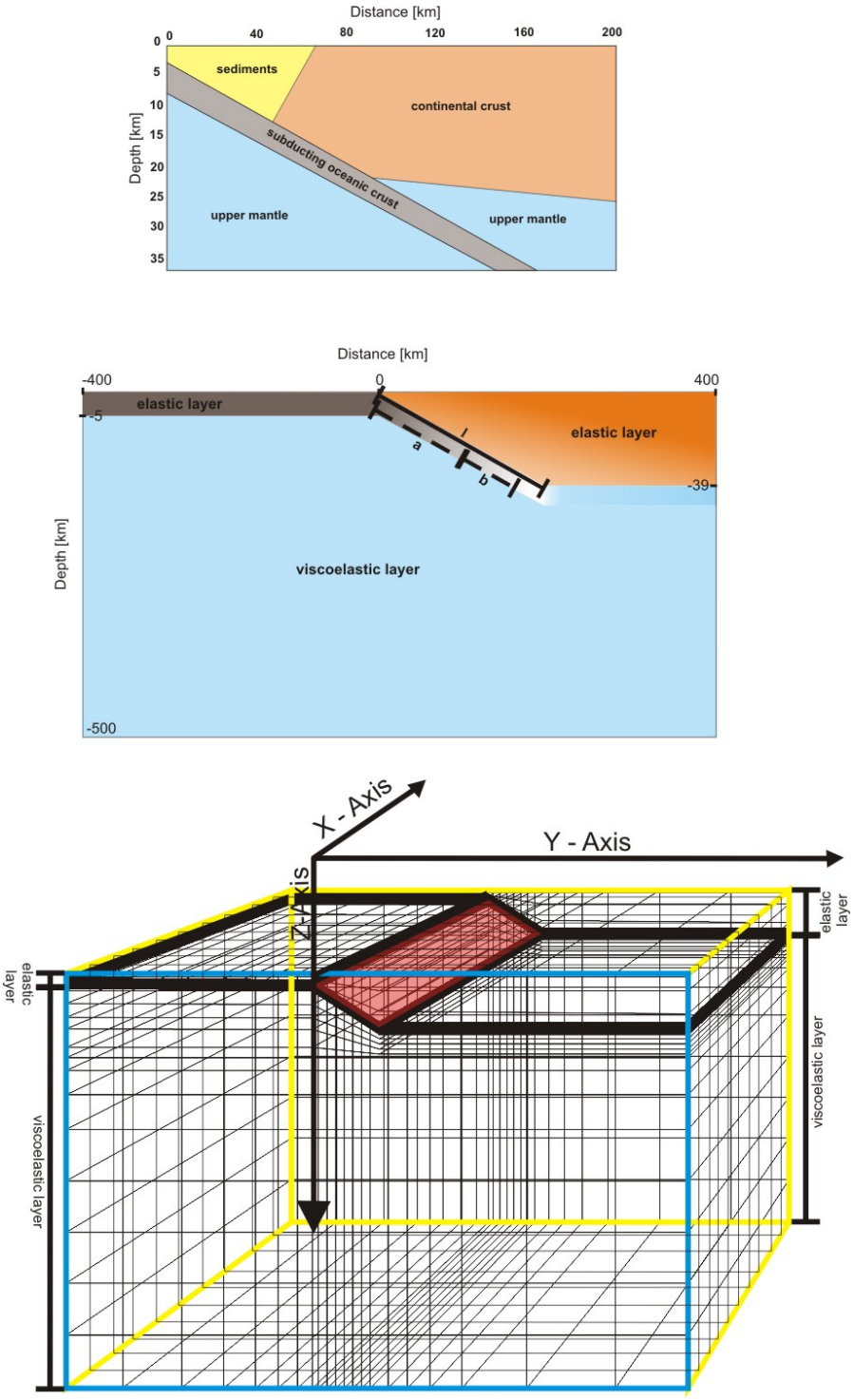

Figure 35: Top: Simplified crustal cross-section based on Line 2 (Chapter 2). Middle: simple 1-D model based on crustal cross-section, with the elastic layer and the viscoelastic layer corresponding to the crust and the upper mantle, respectively. l: Length of slab. a: length of locked zone. b: length of transition zone. Bottom: Mesh of the finite element model for the subduction zone system.

4.5.2 Effect of time on modeled deformation

The starting model shows velocity curves for models with a 300 year earthquake cycle, a 5 km thick elastic layer west of the fault a 39 km thick elastic layer east of the fault (portraying the continental crust), an elastic slab subducting at an angle of 20° and with a downdip length of 120 km, and a locked zone from 0 – 20 km followed by a transition zone to 25 km depth. A slip rate of 13.3 mm/yr is applied (following Mazzotti et al., 2003).

Postseismic Deformation

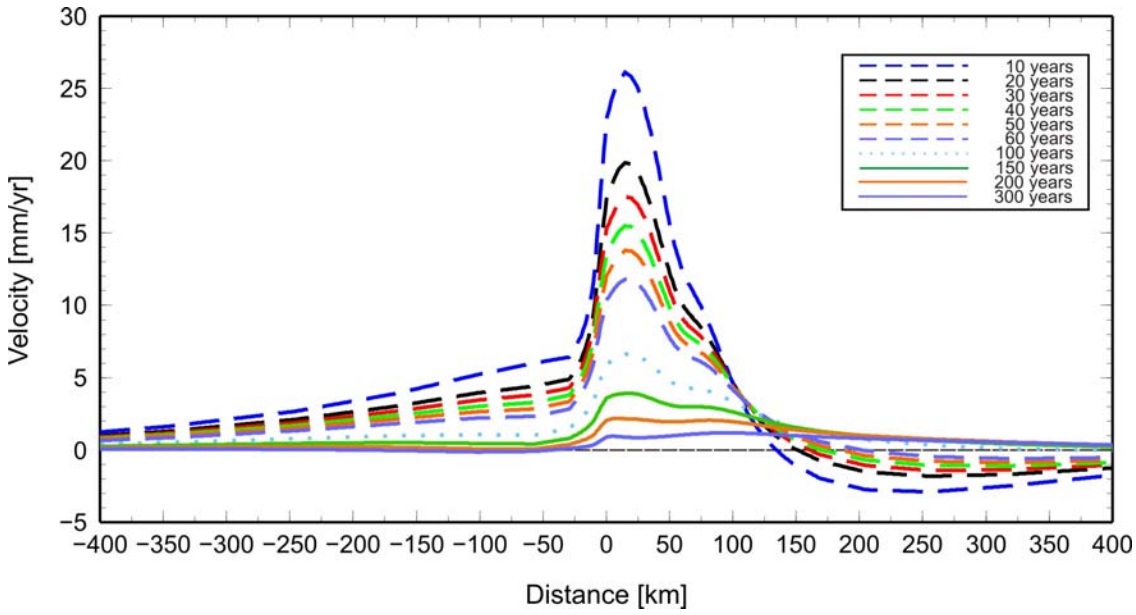

Figure 36: Postseismic margin-normal velocities for models with a upper mantle viscosity of 10^{19} Pas. 10 to 300 years after the event.

Figure 36 shows velocity profiles for 10 to 300 years after an earthquake. Postseismic deformation decays rapidly during the first two decades after a seismic event, and slower in the decades after. The maximum variation of velocity is concentrated within 120 km east of the fault, which coincides with the lateral extent of the downgoing slab. The slight

changes in slope of the velocity curves at 58 and 73 km correspond to the maximum downdip limit of locked and transition zone, respectively. The small negative values (< 3 mm/yr) observed east of the fault for postseismic velocity profiles up to 60 years after the earthquake are indicative of relaxation of earthquake- induced stresses in the upper mantle (Hu, 2011).

Since no thrust earthquake M ≥ 8 has been recorded since recording started in 1899 (Earthquakes Canada), I focus on velocity profiles for 150, 200, and 300 years after the event. The maximum velocity is reached ~ 15 km east of the fault, where values are ~ 4 mm/yr at a time of 150 years after an event, ~ 2 mm/yr at a time of 200 years, and <1 mm/yr at a time of 300 years.

Interseismic Deformation

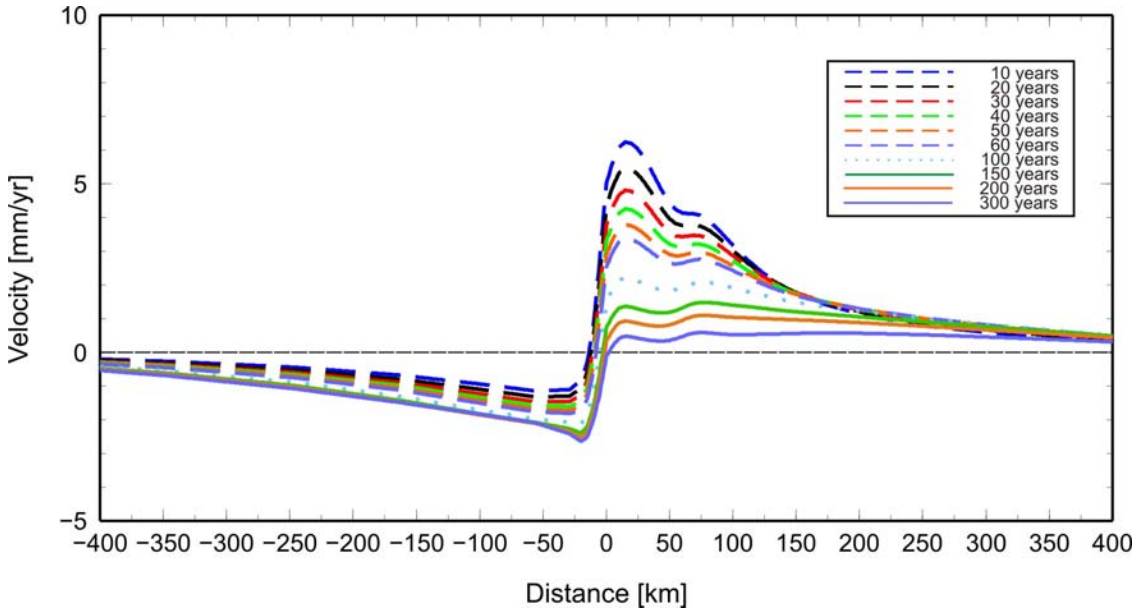

Figure 37: Interseismic velocity profiles for models with a upper mantle viscosity of 10^{19} Pas, The velocity profiles are plotted relative to the location of the fault.

Time has less influence on interseismic velocity profiles than it has on the coseismic velocities. Hence the decline in maximum velocity with time is less pronounced, from ~ 6 mm/yr in the decade after the seismic event, to ~ 2 mm/yr 150 years after and < 1mm/yr 200 years after. Similar to the postseismic velocity distribution, the maximum is reached close to the fault and velocities decrease eastwards; however, the decay is less pronounced and velocity curves are wider and less steep (Figure 37). The locked and transition zones can be identified at ~ 58 and 73 km east of the fault, respectively.

Combined Deformation

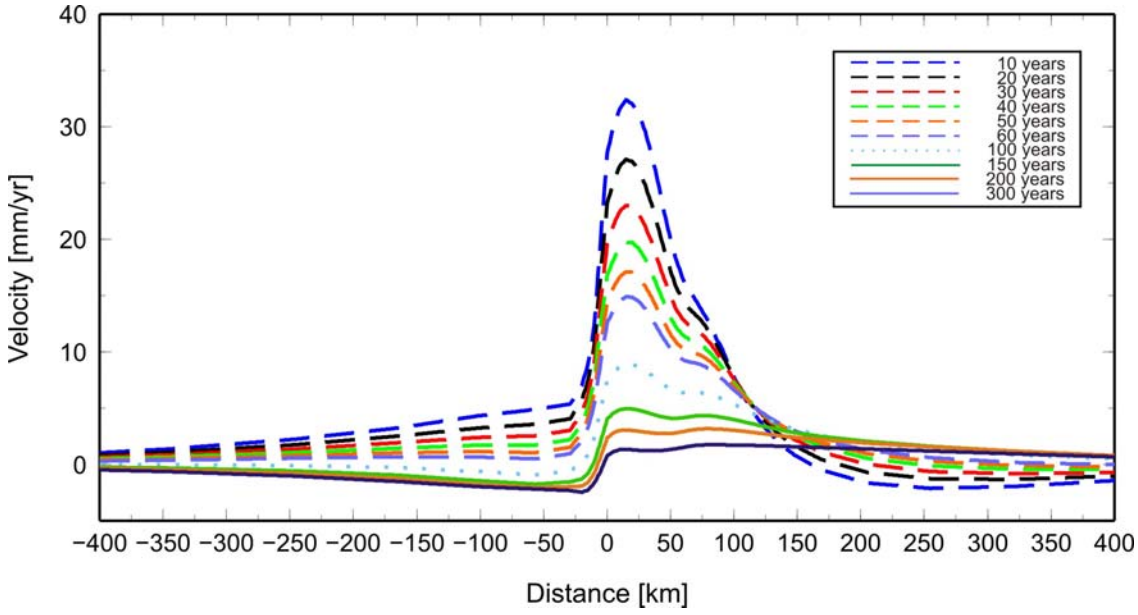

Figure 38: Combined velocity profiles for models with a upper mantle viscosity of 10^{19} Pas.

The combined velocity profiles represent the complete response of the system to a seismic event. As seen previously, the postseismic response is the dominating process during the first ~100 years, then both processes (post- and interseismic) contribute similarly to the overall deformation (Figure 38). However, for the time period 150 and

more years after an event, the velocities are generally very low, with a maximum of ~ 5 mm/yr about 15 km east of the fault.

For the following models, only the 150 year velocity profile is shown, assuming that this is the minimum time that has passed since an earthquake with a thrust component M>8 has occurred. Velocity profiles for more than 150 years after an event are not shown for the tests, since the velocities are too low to easily recognize changes due to variations in the parameters tested. Post- and interseismic deformation contribute roughly in equal parts to the total velocity at that point, and so only the combined deformation is shown in the following.

4.5.3 Effect of changes in viscosity on modeled deformation

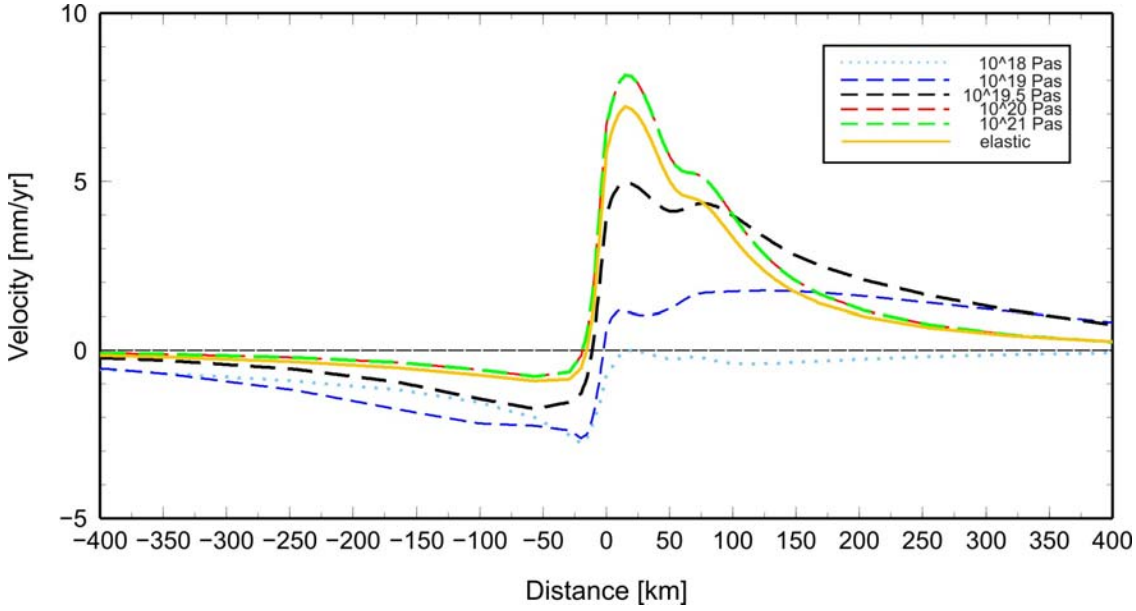

Figure 39: Influence of changes in viscosities on the combined velocity profiles, 150 years after event.

Five velocity profiles are shown, representing models with different viscosities (10^{18}, 10^{19}, $3.2x10^{19}$, 10^{20}, 10^{21} Pas). It has to be noted that the numerical model is not set up for viscosities below 10^{19} Pa s, so velocities for these smaller viscosities are not reliable.

Viscosities of ≥ 10^{20} Pa s yield effectively elastic velocity curves, represented by a steep decline in velocity at ~ 130 km away from the fault. Similar to the previously discussed strike-slip system, the lower the viscosity, the more spread out the deformation becomes, leading to a diffuse velocity profile for viscosities of 10^{18} and 10^{19} Pa s, with no clear maximum, and very low velocities (< 2mm/yr) throughout the system. Higher viscosities yield steeper curves and clearly defined maxima (e.g., ~ 5 mm/yr ~ 15 km away from the fault for 3.2 x 10^{19} Pa s) (Figure 39).

4.5.4 Effects of changes in dip angle of subducting plate on modeled deformation

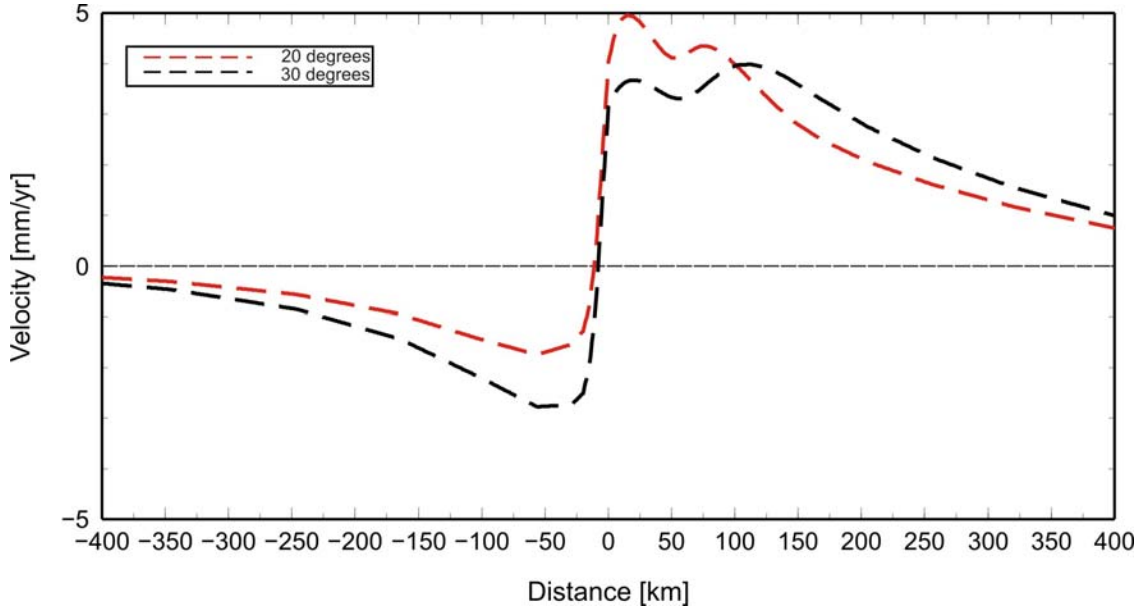

Figure 40: Influence of change of the angle of the downgoing slab from 20 ° to 30° on combined velocity profiles, 150 years after event.

A change of the angle of the downgoing slab from 20° to 30° has very little effect on the overall velocity profile (Figure 40). The maximum velocity is ~ 5 mm/yr for a 20° angle, and it reduces to 3.5 mm/yr for a 30° angle). The observed differences are due to the change in width of the locked and transition zones, which become narrower with a steeper angle.

4.5.5 Effect of changes in length of subducting slab on modeled deformation

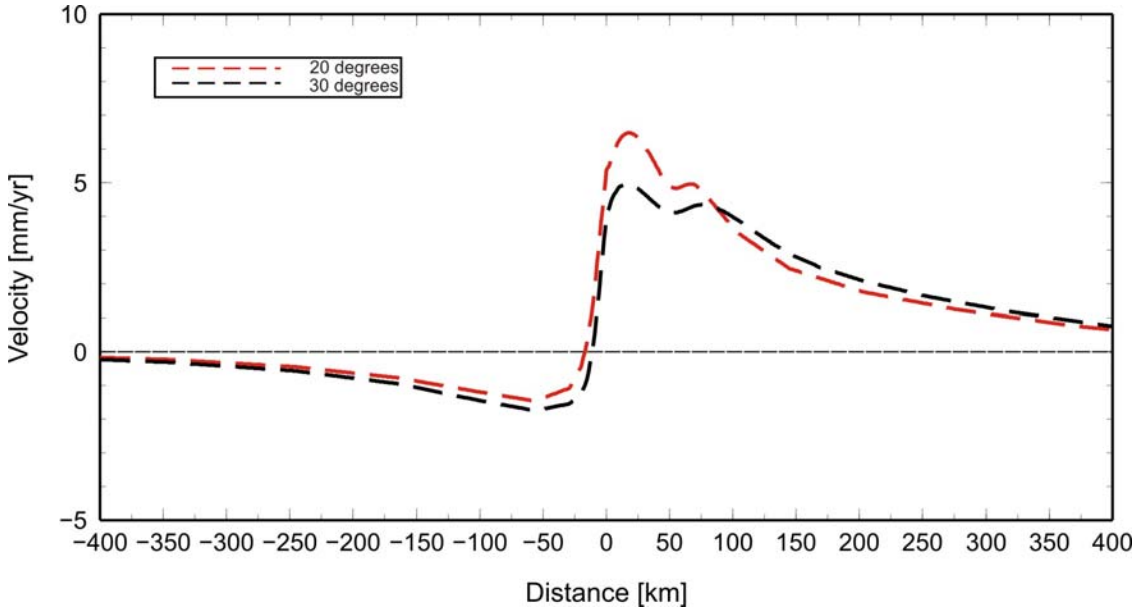

Figure 41: Effect of different slab length on combined velocity profile, 150 years after event.

Changes in the slab length have little effect on the combined velocity profile. A shorter slab length results in a steeper velocity profile, with a velocity distribution concentrated closer to the fault (Figure 41). At about 15 km east of the fault the maximum velocity is ~ 6.5 mm/yr for the short slab and ~ 4.5 mm/yr for the long slab. The shorter slab yields a slightly flatter velocity distribution, but the differences between the two models are generally less than 2 mm/yr.

4.5.6 Effect of changes on locked portion and transition zone of fault

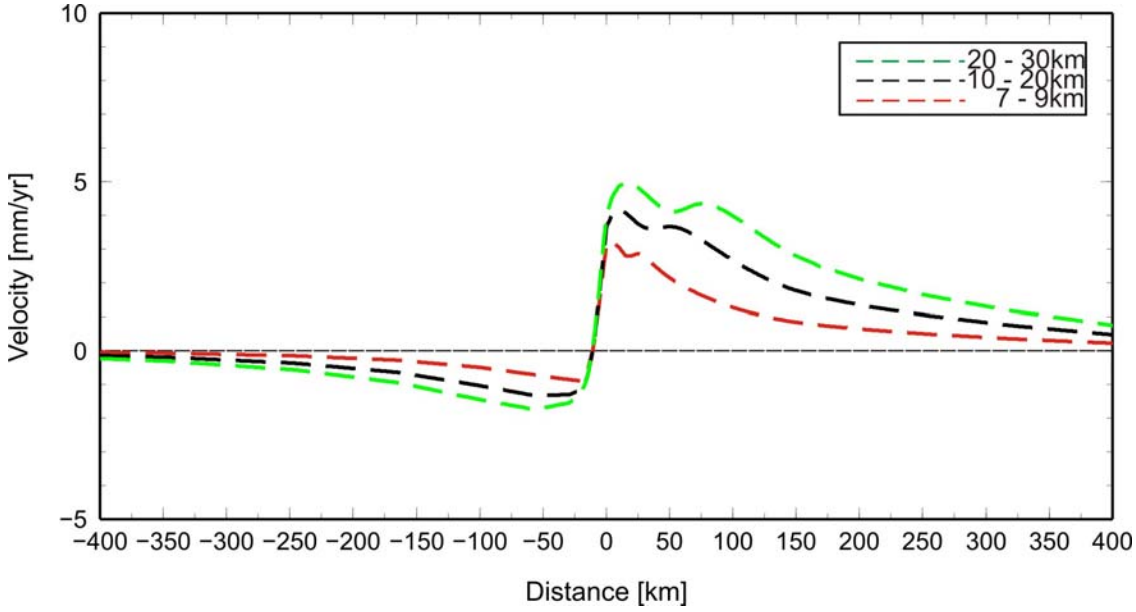

Figure 42: Effect of changes to locking depth and transition zone depth on combined velocity profiles. First number indicates maximum depth of locking zone, second number maximum depth of transition zone, 150 years after event.

A deeper locked/transition zone results in a wider locked/transition zone if the dip angle of the subducting slab is kept constant. The velocity profiles for the different locked/transition zones reflect those changes accordingly, with a wider velocity distribution for a deeper locked/transition zone, and a steeper profile for a shallower locked/transition zone (Figure 42).

Summary of effects of tested changes

Most changes only yield minor effects on the velocity profiles, mostly because 150 years have passed since the seismic event and the velocities are generally very low (mostly ≤ 5 mm/yr). The most significant changes can be achieved by changing the depth of the locked and/or the transition zone as well as viscosities, whereas changes in the dip angle or the length of the downgoing slab only result in minor changes (≤ 1.5 mm/yr).

4.6 Preferred model

The preferred model is constrained based on the parameters discussed in Chapter 2. The oceanic elastic layer has a thickness of 5 km, and the elastic layer representing the continental crust is 39 km. Tests for the strike-slip model have shown that changes in crustal thickness yield only very minor effects (Figure 32); hence those values have been kept constant for the subduction model. The slip rate is chosen to be 13.3 mm/yr (Mazzotti et al., 2003); the dip angle and the length of the subducting slab are 20° and 120 km, respectively. The viscosity is 3.2 x10^{19} Pa s. The fault is locked to a depth of 20 km, followed by a transition zone to 25 km.

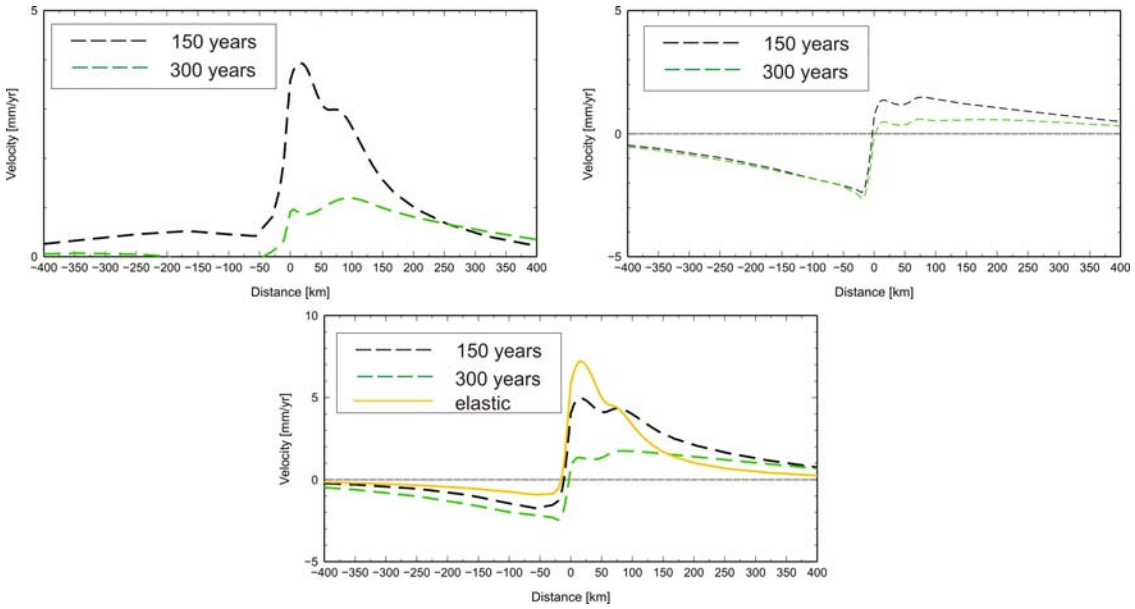

Figure 43: Preferred model. Velocity profiles for postseismic (top left), interseismic (top right), and combined (bottom) deformation, for 150 and 300 years after event. Elastic model plotted for comparison in plot showing velocity profile for combined model (solid yellow line).

Chapter 5
Current tectonics and deformation distribution of the west coast of British Columbia

5.1 Current tectonics based on GPS data and numerical modeling

The combination of velocities determined from GPS and viscoelastic modeling provides an improved picture of the deformation distribution on the west coast of British Columbia. In an area where there is little seismicity recorded and the geological record of surface faults is sparse (in part due to the inaccessibility of the area), numerical modeling is an important tool to understand the observed GPS deformation. In this study it is used to qualify observed deformation as either related to the earthquake-cycle or long-term. Based on the observed horizontal deformation, three different tectonic zones are identified (Queen Charlotte transform fault, Cascadia subduction zone, transition between transform fault and subduction zone) (Figure 44). The Queen Charlotte fault is a dextral transpressive fault system, and deformation can be observed as far east from the fault as 400 km. The modeling will address the question whether the observed inland deformation is linked to the Queen Charlotte fault, and whether the deformation is associated with possible subduction at the Queen Charlotte fault. Further south, the tectonic setting is highly complex with a triple junction offshore, and the influence from a underthrusting Explorer (and possibly Winona) plate is uncertain.

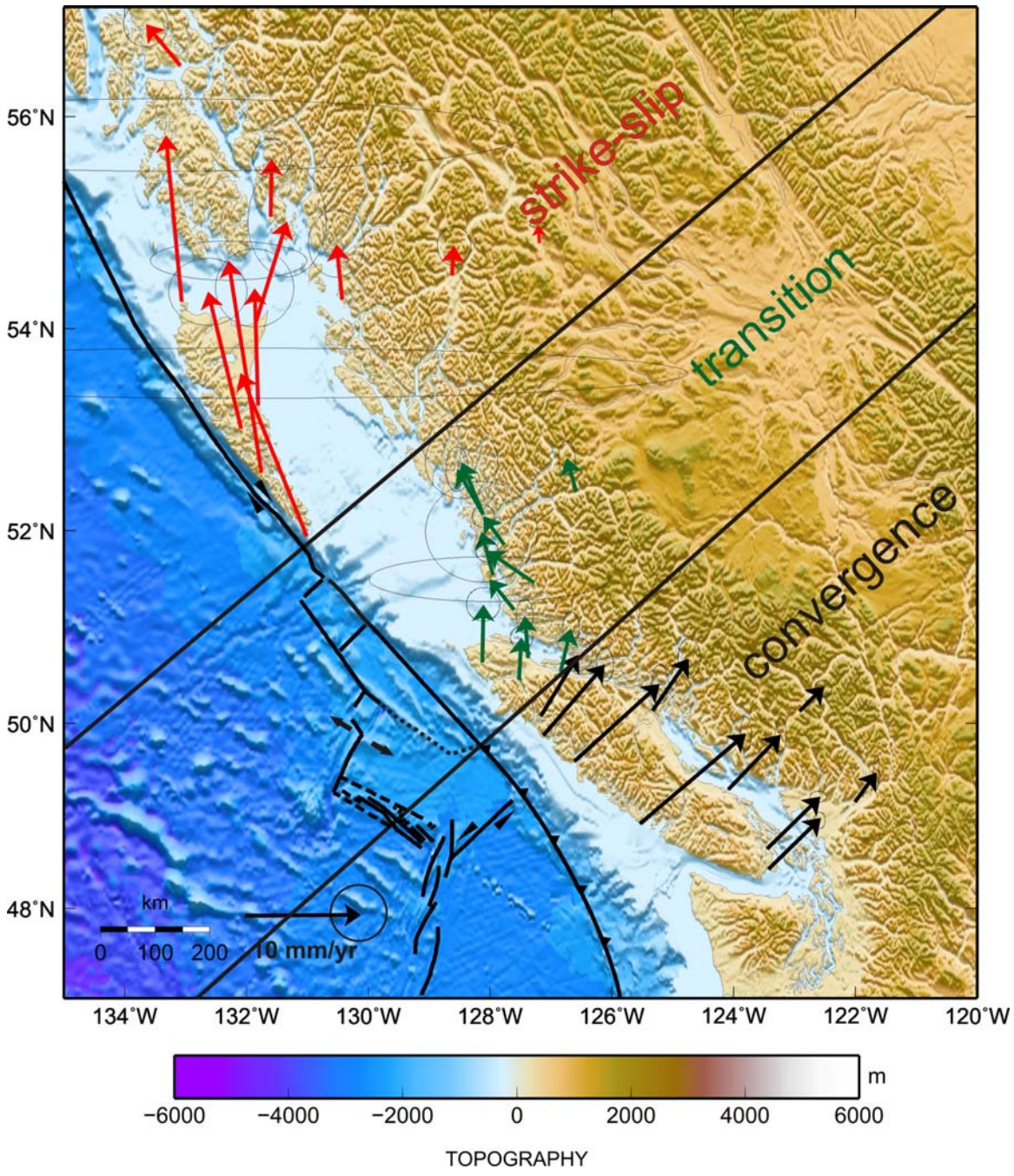

Figure 44: Map of northwest pacific margin, showing observed horizontal deformation. Three separate tectonic areas are indicated: strike-slip (in red), transition area between strike-slip and convergence (dark green), converging system (black).

5.1.1 Northern Cascadia Subduction Zone

At the Cascadia subduction zone, the Juan de Fuca plate subducts underneath the North American plate at a rate of up to ~ 4 cm/yr (e.g., Mazzotti et al., 2003b). Thanks to numerous studies based on continuous and campaign GPS data (McCaffrey et al., 2000, 2002; Miller et al., 2001; Svarc et al., 2002; Mazzotti et al., 2003), as well as extensive seismicity and tectonic studies (e.g., Riddihough, 1984; Walcott, 1993; Wells et al., 1998), the main aspects of the present-day Cascadia tectonics and dynamics are well constrained. The subduction thrust is currently fully locked, leading to margin-normal shortening and uplift of the forearc (e.g., Dragert and Hyndman, 1995; Miller et al., 2001).

Extensive modeling has already been done on the north-western part of the Cascadia subduction zone. Flück et al. [1997] developed a three-dimensional elastic dislocation model (based on a 2-D elastic model for Cascadia (Hyndman and Wang, 1993)), with the best fit provided by a model with a thrust locked along the whole margin and an average downdip width of 60 km, below which is a 60 km wide transition zone. Wang et al. [2003] developed CAS3D-2, a 3-D dislocation model that calculates the interseismic deformation rates at the Cascadia subduction zone. The main difference compared to the previous models is that the slip deficit rate from fully locked to full slip in the transition zone decreases exponentially with downdip, whereas previous models used a linear downdip transition (Hyndman and Wang, 1995; Flück et al., 1997). Using an exponential decrease for the slip deficit rate prevents the over-prediction of coastal GPS velocities and the under-prediction of inland velocities (Wang et al., 2003).

All types of models explain the observed horizontal GPS data reasonably well; however, there are residual values that cannot be explained by transient deformation, and the vertical velocity models do not fit the observed data. Hence long-term deformation is possibly responsible for part of the observed velocities, and fore-arc deformation is proposed (Mazzotti et al, 2003a). The new campaign data in this thesis confirms that the subduction of the Explorer plate does not extend south of Brooks Peninsula (see Chapter 3). Detailed explanations of the models as well as of the results can be found in Hyndman and Wang, [1993]; Flück et al., [1997], and Wang et al., [2003].

5.1.2 Queen Charlotte Fault

5.1.2.1 Margin – parallel deformation

The Queen Charlotte Fault is a dextral transpressive strike-slip fault system; hence the main slip component expected is the margin-parallel slip (Figure 45). The slip decomposition into margin-parallel and –normal is based on the azimuth of the fault trace closest to each station. The observed horizontal margin-parallel velocities of all stations north of the southern tip of Haida Gwaii are plotted on a two-dimensional profile in order to compare them to the modeled velocities (Figure 46).

The margin-parallel deformation shows a clear gradient, from velocities of ~13.9 mm/yr closest to the fault to ~ 1.2 mm/yr at a distance of 410 km east. As discussed in Chapter 4, the reference model has a upper mantle viscosity of at least 10^{19} Pa s, an elastic layer thickness of 30 km and a fault depth of 15 km. Comparing the resulting velocity profile with the observed horizontal margin-parallel deformation shows that the model significantly under-predicts (by up to 5 mm/yr) the observed horizontal margin-parallel deformation (Figure 46), (Table 10).

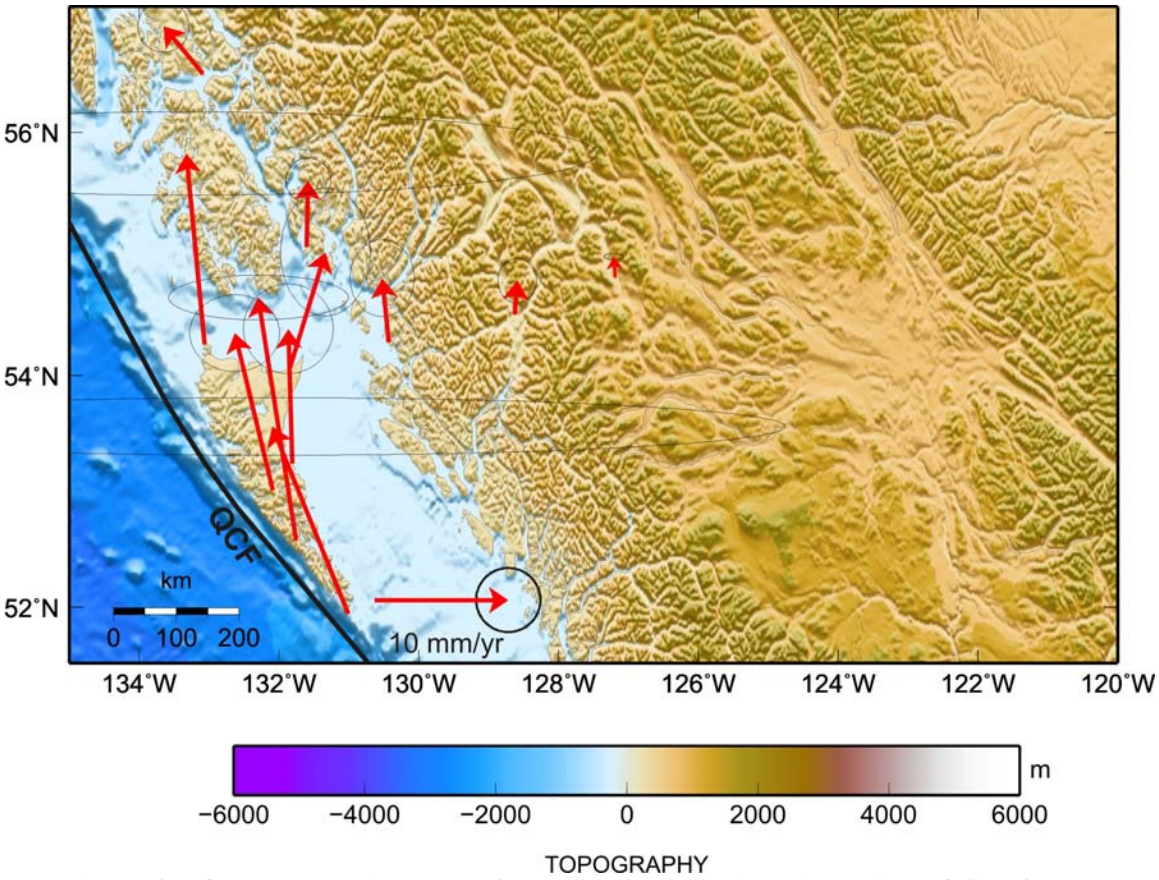

Figure 45: Observed horizontal deformation in the strike-slip regime. QCF: Queen Charlotte Fault.

Table 9: Observed horizontal margin-parallel and margin-normal on the Queen Charlotte margin.

Station	Distance fault [km]	Observed velocity [mm/yr]	margin-parallel velocity [mm/yr]	margin-normal velocity [mm/yr]
STJA	10.84	15.43	13.87	6.76
BARI	19.7	18.82	16.30	9.41
MORE	28.15	12.35	11.10	5.41
LANG	56.72	14.67	12.16	8.20
BCSS	59.56	10.30	8.34	6.06
YAKA	106.28	9.20	4.88	7.81
BCPR	197.77	4.93	4.20	2.57
TRRC	318.72	2.61	2.0	1.68
SMIT	412.57	1.60	1.23	1.01

Table 10: Observed margin-parallel velocities compared to modeled margin-parallel veloctities. First number in modeled velocoties: elastic layer thickness; second number: depth of fault; third number: viscocity

Station	margin-parallel velocity [mm/yr]	30/15; 10^{19}Pa s	residual velocities [mm/yr]	reduced chi^2	30/20; 10^{19}Pa s	residual velocities [mm/yr]	reduced chi^2	30/30; 10^{19}Pa s	residual velocities [mm/yr]	reduced chi^2
STJA	13.87	14.68	-0.81	254.01	15.41	-1.54	242.40	16.93	-3.06	222.28
BARI	16.30	11.82	4.48		12.74	3.56		14.68	1.62	
MORE	11.10	9.88	1.22		10.78	0.32		12.74	-1.64	
LANG	12.16	5.49	6.67		6.09	6.07		7.43	4.73	
BCSS	8.34	5.14	3.20		5.72	2.62		6.99	1.35	
YAKA	4.88	1.06	3.82		1.18	3.70		1.13	3.75	
BCPR	4.20	-2.04	6.24		-2.26	6.46		-2.15	6.35	
TRRC	2.00	-2.91	4.91		-3.46	5.46		-4.12	6.12	

Station	margin-parallel velocity [mm/yr]	30/15; 10^{18}Pa s	residual velocities [mm/yr]	reduced chi^2	30/20; 10^{18}Pa s	residual velocities [mm/yr]	reduced chi^2	30/30; 10^{18}Pa s	residual velocities [mm/yr]	reduced chi^2
STJA	13.87	13.77	0.10	33.92	14.35	-0.48	36.15	15.80	-1.93	80.12
BARI	16.30	12.17	4.13		13.19	3.11		14.53	1.77	
MORE	11.10	11.16	-0.06		12.32	-1.22		14.35	-3.25	
LANG	12.16	8.99	3.17		11.45	0.71		11.88	0.28	
BCSS	8.34	8.70	-0.36		11.16	-2.82		11.74	-3.40	
YAKA	4.88	6.52	-1.64		7.25	-2.37		8.70	-3.82	
BCPR	4.20	4.06	0.14		4.64	-0.44		5.51	-1.31	
TRRC	2.00	3.19	-1.19		3.25	-1.25		3.91	-1.91	

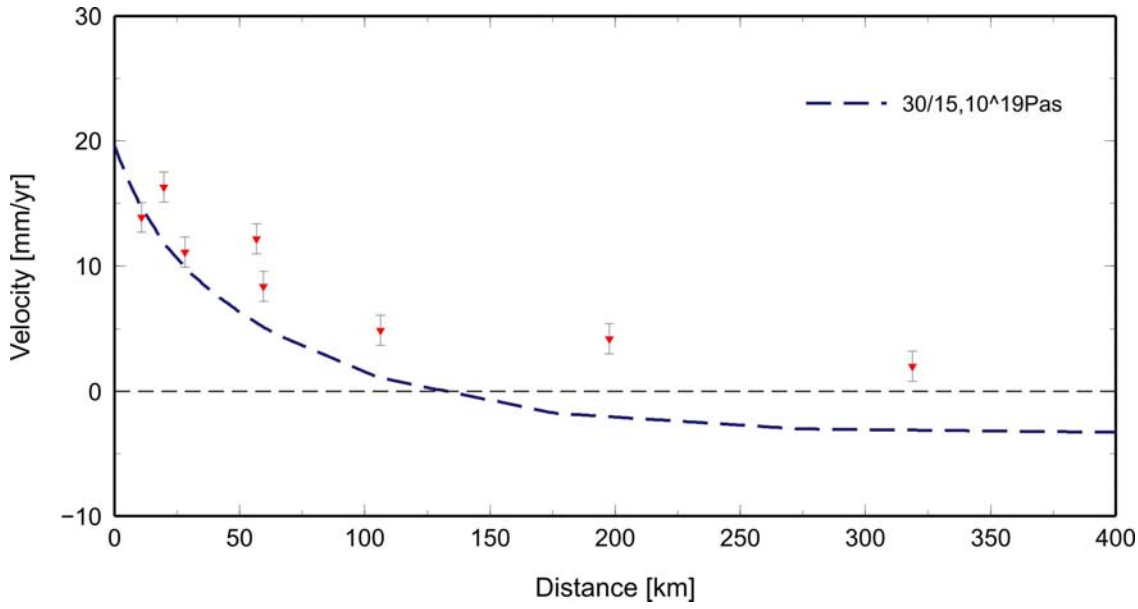

Figure 46: Observed horizontal margin-parallel deformation (red triangles) compared to the preliminary model (blue dashed line). Elastic layer thickness 30 km, fault depth 15 km, viscosity 10^{19} Pa s.

The modeled velocities are largest close to the fault, and the velocities at distances of ~ 130 km east of the fault are small and negative. In contrast observed velocities are still > 4 mm/yr at a distance of 200 km east of the fault zone. To match the observed velocities, a velocity profile based on a model with a lower viscosity in the viscous layer is needed. The best-fit model is achieved using an elastic layer thickness of 30 km, and a fault with a locking depth of 15 km. The viscosity is 10^{18} Pa s (Table 10, Figure 47). For larger fault depths, the modelled velocities at distances > 100 km are larger than the observed values.

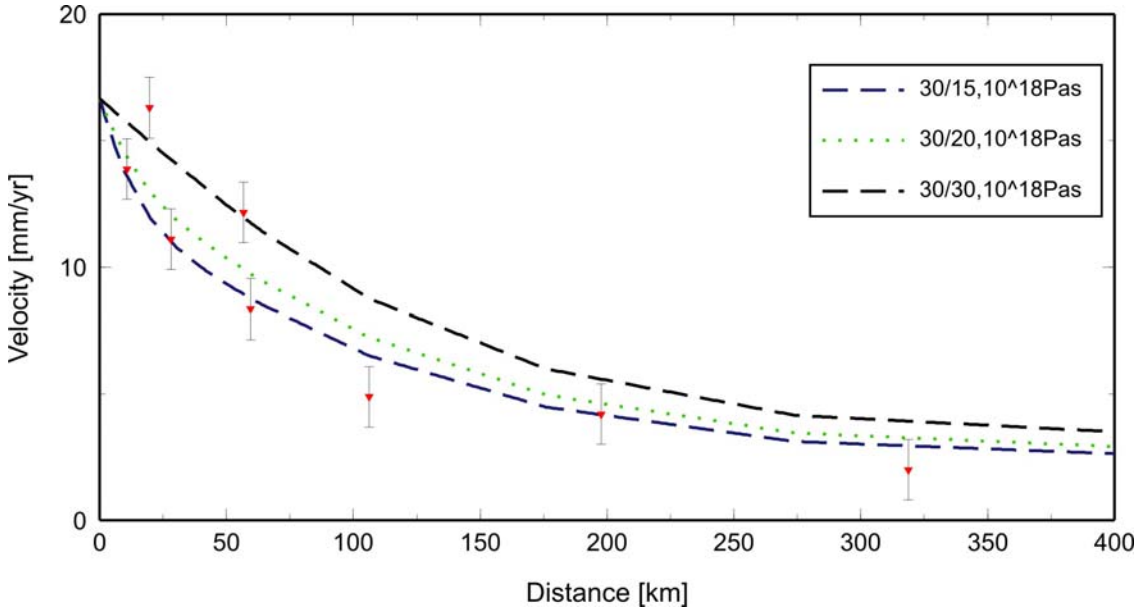

Figure 47: Comparison of observed horizontal margin-parallel deformation with the three best fitting models (viscosity 10^{18} Pa s, elastic layer thickness 30 km, fault depth 30 km (black); 20 km (green); 15 km (blue)).

The model with a fault depth of 15 km provides a better fit for the stations with lower velocities closer to the fault, whereas the model with the 30 km deep fault provides a better fit for the stations with higher observed velocities close to the fault (Figure 47). The goodness of the fit of the models is estimated using a reduced chi square misfit:

$$X_R^2 = \frac{1}{(N-P)} \sum_N \frac{(V_o - V_M)^2}{\sigma_o^2};$$

where N is the number of observation points; P is the number of parameters tested, and (N – P) is the number of degrees of freedom. V_o and V_M are observed and modeled velocities, respectively, and σ_o (Chapter 3) is the observed data uncertainty. A reduced chi square misfit of 1 implies that the model explains 100% of the variance of the data within their uncertainties. $X_R^2 >> 1$ indicates a poor fit and /or underestimation of the data uncertainty. The number of parameters varied in the models is three (viscosity, elastic layer thickness, fault depth). The reduced chi square misfits are much larger than 1 for every model, since the observed margin-parallel velocities within the first 100 km landward of the fault show a wide range (~ 10 mm/yr). The models with an elastic layer of 30 km, viscosity of 10^{18} Pa s and a fault depth of 15 or 20 km have the smallest reduced chi squares of ~ 34 and 36, respectively. The map view showing the model with a 15 km deep fault compared to the observed horizontal velocities (Figure 49, red arrows) underlines the fact that this is not a pure strike-slip system. A margin-normal component needs to be addressed (Table 9).

The best-fit model has an elastic layer thickness of 30 km, a fault depth of 15 km, and a low viscosity of 10^{18} Pa s. While the crustal thickness as well as the fault depth are within the parameter ranges determined in Chapter 2 for the Haida Gwaii region, the very low viscosity of 10^{18} Pa s needs to be explained. It is lower than expected based on the constraints discussed previously. However, the calculation of the effective viscosity is based on several first order assumptions. In general, effective viscosity can decrease due to compositional changes (e.g., higher carbonate or volatile/water content), metamorphism, and partial melting (Currie et al., 2007). One area of known high

metamorphism is the Coast Shear Zone (Chapter 2), more than 300 km away from the fault. However, the most recent known deformation was 30 Ma ago, and it could only provide an explanation for lower mantle viscosity more than 300 km away from the fault (e.g., TRRC could be affected). The area is also part of a former subduction zone, which can contribute to a low viscosity due to the wet rheology; however, that factor was considered in the calculation of the expected effective viscosity (Chapter 4.2.1). Further investigation is needed to determine whether any of those reasons can explain a very low mantle viscosity on the Queen Charlotte margin.

5.1.2.2 Margin – normal deformation

A margin - normal signal can also be identified (Table 9), agreeing with previous studies, which stated that a component of convergence between the Pacific and North America plates exists in the Haida Gwaii region (e.g., Riddihough and Hyndman, 1989; Bérubé et al., 1989; Mazzotti et al., 2003b; Ristau et al., 2007). I look at margin-normal deformation, with a viscosity of the upper mantle of 3.2×10^{19} Pa s, a slip rate of 13.3 mm/yr and different locking depths (Figure 48). The numerical model does not yield robust results for viscosities lower than 10^{19} Pa s, and, assuming the results are in fact correct, a viscosity of 10^{18} Pa s leads to very low velocities (max. velocity ~ 0 mm/yr ~ 20 km east of the fault) which does not fit the data. Hence a viscosity of 3.2×10^{19} Pa s is chosen, which differs from the viscosity of 10^{18} Pa s that provided the best-fit model for the margin-parallel component. The reduced chi square misfits are large for every model (≥ 60) (Table 11), and this large misfit is displayed in Figure 48, with each model significantly (up to 5 mm/yr) under-predicting the observed margin-normal velocities within 150 km of the fault. Assuming the fault trace for a underthrusting plate is ~ 35 km

west of the Queen Charlotte Fault (Figure 27) increases the reduced chi square misfits slightly but does not affect the overall result.

Table 11: Observed margin-normal velocities compared to modeled margin-normal velocities. Slip rate: 13.3 mm/yr, viscosity 3.2x10^{19} Pas, locking and transition zone depth noted.

Station	margin-normal velocity [mm/yr]	7km/8.5km [mm/yr]	residuals velocities [mm/yr]	reduced chi^2	10km/20km [mm/yr]	residuals velocities [mm/yr]	reduced chi^2
STJA	6.76	3.00	3.76	236.34	4.15	2.61	130.22
BARI	9.41	2.79	6.62		3.93	5.48	
MORE	5.41	2.82	2.60		3.68	1.73	
LANG	8.20	1.99	6.21		3.63	4.57	
BCSS	6.06	1.93	4.13		3.60	2.46	
YAKA	7.81	1.20	6.61		2.53	5.28	
BCPR	2.57	0.65	1.92		1.36	1.21	
TRRC	1.68	0.35	1.33		0.75	0.93	

Station	margin-normal velocity [mm/yr]	20km/25km [mm/yr]	residuals velocities [mm/yr]	reduced chi^2	20km/25km [mm/yr]; slab 60 km	residuals velocities [mm/yr]	reduced chi^2
STJA	6.76	4.88	1.88	80.43	6.30	0.47	66.52
BARI	9.41	4.93	4.48		6.47	2.94	
MORE	5.41	4.73	0.69		6.21	-0.79	
LANG	8.20	4.12	4.08		4.85	3.35	
BCSS	6.06	4.15	1.90		4.88	1.18	
YAKA	7.81	3.83	3.98		3.45	4.36	
BCPR	2.57	2.14	0.43		1.82	0.76	
TRRC	1.68	1.18	0.50		1.02	0.66	

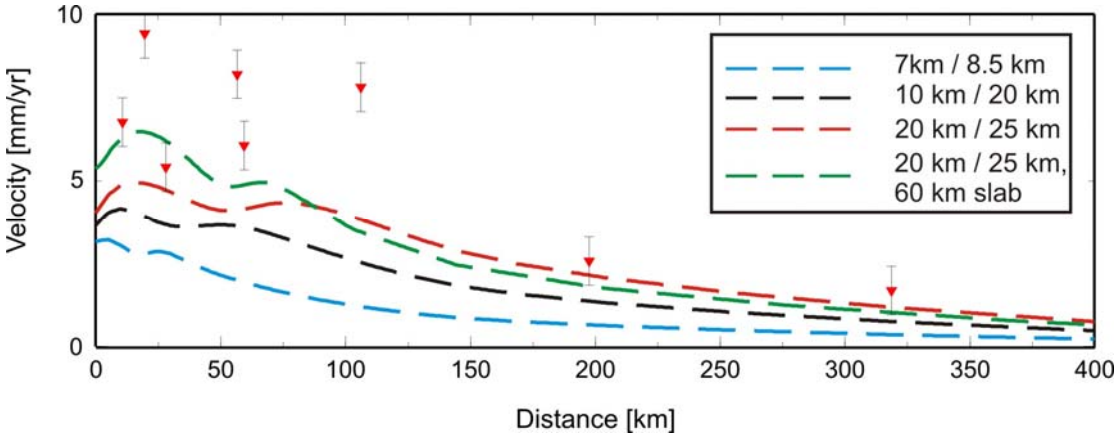

Figure 48: Observed margin-normal velocities, compared to three different modeled velocity profiles with different locking depths of the fault (first number, 7, 10, 20 km) and transition zones (8.5, 20, 25 km) at a slip rate of 13.3 mm/yr, dip angle of 20 degrees and slab length of 120 km. Fourth model has a slab length of 60 km, locked zone to 20 km and transition zone to 25 km depth (green dashed line). Viscosity for all models is 3.2 x 10^{19} Pa s.

Compared to the previous elastic modeling carried out by Mazzotti et al. [2003b], the viscoelastic model provides a slightly better fit (Table 11), especially for the far-field where the velocities can be matched within ~ 1 mm/yr (whereas the elastic model under-predicts the velocity more than 300 km from the fault by more than 5 mm/yr). None of tested models can give a satisfactory explanation for the observed margin-normal velocities, and so transient deformation can not fully account for the observed velocities.

Figure 49 and Figure 50 show the best-fit modeled margin-parallel and margin-normal velocity vectors, respectively. Of importance is the fact that the best-fit models require different upper mantle viscosities (a very low 10^{18} Pa s for the margin-parallel model, and 3.2×10^{19} Pa s for the margin-normal model). The viscosity is the parameter with the biggest influence in both model types, and the same viscosity for both models cannot fit the margin-parallel as well as the margin-normal component.

Figure 49 and Figure 50 also emphasize that, while the margin-parallel best-fit model provides a good fit for the observed deformation, the margin-normal component modeled generally underpredicts the observed deformation significantly.

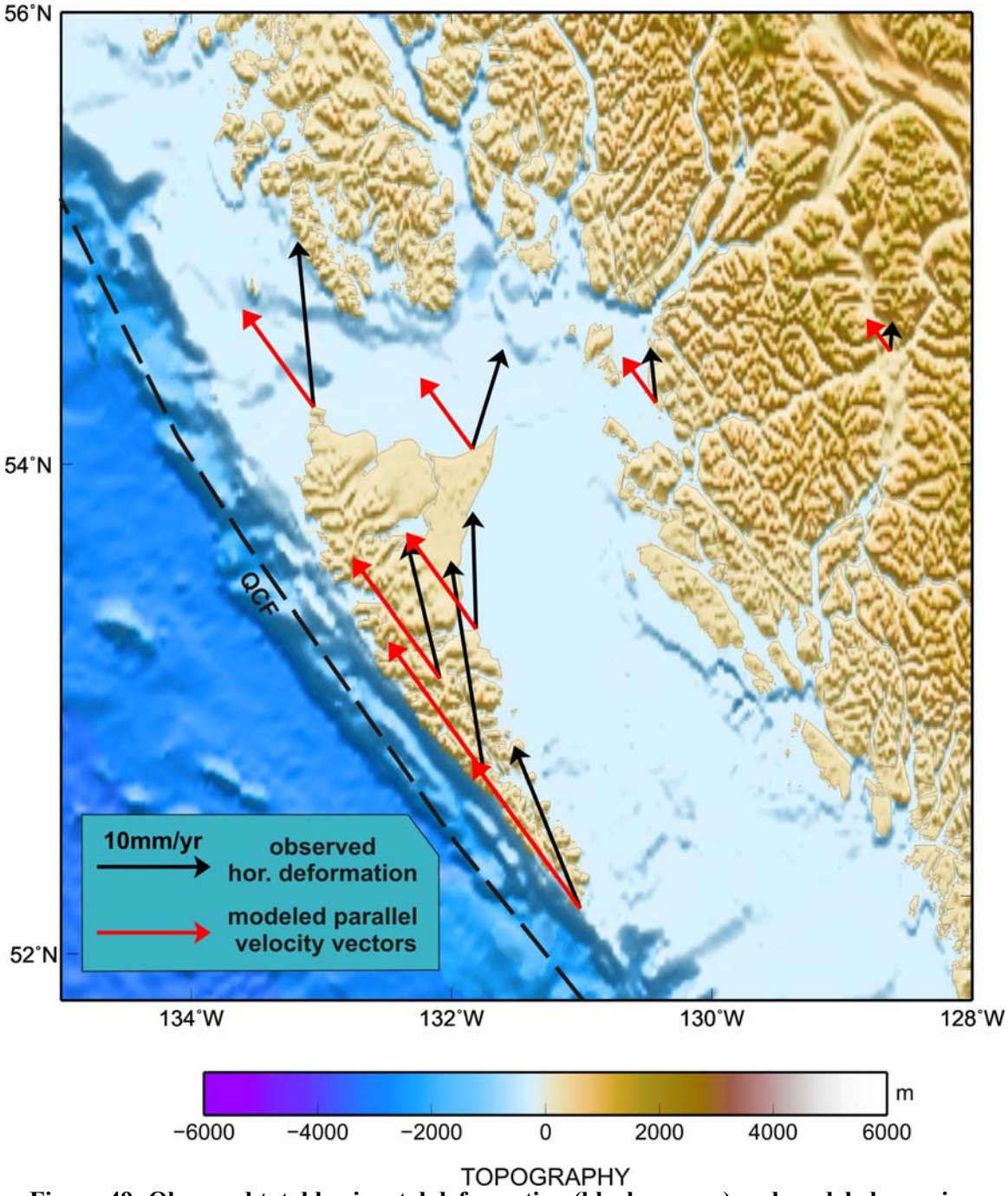

Figure 49: Observed total horizontal deformation (black arrows) and modeled margin - parallel (red arrows) velocity vectors. QCF: Queen Charlotte Fault.

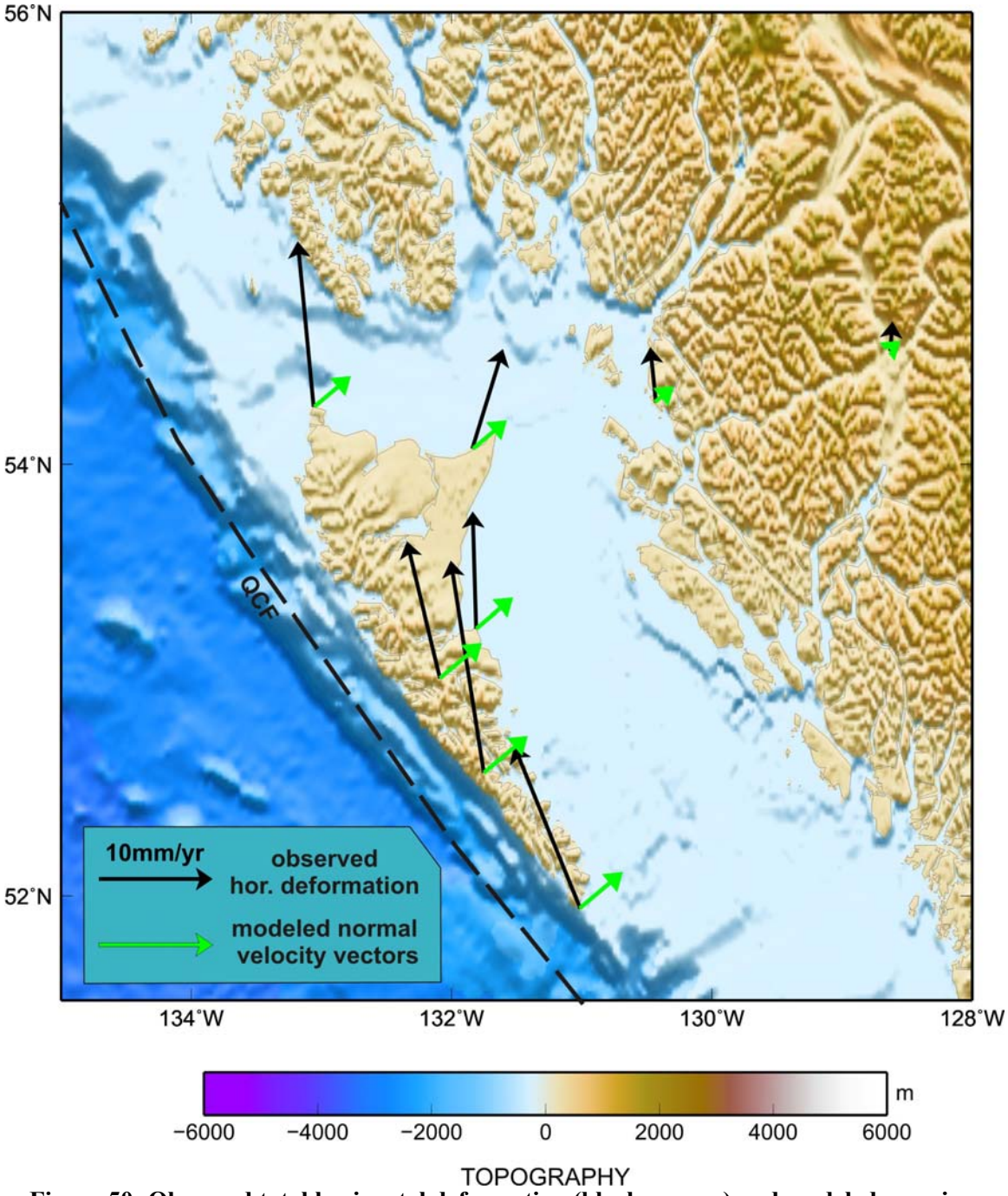

Figure 50: Observed total horizontal deformation (black arrows) and modeled margin - normal (green arrows) velocity vectors. QCF: Queen Charlotte Fault.

5.1.3 Transition area between Queen Charlotte Fault and Cascadia subduction zone

The GPS velocities observed in the region between the Queen Charlotte fault and the Cascadia subduction zone reflect the complicated tectonic system in the area (Figure 51). Influenced by the triple junction and the transition from the Cascadia subduction zone to the Queen Charlotte fault, the observed horizontal deformation rates generally trend north-northwest (Figure 51). The observed horizontal velocities in this region are lower than further north, between 1.8 – 5.2 mm/yr (Figure 51, compared to Figure 45).

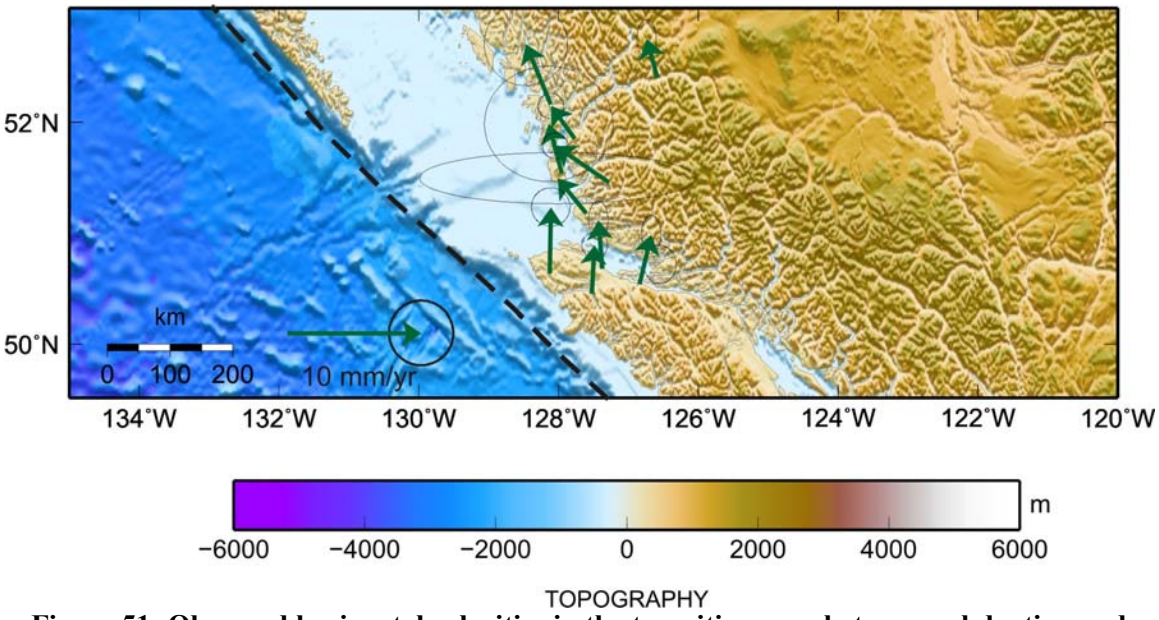

Figure 51: Observed horizontal velocities in the transition area between subduction and strike-slip zone. Black dashed line: position of fault.

Since there are many unknowns in that particular part of the region, developing and constraining a model proved to be difficult. Considering the parameters that can not be constrained (e.g., locking depth of the fault, possible re-occurrence rate of earthquakes that rupture the fault and associated slip), two extreme end-member models were applied:

(1) I assume that the Queen Charlotte fault extends southwards to the Brooks Peninsula, and I apply the strike-slip model to the margin-parallel deformation.

(2) I assume that the Cascadia subduction zone extends north to the southern tip of Haida Gwaii, and I apply the convergence model to the margin-normal deformation.

This approach provides a first order estimate of how much of the observed deformation could be due transient strike-slip and convergence movement.

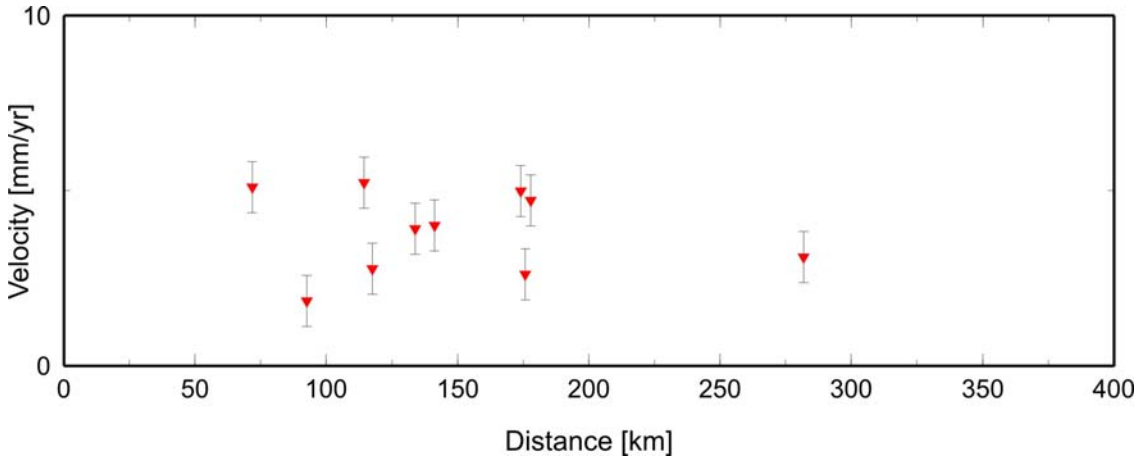

Figure 52: Observed horizontal deformation in the transition area.

Table 12:Observed total horizontal velocity, margin-parallel and margin-normal velocities.

Station	Distance fault [km]	observed horizontal velocity [mm/yr]	margin-parallel velocity [mm/yr]	margin-normal velocity [mm/yr]
ROBI	141.10	4.00	4.00	0.00
CALV	117.48	2.77	2.37	1.43
SEYM	177.87	4.71	4.67	0.57
KING	175.78	2.60	2.51	0.67
BCDI	173.91	4.98	4.55	2.03
BELL	281.71	3.10	2.54	1.78
HOLB	71.67	5.10	3.67	3.54
ALIC	92.51	1.84	1.19	1.39
PTHY	114.30	5.22	3.94	3.42
BCOV	133.77	3.91	2.07	3.32

The margin-parallel component is the main contributing factor to the total horizontal deformation (Table 12). The four stations on Vancouver Island (ALIC, BCOV, HOLB,

and PTHY) show the largest margin-normal component, since they are located closest to the northern edge of the subduction zone; in contrast, the stations further north on the mainland show a strong margin-parallel influence. Stations ROBI and SEYM move fully parallel to the margin, with no margin-normal component in the signal.

5.1.3.1 Strike-slip model applied to the triple junction area

As one extreme end-member model, I calculate velocity profiles for a Queen Charlotte fault that extends all the way south to the Brooks Peninsula. The thickness of the elastic layer can be constrained to ~ 38 km (Chapter 2.4.3), whereas locking and transition zone depth as well as slip rate cannot be constrained based on data. The proposed locking depth of the fault is 15 km, similar to the Queen Charlotte fault, below which is a 10 km deep transition zone. The slip rate is assumed to be slower than on the Queen Charlotte fault. Hence I start with a model with a viscosity of 10^{19}Pa s (effective viscosity calculations in Chapter 3 indicate a higher viscosity of 3.2×10^{19} Pas; however, the modeling for the Haida Gwaii region has already shown that a lower viscosity is needed to be able to match the observed velocities in the far-field), and a slip rate of 10 mm/yr.

Table 13: Observed margin-parallel velocities compared to modeled margin-parallel velocities.

Station	margin-parallel velocity [mm/yr]	38/15; 10^{19} Pa s	residual velocities [mm/yr]	reduced chi^2	38/15; 10^{18} Pa s	residual velocities [mm/yr]	reduced chi^2	38/15; 10^{18}Pa s; 15 mm/yr	residual velocities [mm/yr]	reduced chi^2
ROBI	4.00	0.25	3.75	179.29	1.05	2.95	78.30	1.84	2.16	47.62
CALV	2.37	0.25	2.12		1.58	0.79		2.37	0.00	
SEYM	4.67	-0.26	4.93		1.05	3.62		1.71	2.96	
KING	2.51	-0.25	2.76		1.05	1.46		1.71	0.80	
BCDI	4.55	-0.25	4.80		1.06	3.49		1.72	2.83	
BELL	2.54	-0.53	3.07		0.79	1.75		1.18	1.36	
HOLB	3.67	0.79	2.88		2.11	1.56		3.03	0.64	
ALIC	1.19	0.53	0.66		1.84	-0.65		2.63	-1.44	
PTHY	3.94	0.26	3.68		1.58	2.36		2.37	1.57	
BCOV	2.07	0.01	2.06		1.37	0.70		2.11	-0.04	

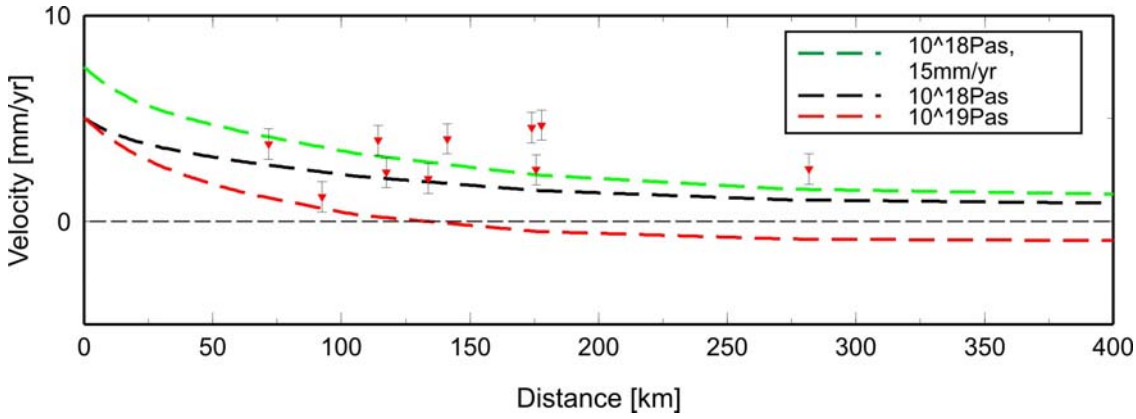

Figure 53: Observed margin parallel velocities, compared to three different modeled velocity profiles. Elastic layer thickness 38 km, locking depth of fault 15 km, slip rate 10 mm/yr (except green dashed line, slip rate 15 mm/yr), viscosity 10^{18} Pas for green and black dashed lines, 10^{19} Pas for red dashed line.

The strike-slip model does not provide a good fit for the observed margin-parallel velocities in the transition area, with the models either over-predicting the lower velocities by up to ~ 1.5 mm/yr, or under-predicting the higher velocities by up to ~ 1.5 mm/yr (Figure 53, Table 13). The lack of GPS stations closer than ~ 75 km to the margin poses a problem; there is no information about deformation close to the fault. While the observed horizontal velocities show a slight increase in velocity away from the fault, the modeled velocities all show a decline in velocity inland (Figure 53). I use three different models for comparison, all with the previously described crustal thickness and locking depth of the fault. A model with a viscosity of 10^{19} Pa s and an assumed slip rate of 10 mm/yr does not provide a fit for the observed margin-parallel deformation, and under-predicts the velocities by more than 5 mm/yr (Figure 53). In order to match the velocities observed in the far-field, a lower viscosity is needed, and a model with a viscosity of 10^{18} Pa s provides a slightly better fit, but with a reduced chi^2 of 78.30 (Table 13) it is still not able to provide a good fit for the observed data. To match the observed velocities less than ~ 180 km east of the fault, a higher slip rate is needed. A model with a viscosity 10^{18}

Pa s and a slip rate of 15 mm/yr does provide the best fit of all three tested models with a reduced chi^2 of 47.62 (Table 13), and provides a better fit for the velocities close to the fault than the models with a lower slip rate (Figure 53). However, the gradient, with a continuous decrease in velocity away from the fault, does not represent the general observed velocities, which show an increase of ~ 2mm/yr from 100 km to about 170 km east of the fault (Figure 53).

These viscoelastic models show that, assuming a low viscosity of 10^{18} Pa s and a slip rate of 15 mm/yr are justifiable, transient margin-parallel deformation in the transition area can account for ~ 75 – 80% of the observed margin-parallel deformation; however, residual velocities can reach almost 3 mm/yr, and long-term deformation is required.

5.1.3.2 Convergence model applied to the triple junction area

Similar to the application of the strike-slip model to the transition area, the dislocation model for the subduction zone is another extreme end-member model.

Table 14: Observed margin-normal velocities compared to modeled margin-normal velocities.

Station	margin-normal velocity [mm/yr]	7km/8.5km [mm/yr]	residual velocities [mm/yr]	reduced chi^2	10km/20km [mm/yr]	residual velocities [mm/yr]	reduced chi^2	20km/25km [mm/yr]	residual velocities [mm/yr]	reduced chi^2
ROBI	0.00	0.71	-0.71	40.94	1.64	-1.64	16.78	2.54	-2.54	29.81
CALV	1.43	0.84	0.59		2.01	-0.58		3.17	-1.74	
SEYM	0.57	0.61	-0.04		1.36	-0.79		2.05	-1.48	
KING	0.67	0.62	0.05		1.37	-0.70		2.07	-1.40	
BCDI	2.03	0.62	1.41		1.39	0.64		2.10	-0.07	
BELL	1.78	0.41	1.37		0.85	0.93		1.21	0.57	
HOLB	3.54	1.43	2.11		3.44	0.10		4.88	-1.34	
ALIC	1.39	1.06	0.33		2.60	-1.21		4.00	-2.61	
PTHY	3.42	0.86	2.56		2.06	1.36		3.24	0.18	
BCOV	3.32	0.75	2.57		1.75	1.57		2.72	0.60	

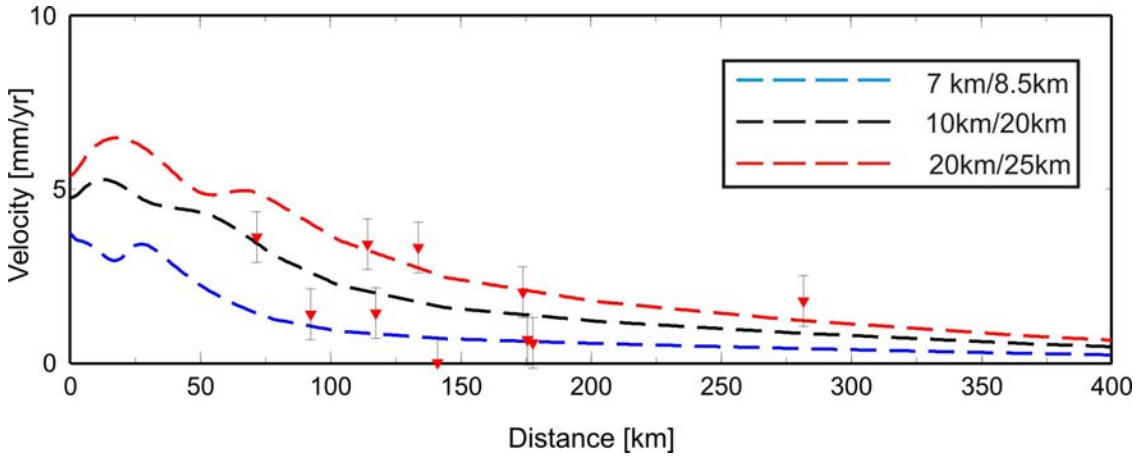

Figure 54: Observed margin-normal velocities, compared to three different modeled velocity profiles with different locking depths of the fault (first numbers, 7, 10, 20 km) and transition zones (8.5, 20, 25 km) at a slip rate of 13.3 mm/yr, dip angle of 20 degrees, length of subducting slab 60 km.

Just to the south of Brooks Peninsula, the Explorer Plate subducts beneath the North American plate at ~ 22 mm/yr, roughly half of the convergence rate of the Juan de Fuca Plate, underneath the North American Plate (Mazzotti et al; 2003a). Hence it is reasonable to assume that north of Brooks Peninsula the convergence rate would be less than that. I run the models with an assumed convergence rate of 13.3 mm/yr. No slab has been imaged subducting underneath North Vancouver Island in previous studies (e.g., Audet et al., 2008; Cassidy et al., 1998), so a maximum slab length is 60 km. The margin-normal component is less of a contributing factor to the total horizontal deformation than the margin-parallel component (Table 12). The highest observed margin-normal velocity is 3.67 mm/yr at HOLB, the site closest to the fault. The variation of the observed velocities is high, more than 2 mm/yr within 50 km; hence none of the three tested models is able to fit all observed data (Figure 54). The velocity profile with the deepest locked (20 km) and transition (25 km) zone provides the best fit for the higher observed margin-normal velocities as well as to the far-field velocity (only one station, BELL, provides a far-field velocity), whereas a shallow locked (7 km) and

transition zone (8.5 km) provides a better fit for lower velocities closer to the fault (Figure 54). Based on the reduced chi^2 values, the velocity profile representing a model with a 10 km deep locked zone and a 20 km deep transition zone provides the best fit ($chi^2 = 16.78$) (Table 14). The models show that a certain amount of the observed velocities can be attributed to transient deformation; however, the difficulty of constraining parameters like slip rate and depth of the locked zone make it impossible to quantify that amount. All tested models either over-predict some of the velocities close to the fault by up to 3 mm/yr (red dashed line in Figure 54), or under-predict velocities in the near-field as well as the far-field (black dashed line in Figure 54). This shows that transient deformation alone is unlikely to be the only deformation process involved, and suggests that long-term deformation does contribute to the observed signal.

Figure 55 and Figure 56 emphasise that neither the best-fit margin-parallel (red arrows, Figure 55) nor the best-fit margin-normal models (green arrows, Figure 56) are able to fit the observed horizontal deformation. Both severely under-predict the observed deformation, especially for the northern-most stations. It also has to be mentioned that, as was the case for the Haida Gwaii region, the best-fit models for the margin-parallel and the margin-normal component use different upper mantle viscosities (10^{18} Pas in the strike-slip model, 3.2×10^{19} Pa s for the convergence model).

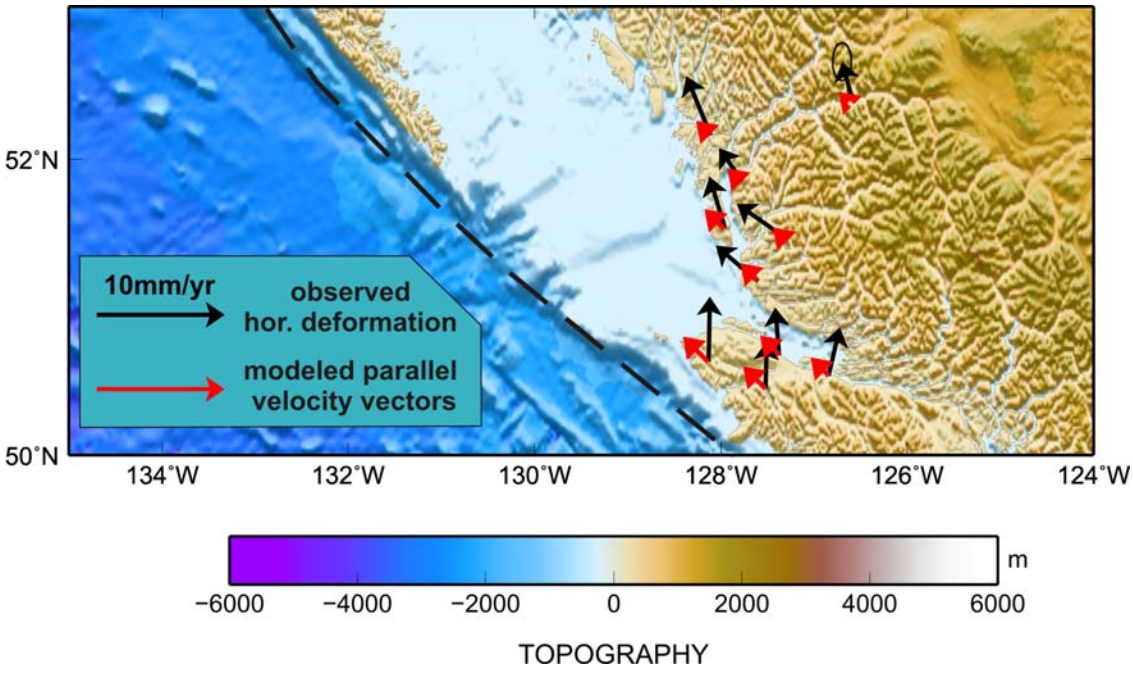

Figure 55: Observed total horizontal deformation (black arrows) and modeled margin - parallel (red arrows) velocity vectors.

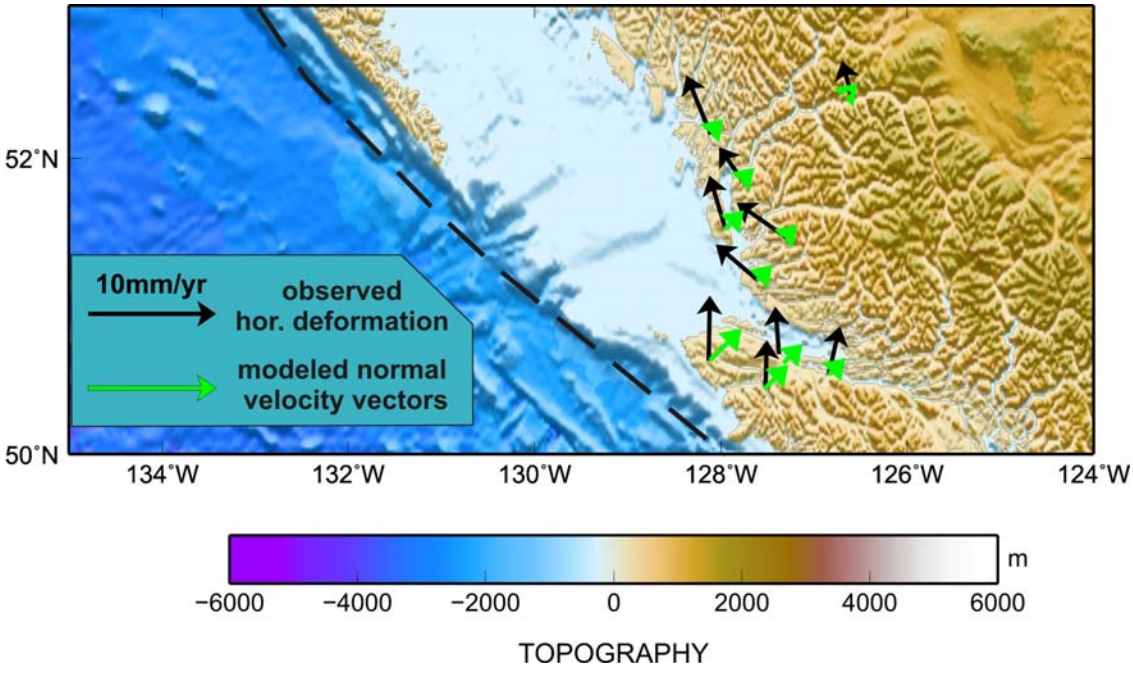

Figure 56: Observed total horizontal deformation (black arrows) and modeled margin-normal (green arrows) velocity vectors.

5.2 Discussion and future work

The combination of observed deformation and viscoelastic modeling provides an improved picture of the crustal deformation and velocity distribution along the margin off the west coast of British Columbia from the northern Cascadia subduction zone to the southern Queen Charlotte fault. In this study, the observations and models are used to try to qualify observed deformation as either earthquake-cycle related or as long-term deformation. Based on the observed horizontal deformation, three different tectonic settings were identified: the Queen Charlotte fault, the transition area between the Queen Charlotte fault and the Cascadia subduction zone, and the northern Cascadia subduction zone. The new campaign data confirm the northern extent of the principal Cascadia subduction zone system as the Brooks Peninsula, where the GPS velocity vectors change from a north-eastern to a more north-north-eastern direction.

5.2.1 Haida Gwaii region

The Queen Charlotte margin is influenced by the interseismic deformation associated with the currently Queen Charlotte fault. However, the 2.5-dimensional viscoelastic models show that not all the observed horizontal margin-parallel deformation can be explained by backslip motion. While a model could be developed to explain ~ 90% of the observed horizontal margin-parallel velocities, the parameters used need further explanation. The three main parameters adjusted are (1) the viscosity of the viscoelastic part of the mantle, (2) the thickness of the elastic layer, and (3) the locking depth of the fault.

(1) A low viscosity of 10^{18} Pa s is needed to be able to mirror observed velocities in the far-field, which disagrees with the effective viscosity of > $3.2*10^{19}$ Pa s calculated for the Queen Charlotte margin on the basis of lab rheology and local geotherms. One

explanation for a lower than expected viscosity could be the Coast Shear Zone, which, while thought to be inactive for the last 30 Ma, is an area with high metamorphism in some areas (Chapter 2.3.4), which can lead to lower viscosities (Currie et al., 2007); however, it is questionable whether a higher metamorphic grade can be responsible for viscosity values more than a magnitude lower than expected in the upper mantle. Additionally, this would only affect the area more than 300 km landward of the fault The fact that the Queen Charlotte region is part of a former subduction zone, which leads to a wet rheology and therefore lower viscosity values is already accounted for in the calculation of the effective viscosity. Other parameters that can decrease effective viscosity are compositional changes (e.g., higher carbonate or volatile/water content), metamorphism, and partial melting (Currie et al., 2007). Further research is needed to determine whether any of these factors can provide an explanation for possible low viscosity values at the Queen Charlotte margin.

(2) The crustal thickness across the Queen Charlotte Basin as well as the Hecate Strait varies quite significantly, and whichever value is chosen for the model can only be an approximation. Hence, crustal thickness between 20 and 30 km is within the constraints established and a justifiable approximation.

(3) A locking depth for the fault of 15 km, as proposed by the best-fit model, does agree with previous studies in that area, which put the maximum seismicity depth for the Queen Charlotte fault at 20 km (Hyndman and Ellis, 1981).

Attributing most of the observed margin-parallel velocities to earthquake-cycle deformation still leaves residual velocities of up to 5 mm/yr, which are considered to be long-term deformation, indicating a N to NNE motion of the central part of the islands.

The residual velocities show a decreasing trend landward, which agrees with Mazzotti et al. [2003b], who propose that the dextral shear is likely accommodated along the NNW-SSE normal faults that formed the Queen Charlotte Basin (Rohr and Dietrich, 1992).

A small part (<15%) of the observed deformation is margin-normal. A component of convergence between the Pacific and North America plates has previously been identified in the Haida Gwaii region (e.g., Riddihough and Hyndman, 1989; Bérubé et al., 1989; Mazzotti et al., 2003b; Ristau et al., 2007). The observed signal is small compared to the strike-slip signal, but it clearly indicates a compression-related component to the deformation. A best fit model has been determined, the most important parameters of which are the upper mantle viscosity of 3.2×10^{19} Pas, and a seismogenic depth of 20 km, below which is a transition zone to 25 km. However, it does not provide a good fit for the data, and only explains a small part of the observed margin-normal velocities. The residual velocities imply a significant component of margin-normal shortening between 0.5 and 5.5 mm/yr.

5.2.2 Northern Vancouver Island region

The new GPS campaign data provide information on the transition between the subduction of the Juan de Fuca slab to the south and the Pacific – North America transform motion to the north. Previous studies (e.g., Riddighough, 1984; Riddighough and Hyndman, 1989; Ristau et al., 2002; Braunmiller and Nabelek, 2002; Bahr and Chase, 1974; Rohr and Furlong, 1995; Rohr and Tyron, 2010) introduced two different end-member models to describe the current tectonic situation in the transition area. The first one regards the Explorer region as an independent microplate under-thrusting underneath North Vancouver Island at a slower rate than the Juan de Fuca/ North

America motion off South Vancouver Island (e.g., Riddihough, 1984). We expect to see transient and/or permanent deformation across Northern Vancouver Island. In the second proposed end-member model, the Explorer region no longer corresponds to an independent plate anymore, and all plate boundary deformation is accommodated offshore along the former Explorer spreading system (Bahr and Chase, 1974; Rohr and Furlong, 1995). The new GPS data clarifies that transient as well as permanent deformation can be observed across North Vancouver Island and the adjacent mainland, which clearly supports a independent Explorer microplate under-thrusting North Vancouver Island as far south as Brooks Peninsula. The possibility of all the deformation being accommodated along the former Explorer system can be excluded. As for the Haida Gwaii region, a best-fit model for the margin-parallel as well as the margin-normal component has been determined. The strike-slip model has a elastic layer thickness of 38 km, a locking depth of the fault of 15 km, both well within the constraints discussed in Chapter 2. A slip rate of 15 mm/yr is assumed, and a low upper mantle viscosity of 10^{18} Pa s. The convergence zone model has a higher upper mantle viscosity of 3.2×10^{19} Pa s, a seismogenic zone to a depth of 10 km, followed by a transition zone to 20 km. It is still not possible to distinguish how much of the deformation is transient and how much is permanent, since the models are too poorly constrained. Hence no definite statement can be made as to whether an independent Winona Block obliquely under-thrusts the North American Plate, or whether permanent deformation within Northern Vancouver Island due to the transition from the Cascadia subduction zone to a transform system can fully explain the observed velocity vectors. Based on the modeling, transient deformation is a possibility (even though it cannot explain all the observed velocities); hence it is possible

that that the Winona Block slowly (< 3.5 mm/yr) underthrusts the North American Plate. The residual values indicate that permanent deformation contributes as well.

5.2.3 Conclusion and future work

Compared to the elastic deformation models utilized previously (Mazzotti et al., 2003 a, b), the viscoelastic models generally do provide an improved fit. However, the viscoelastic model is more complex, using more parameters and hence more uncertainties than an elastic model. Nevertheless, the uncertainties introduced by ignoring the viscous part of the upper mantle in the model outweigh the uncertainties possibly introduced by approximations and assumptions when using a complex viscoelastic model.

The margin off the west coast of British Columbia is a complex tectonic area, and while this study provides a better insight into the processes involved and can resolve most of the observed deformation signals, there is still future work needed in order to clarify the ongoing tectonic processes. More GPS data, especially on the mainland close to the coast would provide much needed information about crustal deformation closer to the margin, especially between 52°N and 54°N.

For both the Haida Gwaii as well as the Northern Vancouver Island region, the viscosities between the best-fit strike-slip and convergence model differ between the very low 10^{18} Pa s and 3.2×10^{19} Pa s, respectively. Hence there is no "combined best fit model" that uses the same parameterisations and is able to explain both the margin-parallel as well as the margin-normal velocity component. A model with the same parameterisation as the best-fit model for the margin-parallel component does not provide a fit for the margin-normal component, and vice versa. Hence the next important step must be to determine more accurately the viscosity of the upper mantle along the Queen

Charlotte margin as well as on Northern Vancouver Island and the adjacent mainland. $3.2x10^{19}$ Pas has been calculated as the minimum approximate value for the effective viscosity in the upper viscous mantle, and has also been used in previous studies for similar tectonic settings (e.g., James et al., 2009); hence it can be regarded as a justifiable value. 10^{18} Pas, however, which is the viscosity used in the best-fit model for the margin-parallel component, is very low, and as shown above, hard to justify. One explanation for the difference in upper mantle viscosities for the margin-parallel and margin-normal component could be anisotropic mantle viscosity. The elastic plate shows anisotropic behaviour with respect to flexural rigidity (Audet et al., 2007), which could possibly lead to the margin-normal shortening extending further into the continent than the margin-normal strain. However, no mantle seismic anisotropy observations north of Brooks Peninsula are available to this date, hence neither theory can be investigated at this point. Differences in viscosity values for the upper mantle in the same region are quite common (e.g., values for the upper mantle in western California range from 10^{18} Pa s (e.g., Deng et al., 1998; Kaufman and Royden, 1994; Bokelmann and Beroza, 2000) to 10^{19} Pa s and more (e.g., Freed and Buergmann, 2000; Pollitz et al., 2001)), and are usually attributed to different assumptions in the calculations (Johnson et al, 2007). However, in no other transpressional system (e.g., San Andreas Fault, Alpine Fault) has a difference in viscosities between margin-parallel and margin-normal component been noted or investigated. Another helpful tool would be the usage of a model with a 3 D geometry, and, in the future, the development of a fully 3D-model. This would be particularly helpful for tectonic setting involving triple junctions and their complex geometries, and

more general all areas where margin-parallel as well as margin-normal crustal deformation is observed.

Part II
Chapter 6
Thermal and structural models of the Sumatra subduction zone: Implications for the megathrust seismogenic zone

6.1 Introduction

This chapter deals with the controls to the area of great earthquake rupture on the subduction thrust of the Sumatra margin. The primary contribution is a detailed 2D numerical thermal model that allows temperatures on the subduction thrust to be estimated, and therefore evaluates potential thermal control of the downdip rupture limit. The work was published in the Journal of Geophysical Research in 2008 (Hippchen, S. and R.D. Hyndman, 2008. Thermal and Structural Models of the Sumatra Subduction Zone: Implications for the Megathrust Seismogenic Zone, J. Geophys. Res., doi:10.1029/2008JB005698). This chapter presents that published work with some additions based on data and information that has become available since the time of that publication.

The margin of Sumatra is the location of numerous megathrust earthquakes, including the two largest great subduction zone earthquakes in recent years, M 9.3 in 2004 and M 8.7 in 2005 (Figure 57). These events provide well-studied examples for very infrequent great earthquakes globally, that assist in understanding their occurrence elsewhere, including Cascadia. Previous global historical M ~9 events were in 1952 in Kamchatka, Russia (9.0), in 1960 in Chile (9.5), and in 1964 in Alaska (9.2), before most modern seismic and geodetic recording systems were installed. Therefore, the Sumatra earthquakes provide unique data for this type of event. In addition, in early 2010 a M=8.8 earthquake occurred on the Chile margin and a M9.0 off NE Japan for which data is just beginning to become available. Important parameters for understanding the rupture

processes in such earthquakes and for both the ground shaking and the tsunami generation are the updip and downdip seismogenic limits, defined by the limits to the seaward and landward extents of rupture. This article deals with two possible limits (e.g., Hyndman et al., 1997): (1) updip and downdip temperature on the thrust fault, based on the assumption that the seismic-aseismic transition is primarily controlled by temperature, (2) downdip limit controlled by the composition change at the thrust intersection with the forearc mantle based on the hypothesis that the partly serpentinized mantle and associated talc in this region is aseismic.

Proposed thermal and structural updip and downdip limits to the seismogenic zone are mainly compared to the rupture limits provided by the recent great earthquakes. As discussed below, the updip and downdip limits of rupture for the recent Sumatra earthquakes are quite constant along strike, and agree with the more limited data for earlier great earthquakes in the region. Also, generally consistent updip and downdip limits along strike and maximum depths of smaller thrust events are characteristic of great events elsewhere (e.g., Tichelaar and Ruff, 1993; Hyndman et al., 1997; Oleskevich et al., 1997), and coseismic rupture limits commonly correspond well to estimates for the interseismic locked zone from geodetic data (e.g., Leonard et al., 2004; Hyndman et al., 1995). Although a longer series of great earthquakes and smaller subduction thrust events would be needed to conclusively establish the updip and downdip seismogenic limits, we conclude that the long-term Sumatra subduction zone seismogenic zone limits are reasonably defined by the rupture extents of the recent events.

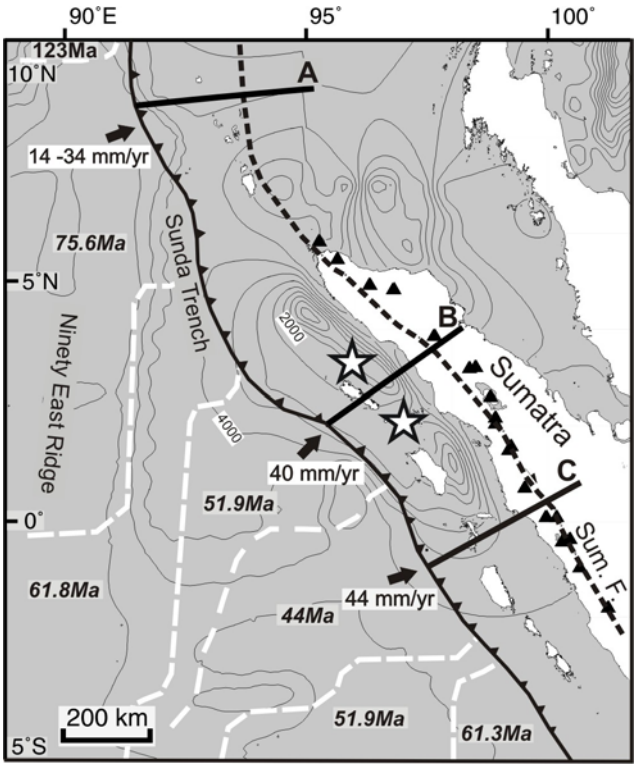

Figure 57: Map of the study area, showing the 3 profiles. Epicentres of the 2 megathrust earthquakes (2004, 2005) indicated by stars; bold line is Sunda Trench, dotted line the Sumatra fault, triangles the volcanic arc. Grey contour lines show sediment thickness.

Prior to the recent great earthquakes, Simoes et al., (2004) concluded that the locked fault zone and the expected downdip limit of great earthquakes of the Sumatra subduction zone extended well into the forearc mantle. With the vast amount of new earthquake and structural data now available it is now possible to thoroughly re-examine the downdip limit for great earthquake rupture.

To test the two suggested seismogenic limits I first generate thermal cross-sections and the temperatures on the subduction thrust using detailed 2-D finite element models. I then examine the position of the thrust intersection with the forearc Moho. The thermal models allow comparison of the rupture extent estimated from seismological and geodetic data to the common temperature limits of 100-150°C for the updip seismogenic limit and 350-450°C for the downdip limit inferred from laboratory data for quartzo-

feldspathic rocks and found for a number of young subduction zones (e.g., Hyndman et al., 1997; Oleskevich et al., 1997, Moore and Saffer, 2001, Currie et al., 2002). The updip limit appears to be thermally controlled but the chemical and physical changes downdip that affect frictional properties of the material appear to be complex (e.g., Underwood, 2007; Moore et al., 2007). For the downdip limit, the critical change in the composition along the interface has been concluded to be the thrust intersection with the forearc mantle that is aseismic due to serpentinization and associated thrust zone talc (e.g., Peacock and Hyndman, 1999).

Another important application of the temperature regimes obtained from the thermal models is the dehydration and upward fluid expulsion from the downgoing slab with increasing temperature and pressure (e.g., Hacker et al., 2003; Peacock, 1990). We do not deal with this consequence of the thermal regime in this study.

The Sumatra margin is the 1600 km long NW-SE striking convergent boundary that absorbs the north-eastward motion of the Indian and Australian plates relative to the Sunda Shelf (Figure 57) (e.g., Chlieh et al., 2004). The direction of relative plate motion changes from nearly orthogonal to the margin in the south to nearly strike-slip in the north. Much of the current margin-parallel motion is accommodated by the transcurrent dextral Sumatra Fault near the volcanic arc, so the subduction direction relative to the forearc is nearly orthogonal along the whole margin. It is this normal component that is relevant to thermal models. We conclude that the margin is sufficiently two-dimensional for the margin-parallel motion not to affect the thermal regime. The margin-normal convergence rate decreases considerably to the north along the margin, from 63-68

mm/yr in the south close to Java (Subarya et al., 2005; Bock et al., 2003), to 14-34mm/yr north of 8°N (Paul et al., 2001; Bilham et al., 2005).

6.2 Constraints on the Megathrust Rupture Width

6.2.1 Controls of the Updip Limit of the Seismogenic Zone

Temperature is one of the proposed important controls on both the updip and the downdip limits to the seismogenic zone (e.g., Hyndman and Wang, 1993), along with composition and state on the thrust fault. Field data indicate that temperature is a primary control of the depth range of continental earthquakes (e.g., Marone and Scholz, 1988). The updip aseismic zone has been attributed to the presence of stable sliding in unconsolidated and semi-consolidated sediments that change in slip properties downdip (Byrne et al., 1988, Vrolijk, 1990). It was proposed earlier that the dehydration of smectite clays to illite and chlorite between 100 and 150°C controlled the updip limit of the seismogenic zone (e.g., Wang, 1980; Vrolijk, 1990; Hyndman and Wang, 1993) (Figure 58). The results of more recent studies have supported the general temperature control of the updip limit. However, recent laboratory studies indicate that factors affecting sediment slip properties are more complex than simple clay dehydration. They include pore fluid pressure and a number of physical and chemical changes in sediments (e.g., Marone et al. 2001; Saffer et al., 2001; Moore and Saffer, 2001; Underwood, 2007; Moore et al., 2007). The origin of the apparent thermal control on the frictional behaviour of sediments along the updip part of subduction faults is still a field of active research.

6.2.2 Controls of the Downdip Limit of the Seismogenic Zone

The downdip limit of seismic rupture for many subduction zones may be explained by one of two processes, whichever is shallowest (e.g., Hyndman et al., 1997): (a) a critical maximum temperature; (b) the intersection of the thrust with the aseismic serpentinized

forearc mantle. The downdip limit of the seismogenic zone in many young hot subduction zones is concluded to be at about 350° (Figure 58), with a transition zone between velocity weakening (seismic) and velocity strengthening (aseismic) between 350°C and about 450°C indicated by laboratory data (Hyndman and Wang, 1993).

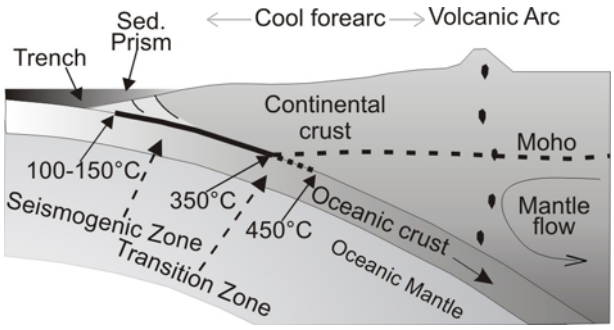

Figure 58: Schematic sketch of subduction zone, showing the location of the seismogenic zone, interpreted to be controlled either by a temperature limit or by the intersection of the slab with the forearc Moho.

The transition from brittle to true ductile behaviour appears to occur at about 450°C, although limited rupture displacement may decrease smoothly to greater depths (e.g., Wang et al., 2003, Wang, 2007). However, it has been argued that the downdip rupture limit in a few places is at greater depths, e.g., NE Japan (e.g., Seno, 2005) where it is still not known what constrains the downdip limit and an earlier study of a part of Sumatra (Simoes et al., 2004) for which we provide a new assessment with additional data and analysis.

The maximum depth of crustal earthquakes generally corresponds to a temperature of about 350°C (e.g., Scholz, 1990), and laboratory measurements on quartzofeldspathic rocks show that the critical maximum temperature for velocity weakening also is about 350°C for either wet or dry conditions (Tse and Rice, 1986; Blanpied et al., 1991, 1995; Moore and Lockner, 2007).

In the transition zone, rupture initiated at shallower depth (in the seismogenic zone) is concluded to continue downdip with decreasing slip offset. For very hot subduction zones such as Cascadia (Hyndman and Wang, 1995), the 350°C temperature limit occurs on the thrust as shallow as 15 km, whereas for cold subduction zones 350°C is reached as deep as 100 km (e.g., NE Japan, Peacock and Wang, 1999). In the models for Sumatra described below, the 350°C temperature is reached at depths between 30 and 45 km.

6.2.3 Serpentinized forearc mantle corner limit

In many subduction zones, the critical ~350^{o}C temperature is reached at great depths and a second shallower limit is inferred at depths of 30-50 km. The downdip rupture limit often coincides with the forearc mantle corner if the critical temperature is deeper (e.g., Ruff and Tichelaar, 1996; Hyndman et al., 1997; ANCORP Working Group, 2003). A favoured explanation for this downdip limit at the intersection with the forearc Moho is the occurrence of stable sliding mantle serpentinite in the forearc mantle and perhaps associated talc and brucite on the underlying thrust (Hyndman et al., 1997; Peacock and Hyndman, 1999). Large amounts of water carried down with the oceanic crust and subducted sediments (e.g., Peacock, 1990) are expelled upward with downdip increasing temperature and pressure. This water leads to serpentinization of the overlying forearc mantle. Serpentinite is expected to be aseismic because of its layered structure (e.g., Moore et al., 1997, Reinen et al., 1991) and recent laboratory data indicate that antigorite serpentinite (the high P-T form) is weak with very low effective viscosity at high temperatures and pressures (Hilairet et al., 1997). In addition to the probable aseismic behaviour of serpentinite, a layer structure of talc and brucite is expected just above the

thrust boundary underlying the forearc mantle, that may contribute to making the fault weak and aseismic (e.g., Peacock and Hyndman, 1999).

If stable sliding mantle serpentinite or talc provides the downdip seismogenic limit, the seismogenic zone should not reach deeper than the intersection of the forearc Moho with the thrust fault. There are several possible explanations for deeper extent. It is possible that the forearc Moho dips downward closer to the trench, thus placing the intersection between forearc Moho and thrust fault at a greater depth than defined by regional data further landward. The second possibility is that there is no stable sliding serpentinite or talc in contact with the thrust beneath the mantle intersection. The current thrust may be within subducted sediments or within subducted crustal rocks.

As discussed below, the regional forearc Moho depth is estimated to be at about 30 km or less in the Sumatra segment of this subduction zone although it is not known precisely (Simoes et al., 2004; Chlieh et al., 2008; Kieckhefer et al., 1980; Kopp et al., 2001). Some smaller thrust earthquakes nucleate at about this depth of ~30 km (Engdahl et al., 2007).

6.3 Thermal Modeling of the Sumatra Subduction Zone

6.3.1 Numerical Approach

Two-dimensional numerical thermal models on three profiles perpendicular to the Sunda Trench between 10°N and 5°S have been developed in order to examine thermal controls on the updip and downdip extent of the megathrust seismogenic zone (Figure 57). For each profile a steady-state model has been developed using the finite element approach described by Wang et al. (1995b) and a modelling routine provided by K. Wang and J. He at the Pacific Geoscience Centre. I use isoviscous mantle rheology and subduction-induced mantle wedge corner flow (e.g., Peacock and Wang, 1999). More

appropriate temperature-dependent viscosity can be incorporated, but the thermal effects of the mantle wedge flow on the shallow, potentially seismogenic part of the subduction thrust faults are very small, because the corner flow is far enough landward of the shallow seismogenic zone to have little effect (Figure 59) (e.g., Currie et al., 2002). The critical parameters for the thermal models are: (1) the age of the subducting oceanic plate at the trench, (2) the thickness and deposition history of incoming sediments, as well as the amount of sediment subducted, (3) the significance of hydrothermal circulation within the upper incoming oceanic crust, (4) the convergence rate, (5) the dip profile of the subducting plate, (6) the thermal conductivity and radiogenic heat assigned to each of the main geological units in the models, (7) frictional heating along the thrust surface.

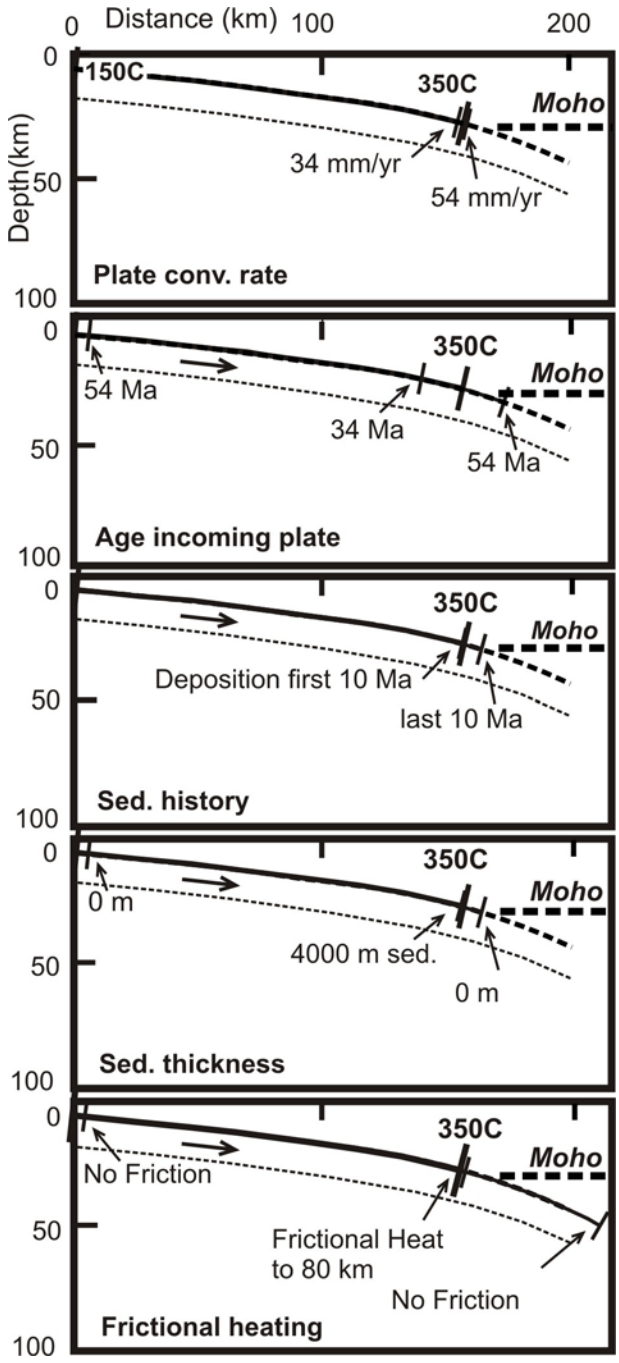

Figure 59: Inferred seismogenic Zone of Model C, showing the effect of changing model parameters. Thick 350°C line indicates the thermally constrained seismogenic zone with preferred parameters; the thinner lines show the effects for parameter indications indicated.

The upper boundary of all models is constrained at 0°C, which approximates the seafloor temperature; the base of the model is fixed at 1450°C, which is approximately the asthenosphere mantle temperature at 100 km or greater depth. Because this boundary

is located so far below the region of interest, and because the primary control on the thermal regime on the thrust is the seaward boundary condition, the choice of the basal boundary condition does not affect the thermal model results (e.g., Currie et al., 2002).

6.3.2 Oceanic Geotherm

The temperature-depth profile of the incoming oceanic plate at the trench provides the seaward boundary condition for the two-dimensional models. This one-dimensional geotherm is controlled mainly by: 1) conductive cooling of the plate as it ages away from being nearly isothermal at its spreading ridge origin, 2) deposition of lower thermal conductivity insulating sediments on top of the plate that slow the rate of cooling, 3) an increase in sediment thickness over time, resulting in a transient cooler sediment column, 4) compaction of deeper sediments with increasing sedimentation, resulting in the expulsion of pore water, causing advective upward heat transfer within the sediments, and 5) hydrothermal circulation cooling in the upper oceanic crust (e.g., Davis et al., 1996).

The oceanic geotherm is calculated by cooling the plate from isothermal at the ridge to its age at the trench (Wang and Davis, 1992), using the time-dependent sedimentation history and assuming the porosity-depth profile of the sediment column does not change with time and increasing thickness (Hutchison, 1985).

6.3.3 Model Parameters and Sensitivity Tests

Plate Age

For my models, I use a plate age of 75.6 Ma for Model A, 51.9 Ma for Model B, and 44 Ma for Model C (e.g., Chlieh et al., 2004 and references therein) (Table 15). Varying the incoming plate age by +/- 10 Ma moves the upper thermal limit ~5 km landward (older age) (Figure 59). The lower limit of the seismogenic zone is more effected, with a

shift of the lower limit of ~15 km landward (older age) and ~15 km seaward (younger age), with a depth range of +/-5 km. The plate age at the trench has not varied enough over the last several million years to require a transient model, as used in Hyndman and Wang [1995] for the Nankai Trough.

Sediment Thickness and Deposition History

The sediment thickness along the trench is greatly influenced by the deposition of sediments from the Himalaya Mountains into the Bengal Fan to the north of our study area. As a consequence, the sediment thickness at and near the trench generally decreases southward. Significant sediment in the south is derived from erosion from Sumatra. I tested the models with a range of sediment thickness of 0 - 4000 m. Those variations change the width of the seismogenic zone ~10 km for the upper limit and ~ 3 km for the lower limit (Figure 59). I use a sediment thickness of 1500 m for Model A, 2000 m for Model B, and 1000 m for Model C (Table 15). The deposition history is poorly known for the Sunda Trench. Models with three extreme deposition histories (all sediments deposited within the last 10 Ma, all sediments deposited in the first 10 Ma, constant deposition throughout time (steady-state)) had no significant effect on the thermal regime (Figure 59). I used the steady-state deposition history. I have assumed based on limited data that the incoming sediment is scraped off (Moore and Curray, 1980).

Table 15: Main Model Parameters

	Plate Age [Ma]	**Convergence rate [mm/yr]**	**Plate dip at trench[deg]**	**Sediment thickness [m]**	**Depth at trench [m]**
Model A	75.6	30	~6°	1500	5500
Model B	51.9	40	~5°	2000	5000
Model C	44.0	44	~6	1000	6000

Since the incoming plate age as well as the sediment thickness are both defined in the oceanic boundary condition, it is reasonable that changes of those two parameters affect the upper limit of the seismogenic zone more than the lower limit of the seismogenic zone.

Hydrothermal Circulation

The effects of hydrothermal circulation are neglected for this study, because (a) circulation is concluded to commonly become less important at greater ages and thicker sediment (e.g., Von Herzen, 2004), and (b) cooling is only important for the upper few hundred meters of the crust which is not significant for our models. The upward expulsion of porewater into the forearc has also been found not to be important to the deep thermal regime, although it may affect the surface heat flow (Harris and Chapman, 2004).

Plate Convergence

The plate convergence along the Sunda Trench is substantially oblique, and I model only the orthogonal component, assuming that the parallel component has no effect on the thermal regime. Much of the margin-parallel motion is taken up on the strike-slip Sumatra fault located near the volcanic arc (Figure 57), such that the oceanic plate converges approximately orthogonal with the forearc (Newcomb and McCann, 1987; Simons et al., 1999; Michel et al., 2001). The orthogonal convergence rate shows great variations along the Sunda Trench. It is highest in the southern part, (63 – 68 mm/yr at Java (Bock et al., 2003) and 45 mm/yr off the southern part of Sumatra) and decreases further north (40 mm/yr at the 2004 epicentre). North of 8°N, the convergence rate normal to the trench is 14 - 34 mm/yr (Paul et al., 2001; Bilham et al., 2005). The plate

model uncertainties and the sparse geodetic data limit the convergence rate accuracy. For all three models we use steady-state convergence rates (Table 15). After ceasing of spreading at Wharton Ridge about 42 Ma ago, I assume little convergence rate change with time for the critical past several 10's of millions of years.

Since the convergence rate is one of the most important variables in the thermal models, this change along the trench has a clear impact on the thermal model results. The margin-normal convergence rate is well determined for the two southern profiles, Models B and C. However, the uncertainties in northern Model A introduce a temperature uncertainty at 30 km depth of about 15°C, which results in a change of the width of the thermally inferred seismogenic zone of ~20 km per 10 mm/yr change in the convergence rate. For comparison, changing the convergence rate by +/-10 mm/yr for Model C has no noticeable effect on the seismogenic zone (Figure 59).

Dip Profile of the Subducting Plate

Changes in the dip profile have a major effect on the model seismogenic zones, because, (a) changes in the dip influence the thermal structure of the model, and (b) a different dip profile leads to a change in the intersection between forearc Moho and subducting slab surface. The dip profile of the thrust is assumed to be at the top of the oceanic crust as derived mainly from single channel and multichannel seismic reflection data seaward of the trench (Moore and Curray, 1980), Wadati-Benioff earthquakes within the plate landward of the trench, great earthquake pre-mainshocks, mainshock earthquakes, aftershocks, and local thrust earthquakes that are interpreted to be on the megathrust fault (data from Engdahl et al., 1998). The top of the plate is taken to be about 10 km above the centre of the Wadati-Benioff seismicity, i.e., it is assumed that most of

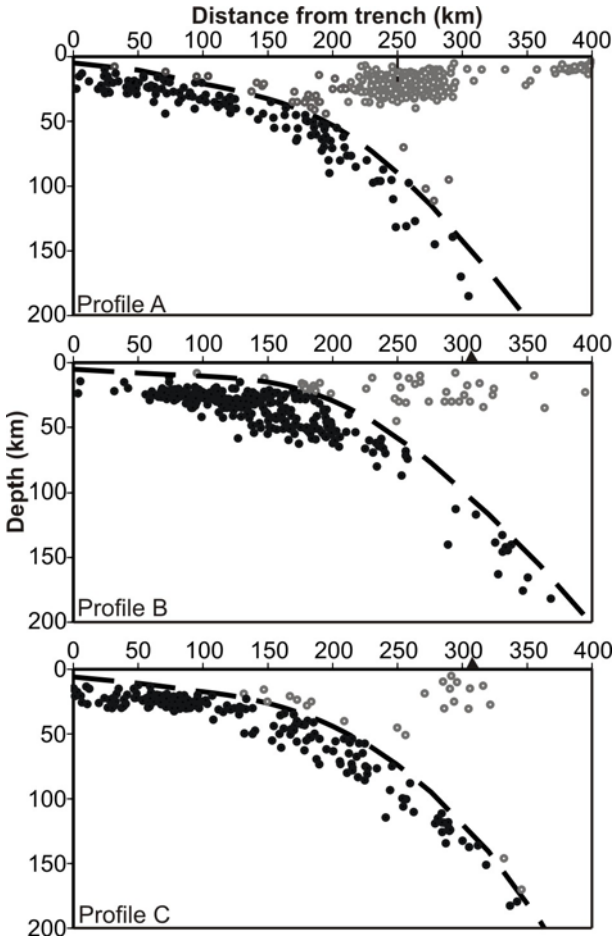

Figure 60: The slab geometries, derived from depth constrained Benioff-Wadati hypocentres (Data from Engdahl et al., 1998). Grey circle hypocenters mainly in forearc crust were not used in the thrust profile fit. Triangles indicate volcanic arc.

the seismicity is in the lower oceanic crust and uppermost oceanic mantle. In the area of the trench there is reasonable agreement of the offshore reflection top of the crust and the Wadati-Benioff seismicity constraint with this assumption. The depth directly at the trench was defined from bathymetry data and the sediment thickness. The dip profiles of the models are well constrained within a depth error of about +/-2 km at 150 km landwards from the trench. The dip is relatively shallow compared to the global compilation of Lallemand et al. (2005).

The constraining data within 500 km of each profile were projected onto the cross section, and the best fit was determined using 5th and 6th order polynomials (Figure 60). These models agree with the dip profiles of Chlieh et al. [2006] within a reasonable uncertainty, and they agree well with the dip profile models developed by Engdahl et al. [2007].

Table 16: Parameters for the Continental Geotherm

Model Unit	Thickness [km]	Thermal conductivity [W $m^{-1}K^{-1}$]	Radiogenic heat production [$\mu W/m^3$]
Upper crust	15	2.5	1.3 – 4.5
Lower crust	15	2.5	0.27
Mantle wedge	--	3.1	0.02
Oceanic Plate	95	2.9	0.02

Thermal Conductivity and Radioactive Heat Generation

For both the upper and lower continental crust the thermal conductivity is taken as 2.5 W m^{-1} K^{-1}, commonly used for average forearc continental crust material (e.g., Peacock and Wang, 1999; Chapman, 1986; Sclater and Francheteau, 1970). The conductivity in the mantle wedge is taken as 3.1 W m^{-1} K^{-1}, and 2.9 W m^{-1} K^{-1} for the oceanic plate (Table 16).

No measurements of typical upper crustal radioactive heat generation have been found for Sumatra and I have taken high crustal values between 3.0 and 4.5 μWm^{-3} for the upper 15 km, as required to match the heat flow (see heat flow discussion below), 0.27 μW m^{-3} for the deeper crust and 0.02 μW m^{-3} for the mantle wedge. They reflect the roughly exponential decrease in crustal radioactive heat production with depth commonly estimated (e.g., Lachenbruch, 1968; Blackwell, 1971). Variation in radiogenic heat

production in the continental crust has very little effect on the temperatures on the subduction thrust fault, but affects the surface heat flow directly. The model cross-sections consist of five units: oceanic plate, sediments, upper continental crust, lower continental crust and mantle wedge. The effect of sedimentation on the incoming plate thermal regime is accounted for in the modeling code. As for the thermal parameters, the same values are used as for the continental crust. The thermal model results are found to be insensitive to small local variations in the conductivity chosen.

Frictional Heating

The temperature on the thrust fault may be affected by frictional heating (e.g., van den Beukel and Wortel, 1987; Molnar and England, 1990; Dumitru, 1991). In my model, I applied frictional heating increasing downward to a depth of ~ 40 km. Changes within +/- 5 km do have a slight effect on the thermal structure, however, it does not effect the inferred seismogenic zone. When assuming no frictional heating, the subducting plate reaches a temperature of 350°C at a depth of 50 km, ~ 200 km away from the trench (Figure 59). Noticeable changes in the width (>20 km) of the thermally inferred seismogenic zone start occurring when changing the depth of frictional heating by more than +/- 15 km. Frictional heating is incorporated into the models by dividing the thrust interface into a shallow updip zone of brittle frictional sliding and a deeper downdip zone of ductile shear (Wang et al., 1995a, 1995b). The shear stress along the thrust surface in the brittle zone is given by Byerlee's law (Byerlee, 1978). Shear stress increases with depth in the frictional zone due to an increase in overburden and therefore normal stress across the interface. However, normal stress is partly balanced by pore pressure, and a decrease in the pore/pressure ratio leads to an increase in frictional heating. In the deeper

plastic regime, the magnitude of heating is a product of shear stress and strain rate, which is determined from the strain rate using power law rheology similar to the one for diabase (e.g., Caristan, 1982; Ivins, 1996). The brittle/ductile transition is determined within the code, at ~ 40 km. Above that transition, heat is generated by frictional heating, below by viscous energy dissipation/ shear heating along the plate interface. Shear heating will diminish downwards.

6.3.4 Continental Crust Thickness

The thickness of the continental crust is needed for the geometry of the thermal units of the thermal model. The thickness also defines the intersection of the thrust with the forearc continental Moho and with potential stable sliding serpentinite and talc in the downgoing slab.

The depth of the Moho is not well resolved for the study area, but available estimates are fairly shallow at about 30 km (Simoes et al., 2004; Kepp et al., 2001; Kieckhefer et al., 1980), based on gravity modeling and seismic refraction data. It is known that several thrust earthquakes nucleated at a depth of 30 km, and we may assume that earthquakes can not nucleate below the intersection of the forearc Moho and the downgoing slab. The regional thickness of the continental crust is assumed to be 30 km. Changing the depth of the Moho does neither considerably influence the results of the models for the subduction zone thermal structure, nor the temperature profile of the oceanic, downgoing slab. If the Moho provides the lower limit to the seismogenic zone, assuming a much different continental crustal thickness of 23 km instead of 30 km has quite a big impact on the lower limit of the seismogenic zone, which then changes from 144 km to then 127 km.

Neither the thermal structure nor the surface heat flow are significantly affected by a Moho depth different from 30 km.

We note that Klingelhoefer et al. [2010] have inferred an unusually shallow continental mantle from seismic structure data of about 22 km. Such a shallow depth seems inconsistent with the gravity data but we have not examined this question in detail.

6.3.5 Surface Heat Flux Observations

Surface heat flux presents one independent constraint on the thermal models, especially on the thrust frictional heating. However, as noted above, the other parameter uncertainties, especially the forearc crustal heat generation, limit this constraint. There is considerable trade-off between frictional heating and crustal heat generation for surface heat flow. For all models, the forearc has modeled heat flux values of ~50 mW m^{-2}, which agrees with the scattered data (Figure 61). Frictional heating is greatest at depths deeper than 20km. The available heat flux measurements in the forearc are quite variable. They are mainly measured on fault zones and concluded by Delisle & Zeibig (2007) to be influenced by hydrothermal activity.

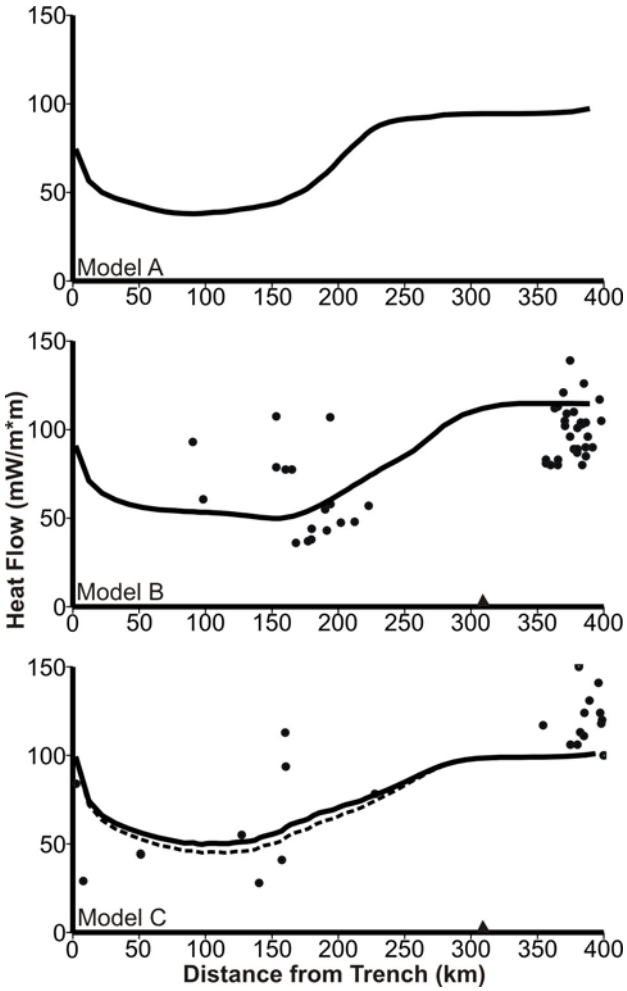

Figure 61: The model heat flux for the 3 profiles. The variations result mainly from differences in model plate age, plate geometry and convergence rate along strike of the trench. No heat flow data available for the area of Model A. Heat flow values in the forearc region are scattered and may be unreliable. For Model C, heat flow assuming no frictional heating is also plotted (dotted line). Triangles indicate volcanic arc.

However, some of the heat flows are unusually high with some values over 100 mW/m^2, probably indicative of hydrothermal activity or possibly unusually high crustal radioactive heat generation as well. Offshore on the continental slope, heat flow has been determined from the depth of the gas hydrate bottom-simulating reflector (BSR), regionally in the central Siberut Basin, between the trench and Sumatra in the area of the Nicorbar-Andaman and the Nias earthquakes. Delisle and Zeibig [2007] concluded that the heat flow in the Central Siberut Basin is characterized by moderate values of 30

mW/m^2. BSR-derived heat flow values found for the central Simulue Basin range from 30 – 60 mW/m^2 (Delisle and Zeibig, 2007). These low values for the forearc are similar to the heat flows predicted by the models.

6.4 Seismogenic Zone

6.4.1 Past Seismic Activity on the Megathrust

During the period of historical record, several great earthquakes dominate the strain relief along the Sumatra subduction megathrust. Most data on the updip and downdip extents of the seismogenic zone come from the Aceh-Andaman Mw=9.15 earthquake of 2004, and the Nias-Simuelue Mw=8.6 earthquake of 2005, with both hypocentres located at ~ 30 km depth on the slab surface. Earlier great thrust events were a Mw~ 9 earthquake in 1833, which likely had a similar rupture extent as the 2005 earthquake, and a Mw~ 8.5 in 1861, which ruptured the entire segment between Banyak and the Pini Islands (Newcomb and McCann, 1987). Smaller thrust events were the 7.3 event which occurred in 2002 at the junction between the 2004 and 2005 ruptures, and a Mw=7.7 event in 1935, which nucleated at a depth of ~ 28 km.

The vertical levels of micro-atolls show that most of the convergence strain in the region was accommodated aseismically for at least the past half century (Natawidjaja et al., 2006). This section of the megathrust separates the sections to the south and the north that generate great and giant earthquakes (Natawidjaja et al., 2006). No great earthquakes (M≥8) have been reported for the Andaman-Nicobar and northern Sumatra region, but there were large events in 1847 (M7.5), 1868, 1881 (M7.9) and 1941 (M7.7). More recent events are the Mw=8.4 earthquake in September 2007 to the south at 4°31’S and 101°23’, which nucleated at ~ 23 km depth (CMT catalogue), and a Mw=7.8 event at 2.36°S and 97.132°E at ~ 30 km depth.

6.4.2 Comparison of Rupture Areas to Thrust Temperatures and Forearc Mohos

Modeled Limits to the Seismogenic Zone

Temperatures on the subduction thrust from the detailed thermal model and the intersection with the forearc Moho provide model constraints for the updip and downdip limits for the thrust seismogenic zone. The suggested updip temperature limit of 100-150°C geotherm is situated 0 - 38 km landwards from the trench at a depth of 5.5 - 9 km for northern model A, 0 - 26 km at a depth of 5 - 8 km for model B and it is very close to the trench for southern model C. The suggested downdip temperature limit of 350-450°C geotherms is 183-201 km landwards from the trench at a depth of 44 - 54 km for northern model A, 214-254 km landwards from the trench at a depth of 34 - 60 km for model B and 156-230 km landward from the trench at a depth of 29 - 57 km for model C (Figure 62). The forearc Moho, estimated to be at a depth of 30 km, is intersected 144 km landwards from the trench for northern model A, 200 km landward from the trench for model B and 168 km landward from the trench for model C (Figure 62). For profiles A and B the Moho intersection is shallower than the 350^{o}C isotherm and agrees with the great earthquake rupture limits. The 350^{o}C isotherm is reached just seaward of the Moho intersection for profile C. Changing the depth of the Moho by 5 km results in lateral changes of the intersection of ~ 10 km for each profile.

Coseismic Rupture Area

The updip and downdip limits for the seismogenic zone have been estimated from a number of constraints for the coseismic rupture of great earthquakes, from the depths of other thrust events, and from the extent of the interseismic locked zone. Chlieh et al [2007] provide an excellent summary. These constraints for the landward limit include:

1. The updip and downdip extent of aftershock seismicity for recent great earthquakes;

2. The downdip extent of smaller thrust events;

3. Waveform modelling for great thrust earthquakes;

4. Landward distribution of coseismic vertical motions in great earthquakes compared to the predictions of dislocation models, from geodetic data and from coastal and shallow water field data such as coral heads (usually little sensitivity to updip limit);

5. Landward distribution of interseismic strain build-up from GPS etc. data compared to predictions of locked zone dislocation models.

Table 17: Modeled Width and Depth of the Thermally Inferred Seismogenic and Transition Zones

	150-350°C (Thermal Seism. Zone)		**350-450°C (Thermal Trans. Zone)**	
	Distance from Trench (km)	Depth (km)	Distance from Trench (km)	Depth (km)
Model A	38 – 183	9 – 44	183 – 201	44 – 54
Model B	26 – 214	8 – 34	214 – 254	34 – 60
Model C	0 - 156	0 – 29	156 – 230	29 – 57

Constraints to the updip seismogenic limit are limited, primarily from the aftershock distribution, with additional information from tsunami modeling. The main available constraints are discussed below.

Meltzner et al. [2006] used satellite imagery and ground observations to map the extent and magnitudes of coseismic uplift and subsidence in the coastal region and offshore islands. The region of coseismic uplift first constrains the north-to south rupture extent. Secondly, comparison of the pattern of vertical motion with the predictions of dislocation models allows estimates of the downdip width of faulting. To a first order, the downdip limit corresponds to the hinge line (pivot line) between offshore subsidence and onshore

uplift. For the study, the vertical positions relative to sea level of shallow water coral heads in coral reefs before and after great earthquakes were measured in situ and in satellite images to determine the position of the pivot line (Meltzner et al., 2006), and a rupture downdip width of 80–120 km and an along strike rupture length of about 1600 km for the 2004 earthquake.

Subarya et al [2006] used near-field GPS observation of vertical and horizontal deformation, and in situ and remote sensing observations of uplift and subsidence of coral reefs to constrain the distribution of slip on the Sunda megathrust during and soon after the 26 December 2004 earthquake. Decade-long pre-earthquake campaign GPS measurements were used to constrain a kinematic model of interseismic deformation that allows correction of the measured displacements for steady interseismic motions associated with elastic strain buildup on the locked fault. The three-dimensional distribution of slip on the megathrust was then estimated by inverting the geodetic observations, GPS measurements from the Nicobar and Andaman Islands and continuous GPS offsets in Phuket and Medan. The rupture length inferred from that study is more than 1500 km, with a downdip width of less than 150 km. They conclude that earthquake slip occurred mostly at depths shallower than 30 km.

Galahaut et al. [2006] used campaign mode GPS measurements of coseismic displacement at 13 sites in the Andaman-Nicobar Islands before and after the 2004 Sumatra-Andaman earthquake. The measurements provided improved estimates of rupture characteristics in the region. They concluded that to the north of Sumatra, in the region of the Nicobar Islands, the rupture width is ~155 km, decreasing to ~120 km further north beneath the Andaman Islands.

In the area of central Sumatra, based on geodetic data and gravity modeling prior to the great 2004 event, Simoes et al. [2004] concluded that the downdip limit beneath the Butu Islands extends below the forearc. However, the Butu Islands lie above the Investigator Fracture Zone, which makes the tectonic and structure of the megathrust zone more complex and different from Southern and Northern Sumatra (Grevemeyer and Tiwari, 2006).

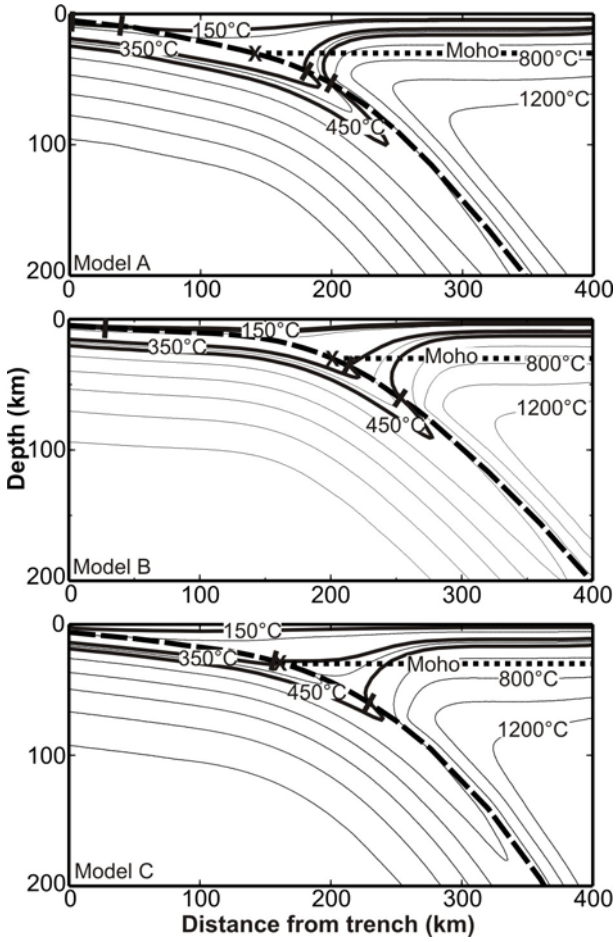

Figure 62: Position of the 100-150°C, 350° and 450° geotherms and their intersection with the slab, as well as position of the Moho and intersection with the slab (X). In model C, the intersection of the100–150°C geotherm with the slab occurs seawards from the trench.

Grevemeyer and Tiwari [2006] used structural constraints derived from seismic and gravity data to explain the seismogenic behaviour in the Sunda subduction zone, which

implies a width of the coupling zone offshore of Sumatra of >120 km. They also made comparisons with the results of initial thermal models and suggested that the thermal limits are probably deeper than that estimate. In southern Sumatra, two large thrust earthquakes (Mw 6.8 and Mw 7.8 on January 16th, 2001 and February 13th, 2001, respectively) nucleated roughly 180 km landwards of the trench axis. The termination of major slip at ~ 30 km depth supports the idea that the intersection of the downgoing plate with the forearc Moho is governing the downdip limit of the seismogenic zone in northern Sumatra (Grevemeyer and Tiwari, 2006).

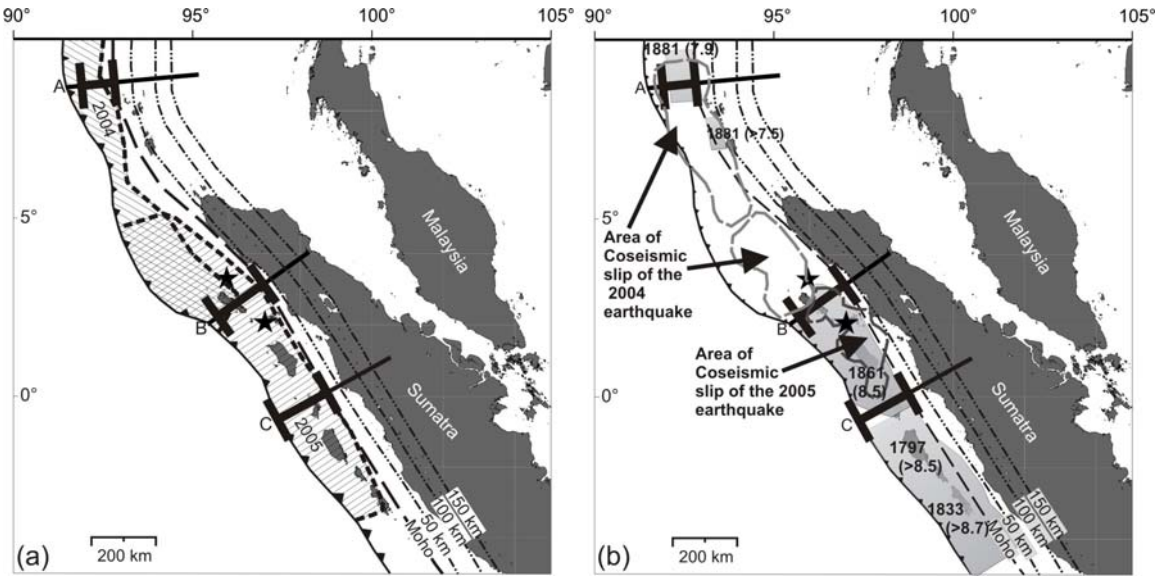

Figure 63: (a) Aftershock seismicity areas of the 2004 and 2005 megathrust earthquakes, indicating the updip and downdip rupture extent (Engdahl et al., 2007). (b) Summary rupture area results of Chlieh et al., [2007], the grey shaded areas represent rupture areas of previous earthquakes (Chlieh et al., 2007). Solid black lines marked A, B, C indicate profiles and rupture limits discussed in this study.

The downdip width of the aftershock zone is a critical constraint on the updip and downdip rupture extent of great earthquakes. For the 2004 Mw 9.0 earthquake, the landward aftershock extent varies from ~ 200 km at its northern end to ~ 275 km at its southern end; for the 2005 Mw 8.7 earthquake the downdip width of the aftershock zone varies from ~ 220 km at 8°N to ~ 100 km at 2 °N (Engdahl et al., 2007). This extent is

shown in Figure 63. The updip limit to aftershocks is close to the trench. The downdip limit is close to the thrust intersection with the forearc Moho.

Modeled Temperature Limits compared to rupture areas

Based on the thrust temperatures from this study and the estimated depth of the forearc Moho, these constraints to the seismogenic zone width (e.g., Bock et al., 2003; Simoes et al., 2004, Subarya et al., 2006, Grevemeyer and Tiwari, 2006), indicate that the Moho downdip limit fits best for all profiles, although for profiles B and C, 350°C occurs near the Moho limit. A temperature of 350°C occurs at greater depth than the Moho limit for the northern profile A, well landward downdip of the great earthquake rupture limits from a considerable variety of data.

The 100-150°C temperatures occur on the thrust very close to the trench for profile C. For profiles A and B they occur at 38 km and 26 km from the trench respectively. These locations are in reasonable agreement with the main constraint to the updip great earthquake rupture limit, the aftershock updip limit (Figure 63 a).

An important summary of the great earthquake rupture limits and inferred seismogenic zone has been compiled by Chlieh et al. [2007] that included many of the constraints considered above. Their model of the rupture width is mainly based on geodetic data (far field and near field GPS, continuous and campaign GPS), field measurements of uplifted and subsided coral heads and remote sensing measurements of uplift or subsidence using optical or Synthetic Aperture Radar (SAR) images. They used similar constraints to the slab geometry as in my models, [i.e., Engdahl et al., 2007]. Comparing our thermal model temperatures and the position of the thrust intersection with the forearc Moho results with the numerous constraints for the seismogenic zone (e.g., model of Chlieh et al., 2007, and

references therein) (Figure 63b) shows that the updip limit fits the model thermal control and the downdip limit fits best with the intersection of the thrust with the forearc Moho. The transition zone for the downdip limit appears to be quite narrow, probably controlled rheologically by stable sliding serpentinite at the base of the forearc mantle.

6.5 Other Applications for Thermal Models

Although the main objective of this study is to investigate thermal and structural models of the Sumatra subduction zone and their effects for the seismogenic zone, temperature estimates from the thermal models are useful for a number of other applications, especially for metamorphic dehydration reactions in the subducted slab. Figure 64 shows the temperature on the slab surface for the three profiles A, B and C for Sumatra.

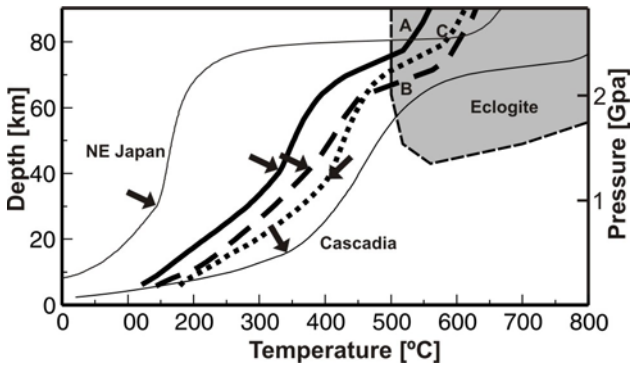

Figure 64: Temperature of the slab surface of Profiles A, B, and C, as well as comparisons with cool NE Japan and very hot Cascadia (I. Wada, personal communication, 2008). Arrows indicate the maximum depth for model frictional heating.

These estimates are compared to the temperatures on the slab surface for the cooler subduction zone in NE Japan and for the warmer Cascadia subduction zone. Although there should be progressive dehydration downdip, an especially important metamorphic boundary is the pressure-temperature stability of eclogite, both because this represents one of the greatest source of upward fluid expulsion, and also it represents a phase change to a substantially higher density and velocity for the subducting oceanic crust. For

the Sumatra profiles, this phase boundary is estimated to be reached at a depth of about 60 km and temperature of about 500^{o}C.

6.6 Discussion

In this study I have evaluated constraints on the updip and downdip controls to the seismogenic zone of subduction thrust faults, using the extensive newly available data from two great earthquakes on the Sumatra subduction zone. Although a longer series of great earthquakes and smaller thrust events would be needed to conclusively establish the updip and downdip seismogenic limits, it is concluded that the long-term limits are reasonably defined by the updip and downdip rupture limits for the two recent great events.

The thermal models are well constrained for most important parameters. However, there is limited and scattered measured heat flow in the forearc region that can be compared to the thermal model predictions. Generally heat probe heat flow in the central Siberut Basin is about 30 mW/m^2 and hydrate BSR – derived heat flow values range from 30 to 60 mW/m^2 (Delisle & Zeibig, 2007) in agreement with my modeled results (Figure 61). The differences in the modeled heat flux values for the three profiles reflect mainly the differences in age of the incoming oceanic plate, with the incoming plate in the north being the oldest and therefore coolest (an effect partly offset by the thicker sediments in the north).

On the profile 500 km north of Sumatra thermal models predict 350°C and 450°C temperatures on the Sunda subduction thrust 183 and 201 km from the trench, and depths of 44 km and 54 km, i.e., well below the intersection with the forearc Moho at about 30 km. For the central profile (northern Sumatra) the distances are 214 km and 254 km and

depths 34 and 60 km, also deeper than the forearc Moho. For the southern profile (central Sumatra) the distances are 156 km and 230 km and depths 29 and 57 km so either postulated limit may apply, although the common 450°C transition zone limit is deeper so the forearc Moho limit is preferred.

The great earthquake behaviour at the downdip limit may be different for a thermal downdip limit versus a structural limit. From earthquake data the downdip limit of rupture appears to be quite abrupt as expected for a structural limit, but there are no recent well-studied great earthquakes with a thermal downdip limit for comparison.

The predicted updip limit of 100-150°C is located near the trench for the central Sumatra profile and 26 and 38 km landward for the two northern profiles. The updip rupture limit for the recent great events is not well constrained, but aftershocks indicate that the limits are near the trench, in agreement with these model updip limits.

These summaries of the great earthquake rupture limits are in good agreement with the rupture areas defined in previous studies, concluding that the rupture extended approximately to the forearc continental Moho. This limit is interpreted to be due to the stable sliding serpentinized mantle corner. The updip limit of the model seismogenic zone is less well determined than the downdip limit. An important model limitation is that the depth of the thrust is not well constrained in that region. The thermal models can be further constrained, tested and if necessary refined when more accurate depths to the updip portion of the thrust are obtained and more modern heat flow observation in the forearc region are available.

6.7 Discussion of recently published results

One recently published study suggests that, based on new seismic refraction and wide-angle reflection data, the continental Moho is very shallow in the region of the 2004 Mw9.3 rupture area, at a depth of about 20 km (Klingelhoefer et al., 2010; Dessa et al, 2009). This is a very unusually thin continental crust.

This interpretation of a shallow continental Moho intersects with the downgoing oceanic slab at a depth of ~ 20 km, which is, according to my thermal model as well as Klingelhoefer et al. [2010], at a temperature well below the seismogenic limit of 350°C. If correct, this means that the Moho is shallower than the observed downdip extent of the seismogenic zone, as defined by aftershocks, which is at depth of ~ 30 km. These findings do not support the hypothesis that the Moho is its downdip limit. The results of Klingelhoefer et al. [2010] imply that a significant portion (>50 km) of the rupture occurred along the interface between the oceanic crust of the downgoing plate and the fore-arc mantle of the upper plate, which contradicts the conclusion presented earlier (Hippchen and Hyndman, 2008), that the 30 km downdip limit was controlled by the presence of a serpentinized mantle wedge beneath the continental Moho. Since the thermal and structural models are very similar and the results are identical, it comes down to the exact position of the continental Moho. If the constraints provided by Klingelhoefer et al. [2010] are valid, the downdip limit of the Sumatra Subduction Zone may be temperature controlled, and extend below the continental Moho intersection. Better constraints on the continental forearc crustal thickness is needed to test this conclusion, for example using receiver function studies across the margin.

Bibliography

Altamimi, Z., P. Sillard, and C. Boucher (2002), ITRF2000: A new release of the International Reference Frame for earth science applications, *J. Geophys. Res.*, *107*(B1), 2214, doi:10.1029/2001JB000561.

Ammon, C., C. Ji, H.-K. Thio, D. Robinson, S. Ni, V. Hjorleifsdottir, H. Kanamori, T. Lay, S. Das, D. Helmberger, G. Ichinose, J. Polet, and D. Wald (2005), Rupture process of the 2004 Sumatra-Andaman earthquake, *Science, 308***,** 1133–1139.

Atwater, T. (1989), Plate tectonic history of the northeast Pacific and western North America, in *The Eastern Pacific Ocean and Hawaii*, edited by E. L. Winterer, D. M. Hussong, and R. E. Decker, pp. 21-72, Geol. Soc. of Am., Boulder, Colo.

Audet, P.; M. Jellinek; and H. Uno (2007), Mechanical controls on the deformation of continents at convergent margins, *EPSL, 264*, 151-166.

Audet, P., M. G. Bostock, J.-P. Mercier, and J. F. Cassidy (2008), Morphology of the Explorer–Juan de Fuca slab edge in northern Cascadia: Imaging plate capture at a ridge-trench-transform triple junction, *Geology*, *36*(11), 895, doi:10.1130/G25356A.1.

Barr, S. M., and R. L. Chase (1974), Geology of the northern end of the Juan de Fuca Ridge and sea-floor spreading, *Can. J. Earth Sci.*, *11*, 1384-1406.

Berube, J., G. C. Rogers, R. M. Ellis, and E. O. Hasselgren (1989), A microseismicity study of the Queen Charlotte Islands region, *Can. J. Earth Sci.*, *26*, 2556-2566.

Beutler, G. (1999), The International GPS Service (IGS): An interdisciplinary service in support of Earth sciences, *Advances in Space Research*, *23*(4), 631-653, doi:10.1016/S0273-1177(99)00160-X.

Bokelmann, G., and G. Beroza (2000), Depth-dependent earthquake focal mechanism orientation: Evidence for a weak zone in the lower crust, *J. Geophys. Res., 105,* 21,683–21,695.

Bostwick, T. K. (1984), A Re-examination of the 1949 Queen Charlotte Earthquake, Master's Thesis, UBC, pp.115.

Botros, M., and H. P. Johnson (1988), Tectonic Evolution of the Explorer-northern Juan de Fuca region from 8 Ma to the present, *J. Geophys. Res.*, *93*, 10421-10437.

Braunmiller, J.; Nabelek, J. (2002), Seismotectonics of the Explorer region, *J. Geophys. Res.*, *107*(B10), doi:10.1029/2001JB000220.

Bustin, A. M. M. (2006), The Crustal Structure, Deformation from GPS, and Seismicity Related to Oblique Convergence along the Queen Charlotte Margin, British Columbia, PhD thesis, UVic, pp. 226.

Bustin, A. M. M., R. D. Hyndman, H. Kao, and J. F. Cassidy (2007), Evidence for underthrusting beneath the Queen Charlotte Margin, British Columbia, from teleseismic receiver function analysis, *Geophysical Journal International*, *171*(3), 1198-1211.

Byerlee, J., Friction of rocks, (1978), *Pure and applied Geophysics, 16*, 615-626.

Byrne, D. E., D. M. Davis, and L. R. Sykes (1988), Loci and maximum size of thrust earthquakes and the mechanics of the shallow region of subduction zones, *Tectonics, 7*, 833– 857.

Carbotte, S. M., J. M. Dixon, E. Farrar, E. E. Davis, and R. P. Riddihough (1989), Geological and geophysical characteristics of the Tuzo Wilson Seamounts: implications for plate geometry in the vicinity of the Pacific – North America – Explorer triple junction, *Can. J. Earth Sci.*, *26*, 2365-2384.

Caristan, Y. (1982), The transition from high temperature creep to fracture in Maryland diabase, *J. Geophys. Res.*, *87*, 6781-6790.

Carter, M. L., and N. C. Tsenn (1987), Flow properties of continental lithosphere, *Tectonophysics*, *186*(1-2), 27-63.

Cassidy, J. F., R. M. Ellis, C. Karavas, and G. C. Rogers (1998), The northern limit of the subducted Juan de Fuca plate system, *J. Geophys. Res., 103 (B11),* 26,949-26,961.

Catherine, J. K., V. K. Galahaut, V. K. Sahu (2005), Constraints on rupture of the December 26, 2004, Sumatra earthquake from far-field GPS observations, *Earth and Planetary Science Letters*, *237*, 673-679.

Chase, R. L., D. L. Tiffin, and J. W. Murray (1975), The western Canadian continental margin, in *Canada's Continental Margins and Offshore Petroleum Exploration*, edited by C. J. Yorath, E. R. Parker, and D. J. Glass, pp. 701-721, Mem. Can. Soc. Pet. Geol.

Chlieh, M., J. Avouac, K. Sieh, D.H. Natawidjaja and J. Galetzka (2004), Investigating lateral variations of interseismic strain along the Sumatra Subduction Zone, *Eos Trans. AGU*, *85(47)*, Fall Meet. Suppl., Abstract T13C-1385.

Chlieh, M., J.P. Avouac, V. Hjorleifsdottir, T.-R. A. Song, C. Ji, K. Sieh, A. Sladen, H. Hebert, L. Prawirodirdjo, Y. Bock, and J. Galetzka (2007), Coseismic slip and afterslip of the great M_W 9.15 Sumatra-Andaman earthquake of 2004, *BSSA, 97*, 152-173.

Chlieh, M, J.P. Avouac, K. Sieh, D.H. Natawidjaja, J. Galetzka (2008) Heterogeneous coupling of the Sumatran megathrust constrained by geodetic and paleogeodetic measurements*, J. Geophys. Res*, *113* (B5), doi:10.1029/2007JB004981.

Currie, C.A., R.D. Hyndman, K.Wang, and V. Kostoglodov (2002), Thermal models of the Mexico subduction zone: Implications for the megathrust seismogenic zone, *J. Geophys. Res*., *107*, 2370-2382.

Currie, C., J. F. Cassidy, R. D. Hyndman, and M. G. Bostock (2004), Shear wave anisotropy beneath the Cascadia subduction zone and western North American craton, *Geophysical Journal International*, *157*(1), 341-353, doi:10.1111/j.1365-246X.2004.02175.x.

Currie, C. a, C. Beaumont, and R. S. Huismans (2007), The fate of subducted sediments: A case for backarc intrusion and underplating, *Geology*, *35*(12), 1111, doi:10.1130/G24098A.1.

Dach, R., U. Hugentobler, P. Fridez, and M. Meindl (Eds.) (2007), *Bernese GPS software, Version 5.0*, Astronomical Institute, University of Bern.

Davidson, C., K. J. Davis, C. M. Bailey, C. H. Tape, J. Singleton, and B. Singer (2003), Age, origin, and significance of brittle faulting and pseudotachylyte along the Coast shear zone, Prince Rupert, British Columbia, *Geology*, *31*(1), 43 – 46.

Davis, E. E., and R. P. Riddihough (1982), The Winona Basin: Structure and Tectonics, *Can. J. Earth Sci.1*, *19*, 767-788.

Davis, E. E., and R. D. Hyndman (1989), Accretion and recent deformation of sediments along the northern Cascadia subduction zone, *Geological Society of America Bulletin*, *101*(11), 1465-1480.

Davis, E. E., D. S. Chapman, and C. B. Forster (1996), Observations concerning the vigor of hydrothermal circulation in young oceanic crust, *J. Geophys. Res.*, *101*, 2927–2942.

Deng, J., M. Gurnis, H. Kanamori, and E. Hauksson (1998), Viscoelastic flow in the lower crust after the 1992 Landers, California, earthquake, *Science*, *282*, 1689–1692.

Dehler, S. A., and R. M. Clowes (1988), The Queen Charlotte Island refraction project, part I, *Can. J. Earth Sci.*, *25*, 1857-1870.

deGroot-Hedlin, C. (2005), Estimation of the rupture length and velocity for both the Dec 26, 2004 and March 28, 2005 events using hydroaccoustic signals, *Eos Trans. AGU*, *86(18)*, Jt Assem. Suppl., Abstract U53B-02.

Delisle, G., and Zeibig, M, (2007), Marine heat flow measurements in hard ground offshore Sumatra, *Eos*, *88*, 38-39.

Dewey, J. W., G. Choy, B. Presgrave, S. Sipkin, A. C. Tarr, H. Benz, P. Earle, and D. Wald (2007), Seismicity associated with the Sumatra-Andaman Islands earthquake of 26 Decmeber 2004, *BSSA, 97*, 25-42.

DeMets, C., R. G. Gordon, S. Stein, and F. A. Donald (1987), A revised estimate of Pacific - North America motion and implications for western North America plate boundary zone tectonics, *Geophysical Research Letters*, *14*(9), 911-914.

DeMets, C., R. G. Gordon, D. F. Argus, and S. Stein (1990), Current Plate motions, *Geophysical Journal Internationa1*, *101*, 424-478.

Dessa, J.X., Klingelhoefer, F., Graindorge, D., André, C., Permana, H., Gutscher, M.-A., Chauhan, A., Singh, S.C.&SUMATRA-OBS Scientific Team (2009), egathrust earthquakes can nucleate in forearc mantle: evidence from the 2004 Sumatra event, *Geology*, *37,* 659–662.

Dieterich, J. H. (1978), Time-dependent friction and the mechanics of stick-slip, *Pure and Applied Geophysics PAGEOPH*, *116*(4-5), 790-806, doi:10.1007/BF00876539.

Dragert, H., and R. D. Hyndman (1995), Continuous GPS monitoring of elastic strain in the Northern Cascadia Subduction Zone, *Geophysical Research Letters*, *22*(7), 755-758.

Dragert, H., S. Mazzotti, and K. Wang (2002), Aseismic Slip on the Northern Cascadia Subduction Zone: Impacts on Seismic Hazard Estimates, *Eos Trans. AGU, Fall Meet. Suppl.*, *83*(47).

Dumitru, T. A., Effects of subduction parameters on geothermal gradients in forearcs, with an application to Franciscan subduction in California, *J. Geophys. Res.*, *96*, 621-641.

Engdahl, E., R. van der Hilst, and R. Buland, (1998), Global teleseismic earthquake relocation with improved travel times and procedures for depth determination, *BSSA, 88*, 722-743.

Engdahl, R., A. Villaseñor, H. R. DeShon, and C. H. Thurber, (2007), Teleseismic relocation and assessment of seismicity (1918-2005) in the region of the 2004 M_W 9.0 Sumatra-Andaman and 2005 M_W 8.6 Nias Island great earthquakes, *BSSA*, *97*, 43-61.

Engebretson, D. C., A. Cox, and R. G. Gordon (1985), Relative motions between oceanic and continental plates in the Pacific Basin, *Spec. Pap. Geol. Soc. Am.*, *206*, 59 pp.

Enkin, R.J., s. T. Johnston, K. P. Larson, J. Baker (2008), Paleomagnetism of the 70 Ma Carmacks Group at Solitary Mountain, Yukon, confirms and extends controversial results: Further evidence for the Baja British Culumbia model, *Geol. Assoc. Canada, Special paper 46*, 221-232.

Flück, P., R. D. Hyndman, and K. Wang (1997), Three-dimensional dislocation model for great earthquakes of the Cascadia subduction zone, *J. Geophys. Res.*, *102*(B9), 20539-20550, doi:10.1029/97JB01642.

Flück, P. (2003), Effective elastic thickness T_e of the lithosphere in western Canada, *J. Geophys. Res.*, *108*(B9), doi:10.1029/2002JB002201.

Freed, A. M., and R. Bu¨rgmann (2004), Evidence of power-law flow in the Mojave Desert mantle, *Nature, 430*, 548–551.

Freed, a, R. Bürgmann, E. Calais, and J. Freymueller (2006), Stress-dependent power-law flow in the upper mantle following the 2002 Denali, Alaska, earthquake, *Earth and Planetary Science Letters*, *252*(3-4), 481-489, doi:10.1016/j.epsl.2006.10.011.

Freed, A. M., R. Bürgmann, E. Calais, J. Freymueller, and S. Hreinsdóttir (2006), Implications of deformation following the 2002 Denali, Alaska, earthquake for postseismic relaxation processes and lithospheric rheology, *J. Geophys. Res.*, *111*(B1), 1-23, doi:10.1029/2005JB003894.

Freed, A. M., T. Herring, and R. Bürgmann (2010), Steady-state laboratory flow laws alone fail to explain postseismic observations, *Earth and Planetary Science Letters*, *300*(1-2), 1-10, doi:10.1016/j.epsl.2010.10.005.

Frisch, W., and M. Meschede (2005), Plattentektonik, *Primus Verlag Darmstadt*.

Galahaut, V. K., B. Nagarajan, J. K. Catherine, and S. Kumar, (2006), Constraints on 2004 Sumatra-Andaman earthquake rupture from GPS measurements in Andaman-Nicobar Islands, *Earth and Planetary Science Letters*, *242*, 365-374.

Grevemeyer, I., and V. M. Tiwari (2006), Overriding plate controls spatial distribution of megathrust earthquakes in the Sunda-Andaman subduction zone, *Earth and Planetary Science Letters, 251*, 199-208.

Guilbert, J., J. Vergoz, E. Schisselé, A. Roueff, and Y. Cansi (2005), Use of hydroacoustic and seismic arrays to observe rupture propagation and source extent of the M_w = 9.0 Sumatra earthquake, *Geophys. Res. Lett.*, *32*, L15310.

Gurtner, W., G. Mader, and D. MacArthur (1989), A common exchange format for GPS data, in *Fith International Geodetic Symposium on Satellite Systems*, pp. 917, Las Cruces.

Gutenberg, B., C. F. Richter (1945), Seismicity of the Earth (Supplementary Paper), *Bull. Geol. Soc. Am.*, *56*, 603-668.

Hacker, B. R., S.M. Peacock, G.A. Abers, and S.D. Holloway (2003), Subduction factory 2. Are intermediate-depth earthquakes in subducting slabs linked to metamorphic dehydratation reactions? *J. Geophys. Res., 108*, 2030-2050.

Hansen, F. D., and N. L. Carter (1982), Creep of selected crustal rocks at 1000 MPa., *Eos, Trans. Am. Geophys. Union*, *63*, 437.

Harris, N.H, and D.S. Chapman (2004), Deep-seated oceanic heat flux, heat deficits, and hydrothermal circulation, in *Hydrology of the Oceanic Lithosphere*, edited by E. Davis and H. Elderfiled, pp.311-336, Cambridge University Press.

Henton, J., H. Dragert, R. McCaffrey, K. Wang, and R. D. Hyndman (2002), GPS monitoring of deformation at the northern Cascadia subduction zone, *EOS Trans. AGU*, *81*, F328.

Hetland, E. a, and B. H. Hager (2006), Interseismic strain accumulation: Spin-up, cycle invariance, and irregular rupture sequences, *Geochemistry Geophysics Geosystems*, *7*(5), doi:10.1029/2005GC001087.

Hilairet, N., B. Reynard, Y. Wang, I. Daniel, S. Merkel, N. Nishiyama, and S. Petitgirard (2007), Serpentine Rheology and Dehydration at high-pressure, implications for intermediate-depth seismicity, *Science, 318,* 1910-1913.

Hippchen, S., and R. D. Hyndman (2008), Thermal and structural models of the Sumatra subduction zone: Implications for the megathrust seismogenic zone, *Journal of Geophysical Research*, *113*(B12), 1-12, doi:10.1029/2008JB005698.

Hirth, G., and D. L. Kohlstedt (1996), Water in the oceanic upper mantle: implications for rheology, melt extraction and the evolution of the lithosphere, *Earth and Planetary Science Letters*, *144*, 93-108.

Hofmann-Wellenhof, B., B. H. Lichtenegger, and J. Collins (2001), *Global Positioning Theory and Practice*, Springer, Wien New York.

Hollister, L., and C. Andronicos (2006), Formation of new continental crust in Western British Columbia during transpression and transtension, *Earth and Planetary Science Letters*, *249*(1-2), 29-38, doi:10.1016/j.epsl.2006.06.042.

Horn, J. R., R. M. Clowes, R. M. Ellis, and D. N. Bird (1984), The seismic structure across an active oceanic/continental transform fault zone, *J. Geophys. Res.*, *89*, 3107-3120.

Hsu, Y.-J., M. Simons, J.-P Avouac, J. Galetzka, K. Sieh, M. Chlieh, D. Natawidjaja, L. Prawirodirdjo, Y. Bock (2006), Frictional afterslip following the 2005 Nias-Simeulue earthquake, Sumatra, *Science, 312*, 1921-1926.

Hu, Y. (2004), Three-dimensional viscoelastic finite element model for postseismic deformation of the great 1960 Chile earthquake, *J. Geophys. Res.*, *109*(B12), 1-14, doi:10.1029/2004JB003163.

Hu, Y. (2011), Deformation processes in great subduction zone earthquake cycles, PhD Thesis, University of Victoria.

Hutchison, I. (1985), The effects of sedimentation and compaction on oceanic heatflow, *Geophys. J. R. Astron. Soc., 82*, 439– 459.

Hyndman, R. D., R. P. Riddihough, and R. Herzer (1979), The Nootka Fault Zone - a new plate boundary off western Canada, *Geophysical Journal International*, *58*(3), 667-683, doi:10.1111/j.1365-246X.1979.tb04801.x.

Hyndman, R. D., and R. M. Ellis (1981), Queen Charlotte fault zone: Microearthquakes from a temporary array of land stations and ocean bottom seismographs, *Can. J. Earth Sci.*, *18*, 776-788.

Hyndman, R. D., and G. Rogers (1981), Seismicity surveys with Ocean Bottom Seismographs off Western Canada, *J. Geophys. Res., 86,* 3867-3880.

Hyndman, R. D., T. J. Lewis, J. A. Wright, M. Burgess, D. S. Chapman, and M. Yamano (1982), Queen Charlotte fault zone: Heat flow measurements, *Can. J. Earth Sci.*, *19*, 1657-1669.

Hyndman, R. D., and T. S. Hamilton (1993), Queen Charlotte Area Cenozoic Tectonics and Volcanism and Their Association With Relative Plate Motions Along the Northeastern Pacific Margin, *J. Geophys. Res.1*, *98*(B8), 14,257-14,277.

Hyndman, R. D., and K. Wang (1993), Thermal constraints on the zone of major thrust earthquake failure: The Cascadia subduction zone, *J. Geophys. Res.*, *98*, 2039–2060.

Hyndman, R. D., and K. Wang (1995), The rupture zone of Cascadia great earthquakes from current deformation and the thermal regime, *J. Geophys. Res.*, *100*, 22,133–22,154.

Hyndman, R.D., K. Wang, and M. Yamano (1995), Thermal constraints to the seismogenic portion of the southwestern Japan subduction thrust, *J. Geophys. Res., 100*, 15,373-15,392.

Hyndman, R.D., M. Yamano, and D.A Oleskovich (1997), The seismogenic zone of subduction thrust faults: *The Island Arc*, *6*, 244-260

Hyndman, R., C. Currie, S. Mazzotti, and a Frederiksen (2009), Temperature control of continental lithosphere elastic thickness, Te vs Vs, *Earth and Planetary Science Letters*, *277*(3-4), 539-548, doi:10.1016/j.epsl.2008.11.023.

Irving, E. (2000), Evolution of the Queen Charlotte Basin; further paleomagnetic evidence of Tertiary extension and tilting, *Tectonophysics*, *326*(1-2), 1-22, doi:10.1016/S0040-1951(00)00143-8.

Irving, E., and M. T. Brandon (1990), Paleomagnetism of the Flores volcanics, Vanocuver Island, in place by Eocene time, *Can. J. Earth Sci.*, *27*, 811-817.

Irving, E., J. G. Souther, and J. Baker (1992), Tertiary extension and tilting in the Queen Charlotte Islands, evidence from dyke swarms and their paleomagnetism, *Can. J. Earth Sci.*, *29*, 1878-1898.

Ishii, M., P. M. Shearer, H. Houston, and J. E. Vidale (2005), Rupture extent, duration, and speed of the 2004 Sumatra-Andaman earthquake imaged by the Hi-Net array, *Nature*, *435*, 933– 936.

Ivins, E. R. (1996), Transient creep of a composite lower crust: 2 a Polymineralic Basis for rapidly evolving postseismic deformation modes, *J. Geophys. Res.*, *101*, 28005-28028.

James, T. S., E. J. Gowan, I. Wada, and K. Wang (2009), Viscosity of the asthenosphere from glacial isostatic adjustment and subduction dynamics at the northern Cascadia subduction zone, British Columbia, Canada, *Journal of Geophysical Research*, *114*(B4), 1-13, doi:10.1029/2008JB006077.

Johnson, K. M., G. E. Hilley, and R. Bürgmann (2007), Influence of lithosphere viscosity structure on estimates of fault slip rate in the Mojave region of the San Andreas fault system, *J. Geophys. Res., 112,* B07408, doi:10.1029/2006JB004842.

Johnston, S. T. (2008), The Cordilleran Ribbon Continent of North America, *Annual Review of Earth and Planetary Sciences*, *36*(1), 495-530, doi:10.1146/annurev.earth.36.031207.124331.

Karato, S., and P. Wu (1993), Rheology of the upper mantle: A synthesis, *Science*, *260*, 771-778.

Kaufman, P., and L. Royden (1994), Lower crustal flow in an extensional setting: Constraints from the Halloran Hills region, eastern Mojave Desert, California, *J. Geophys. Res., 99*, 15,723– 15,739.

Kieckhefer, R. M., G. G. Shor, J. R. Curray, W. SugiarTa, and F. Hehuwat (1980), Seismic refraction studies of the Sunda Trench and forearc basin, *J. Geophys. Res.*, *85*, 863-890.

Klingelhoefer, F., M.-A. Gutscher, S. Ladage, J.-X. Dessa, D. Graindorge, D. Franke, C. André, H. Permana, T. Yudistira, A. Chauhan (2010), Limits of the seismogenic zone in the epicentral region of the 26 December 2004 great Sumatra-Andaman earthquake: Results from seismic refraction and wide-angle reflection surveys and thermal modeling, *J. Geophys. Res.,* doi10.1029/2009JB006569.

Kopp, H., E. R. Flueh, D. Klaeschen, J. Bialas, and C. Reichert (2001), Crustal structure of the central Sunda margin at the onset of oblique subduction, *Geophys. J. Int., 147*, 449-474.

Krishna, K.S., D Gopala Rao, M. V. Ramana, V. Subrahmanyam, K.V.L.N.S. Sarma, A.I. Pilipenko, V.S. Shcherbakov, I.V. Radhakrishna Murthy (1995), Tectonic model for the evolution of oceanic crust in the northeastern Indian Ocean from the Late Cretaceous to the early Tertiary, *J. Geophys. Res*., *100*, 20011-20024.

Kruger, F., and M. Ohrnberger (2005), Tracking the rupture of the Mw = 9.3 Sumatra earthquake over 1,150 km at teleseismic distance, *Nature*, *435*, 937– 939.

Lachenbruch, A.H. (1968), Preliminary geothermal model of the Sierra Nevada, *J. Geophys. Res*., *73*, 6977-6989.

Lallemand, S., A. Heuret, and D. Boutelier (2005), On the relationships between slab dip, back-arc stress, upper plate absolute motion, and crustal nature in subduction zones, *Geochem. Geophys. Geosyst., 6*, Q09006, doi:10.1029/2005GC000917.

Lay, T., H. Kanamori, C. J. Ammon, M. Nettles, S. N. Ward, R. C. Aster, S. L. Beck, S. L. Bilek, M. R. Brudzinski, R. Butler, H. R. DeShon, G. Ekstroem, K. Satake, and S. Sipkin (2005), The great Sumatra-Andaman earthquake of 26 December 2004, *Science*, *308*, 1127-1133.

Leonard, L.J., R.D. Hyndman, and S. Mazzotti (2004), Coseismic subsidence in the 1700 great Cascadia earthquake: Coastal estimates versus elastic dislocation models. *Geological Soc. Am. Bulletin, 116*, doi: 10.1130/B25369.2.

Lewis, P. D., R. G. Anderson, C. J. Hickson, and R. I. Thompson (1991), Triassic to Neogene geologic evolution of the Queen Charlotte region1, *Earth*, *869*, 854-869.

Lewis, T. J., A. M. Jessop, and A. S. Judge (1985), Heat flux measurements in southwestern British Columbia : the thermal consequences of plate tectonics1, *Can. J. Earth Sci*, *22*, 1262-1273.

Lewis, T. J., C. Lowe, and T. S. Hamilton (1997), Continental signature of a ridge-trench-triple junction: Northern Vancouver Island, *J. Geophys. Res.*, *102*, 7767-7781.

Linde, A. T., and P. G. Silver (1989), Elevation Changes and the great 1960 Chilean earthquake: support for aseismic slip, *Geophysical Research Letters*, *16*(11), 1305-1308.

Lonsdale, P. (1991), Structural Patterns of the Pacific Floor offshore of Peninsular California, in *Gulf and Peninsular Province of the Californias*, pp. 87-143.

Lowe, C., and S. A. Dehler (1995), Crustal thickness beneath the Queen Charlotte Basin, Canada: Results of a seismically constrained gravity inversion, *J. Geophys. Res.*, *100*(B12), 24,331-24,345.

Mackie, D. J., R. M. Clowes, S. A. Dehler, R. M. Ellis, and P. M.-a-l Huissier (1989), The Queen Charlotte Islands refraction project . Part 11 . Structural model for transition from Pacific plate to North American plate ', *Earth*, *1725*, 1713 - 1725.

Mahoney, J. B., P. S. Mustard, J. W. Haggart, R. M. Friedman, C. M. Fanning, V. J. Mcnicoll, and B. C. Va (1999), Archean zircons in Cretaceous strata of the western Canadian Cordillera : The " Baja B . C ." hypothesis fails a " crucial test ," *Geology*, doi:10.1130/0091-7613(1999)027<0195.

Marone,C. and Scholz,C.H. (1988), The depth of seismic faulting and the upper transition from stable to unstable slip regimes, *Geophys. Res. Lett.*, *15*, 621-624.

Mazzotti, S., H. Dragert, J. Henton, M. Schmidt, R. Hyndman, T. James, M. Craymer (2003a), Current tectonics of Northern Cascadia from a decade of GPS measurements, *J. Geophys. Res.*, *108*, doi: 10.1029/2003JB002653.

Mazzotti, S., R. D. Hyndman, P. Flueck, A. J. Smith, and M. Schmidt (2003b), Distribution of the Pacific/North America motion in the Queen Charlotte Islands-S. Alaska plate boundary zone, *Geophysical Research Letters*, *30*(14), 1762.

Mazzotti, S., T. S. James, J. Henton, and J. Adams (2005), GPS crustal strain, postglacial rebound, and seismic hazard in eastern North America: The Saint Lawrence valley example, *J. Geophys. Res.*, *110*(B11), 1-16, doi:10.1029/2004JB003590.

Mazzotti, S., L. J. Leonard, and J. F (2008), Tectonics , dynamics , and Seismic Hazard in the Canada – Alaska cordillera, *Earthquake*, 297-320.

McCaffrey, R. (2005), Block kinematics of the Pacific–North America plate boundary in the southwestern United States from inversion of GPS, seismological, and geologic data, *J. Geophys. Res.*, *110*(B7), 1-27, doi:10.1029/2004JB003307.

McCaffrey, R., M. D. Long, C. Goldfinger, P. C. Zwick, J. L. Nabelek, C. K. Johnson, and C. Smith (2000), Rotation and plate locking at the Southern Cascadia Subduction Zone, *Geophysical Research Letters*, *27*(19), 3117, doi:10.1029/2000GL011768.

Melosh, H. J., and A. Raefsky (1981), A simple and efficient method for introducing faults into finite element computations, *Bull. Seismol. Soc. Am.*, *71*(5), 1391-1400.

Michel, G. W., Y. Q. Yu, S. Y. Zhu, C. Reigber, M. Becker, E. Reinhart, W. Simons, B. Ambrosius, C. Vigny, N. Chamot-Rooke, X. Le Pichon, P. Morgan, and S. Matheussen (2001), Crustal motion and block behaviour in SE-Asia from GPS measurements, *Earth Planet. Sci. Lett. 187***,** 239–244.

Miller, M. M., D. J. Johnson, C. M. Rubin, H. Dragert, K. Wang, A. Qamar, and C. Goldfinger (2001), GPS-determination of along-strike variation in Cascadia margin kinematics: Implications for relative plate motion, Subduction zone coupling, and permanent deformation, *Tectonics*, *20*(2), 161-176.

Molnar, P., and P. England (1990),Temperatures, heat flux, and frictional stress near major thrust faults, *J. Geophys. Res*, *95*, 4833-4856.

Monger, J. W. H., R. A. Price, and D. J. Tempelman-Kluit (1982), Tectonic accretion and the origin of the two major metamorphic and plutonic welts in the Canadian Cordillera, *Geology*, *10*(2), 70-75.

Moore, G. F., and J. R. Curray (1980), Structure of the Sunda Trench lower slope off Sumatra from multichannel seismic reflection data, *Marine Geophysical Researches, 4*, 319-340.

Moore, D. E., D. A. Lockner, S. Ma, R. Summers, and J. D. Byerlee (1997), Strength of serpentinite gouges at elevated temperatures, *J. Geophys. Res., 102*, 14787-14801.

Moore, J.C. and D. Saffer (2001), Updip limit of the seismogenic zone beneath the accretionary prism of southwest Japan: An effect of diagenetic to low-grade metamorphic processes and increasing effective stress, *Geology*, *29,* 183-186.

Moore, J.C., C. Rowe, and F. Meneghini (2007), How accretionary prisms elucidate seismogenesis in subduction zones, in *The Seismogenic Zone of Subduction Thrust Faults*, edited by T.H. Dixon and J.C. Moore, pp.15-40, Columbia University Press.

Mueller, R.D. W.R. Roest, J.-Y. Royer, L.M. Gahagan, and J.G. Sclater (1997), Digital isochrones of the world's ocean floor, *J. Geophys. Res. 102,* 3211.

Muller, J. E. (1977), Evolution of the Pacific Margin, Vancouver Island and adjacent regions, *Can. J. Earth Sci.1*, *14*, 2062-2085.

Natawidjaja, D. H., K. Sieh, M. Chlieh, J. Galetzka, B. W. Suwargadi, H. Cheng, R. L. Edwards, J.-P Avouac, and S. N. Ward, (2006), Source parameters of the great Sumatran megathrust earthquakes of 1797 and 1833 inferred from coral microatolls, *J. Geophys. Res*., *111*, B06403.

Natawidjaja, D. H., K. Sieh, J. Galetzka, B. W. Suwargadi, H. Cheng, R. L. Edwards, and M. Chlieh (2007), Interseimsic deformation above the Sunda megathrust recorded in corall microatolls of the Mentawai islands, West Sumatra, *J. Geophys. Res*., *112*, B02404.

Newcomb, K. R., and McCann, W.R. (1987), Seismic history and seismotectonics of the Sunda Arc, *J. Geophys. Res., 92*, 421-440.

Ni, S., H. Kanamori, and D. Helmberger (2005), Energy radiation from the Sumatra earthquake: *Nature*, *434*, 582.

Niell, A. E. (1996), Global Mapping functions for the atmosphere delay at radio wavelength, *J. Geophys. Res.*, *10*(B2), 3227-3246.

Nur, A., and G. Mavko (1974), Postseismic viscoelastic rebound, *Science, 183*, 204-206.

Oleskovich, D.A., R.D. Hyndman, and K. Wang (1999), The updip and downdip limits to great subduction earthquakes: Thermal and structural models of Cascadia, south Alaska, SW Japan, and Chile, *J. Geophys. Res*., *104*, 14965-14992.

Ortiz, M., and R. Bilham (2003), Source area and rupture parameters of the 31 December 1881 MW=7.9 Car Nicobar earthquake estimated from tsunamis recorded in the Bay of Bengal, *J. Geophys. Res., 108*, 2215-2231.

Peacock, S.M., (1990), Numerical simulation of metamorphic pressure-temperature-time paths and fluid productions in subducting slabs, *Tectonic*s, 9, 1197-1211.

Peacock, S.M. (1990), Fluid processes in subduction zones. *Science, 248*, 329−337

Peacock, S.M., and R.D. Hyndman (1999), Hydrous minerals in the mantle wedge and the maximum depth of subduction thrust earthquakes. *Geophysical Research Letters, 26***,** 2517–2520.

Peacock, S.M., and K. Wang (1999), Seismic consequences of warm versus cool subduction metamorphism: Examples from Southwest and Northeast Japan. *Science, 286*, 937–939.

Peltier, W. R. (1974), The impulse response of a Maxwell Earth, *Reviews of Geophysics*, *12*(4), 649, doi:10.1029/RG012i004p00649.

Plafker, G. (1972), Alaskan Earthquake of 1964 and Chilean Earthquake of 1960: Implications for Arc Tectonics, *J. Geophys. Res.*, *77*(5), 901-925, doi:10.1029/JB077i005p00901.

Pollitz, F., C. Wicks, and W. Thatcher (2001), Mantle flow beneath a continental strike-slip fault: Postseismic deformation after the 1999 Hector Mine earthquake, Science, 293, 1814– 1818.

Pollitz, F. (2003), Transient rheology of the uppermost mantle beneath the Mojave Desert, California, *Earth and Planetary Science Letters*, *215*(1-2), 89-104, doi:10.1016/S0012-821X(03)00432-1.

Prims, J., K. P. Furlong, K. M. M. Rohr, and R. Govers (1997), Lithospheric structure along the Queen Charlotte margin in western Canada: constraints from flexural modeling, *Geo-Marine Letters*, *17*(1), 94-99, doi:10.1007/s003670050013.

Reid, H. F. (1910), The mechanics of the earthquake, in *Report of the State InvestigationCommission*, p. 2, Carnegie Institute of Washington, Washington D.C.

Reinen, L.A., J. D. Weeks, and T.E. Tullis (1991), The frictional behaviour of Serpentinite: Implications for aseismic creep on shallow crustal faults, *Geophysical Research Letters*, *18,* 1921-1924.

Riddihough, R. (1984), Recent Movements of the Juan de Fuca Plate System, *Journal of Geophysical Research*, *89*(B8), 6980-6994, doi:10.1029/JB089iB08p06980.

Riddihough, R. P. (1977), A model for recent plate interactions off Canada's west coast, *Can. J. Earth Sci.*, *14*, 384-396.

Riddihough, R. P. (1980), Gorda plate motions from magnetic anomaly analysis, *Earth planet. Sci. Lett.*, *51*, 163-170.

Riddihough, R. P., R. G. Currie, and R. D. Hyndman (1980), The Dellwood Knolls and their role in triple junction tectonics off northern Vancouver Island, *Can. J. Earth Sci.*, *17*, 577-593.

Riddihough, R. P., and R. D. Hyndman (1989), Queen Charlotte Islands margin, in *The Geology of North America, vol. N, The Eastern Pacific Ocean and Hawaii*, edited by E. L. Winterer et al., pp. 403-411, Geol. Soc. of Am., Boulder.

Ristau, J., G. C. Rogers, and J. F. Cassidy (2002), Relative plate motions and stress orientation in western Canada from regional moment-tensor analysis, *Seismological Research Letters*, *73*, 261.

Ristau, J., G. C. Rogers, and J. F. Cassidy (2007), Stress in western Canada from regional moment tensor analysis, *Canadian Journal of Earth Sciences*, *44*(2), 127-148, doi:10.1139/E06-057.

Rivera, L., K. Sieh, D. Helmberger, and D. Natawidjaja (2002), A comparative study of the Sumatran subduction-zone earthquakes of 1935 and 1984, *Bull. Seism. Soc. Am.*, *92*, 1721-1736.

Rogers, G. C. (1986), Seismic gaps along the Queen Charlotte Fault, *Earthquake Prediction Res.*, *4*, 1-11.

Rohr, K. M. M., and A. J. Tryon (2010), Pacific - North America plate boundary reorganization in response to initiation of transpression : offshore Canada, *Geochemistry Geophysics Geosystems*, *11*(6), 1-23.

Rohr, K. M. M., and J. R. Dietrich (1992), Strike-slip tectonics and development of the Tertiary Queen Charlotte Basin, offshore western Canada: evidence from seismic reflection data, *Basin Research*, *4*(1), 1-20, doi:10.1111/j.1365-2117.1992.tb00039.x.

Rohr, K. M. M., M. Scheidhauer, and A. M. Trehu (2000), Transpression between two warm mafic plates: The Queen Charlotte Fault revisited, *J. Geophys. Res.2*, *105*, 8147-8172.

Rohr, K. M. M., and L. Currie (1997), Queen Charlotte basin and Coast Mountains : Paired belts of subsidence and uplift caused by a low-angle normal fault, *Geology*, doi:10.1130/0091-7613(1997)025

Rohr, K. M. M., and K. P. Furlong (1995), Ephemeral plate tectonics at the Queen Charlotte triple junction, *Geology*, *23*(11), 1035, doi:10.1130/0091-7613(1995)023

Rusmore, M. E., S. W. Bogue, K. Dodson, K. a Farley, and G. J. Woodsworth (2010), Deformation of continental crust along a transform boundary, Coast Mountains, British Columbia, *Tectonics*, *29*(4), doi:10.1029/2009TC002502.

Saffer, D. M., K. M. Frye, C. Marone, and K. Mair (2001), Laboratory results indicating complex and potentially unstable frictional behaviour of smectite clay, *Geophysical Research Letters, 28,* 2297– 2300.

Savage, J. C. (1983), Dislocation model of strain accumulation and release at a subduction zone, *J. Geophys. Res.*, *88*, 4984-4996.

Savage, J. C., and R. O. Burford (1973), Geodetic Determination of Relative Plate Motion in Central California, *J. Geophys. Res.*, *78*(5), 832-845.

Savage, J. C., and W. Prescott (1978), Asthenosphere Readjustment and the Earthquake Cycle ,*J. Geophys. Res., 83*, 3369-3376.

Scheidhauer, M. (1997), Crustal Structure of the Queen Charlotte transform fault zone from multichannel seismic reflection and gravity data, Master's Thesis, Oregon State University, 184 pp.

Schell, M., and L. Ruff (1989), Rupture of a seismic gap in southeastern Alaska: the 1972 Sitka earthquake (Ms 7.6), *Physics of the Earth and Planetary Interiors*, *54*(3-4), 241-257.

Scholz, C.H., and P.A. Cowie (1990), Determaination of total strain faulting using slip measurements, *Nature*, *346*, 837-839.

Sclater,G., and J. Francheteau (1970), The Implications of Terrestrial Heat Flow Observations on Current Tectonic and Geochemical Models of the Crust and Upper Mantle of the Earth, *Geophysical Journal International* ,*20*, 509–542.

Schmid, R., and M. Rothacher (2003), Estimation of elevation-dependent satellite antenna phase center variations of GPS satellites, *Journal of Geodesy*, *77*(77), 440-446.

Seno, T. (2005), Variation of downdip limit of the seismogenic zone near the Japanese islands: implications for the serpentinization mechanism of the forearc mantle wedge, *Earth and Planetary Science Letters*, *231*, 249-262.

Shelton, G., and J. Tullis (1981), Experimental flow laws for crustal rocks, *EOS Trans. AGU, Abstract*, *62*, 369.

Sieh, K., D. H. Natawidjaja, M. Chlieh, J. Galetzka, J. Avouac, B. W. Suwargadi, R. Edwards, and H. Cheng (2004), The giant subduction earthquake of 1797 and 1833, West Sumatra: Characteristic couplets, uncharacteristic slip, *Eos Trans. AGU, 85(47)*, Fall Meet. Suppl., Abstract T12B-04.

Simoes, M., J.P. Avouac, R. Cattin, and P. Henry (2004), The Sumatra subduction zone: A case for a locked fault zone extending into the mantle, *J. Geophys. Res., 109*, B10402, doi:10.1029/2003JB002958.

Simons, W. M. F., B.A.C. Ambrosius, R. Noomen, D. Angermann, P. Wilson, M. Becker, E. Reinhard, A. Walpersdorf, and C. Vigny (1999), Observing plate motions in South East Asia: Geodetic results of the GEODYSSEA Project. *Geophys. Res. Lett. 26*, 2081–2084.

Spence, G., and I. Asudeh (1993), Seismic velocity structure of the Queen Charlotte Basin beneath Hecate Strait, *Can. J. Earth Sci*, *30*, 787-805.

Spence, G., and D. T. Long (1995), Transition from oceanic to continental crustal structure : seismic and gravity models at the Queen Charlotte transform margin, *Earth*, *717*, 699-717.

Spindler, C., G. C. Rogers, and J. F. Cassidy (1997), The 1978 Brooks Peninsula , Vancouver Island Earthquakes, *Bull. Seismol. Soc. Am.*, *87*(4), 1011-1023.

Stein, S., and E. Okal (2205), Seismology: speed and size of the Sumatra earthquake, *Nature*, *434*, 581 (2005).

Stock, J. M., and P. Molnar (1988), Uncertainties and implications of the Cretaceous and Tertiary position of North America relative to Fallaron, Kula, and Pacific plates, *Tectonics*, *6*, 1339-1384.

Subarya, C., M. Chlieh, L. Prawirodirdjo, J.-P. Avouac, Y. Bock, K. Sieh, A. J. Meltzner. D. H. Natawidjaja, and R. McCaffrey (2006), Plate-boundary deformation associated with the great Sumatra-Andaman earthquake, *Nature*, *440*, 46-51.

Svarc, J. L. (2002), Strain accumulation and rotation in western Oregon and southwestern Washington, *Journal of Geophysical Research*, *107*(B5), doi:10.1029/2001JB000625.

Tichelaar, B.W. and L.J, Ruff (1993), Depth of seismic coupling along subduction zones, *J. Geophys. Res.*, *98*, 2017-2038.

Tranquilla, J. M., J. P. Carr, and H. M. Alrizzo (1994), Analysis of a choke ring groundplane for multipath control on Global Positioning System (GPS) applications, *Institute of Electrical and Electronics Engineers Transactions on Antennas and Propagation*, *42*(7), 905-911.

Tsai, V. C., M. Nettles, G. Ekstroem, and A. M. Dziewonski (2005), Multiple CMT source analysis of the 2004 Sumatra earthquake, *Geophys. Res. Lett.*, *32*, L17304.

Tse, S. T., and J.R. Rice (1986), Crustal earthquake instability in relation to the depth variation of frictional slip properties, *J. Geophys. Res., 91*, 9452-9472.

Underwood, M.B. (2007), Sediment inputs to subduction zones: why lithostratigraphy and clay matter, in *The Seismogenic Zone of Subduction Thrust Faults*, edited by T.H. Dixon and J.C. Moore, pp.42-85, Columbia University Press.

Von Herzen, R. P. (2004), Geothermal evidence for continuing hydrothermal circulation in older (>60 M.y.) ocean crust, in *Hydrology of the Oceanic Lithosphere*, edited by E. Davis and H. Elderfiled, pp. 414-447, Cambridge University Press.

Vrolijk, P. (1990), On the mechanical role of smectite in subduction zones, *Geology, 18*, 703-707.

Walcott, D. (1993), Neogene tectonics and kinematics of western North America, *Tectonics*, *12*(2), 326-333.

Walker, K. T., M. Ishii, and P. M. Shearer (2005), Rupture details of the 28 March 2005 Sumatra Mw 8.6 earthquake imaged with teleseismic P waves, *Geophys. Res. Lett., 32,* L23303.

Wang, C. Y. (1980), Sediment subduction and frictional sliding in a subduction zone, *Geology, 8,* 530– 533.

Wang, K., and E. E. Davis, (1992), Thermal Effects of marine sedimentation in hydrothermally active areas, *Geophys. J. Int.*, *110*, 70-78.

Wang, K., R.D. Hyndman, and E.E. Davis, (1993), Thermal effects of sediment thickening and fluid expulsion in accretionary prisms - Model and parameter analysis, *J. Geophys. Res.*, *98*, 9975-9984.

Wang, K., R.D. Hyndman, and M. Yamano (1995a), Thermal regime of the south-west Japan subduction zone: Effects of age history of the subducting plate, *Tectonophysics*, *248*, 53-69.

Wang, K., T. Mulder, G. C. Rogers, and R. D. Hyndman (1995b), Case for very low coupling stress on the Cascadia subduction fault, *J. Geophys. Res.*, *100*, 12907-12918.

Wang, K., J. He, H. Dragert, and T. S. James (2001), Three-dimensional viscoelastic interseismic deformation model for the Cascadia subduction zone, *Society*, *1991*(1999), 295-306.

Wang, K., R. Wells, S. Mazzotti, R. D. Hyndman, and T. Sagiya (2003), A revised dislocation model of interseismic deformation of the Cascadia subduction zone, *J. Geophys. Res.*, *108*, 2026, doi:10.1029/2001JB001227.

Wang, K. (2007), Elastic and viscoelastic models of crustal deformation in subduction earthquake cycles, in *The Seismogenic Zone of Subduction Thrust Faults*, edited by T.H. Dixon and J.C. Moore, pp.540-575, Columbia University Press.

Wells, R. E., S. C. Weaver, and R. J. Blakely (1998), Fore-arc migration in Cascadia and its neotectonic significance, *Geology*, *26*(8), 759-762.

Wheeler, J. O., and P. McFeely (1991), Tectonic assemblage map of the Canadian Cordillera and adjacent parts of the United States of America, *Map 1712A, Geological Survey of Canada*.

Wilks, K. R., and N. L. Carter (1990), Rheology of some continental lower crustal rocks, *Tectonophysics*, *182*(1-2), 57-77.

Wilson, D.S. (1993), Confidence interval for motion and deformation of the Juan de Fuca plate, *J. Geophys. Res*., *98* (B9), 16053-16071.

Yorath, C. J., and R. D. Hyndman (1983), Subsidence and thermal history of Queen Charlotte Basin, *Canadian Journal of Earth Sciences*, *20*(1), 135-159, doi:10.1139/e83-013.

Yuan, T., G. Spence, and R. D. Hyndman (1992), Structure beneath Queen Charlotte Sound from seismic-refraction and gravity interpretations, *Can. J. Earth Sci*, *29*, 1509–1529.

Zhang, Z., and S.Y. Schwartz (1992), Depth distribution moment release in underthrusting earthquakes at subduction zones, *J. Geophys. Res*., *97*, 537-544.

Appendix A
GPS Time-series for Campaign Data
Time-series for campaign GPS data 1999 -2008 using relative PCVs and orbits for the 1999 data

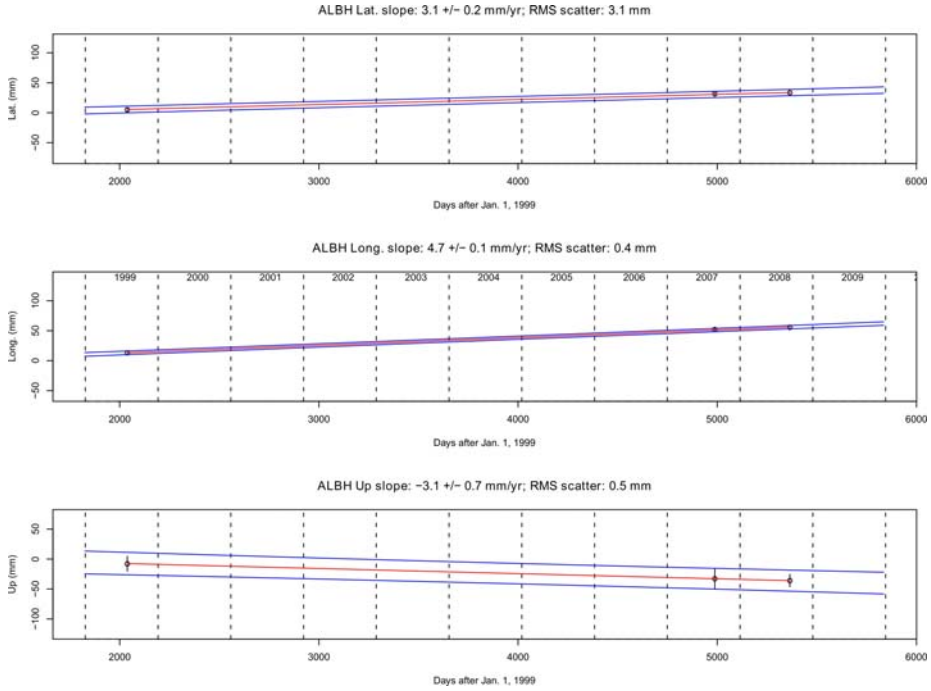

Figure A-65: Time-series for ALBH, reference station DRAO

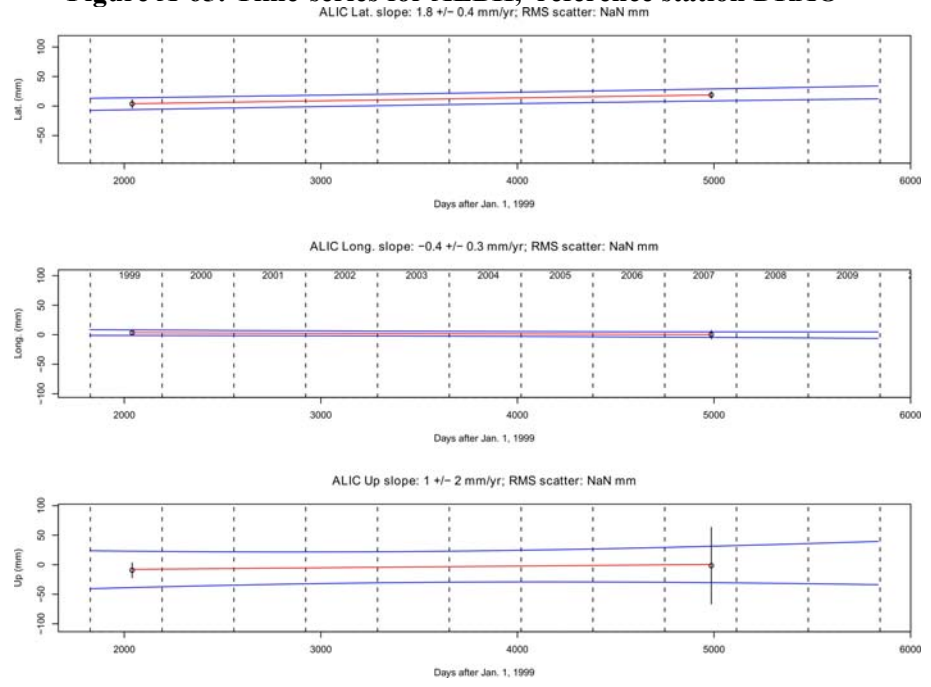

Figure A-66: Time-series for ALIC, reference station DRAO

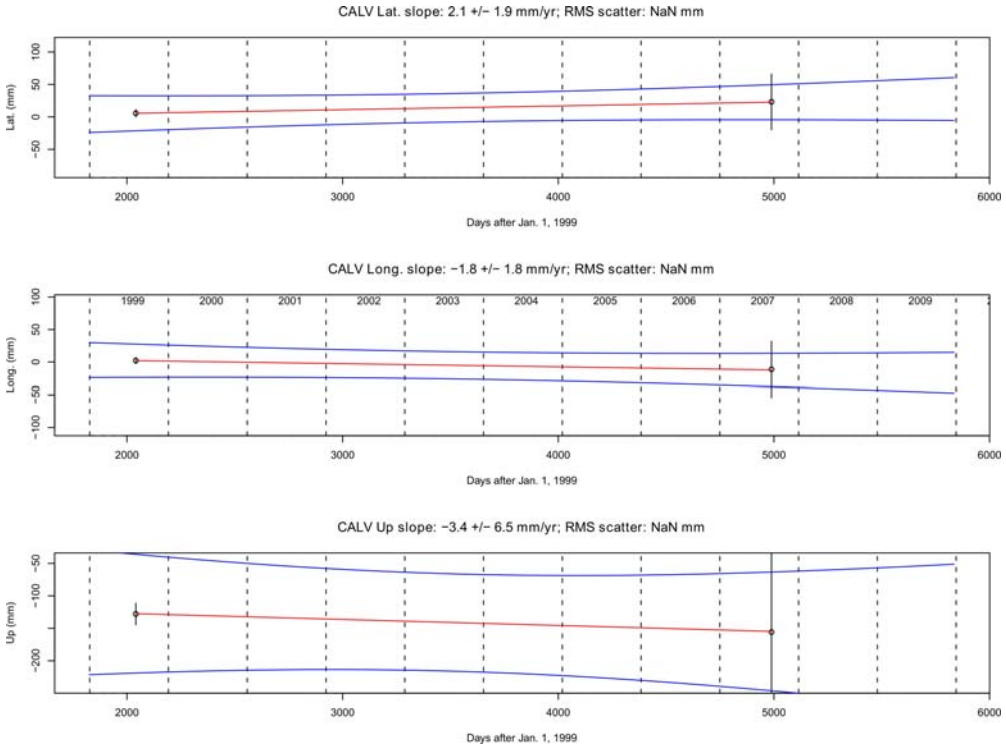

Figure A-67: Time-series for CALV, reference station DRAO

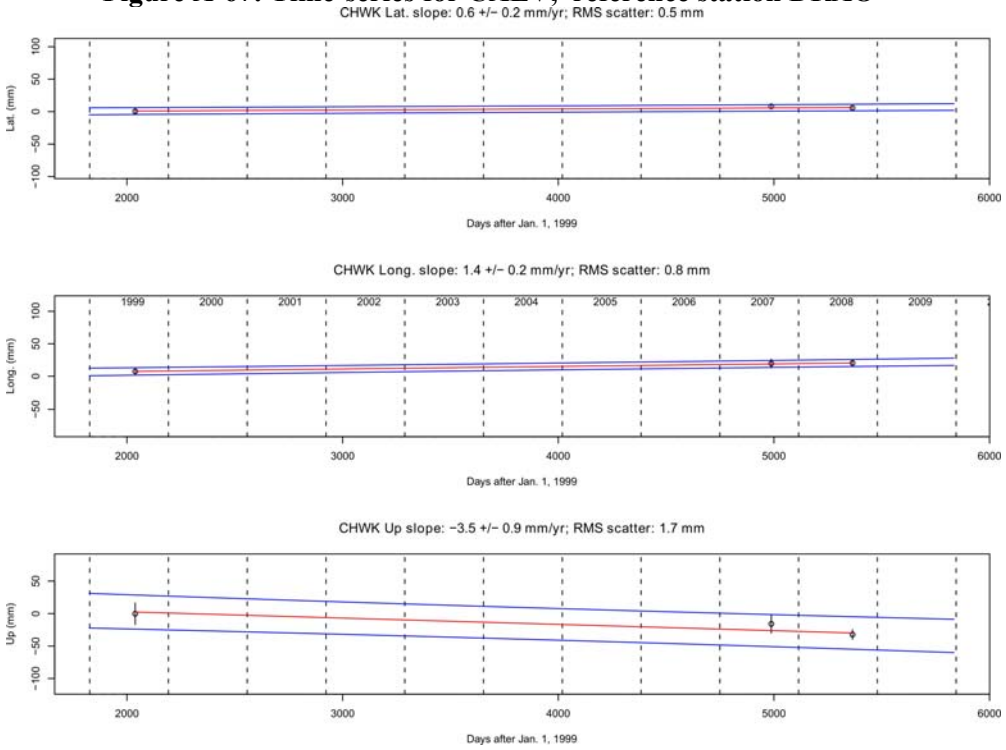

Figure A-68: Time-series for CHWK, reference station DRAO

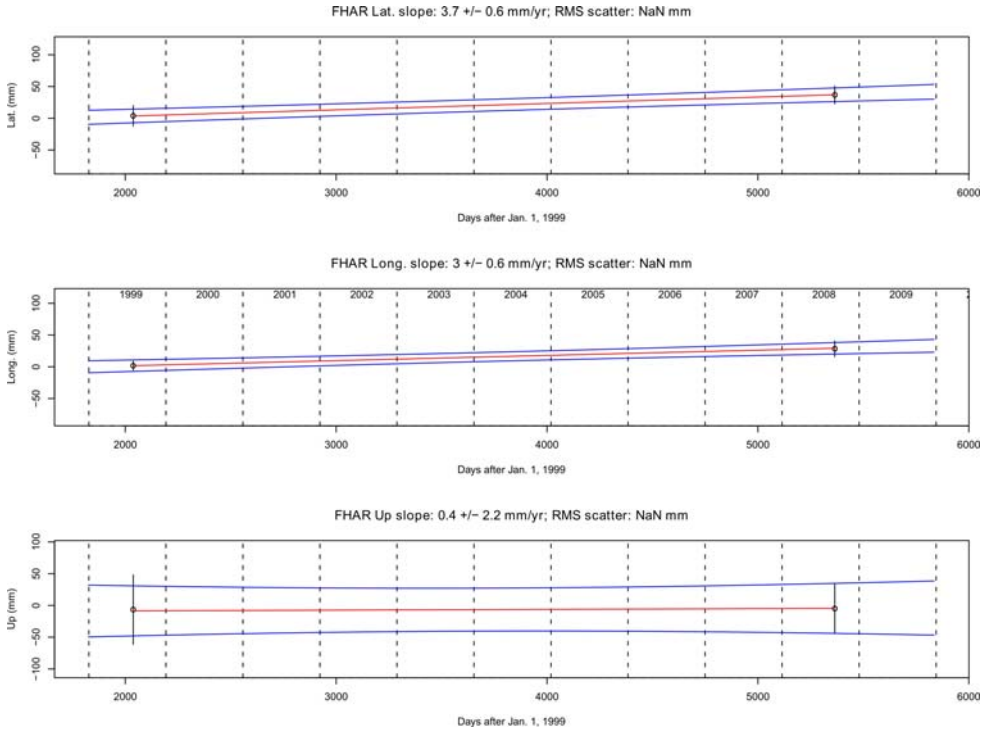

Figure A-69: Time-series for FHAR, reference station DRAO

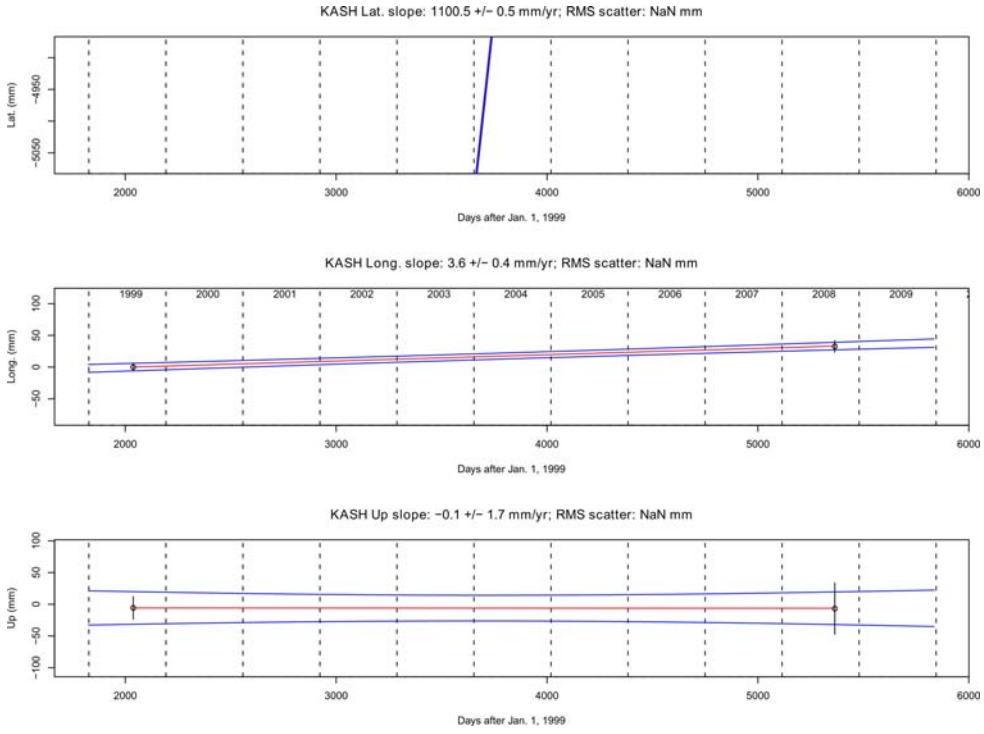

Figure A-70: Time-series for KASH, reference station DRAO

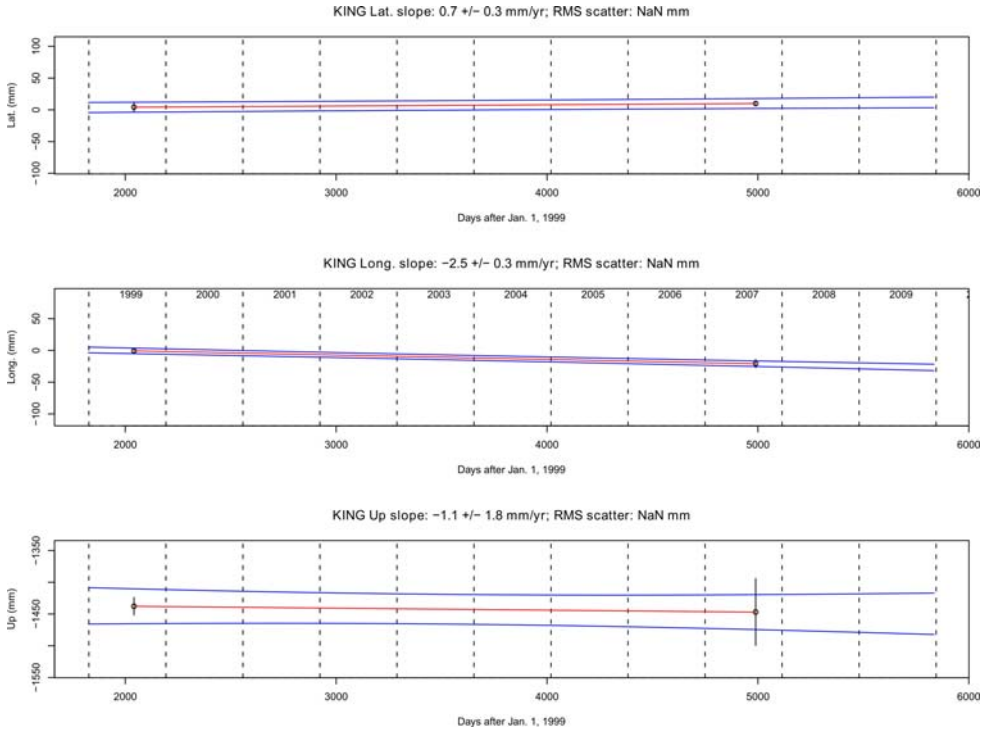

Figure A-71: Time-series for KING, reference station DRAO

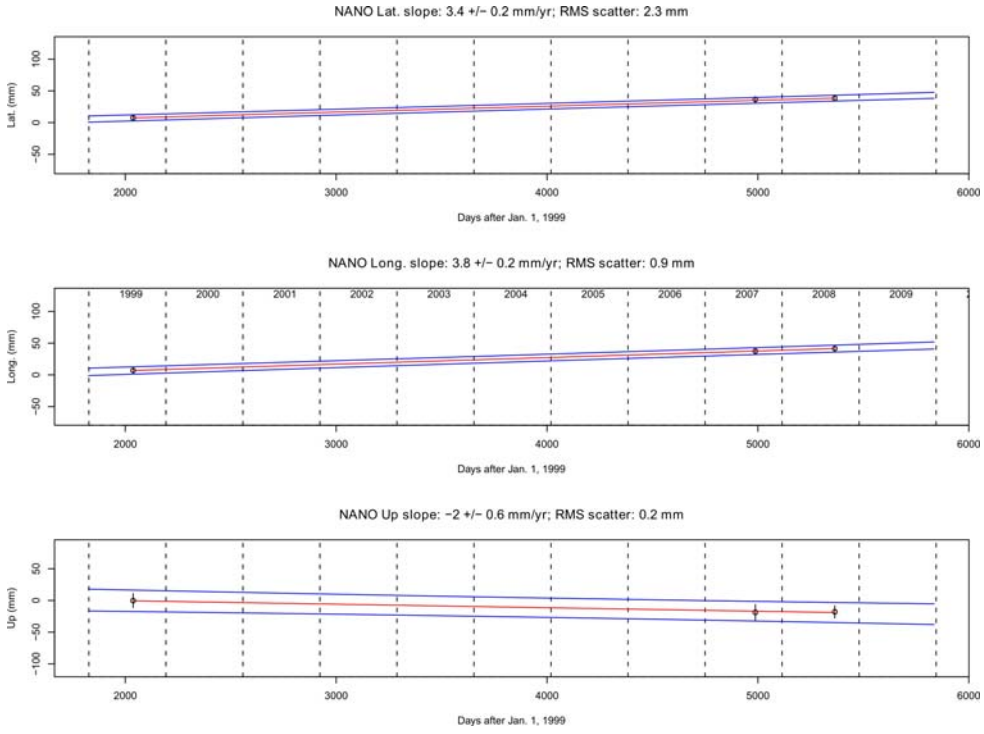

Figure A-72: Time-series for NANO, reference station DRAO

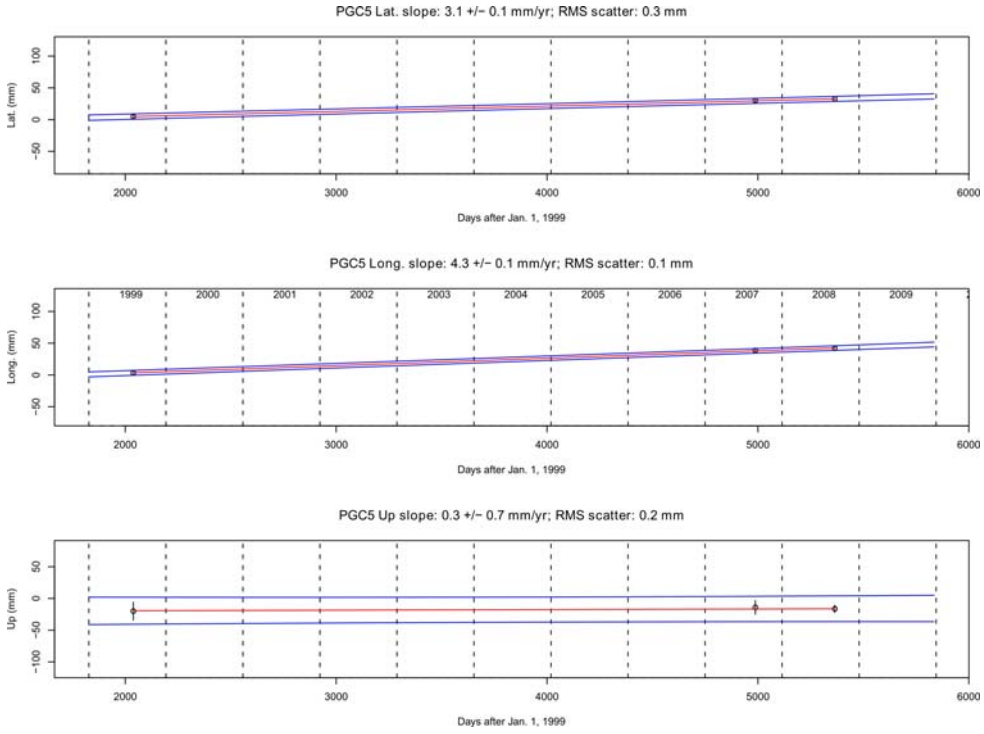

Figure A-73: Time-series for PGC5, reference station DRAO

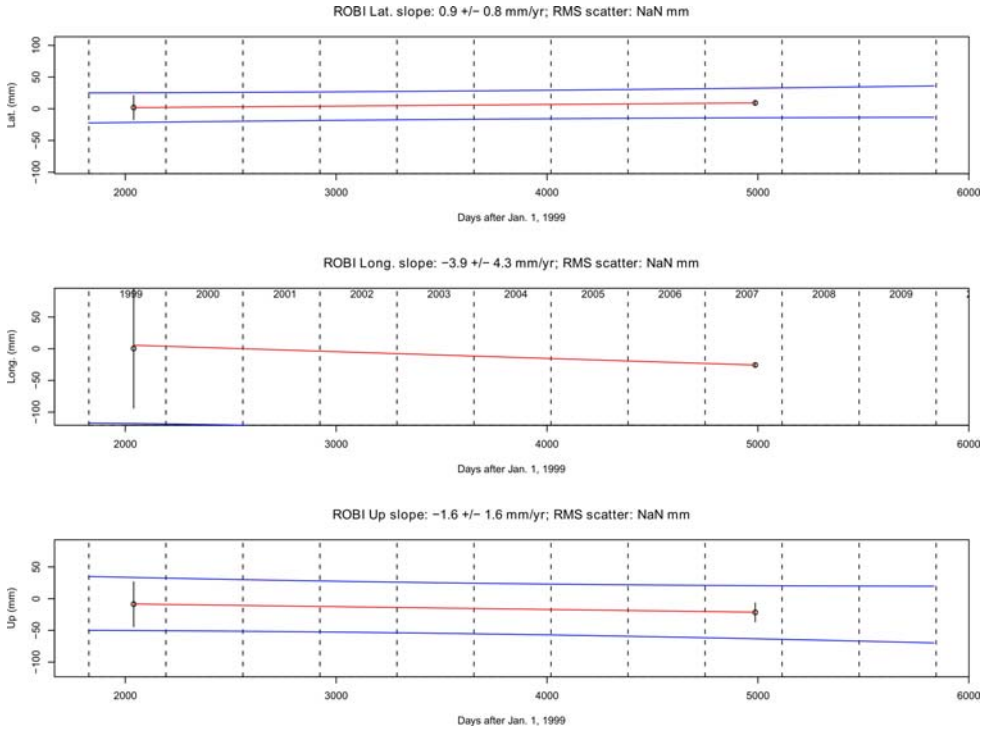

Figure A-74: Time-series for ROBI, reference station DRAO

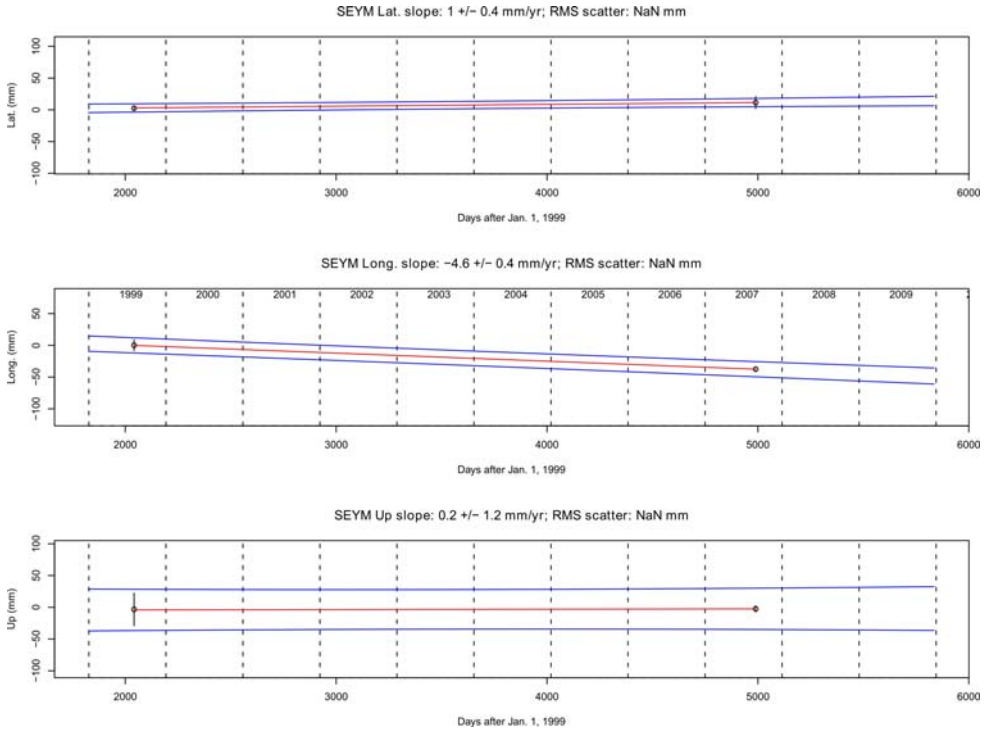

Figure A-75: Time-series for SEYM, reference station DRAO

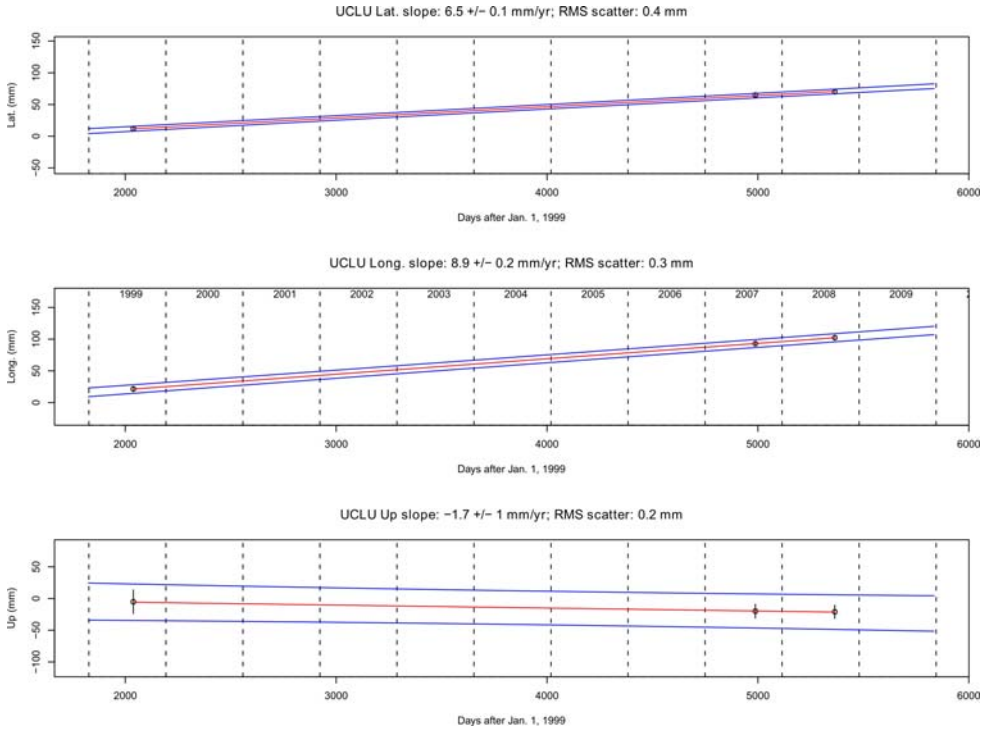

Figure A-76: Time-series for UCLU, reference station DRAO

Table A- 18: GPS site velocities for 1999 – 2008, relative PCVs and orbits for 1999 data

STATION	Latitude °N	Longitude °E	Vn [mm/yr]	Ve [mm/yr]	Vu [mm/yr]	σn [mm/yr]	σe [mm/yr]	σu [mm/yr]	Network
ALBH	48.39	236.51	3.1	4.7	-3.1	0.2	0.1	0.7	WCDA-PANGA
ALIC	50.46	232.48	1.8	-0.4	1	0.4	0.3	2	QCS
CALV	51.54	232.05	2.1	-1.8	-3.4	1.9	1.8	6.5	QCS
CHWK	49.16	237.99	0.6	1.4	-3.5	0.2	0.2	0.9	WCDA-PANGA
FHAR	50.08	232.83	3.7	3	0.4	0.6	0.6	2.2	QCS
KING	51.85	232.23	0.7	-2.5	-1.1	0.3	0.3	1.8	QCS
NANO	49.29	235.91	3.4	3.8	-2	0.2	0.2	0.6	WCDA-PANGA
PGC5	48.65	236.55	3.1	4.3	0.3	0.1	0.1	0.7	WCDA-PANGA
ROBI	51.19	232.40	0.9	-3.9	-1.6	0.8	4.3	1.6	QCS
SEYM	51.46	232.72	1	-4.6	0.2	0.4	0.4	1.2	QCS
UCLU	50.68	231.67	6.5	8.9	-1.7	0.1	0.2	1	WCDA-PANGA
WILL	52.24	237.83	-0.3	-1.7	1.4	0.1	0.2	0.6	WCDA-PANGA
WSLR	50.13	237.08	0.6	1.6	-1.5	0.2	0.2	1	WCDA-PANGA

Time-series for campaign GPS data 1999 -2008 using absolute PCVs and orbits for the 1999 data

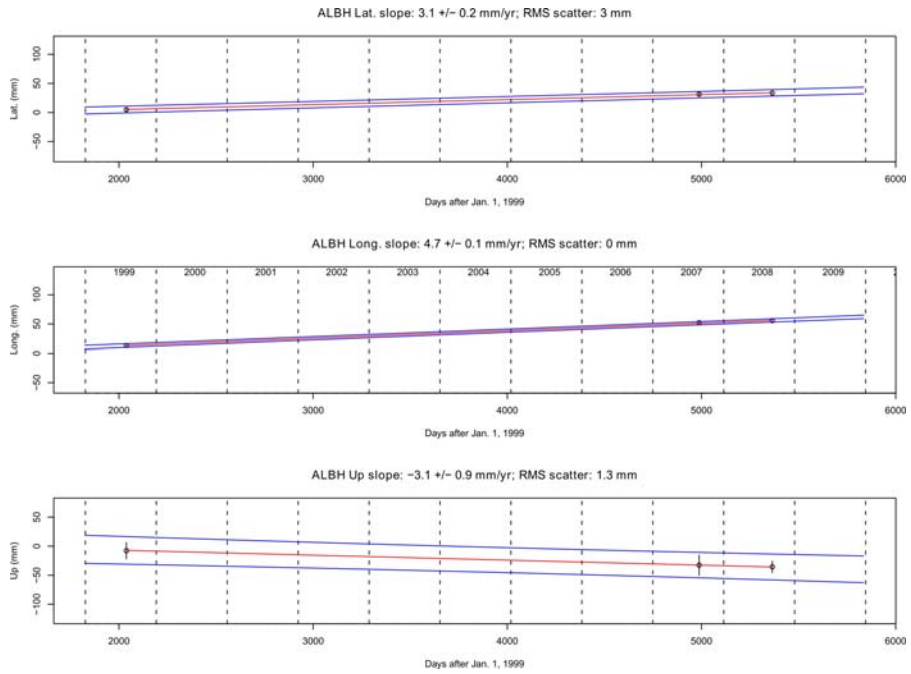

Figure A-77: Time-series for ALBH, reference station DRAO

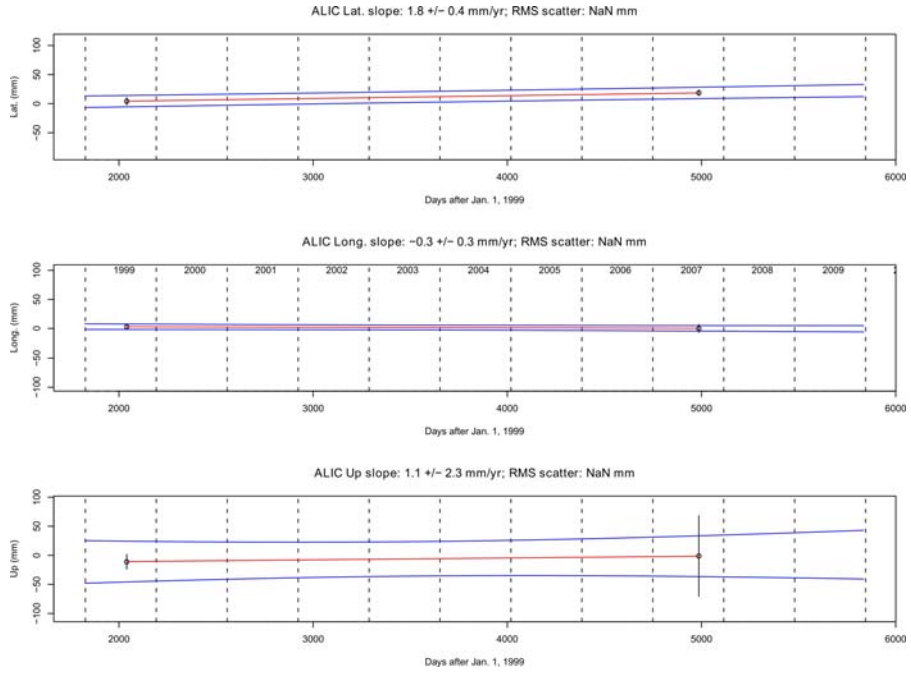

Figure A-78: Time-series for ALIC, reference station DRAO

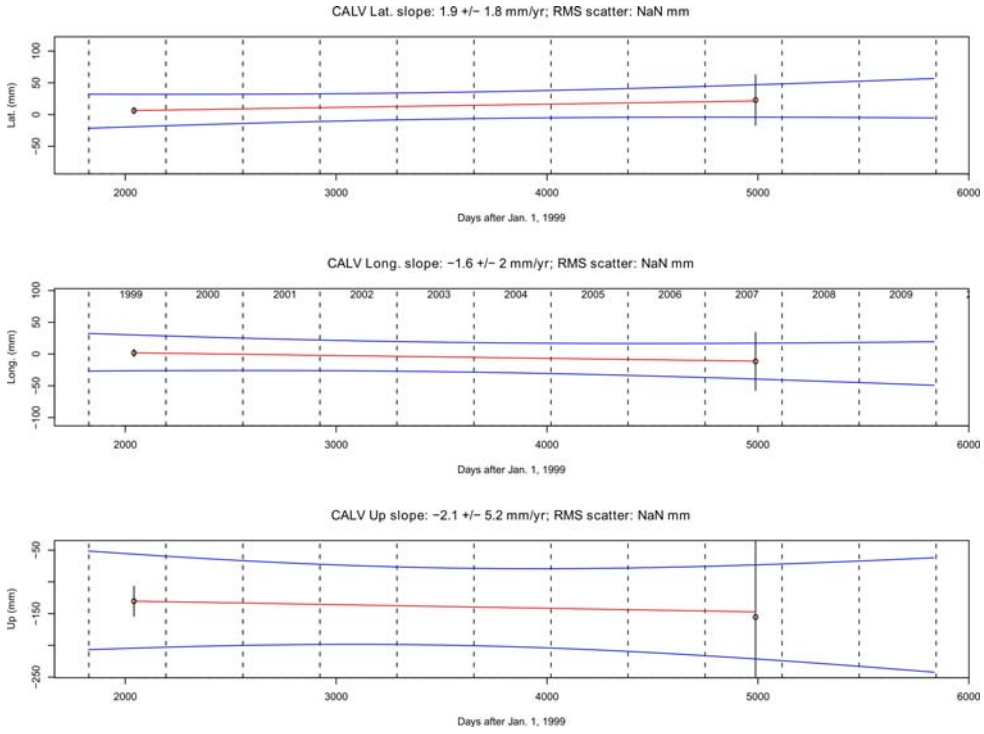

Figure A-79: Time-series for CALV, reference station DRAO

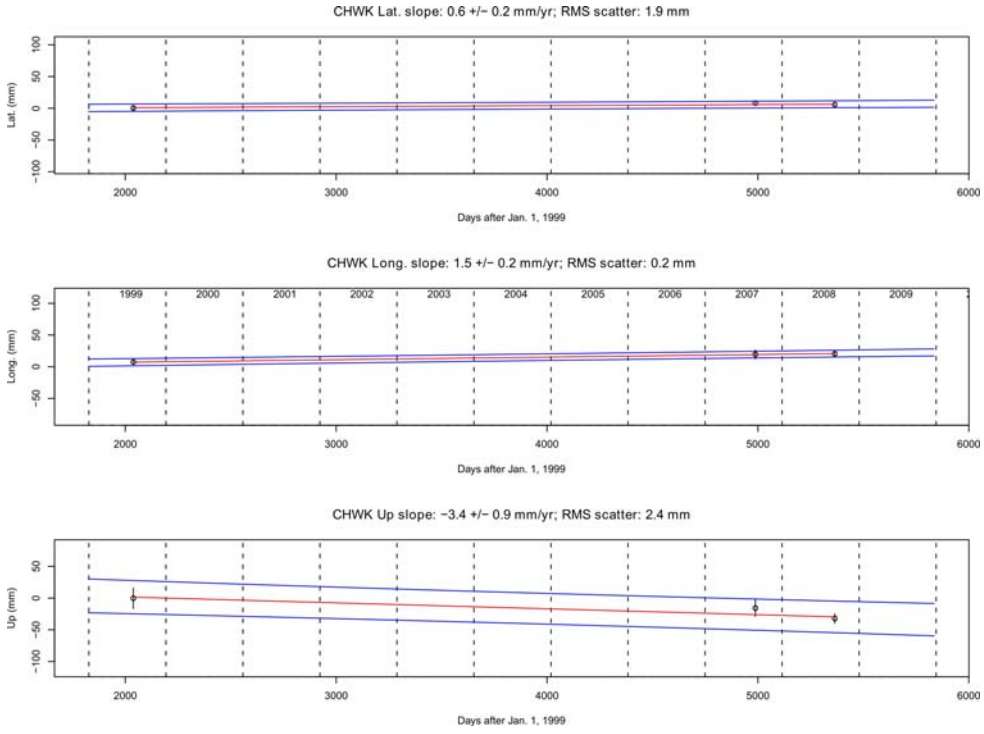

Figure A-80: Time-series for CHWK, reference station DRAO

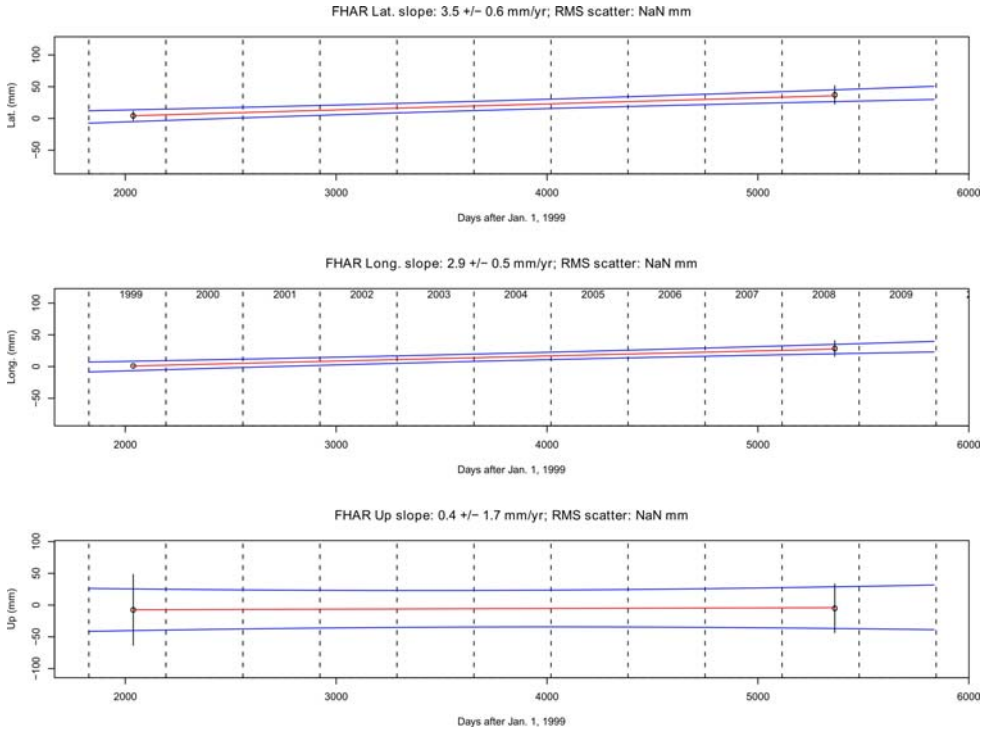

Figure A-81: Time-series for FHAR, reference station DRAO

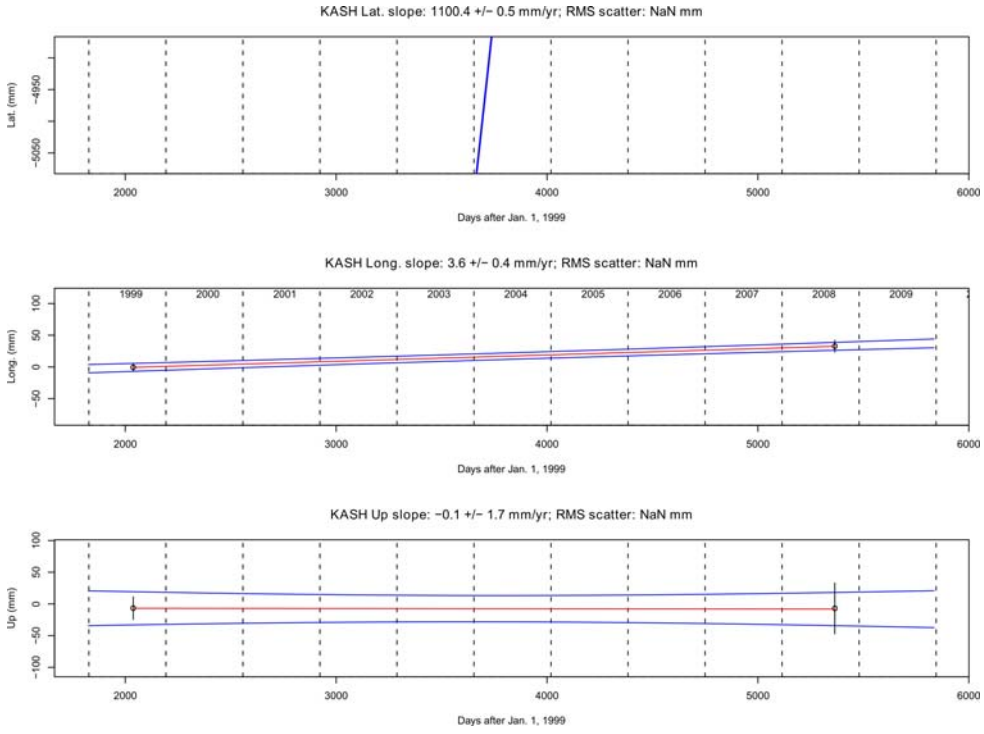

Figure A-82: Time-series for KASH, reference station DRAO

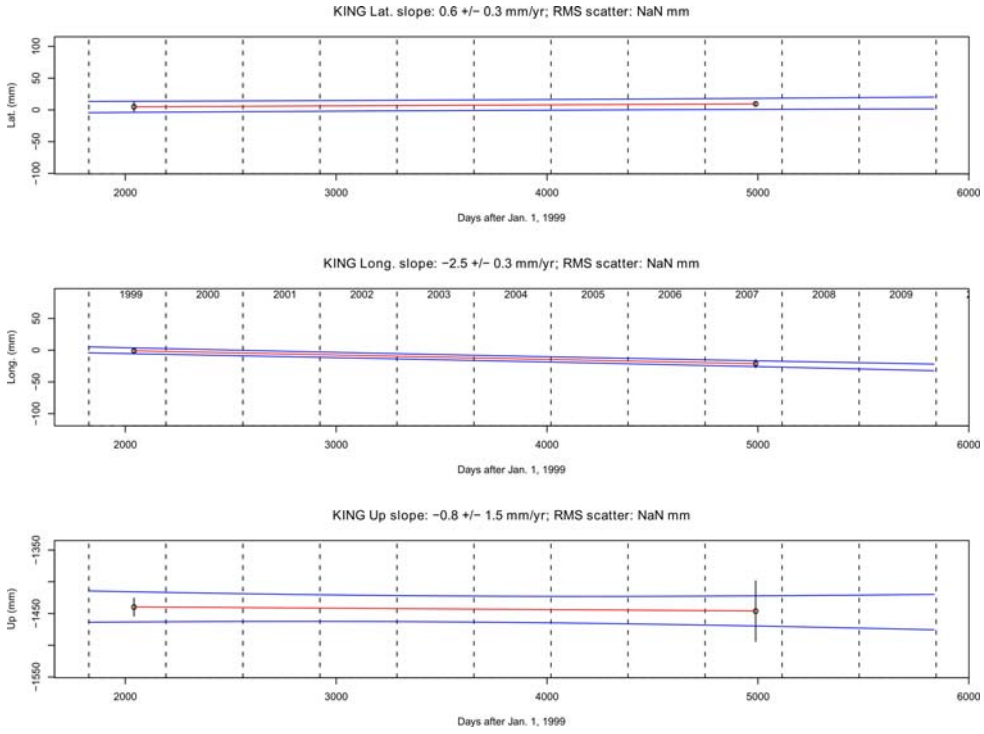

Figure A-83: Time-series for KING, reference station DRAO

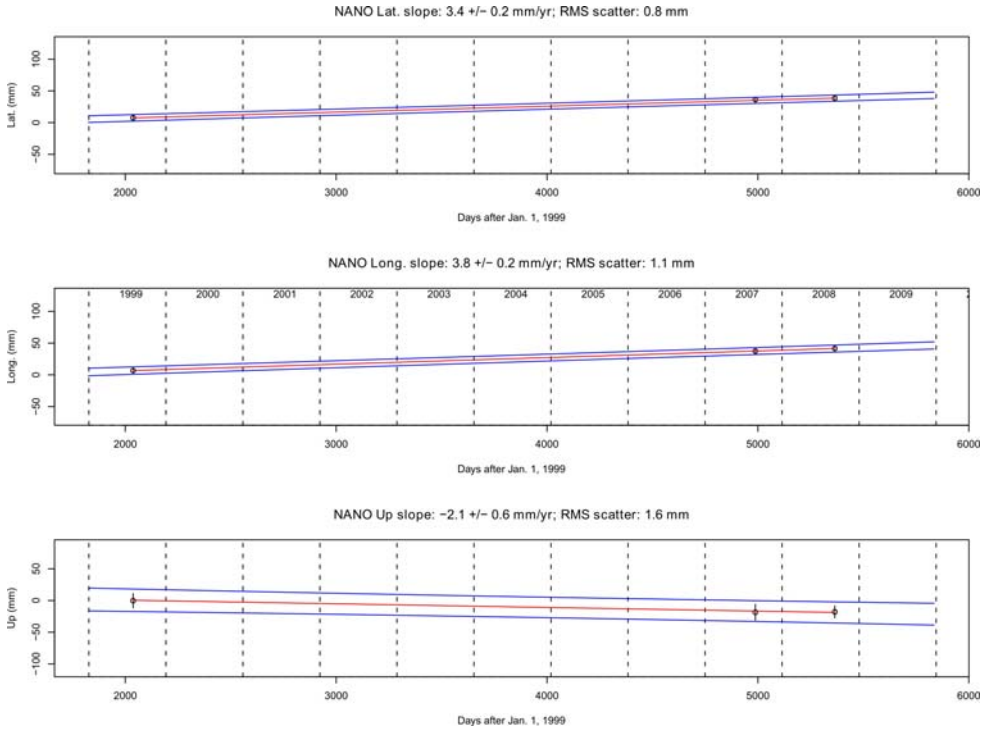

Figure A-84: Time-series for NANO, reference station DRAO

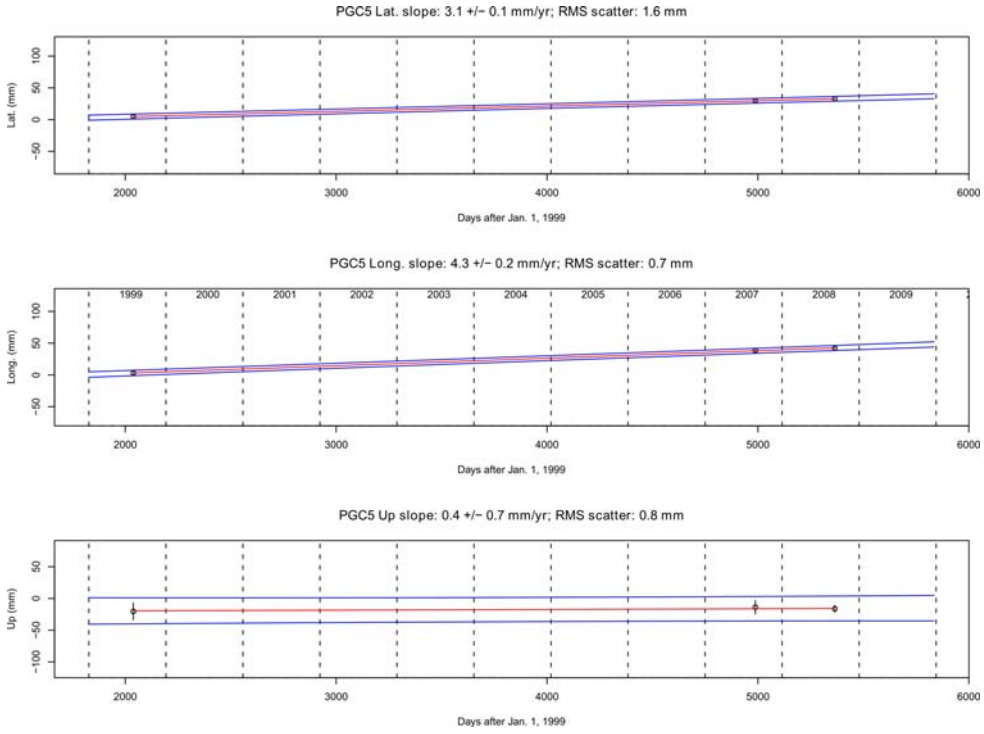

Figure A-85: Time-series for PGC5, reference station DRAO

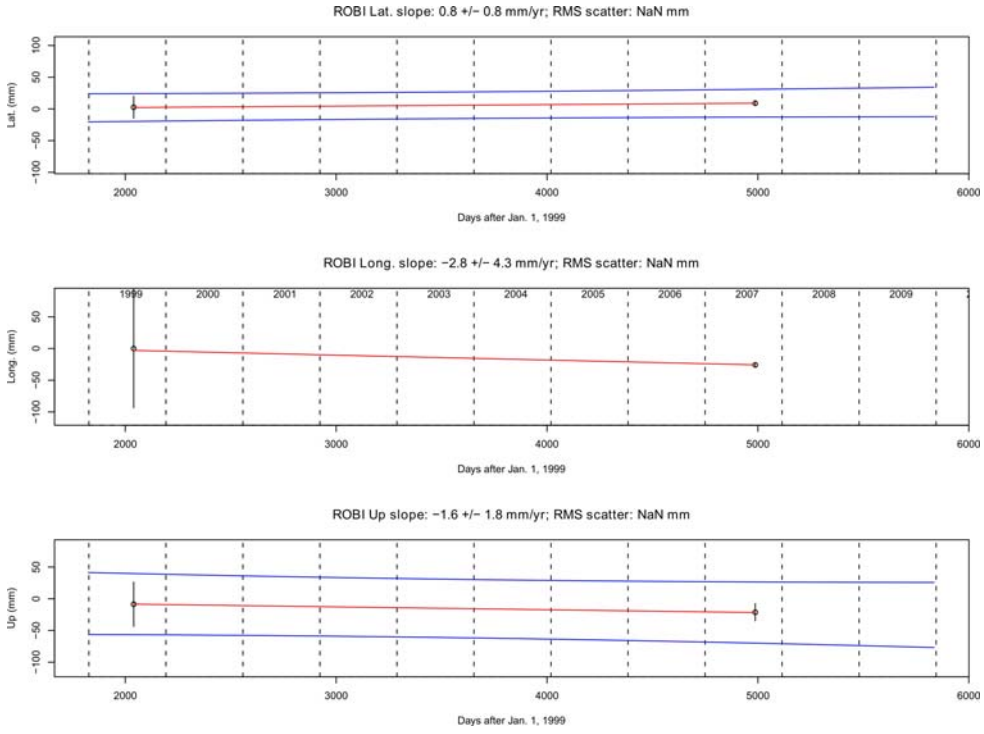

Figure A-86: Time-series for ROBI, reference station DRAO

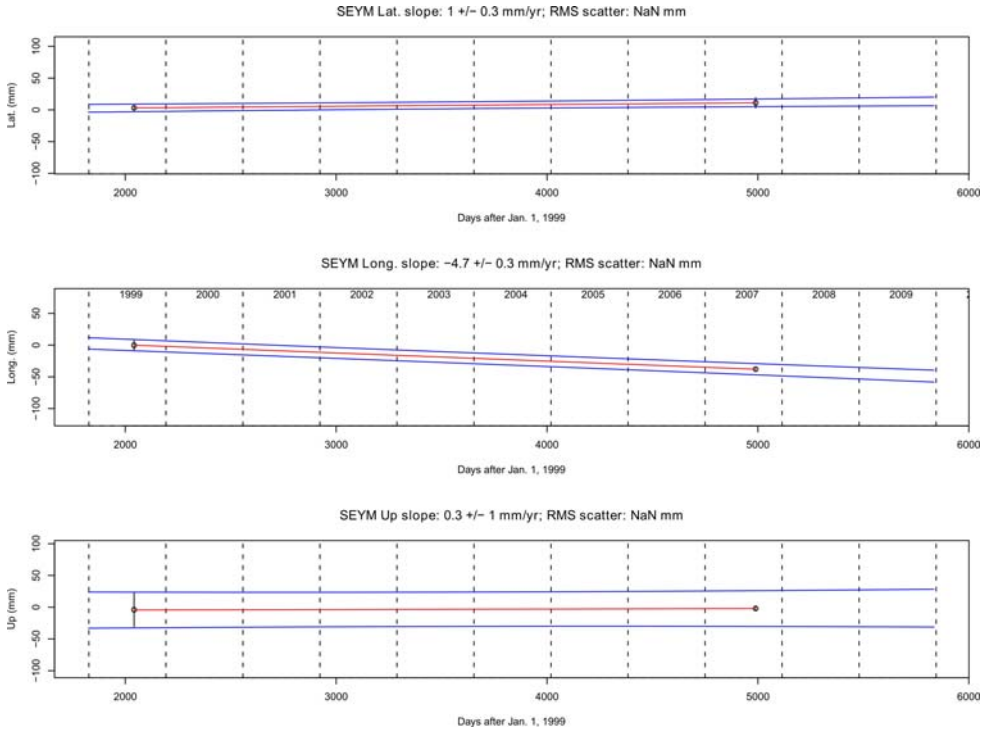

Figure A-87: Time-series for SEYM, reference station DRAO

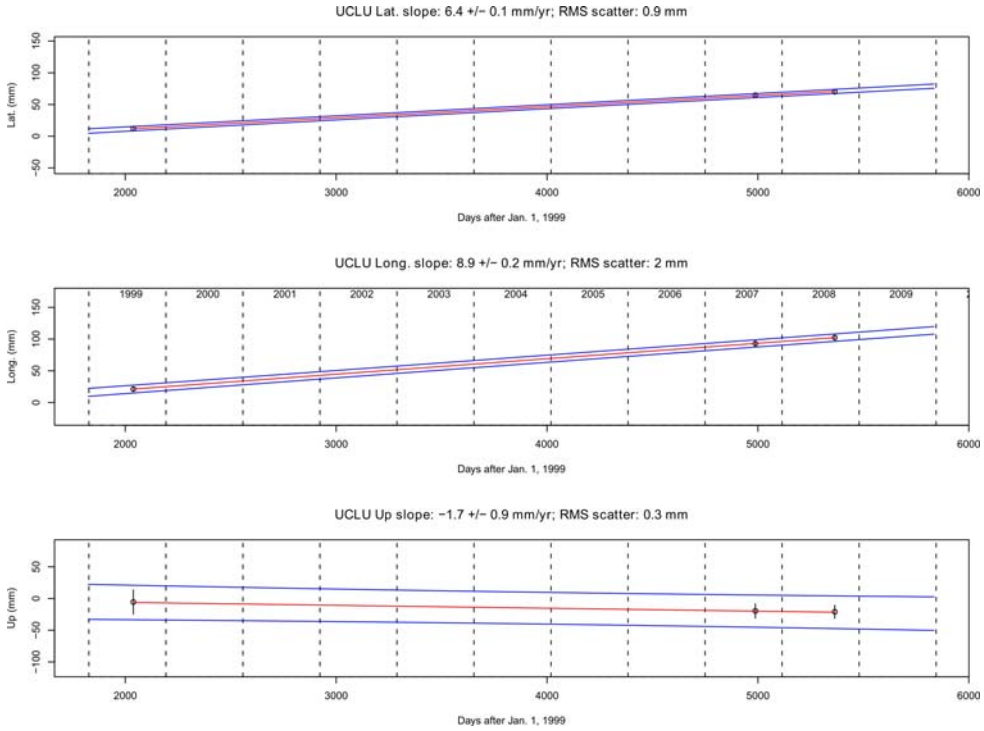

Figure A-88: Time-series for UCLU, reference station DRAO

Table A- 19: GPS site velocities for 1999 – 2008, absolute PCVs and orbits for 1999 data

STATION	Latitude	Longitude	Vn	Ve	Vu	σn	σe	σu	Network
ALBH	48.39	236.51	3.1	4.7	-3.1	0.2	0.1	0.9	WCDA-PANGA
ALIC	50.46	232.48	1.8	-0.3	1.1	0.4	0.3	2.3	QCS
CALV	51.54	232.05	1.9	-1.6	-2.1	1.8	2	5.2	QCS
CHWK	49.16	237.99	0.6	1.5	-3.4	0.2	0.2	0.9	WCDA-PANGA
FHAR	50.08	232.83	3.5	2.9	0.4	0.6	0.5	1.7	QCS
KING	51.85	232.23	0.6	-2.5	-0.8	0.3	0.3	1.5	QCS
NANO	49.29	235.91	3.4	3.8	-2.1	0.2	0.2	0.6	WCDA-PANGA
PGC5	48.65	236.55	3.1	4.3	0.4	0.1	0.2	0.7	WCDA-PANGA
ROBI	51.19	232.40	0.8	-2.8	-1.6	0.8	4.3	1.8	QCS
SEYM	51.46	232.72	1	-4.7	0.3	0.3	0.3	1	QCS
UCLU	50.68	231.67	6.4	8.9	-1.7	0.1	0.2	0.9	WCDA-PANGA
WILL	52.24	237.83	-0.3	-1.6	1.3	0.1	0.2	0.6	WCDA-PANGA
WSLR	50.13	237.08	0.6	1.7	-1.5	0.2	0.2	1	WCDA-PANGA

Time-series campaign GPS sites 1993 – 2008 using relative PCVs and orbits for 1999 data

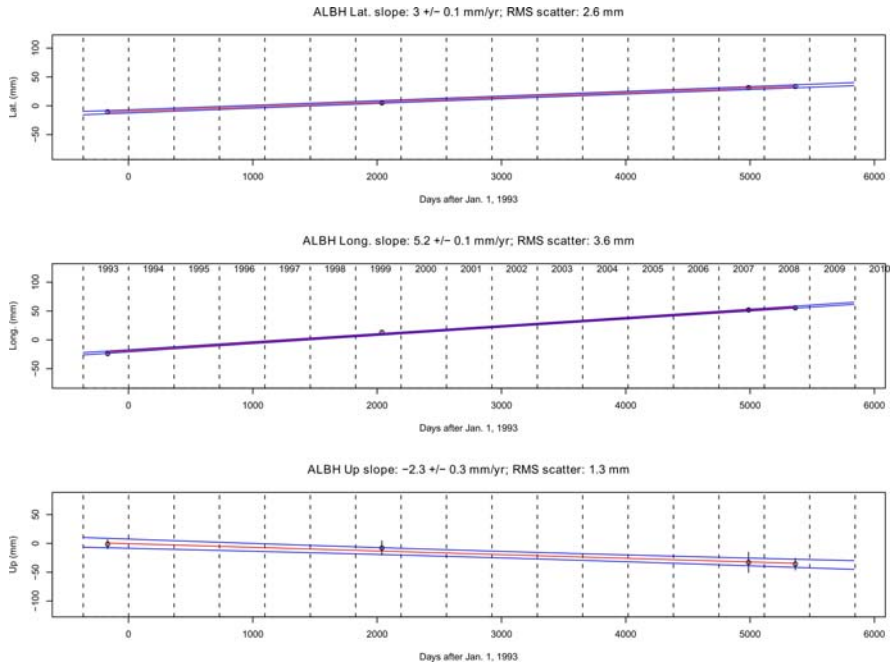

Figure A- 89: Time-series for ALBH, reference station DRAO

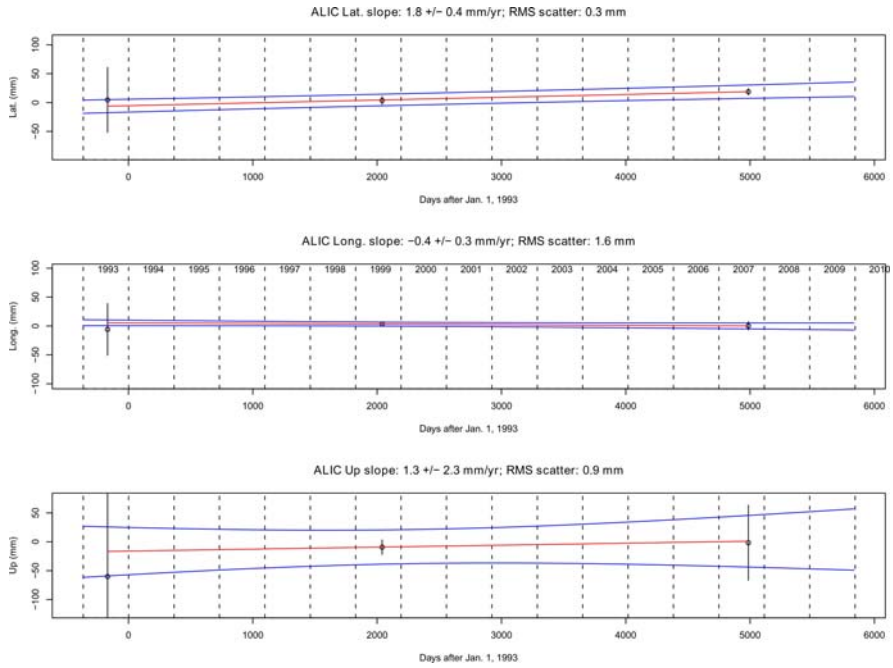

Figure A- 90: Time-series for ALIC, reference station DRAO

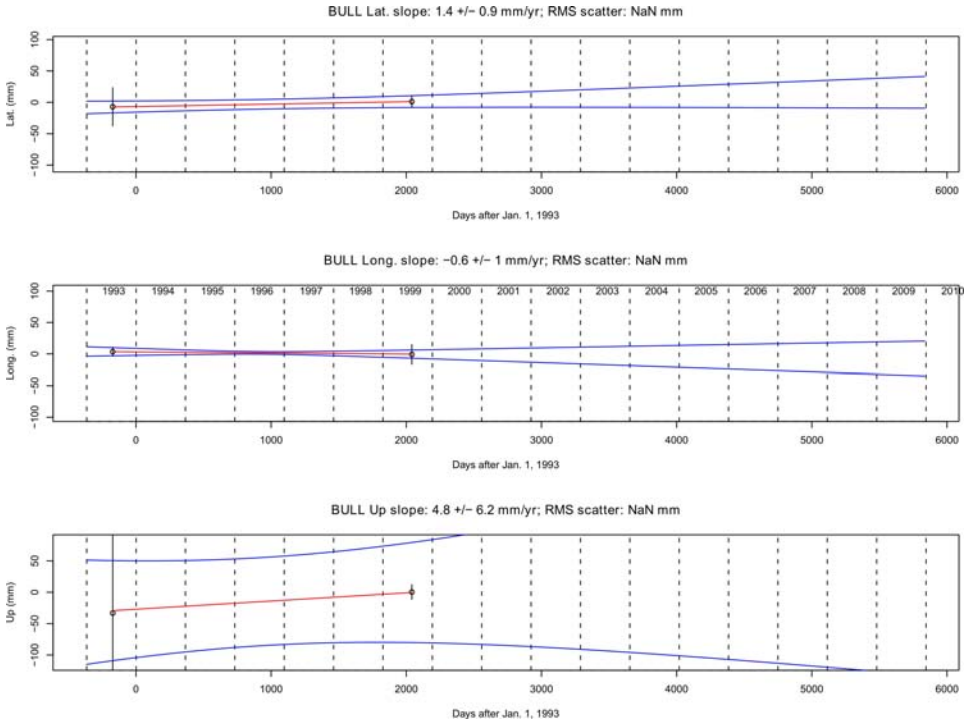

Figure A- 91: Time-series for BULL, reference station DRAO

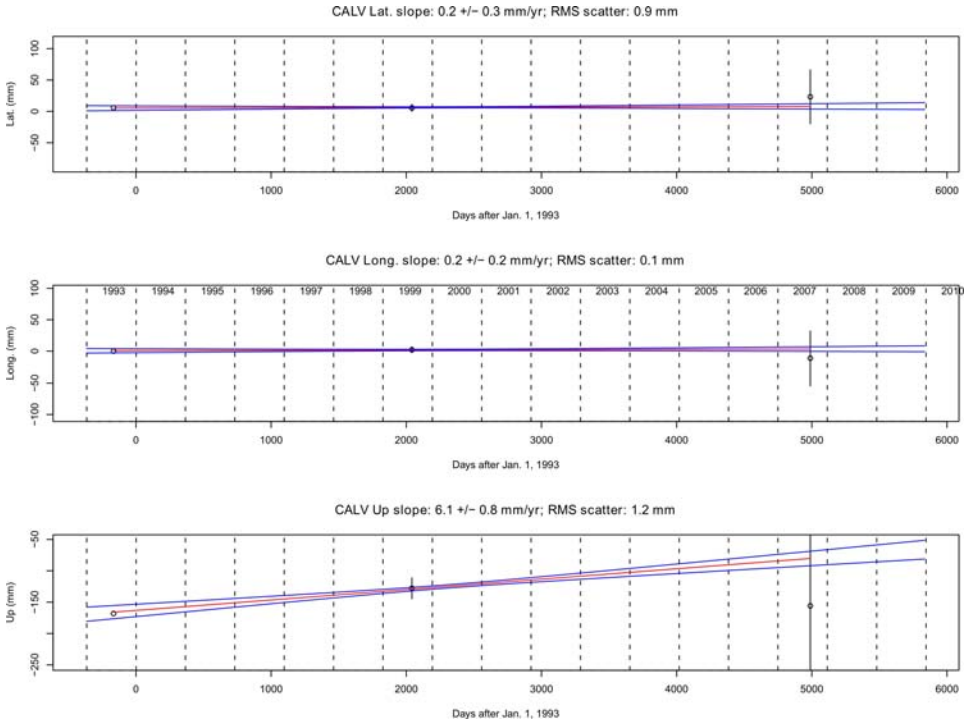

Figure A- 92: Time-series for CALV, reference station DRAO

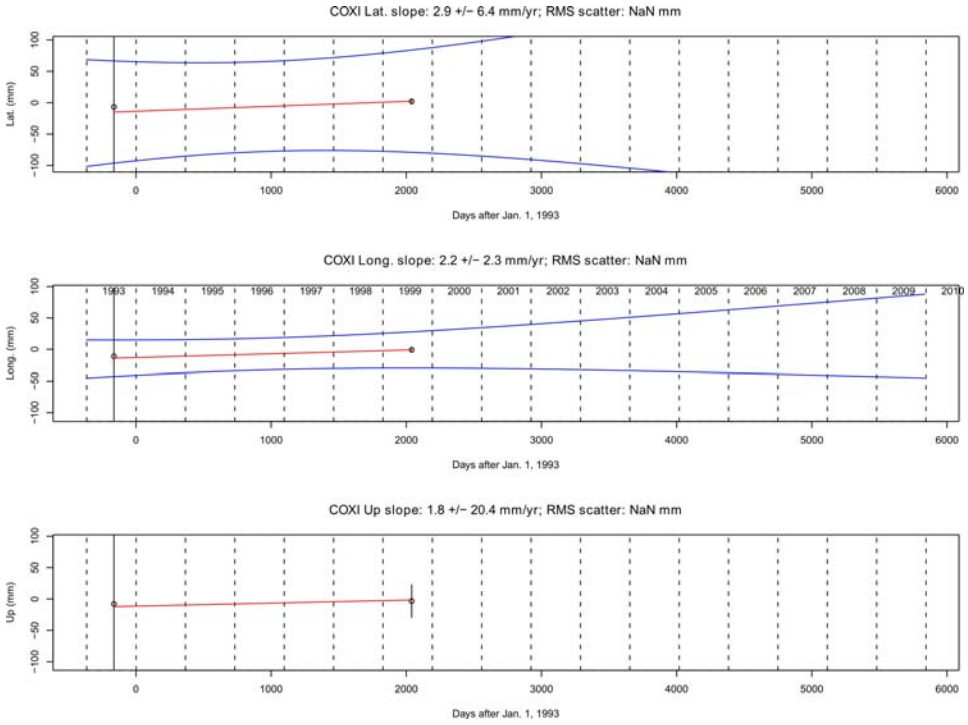

Figure A- 93: Time-series for COXI, reference station DRAO

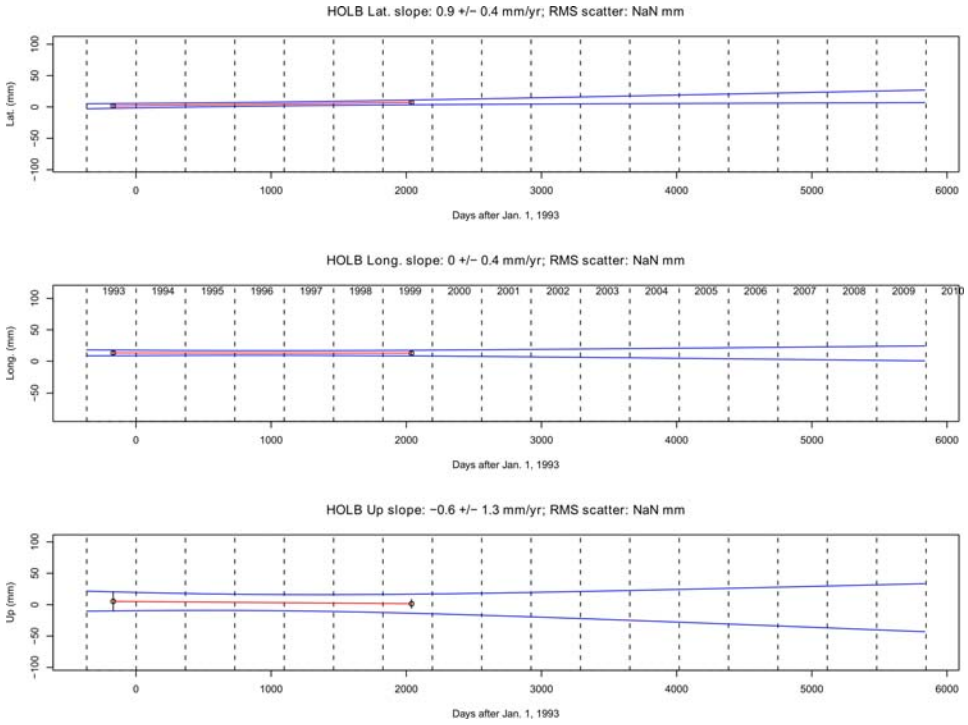

Figure A- 94: Time-series for HOLB, reference station DRAO

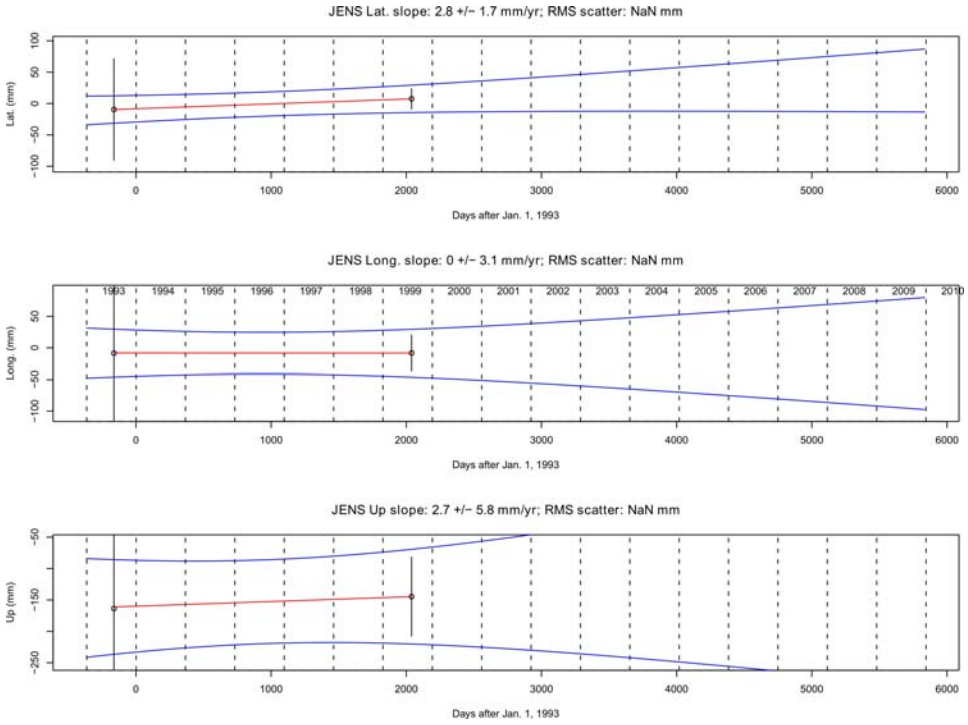

Figure A- 95: Time-series for JENS, reference station DRAO

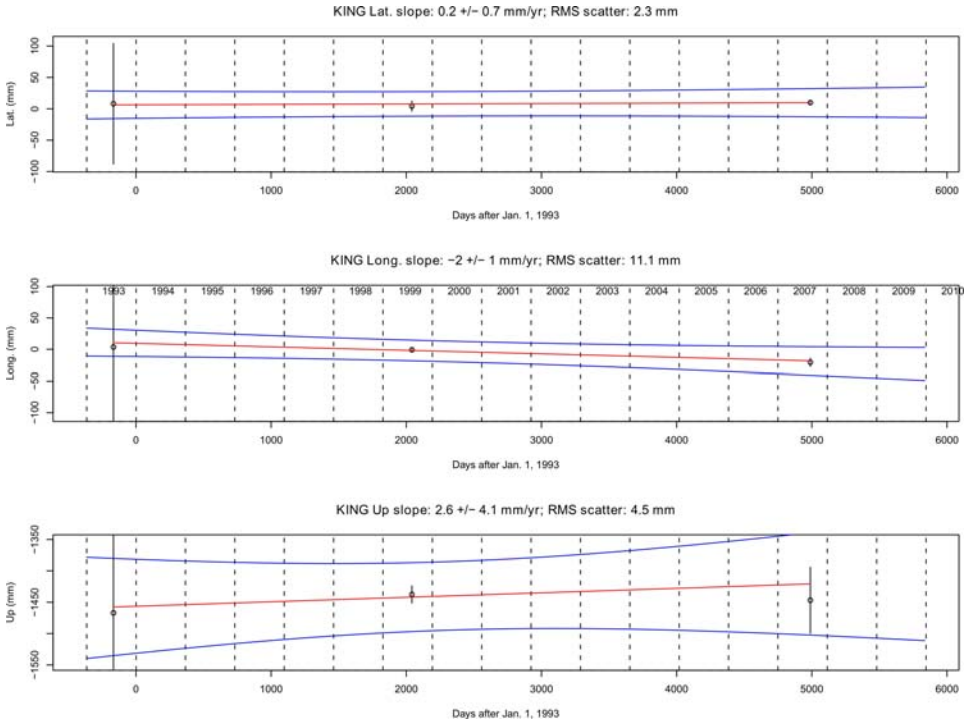

Figure A- 96: Time-series for KING, reference station DRAO

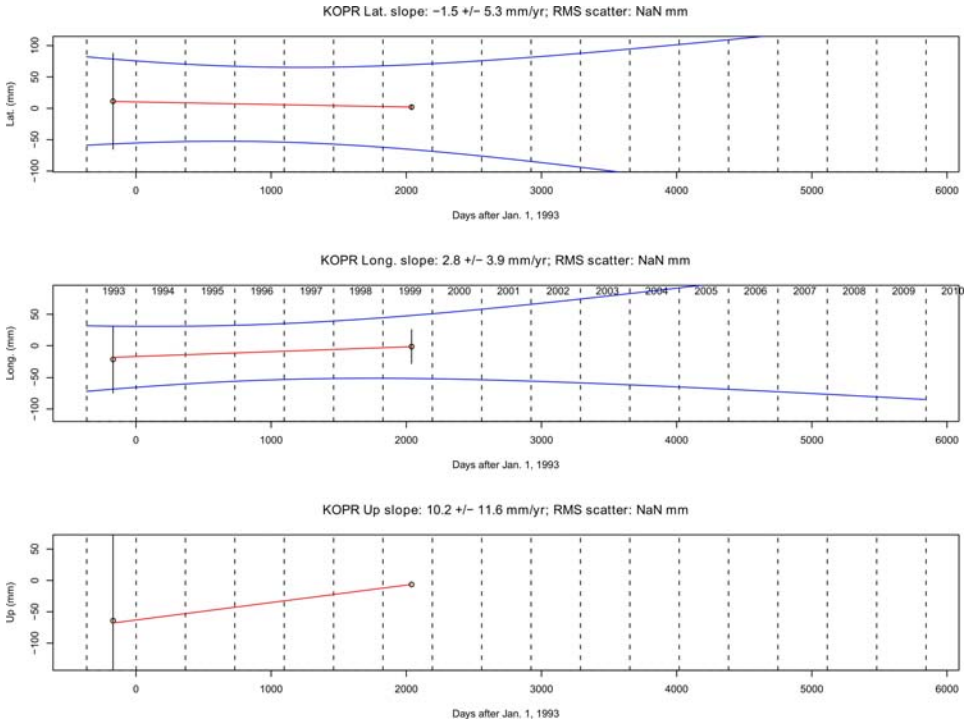

Figure A- 97: Time-series for KOPR, reference station DRAO

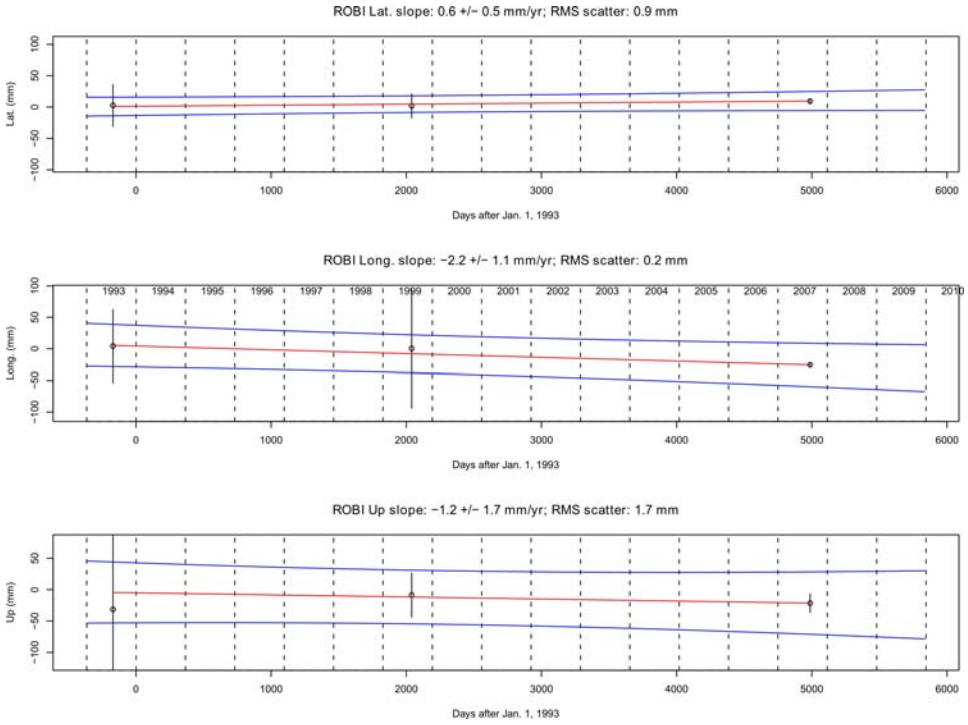

Figure A- 98: Time-series for ROBI, reference station DRAO

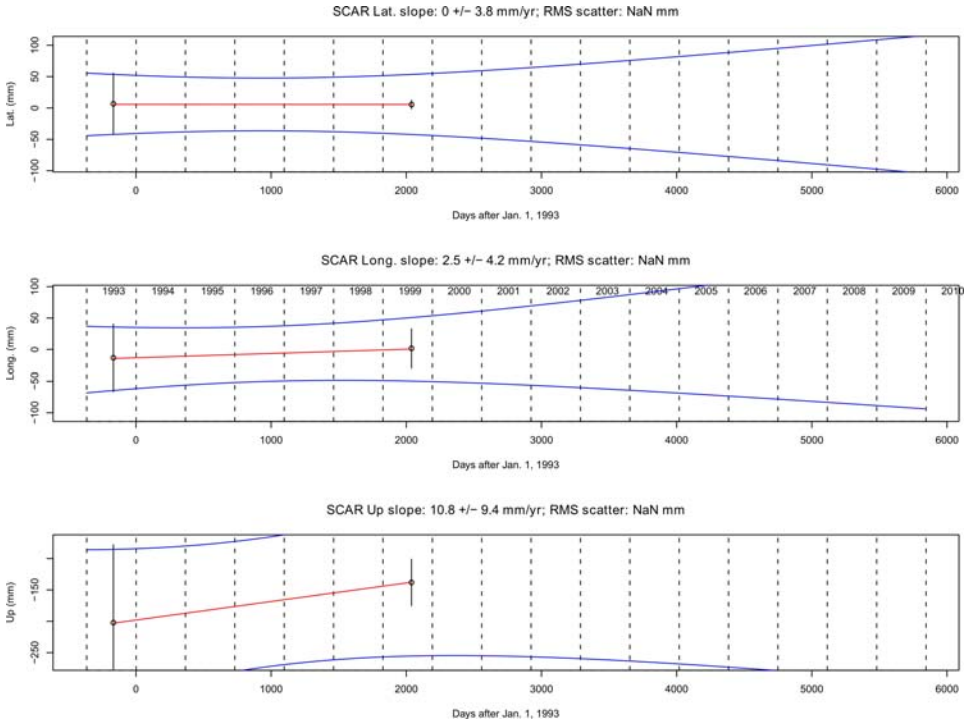

Figure A- 99: Time-series for SCAR, reference station DRAO

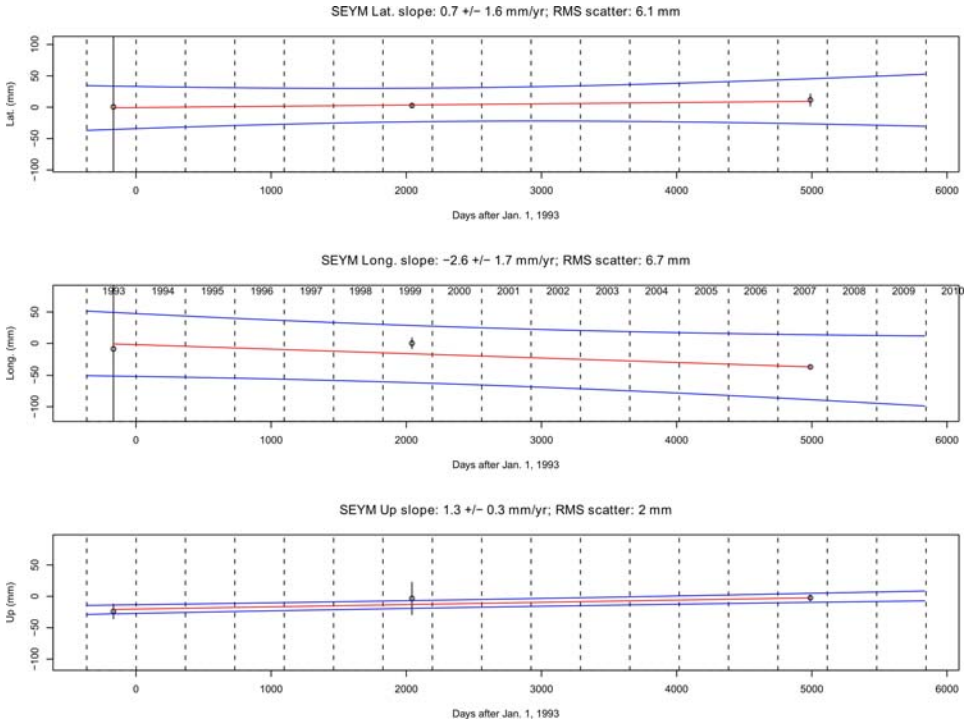

Figure A- 100: Time-series for SEYM, reference station DRAO

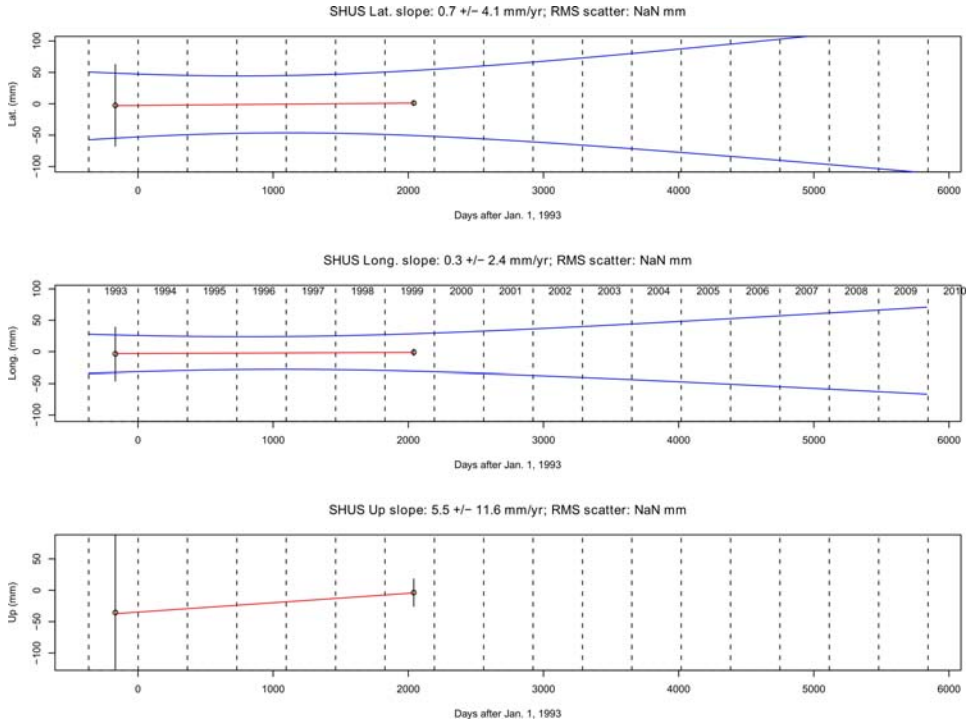

Figure A- 101: Time-series for SHUS, reference station DRAO

Table A- 20: GPS site velocities for 1993 – 2008, relative PCVs and orbits for 1999 data

STATION	Latitude °N	Longitude °E	Vn [mm/yr]	Ve [mm/yr]	Vu [mm/yr]	σn [mm/yr]	σe [mm/yr]	σu [mm/yr]	Network
ALBH	48.39	236.51	3	5.2	-2.3	0.1	0.1	0.3	WCDA-PANGA
ALIC	50.46	232.48	1.8	-0.4	1.3	0.4	0.3	2.3	QCS
BULL	50.96	232.89	1.4	-0.6	4.8	0.9	1	6.2	QCS
CALV	51.54	232.05	0.2	0.2	6.1	0.3	0.2	0.8	QCS
COXI	50.81	231.40	2.9	2.2	1.8	6.4	2.3	20.4	QCS
HOLB	50.65	231.73	0.9	0	-0.6	0.4	0.4	1.3	WCDA-PANGA
JENS	50.65	231.73	2.8	0	2.7	1.7	3.1	5.8	QCS
KING	51.85	232.23	0.2	-2	2.6	0.7	1	4.1	QCS
KOPR	50.49	232.10	-1.5	2.8	10.2	5.3	3.9	11.6	QCS
ROBI	51.19	232.40	0.6	-2.2	-1.2	0.5	1.1	1.7	QCS
SCAR	50.65	231.99	0	2.5	10.8	3.8	4.2	9.4	QCS
SEYM	51.46	232.72	0.7	-2.6	1.3	1.6	1.7	0.3	QCS
SHUS	50.78	232.19	0.7	0.3	5.5	4.1	2.4	11.6	QCS

Time-series campaign GPS sites 1993 – 2008 using absolute PCVs and orbits for 1999 data

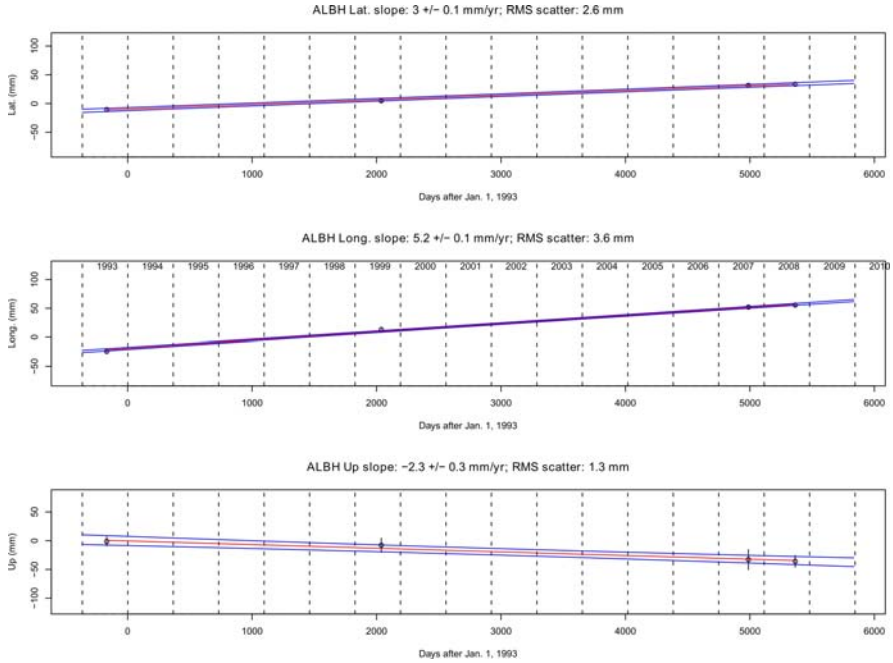

Figure A- 102: Time-series for ALBH, reference station DRAO

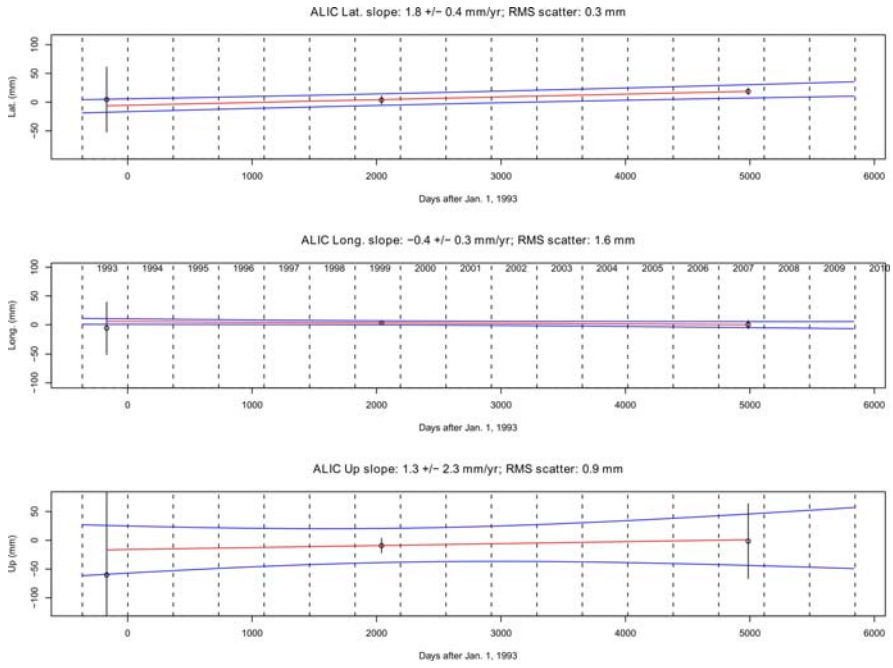

Figure A- 103: Time-series for ALIC, reference station DRAO

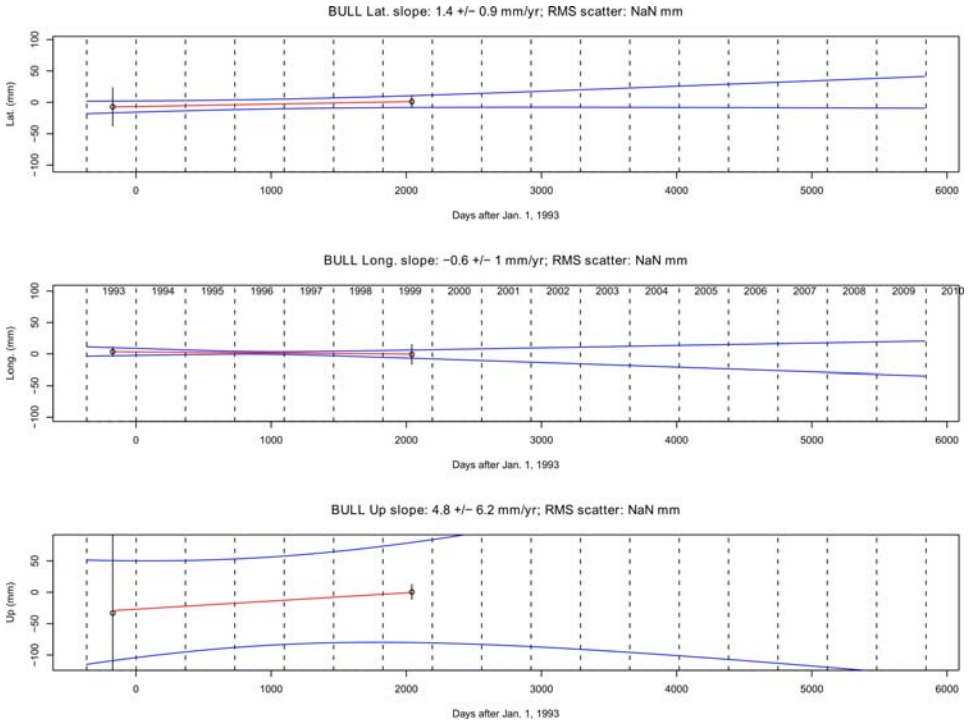

Figure A- 104: Time-series for BULL, reference station DRAO

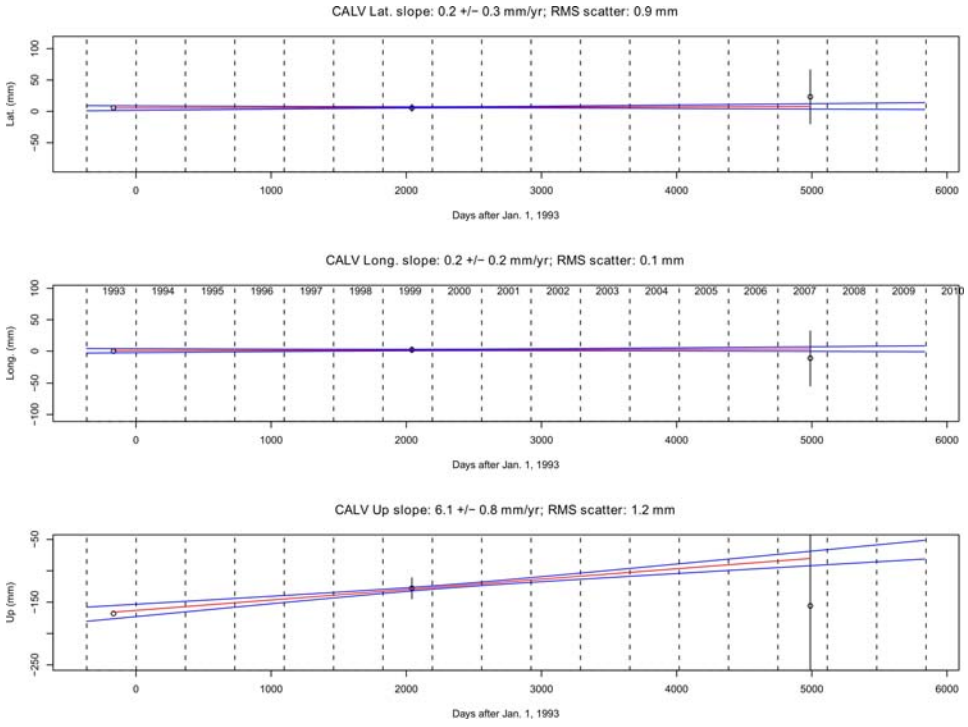

Figure A- 105: Time-series for CALV, reference station DRAO

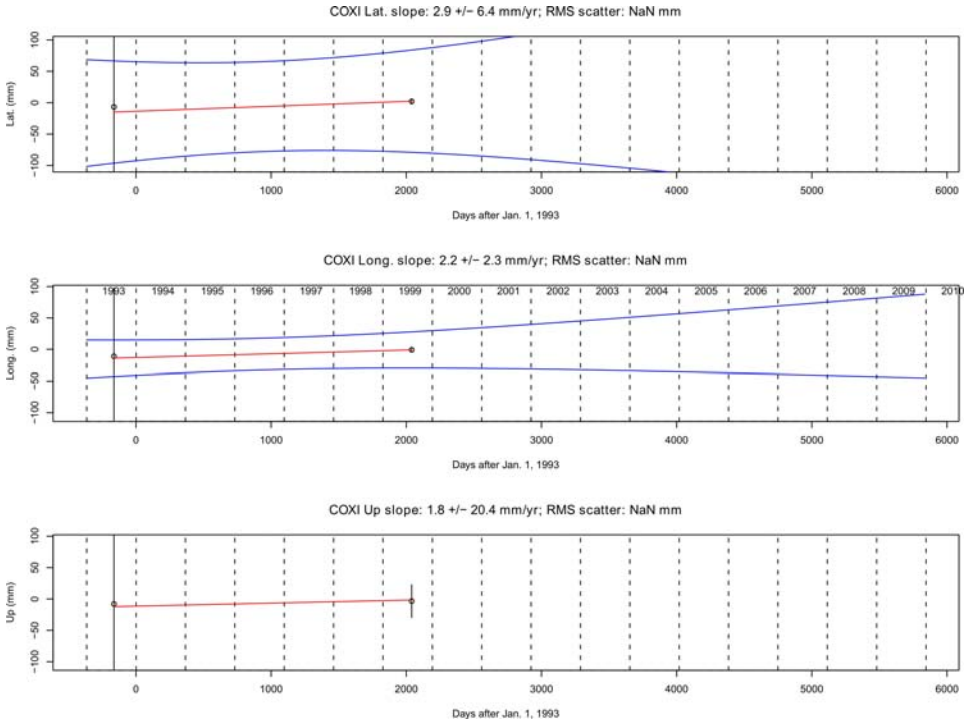

Figure A- 106: Time-series for COXI, reference station DRAO

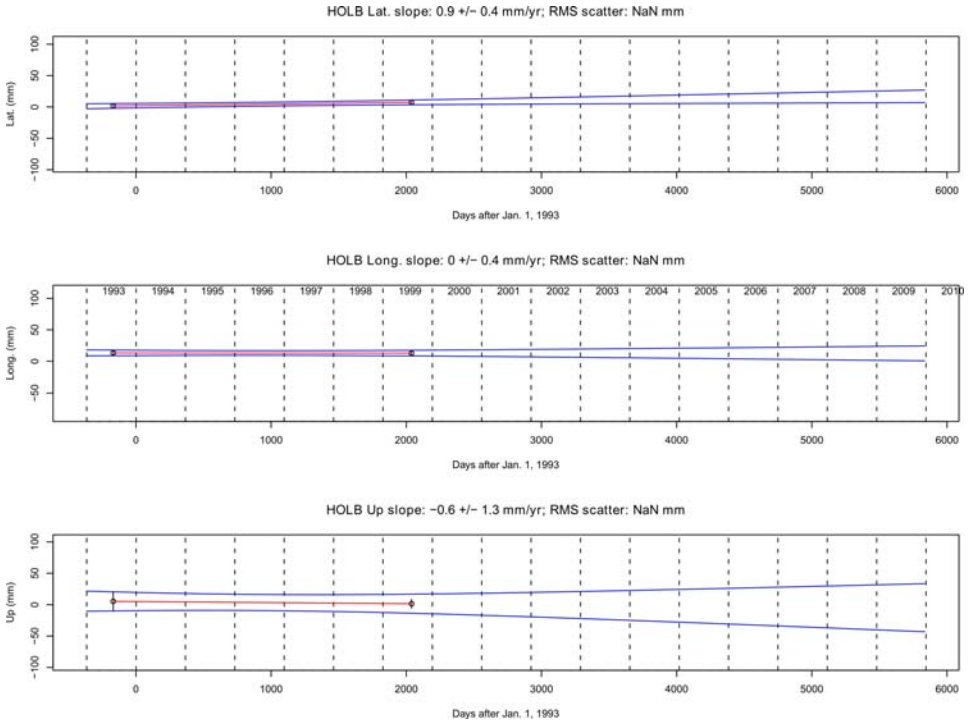

Figure A- 107: Time-series for HOLB reference station DRAO

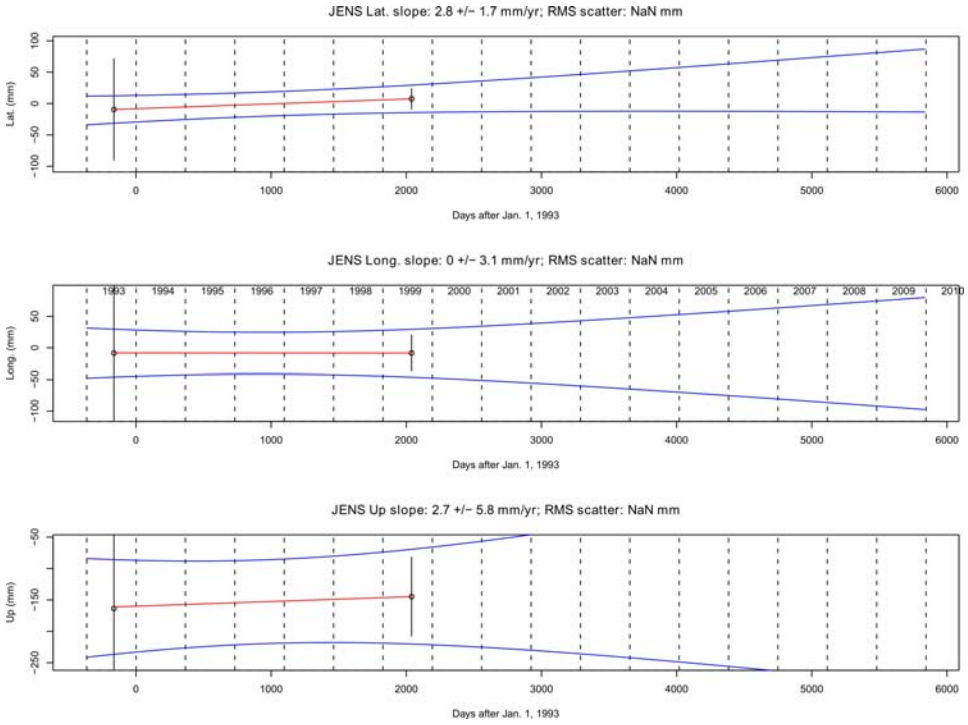

Figure A- 108: Time-series for JENS, reference station DRAO

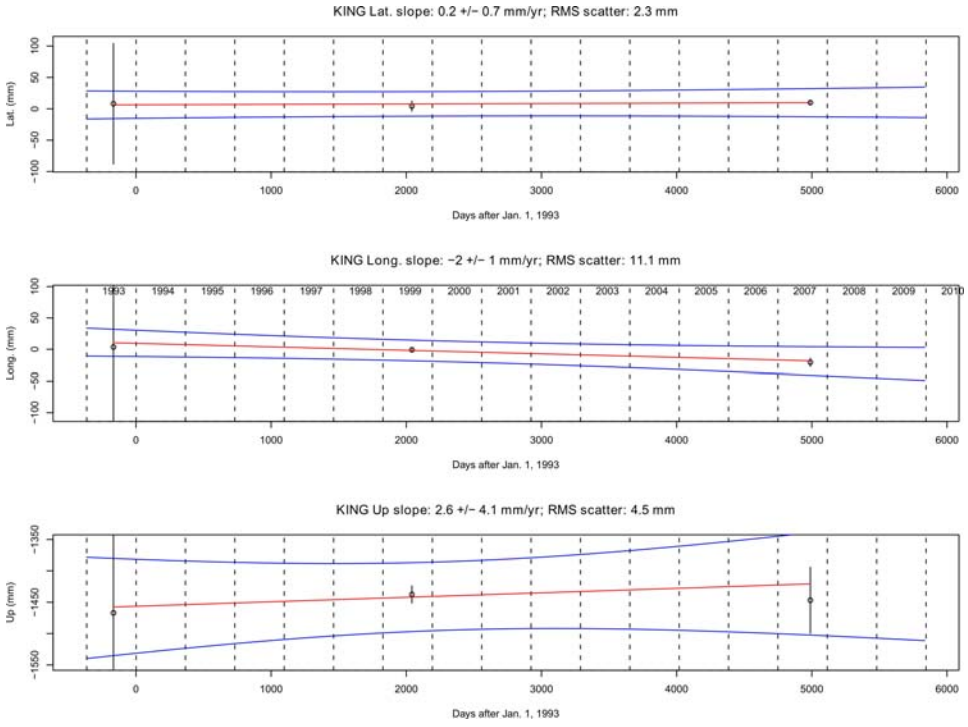

Figure A- 109: Time-series for KING, reference station DRAO

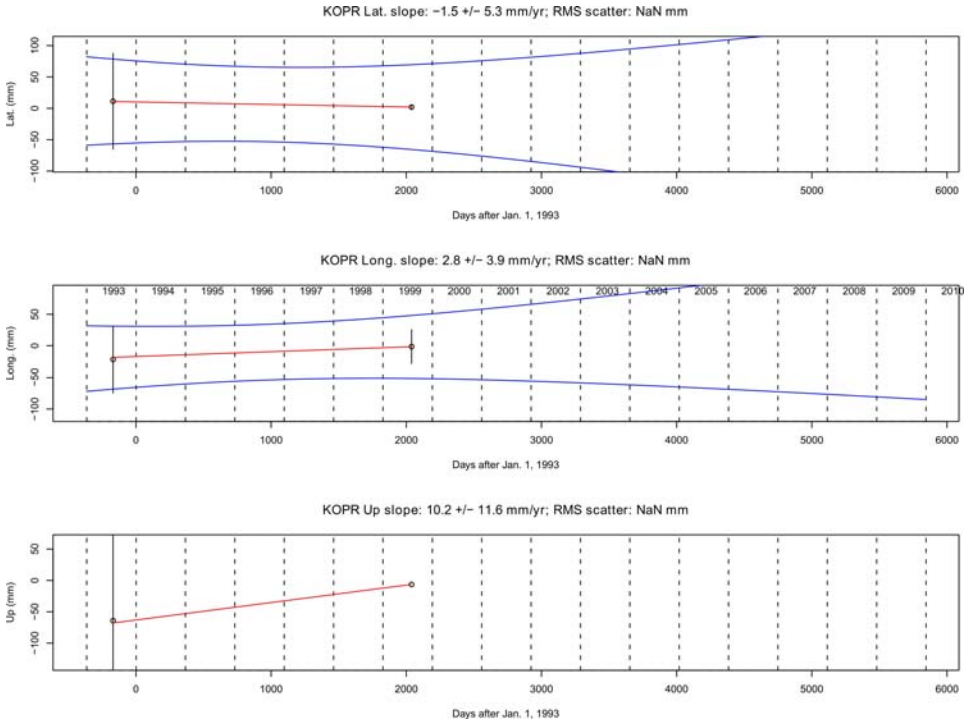

Figure A- 110: Time-series for KING, reference station DRAO

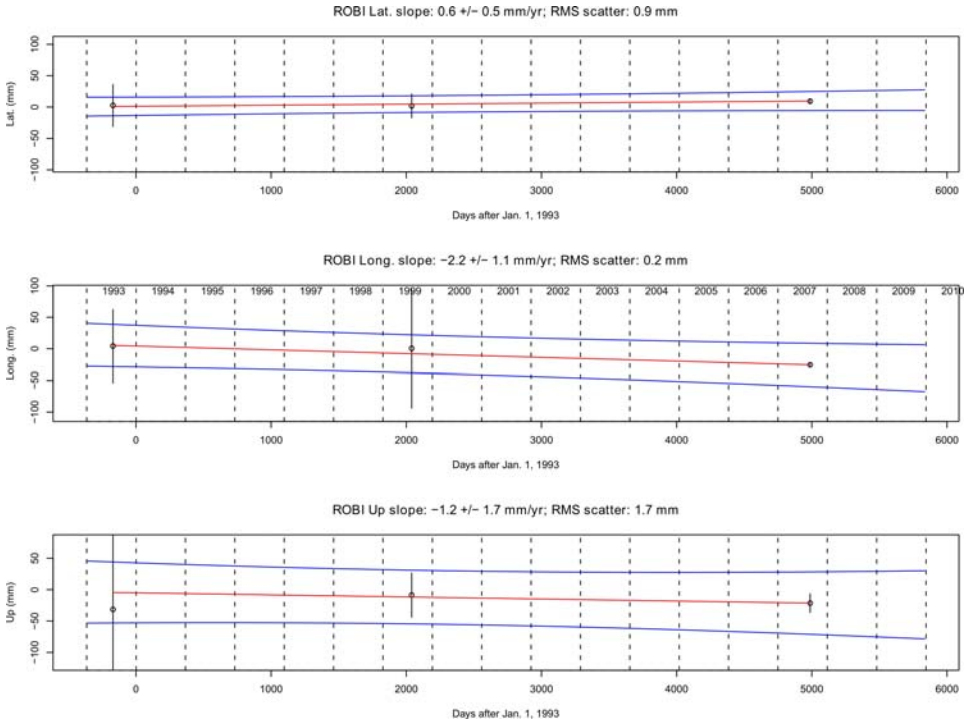

Figure A- 111: Time-series for ROBI, reference station DRAO

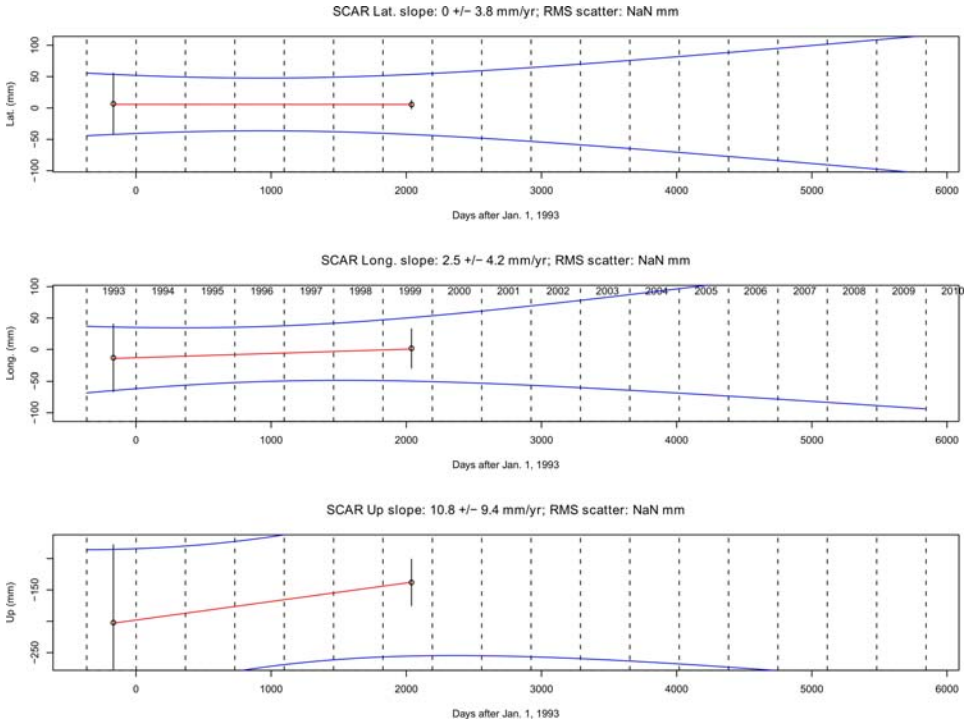

Figure A- 112: Time-series for SCAR, reference station DRAO

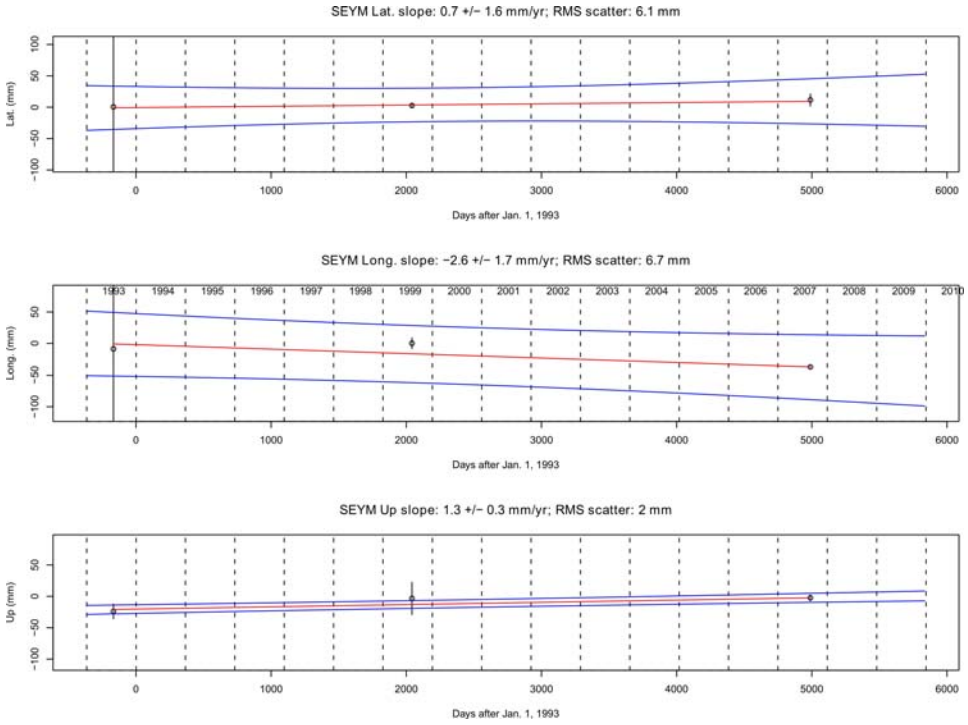

Figure A- 113: Time-series for SEYM, reference station DRAO

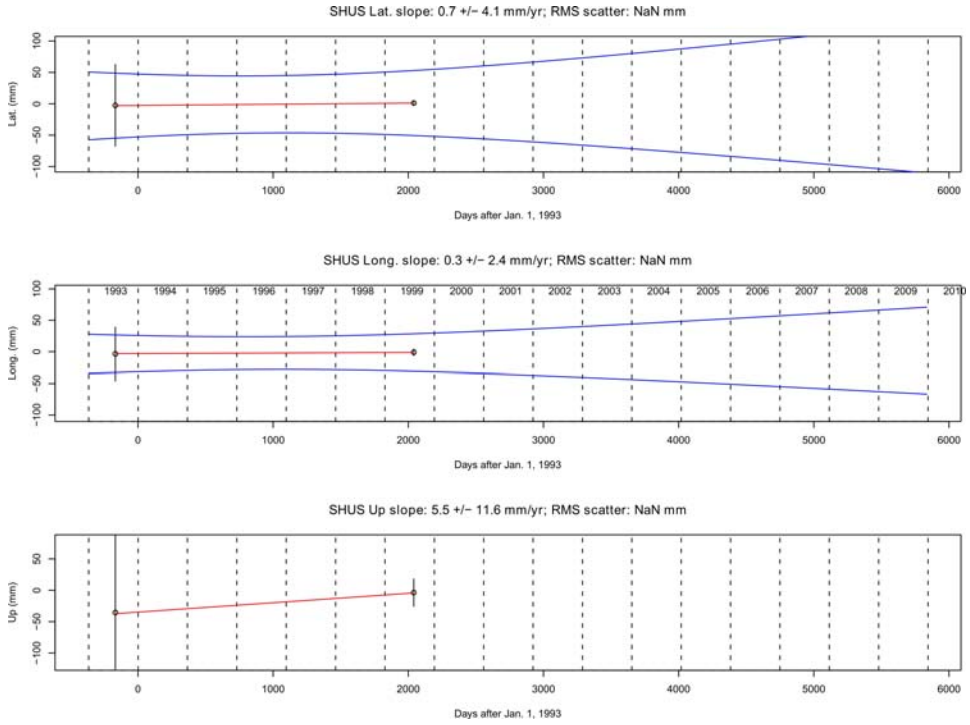

Figure A- 114: Time-series for SHUS, reference station DRAO

Table A- 21: GPS site velocities for 1993 – 2008, absolute PCVs and orbits for 1999 data

STATION	Latitude °N	Longitude °E	Vn [mm/yr]	Ve [mm/yr]	Vu [mm/yr]	σn [mm/yr]	σe [mm/yr]	σu [mm/yr]	Network
ALBH	48.39	236.51	3	5.2	-2.3	0.1	0.1	0.4	WCDA-PANGA
ALIC	50.46	232.48	1.8	-0.3	1.6	0.4	0.3	2.8	QCS
BULL	50.96	232.89	1.5	-0.9	5.1	0.8	0.3	6.7	QCS
CALV	51.54	232.05	0.3	0.2	5.5	0.3	0.3	1	QCS
COXI	50.81	231.40	2.9	1.6	0.9	6.9	2.4	16	QCS
HOLB	50.65	231.73	1	-0.2	-0.9	0.4	0.5	1.2	WCDA-PANGA
JENS	50.65	231.73	3	-0.1	2.5	1.9	2.9	6	QCS
KING	51.85	232.23	0.2	-2.2	2.8	0.6	1.1	4	QCS
KOPR	50.49	232.10	-0.9	3.2	10.9	5.8	3.8	12.2	QCS
ROBI	51.19	232.40	0.6	-2.1	-1.3	0.6	1.2	1.5	QCS
SCAR	50.65	231.99	0.7	2.2	9.2	3.5	3.7	9	QCS
SEYM	51.46	232.72	1.1	-2.8	1.3	1.3	1.7	0.2	QCS
SHUS	50.78	232.19	0.1	0.6	5.3	4	2.4	11	QCS

Appendix B
Different model sets for calculating effective viscosity

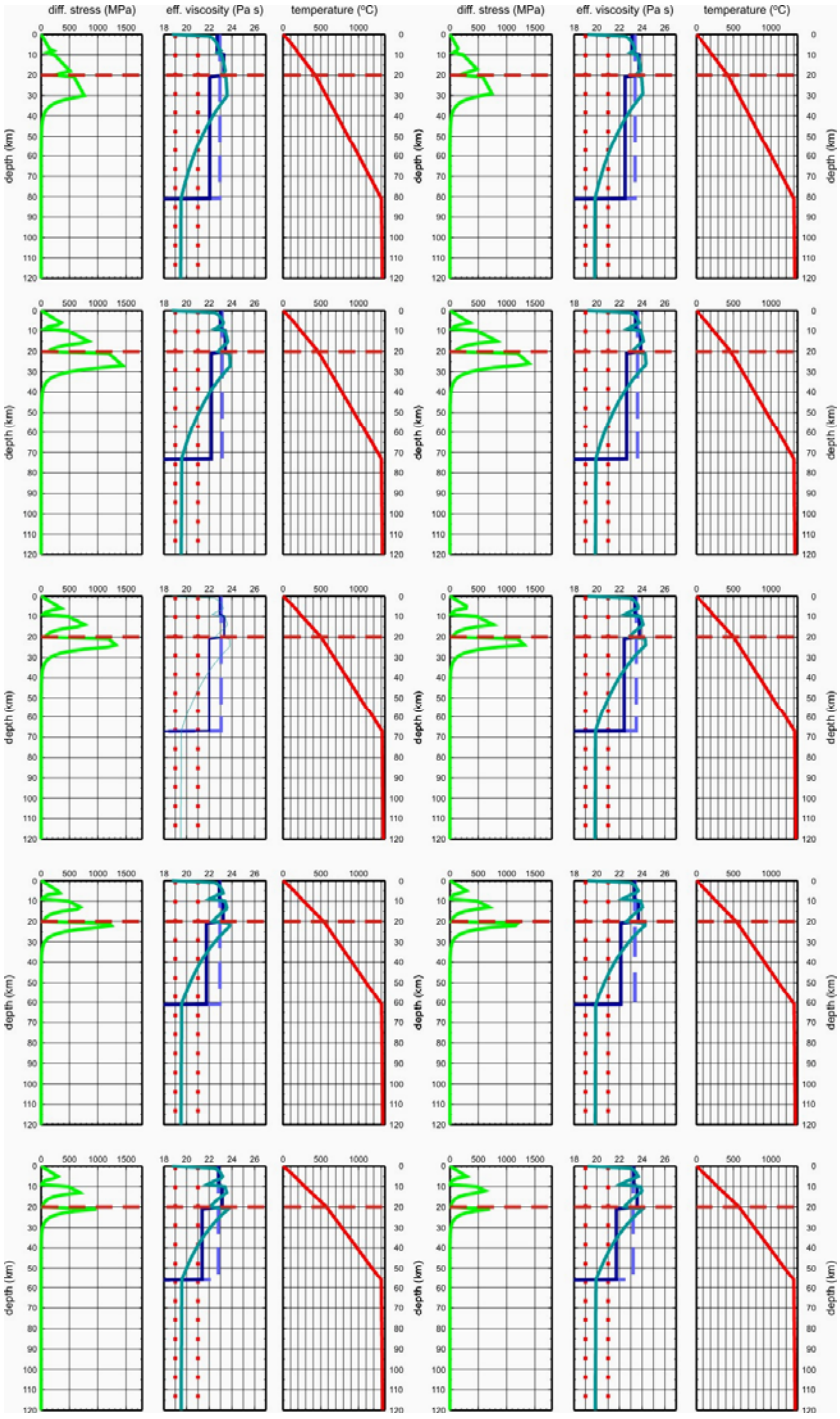

Figure B- 115: Set I (Table 6 -8), strain rate $10^{-15}s^{-1}$ left, $3.2x10^{-16}s^{-1}$ right. Heat flow from top to bottom: 80, 85, 90, 95 mW/m^2. Eff viscosity: dashed dark blue line – av. Viscosity for lithosphere. Solid dark blue line – av. Viscosity for each layer. Solid light blue line – eff. Viscosity.

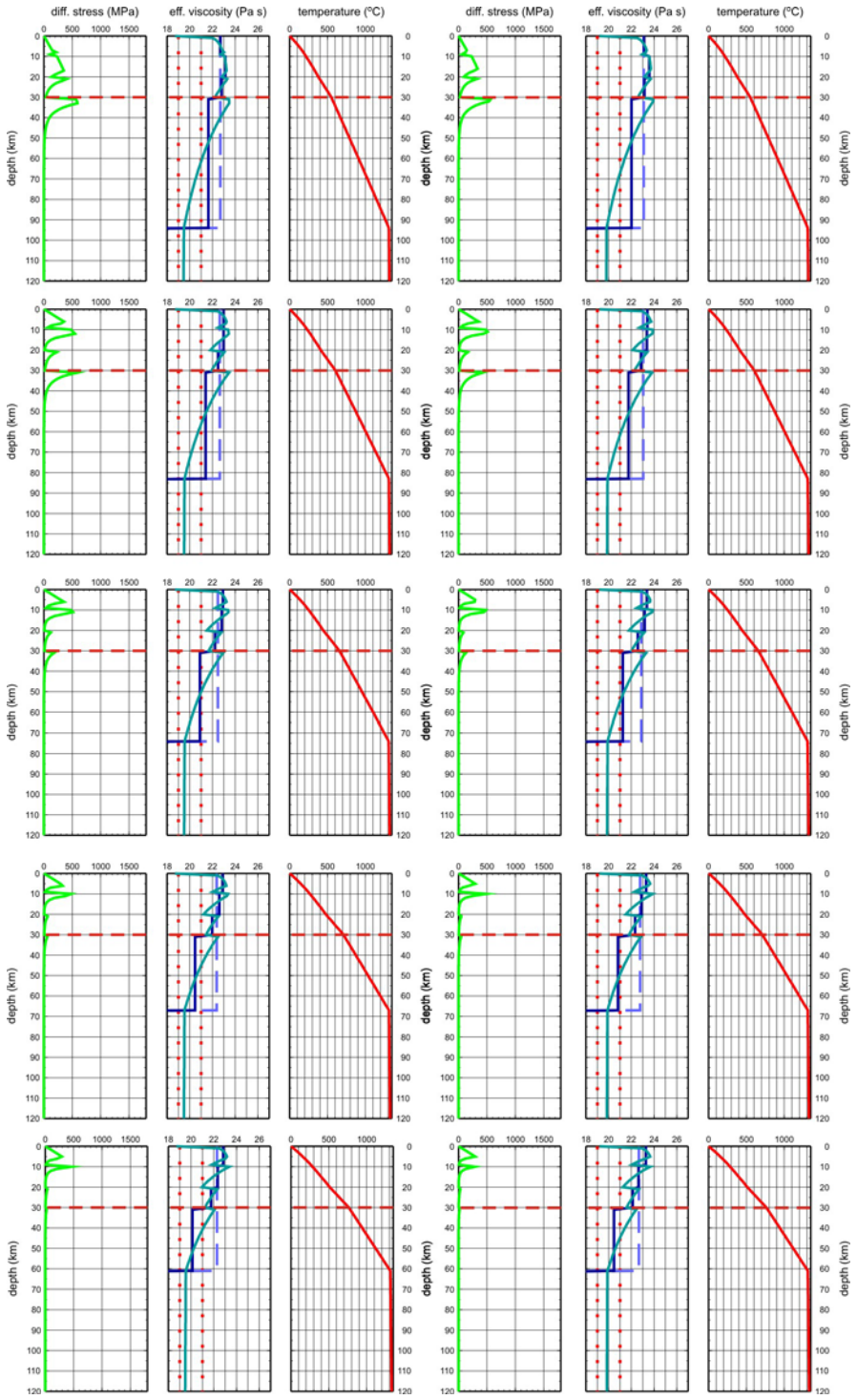

Figure B- 116: Set II (Table 6 – 8), strain rate $10^{-15}s^{-1}$ left, $3.2x10^{-16}s^{-1}$ right. Heat flow from top to bottom: 80, 85, 90, 95 mW/m^2. Eff viscosity: dashed dark blue line – av. Viscosity for lithosphere. Solid dark blue line – av. Viscosity for each layer. Solid light blue line – eff. Viscosity.

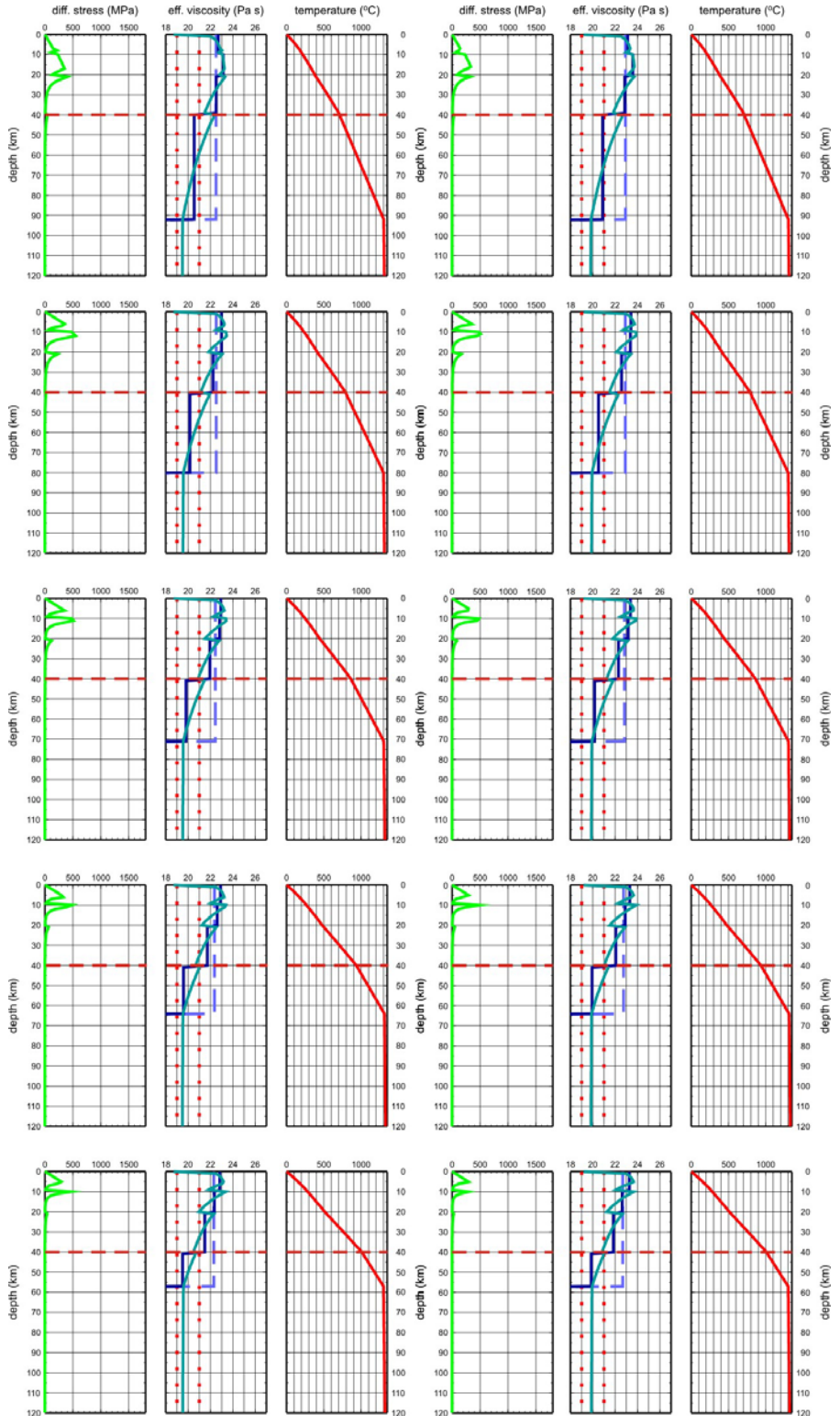

Figure B- 117: Set III (Table 6 – 8), strain rate $10^{-15}s^{-1}$ left, $3.2x10^{-16}s^{-1}$ right. Heat flow from top to bottom: 80, 85, 90, 95 mW/m^2. Eff viscosity: dashed dark blue line – av. Viscosity for lithosphere. Solid dark blue line – av. Viscosity for each layer. Solid light blue line – eff. Viscosity.